

LHCb 上质子-铅核对撞中开粲介子 产生研究

Study of Open Charm Mesons Productions in Proton-Lead Collisions at LHCb

(申请清华大学理学博士学位论文)

培 养 单 位： 工程物理系

学 科： 物理学

研 究 生： 辜 晨 曦

指 导 教 师： 朱 相 雷 副 教 授

二〇二二年十二月

**Study of Open Charm Mesons
Productions in Proton-Lead Collisions at
LHCb**

Dissertation Submitted to

Tsinghua University

in partial fulfillment of the requirement

for the degree of

Doctor of Philosophy

in

Physics

by

Chenxi Gu

Dissertation Supervisor: Professor Xianglei Zhu

December, 2022

学位论文公开评阅人和答辩委员会名单

公开评阅人名单

无（全隐名评阅）

答辩委员会名单

主席	赵 A	教授	A 大学
委员	钱 B	教授	B 大学
	孙 C	研究员	C 科学院
	李 D	教授	D 研究所
	周 E	副教授	E 大学
秘书	吴 F	助理研究员	F 大学
			G 大学

关于学位论文使用授权的说明

本人完全了解清华大学有关保留、使用学位论文的规定，即：

清华大学拥有在著作权法规定范围内学位论文的使用权，其中包括：（1）已获学位的研究生必须按学校规定提交学位论文，学校可以采用影印、缩印或其他复制手段保存研究生上交的学位论文；（2）为教学和科研目的，学校可以将公开的学位论文作为资料在图书馆、资料室等场所供校内师生阅读，或在校园网上供校内师生浏览部分内容；（3）根据《中华人民共和国学位条例暂行实施办法》及上级教育主管部门具体要求，向国家图书馆报送相应的学位论文。

本人保证遵守上述规定。

作者签名： 李晨
日 期： 2022.10.28

导师签名： 李树雷
日 期： 2022.10.28

摘要

量子色动力学 (QCD) 是描述夸克和胶子之间强相互作用的基本理论。在相对论重离子碰撞中, 原本束缚在中子、质子中的夸克、胶子退禁闭形成强耦合 QCD 物质: 夸克胶子等离子体 (QGP)。碰撞中产生的重味强子是 QGP 物态的极好探针: 高横动量重味强子的产额压低有助于定量理解 QGP 的热化和重味夸克在 QGP 中的输运特性; 含奇异夸克的粲强子产额比也有助于理解 QGP 强子化时重味强子的产生机制和 QGP 中的奇异性增强。但是重离子碰撞中与 QGP 产生无关的冷核物质 (CNM) 效应也能影响末态重味强子产生, 如原子核部分子分布函数 (nPDFs) 的修正等。一般认为, 质子-铅核 ($p\text{Pb}$) 对撞由于时空尺度小不足以产生 QGP, 是研究冷核物质效应的理想平台。通过测量其末态重味强子产生能定量约束 nPDFs 等 CNM 效应。另外, 2017 年 ALICE 实验首次在高多重数的质子-质子对撞中观察到了奇异轻强子的产额增强, 意味着在高多重数的小系统中存在 s 夸克产额增强的机制。在高多重数 $p\text{Pb}$ 对撞中寻找奇异粲强子产额增强对于理解这一小系统中的奇异性增强机制和粲强子产生机制也具有重要科学意义。

2016 年, LHCb 探测器采集了积分亮度约为 30.75 nb^{-1} 、核子-核子质心系能量为 8.16 TeV 的 $p\text{Pb}$ 对撞数据。本论文利用这些数据测量了 $p\text{Pb}$ 对撞中前后向瞬发 D_s^+ 和 D^+ 的微分截面, 运动学区间覆盖前向快度区 $1.5 < y < 4.0$ 与后向快度区 $-5.0 < y < -2.5$, 横动量范围为 $1 < p_T < 13 \text{ GeV}/c$ 。基于这些结果计算了核修正因子、前后向截面比, 研究了 CNM 效应对开粲介子截面的影响。此外, 论文还测量了 D_s^+/D^+ 截面比值, 研究了不同横动量和快度区间这一比值随多重数的变化。

核修正因子和前后向截面比的测量表明在 8.16 TeV 的 $p\text{Pb}$ 对撞中存在明显的 CNM 效应。和 pp 对撞相比, D_s^+ 和 D^+ 的微分截面在前向快度区间存在明显的压低, 与 nPDF 和 CGC 的理论计算符合较好, 暗示在小动量分数 x 存在核遮蔽效应。在后向截面的压低效应不明显, 暗示在中等动量分数 x 可能存在核的反遮蔽效应。但在后向高横动量区间, 核修正因子和前后向截面比都与 nPDF 理论存在差异, 预示在 $p\text{Pb}$ 碰撞中后向快度区可能存在未知的核物质效应。测量还首次发现, D_s^+/D^+ 截面比值随碰撞多重数增加而显著增加, 而且在后向低横动量 (12.6σ) 的增强趋势比在高横动量的 (4.9σ) 要更加显著。这一发现表明在高多重数 $p\text{Pb}$ 对撞中, 粲夸克强子化也存在显著的奇异性产额增强, 目前亟需理论对这一增强机制给出解释。

关键词: 夸克胶子等离子体; 冷核物质效应; 质子铅核对撞; 奇异性增强; LHCb

ABSTRACT

Quantum chromodynamics (QCD) is a basic theory to describe the strong interaction between quarks and gluons. In relativistic heavy ion collisions, quarks and gluons originally bound in neutrons and protons are deconfined to form a strong coupling QCD matter: quark gluon plasma (QGP). The heavy flavor hadrons produced in the collision are excellent probes for the state of QGP: the production suppression of high transverse momentum heavy flavor hadrons is helpful to quantitatively understand the QGP and the transport properties of heavy flavor quarks in QGP; The ratio of strange charm hadron to non-strange charm hadron is also helpful to understand the production mechanism of heavy flavor hadrons and the strangeness enhancement in QGP during hadronization. However, cold nuclear matter (CNM) effects can also affect the production of final heavy flavor hadrons in heavy ion collisions, such as the modification of nuclear parton distribution functions (nPDFs). It is generally believed that the proton-lead ($p\text{Pb}$) collision is an ideal platform for studying the effects of cold nuclear matter because the space-time scale is too small to create QGP. CNM effects such as nPDFs can be constrained quantitatively by measuring the final heavy flavor hadron production. In addition, in 2017, ALICE experiment observed for the first time the production enhancement of light strange hadrons in high multiplicity proton-proton collisions, which means that there is an enhancement mechanism for s quark in small systems with high multiplicity. Looking for the enhancement of strange charm hadron yield in high multiplicity $p\text{Pb}$ collisions is also of great scientific significance for understanding the mechanism of strangeness enhancement and charm hadron production in this small system.

In 2016, the LHCb detector collected $p\text{Pb}$ collision data with an integrated luminosity of about 30.75 nb^{-1} and $\sqrt{s_{\text{NN}}} = 8.16 \text{ TeV}$. Using these data, this thesis measured the double differential cross sections of the forward prompt D_s^+ and D^+ in $p\text{Pb}$ collision, covering the forward rapidity region of $1.5 < y < 4.0$ and the backward rapidity region of $-5.0 < y < -2.5$, and the transverse momentum range of $1 < p_{\text{T}} < 13 \text{ GeV}/c$. Based on these results, the nuclear modification factor and the forward-backward ratio are calculated, and the influence of CNM effect on the open charm meson cross section is studied. In addition, this thesis also measured D_s^+/D^+ cross section ratio, and the variation of this ratio with multiplicity in different transverse momentum and rapidity intervals is studied.

The measurements of the nuclear modification factor and the forward-backward ratio show that there is an obvious CNM effect in $p\text{Pb}$ collision at 8.16TeV. Compared with the pp collision, the differential cross sections of D_s^+ and D^+ are significantly depressed in the forward rapidity interval, which is in good agreement with the theoretical calculations of nPDF and CGC, suggesting that there is a nuclear shadowing effect in the small momentum fraction x . The suppression effect in the backward section is not obvious, suggesting that there may be a nuclear anti-shadowing effect in the middle momentum fraction x . However, in the backward high transverse momentum region, there are differences between the nuclear modification factor and the forward-backward ratio and the nPDF theoretical calculation, which indicates that there may be unknown nuclear matter effects in the backward region of $p\text{Pb}$ collision. It is also found for the first time that D_s^+/D^+ cross-section ratio increases significantly with the increase of multiplicity, and the increasing trend in the backward low transverse momentum (12.6σ) is more significant than that in the high transverse momentum (4.9σ). This finding indicates that there is also a significant strangeness enhancement in charm quark hadronization in high multiplicity $p\text{Pb}$ collisions, and there is an urgent need for theory to explain this enhancement mechanism.

Keywords: quark gluon plasma; cold nuclear matter effect; proton-lead collision; strangeness enhancement; LHCb

TABLE OF CONTENTS

摘要.....	I
ABSTRACT	II
TABLE OF CONTENTS	IV
LIST OF FIGURES AND TABLES	VII
LIST OF SYMBOLS AND ACRONYMS	XX
CHAPTER 1 INTRODUCTION	1
1.1 Standard Model and quantum chromodynamics	1
1.2 Deconfinement and Quark–Gluon Plasma	4
1.3 Relativistic heavy ion collisions	5
1.4 Strangeness enhancement	8
1.5 Open heavy flavor in heavy ion collisions.....	9
1.5.1 Open heavy flavor production	10
1.5.2 Hot nuclear matter effects	12
1.5.3 Cold nuclear matter effects.....	13
1.5.4 Heavy flavor hadronisation.....	19
1.6 Strangeness enhancement in small system	21
1.7 Thesis scope	25
CHAPTER 2 THE LHCb EXPERIMENT	28
2.1 The Large Hadron Collider.....	28
2.2 The LHCb experiment	29
2.2.1 Tracking system	31
2.2.2 Particle identification system	37
2.2.3 Trigger system	40
2.3 Datasets	42
2.3.1 Proton-lead data	42
2.3.2 LHCb simulation and proton-lead Monte Carlo data.....	45
2.3.3 Data Preservation.....	46

TABLE OF CONTENTS

CHAPTER 3	ANALYSIS STRATEGY AND SELECTIONS	48
3.1	Analysis strategy.....	48
3.2	Selection criteria.....	50
3.2.1	Online selections	51
3.2.2	Offline selections	52
3.2.3	Event selections.....	53
CHAPTER 4	SIGNAL YIELD DETERMINATION.....	58
CHAPTER 5	EFFICIENCIES CORRECTION	65
5.1	Geometrical acceptance efficiency	65
5.2	Reconstruction and selection efficiency	66
5.2.1	Truth matching.....	67
5.2.2	Tracking correction	67
5.2.3	Multiplicity.....	68
5.3	PID efficiency	70
5.4	Trigger efficiency	72
5.5	Total efficiency	73
CHAPTER 6	SYSTEMATIC UNCERTAINTIES	81
6.1	Signal yield determination	81
6.2	Efficiencies	83
6.3	Other systematics	85
6.4	Summary of systematic uncertainties.....	85
CHAPTER 7	RESULTS AND DISCUSSION	93
7.1	Production cross-section.....	93
7.2	Nuclear modification factor	94
7.3	Forward-backward ratio	97
7.4	D_s^+/D^+ cross-section ratio.....	117
CHAPTER 8	SUMMARY AND OUTLOOK	126
8.1	Summary.....	126
8.2	Outlook	127
REFERENCES	130
APPENDIX A	EFFICIENCY TABLES.....	140

TABLE OF CONTENTS

APPENDIX B	YIELDS AND FRACTIONS	167
APPENDIX C	MASS FIT RESULTS	182
APPENDIX D	$\text{LOG}_{10}\chi_{\text{IP}}^2$ FIT RESULTS	190
APPENDIX E	THE INTERPOLATION OF D_S^+ AND D^+ CROSS-SECTIONS IN PP AT 8.16 TEV	198
ACKNOWLEDGEMENTS	200
声 明	201
RESUME	202
COMMENTS FROM THESIS SUPERVISOR	203
RESOLUTION OF THESIS DEFENSE COMMITTEE	204

LIST OF FIGURES AND TABLES

Figure 1.1	Elementary particles in the Standard Model	2
Figure 1.2	Summary of measurements of α_s as a function of the energy scale $Q^{[7]}$...	3
Figure 1.3	The normalized pressure, energy density, and entropy density as a function of the temperature from lattice QCD calculations ((2+1)-flavor) at zero net baryon density. The predictions of the hadron resonance gas (HRG) model are also shown with same color lines. This horizontal dotted line represents the ideal gas (or Stefan-Boltzmann) limit, which is the limit without interaction. The vertical yellow band indicates the crossover temperature region. This figure is taken from Ref. [10]	5
Figure 1.4	A sketch of the current understanding of the QCD phase diagram as a function of temperature and the baryon chemical potential. This figure is taken from Ref. [13].....	6
Figure 1.5	The main evolution stages of heavy ion collisions ^[23]	7
Figure 1.6	The lowest order QCD diagrams for $s\bar{s}$ production ^[25]	9
Figure 1.7	Hyperon-to-pion ratios as a function of $\langle N_{\text{part}} \rangle$, for AA and pp collisions at LHC and RHIC energies ^[31]	10
Figure 1.8	The parton distribution functions at $Q^2 = 10 \text{ GeV}^2$ and $Q^2 = 10^4 \text{ GeV}^2$ (MMHT2014 NNLO), with associated 68% confidence-level uncertainty bands ^[39]	11
Figure 1.9	The nuclear modification factors, R_{AA} , of prompt D -mesons in the 0–10% centrality class compared to those of charged pions, charged particles, inclusive J/ψ measured by ALICE, and of prompt and non-prompt J/ψ from CMS. This figure is taken from Ref. [43].....	13
Figure 1.10	The R_{AA} and the elliptic flow of prompt D mesons ^[43] and pions as a function of p_T , and compared with predictions from the models based on pQCD calculations (CUJET3.1 ^[44] , DREENA-A ^[45] , SCET _{M,G} ^[46]).....	14
Figure 1.11	The prompt D -meson R_{AA} as a function of p_T measured in Pb–Pb collisions at $\sqrt{s_{NN}} = 5.02 \text{ TeV}$ in different centrality class (0–10%, 30–50% ^[43] , 60–80% ^[47]), compared to that in p –Pb collisions ^[48]	15
Figure 1.12	A typical modification of parton distribution functions in nucleus ^[57] ...	16

LIST OF FIGURES AND TABLES

Figure 1.13	(left) $R_g^{\text{Pb}}(x, Q^2)$ calculated by EPPS16 and EPPS21. (right) The data used in EPPS21 displayed on the (x, Q^2) plane.....	17
Figure 1.14	The (x, Q^2) coverage of several experiments.	17
Figure 1.15	The phase–diagram for QCD evolution ^[68]	18
Figure 1.16	Saturation momentum as a function of momentum fraction x and atomic number A ^[70]	19
Figure 1.17	Charm quark fragmentation into charm hadrons measured in different collisions and energies ^[77]	20
Figure 1.18	Top: D_s^+/D^0 ratios as a function of p_T in 0–10% (left panel) and 30–50% (middle panel) centrality classes in PbPb collisions at $\sqrt{s_{NN}} = 5.02$ TeV and in pp collisions (right panel) at the same centre-of-mass energy. Bottom: D_s^+/D^0 ratios in PbPb collisions divided by those in pp collisions, in 0–10% (left panel) and 30–50% (right panel) centrality classes, compared with theoretical calculations ^[83]	21
Figure 1.19	Top: D_s^+/D^0 ratios as a function of p_T in various centrality classes in AuAu collisions at $\sqrt{s_{NN}} = 200$ GeV ^[84] , compared to a PYTHIA simulation for pp collisions at the same energy. Bottom: STAR results of D_s^+/D^0 ratios as a function of p_T in AuAu collisions at $\sqrt{s_{NN}} = 200$ GeV ^[84] , compared to ALICE results in PbPb ^[43] and pp ^[86] collisions at $\sqrt{s_{NN}} = 5.02$ TeV, as well as to the PYTHIA simulations for pp collisions at the same energies.	22
Figure 1.20	The ratios of strange hadron yields to pions as a function of multiplicity (p_T integrated) from pp , $p\text{Pb}$ and PbPb collisions at LHC energies. The data is compared with theoretical calculations ^[90-92] . This figure is taken from Ref. [87].	23
Figure 1.21	Strange hadrons over non-strange hadrons yield ratios as a function of charged particle multiplicity in different collision systems ^[95]	24
Figure 1.22	Strings overlap with each other in a simulated pp collisions. This figure is taken from Ref. [97].....	25
Figure 1.23	Ratio of yield of strange hadrons to pions as a function of multiplicity at mid-rapidity from PYTHIA8 with and without rope hadronization, and compared to ALICE data ^[103]	26
Figure 1.24	B_s^0/B^0 ratios as a function of normalized event multiplicity in different p_T ranges in pp collisions at $\sqrt{s} = 13$ TeV ^[104]	27

LIST OF FIGURES AND TABLES

Figure 1.25	D_s^+/D^+ ratios as a function of the event charged particle multiplicity in pp , pPb and $PbPb$ collisions at 5 TeV ^[48]	27
Figure 2.1	Schematic layout of the CERN accelerator complex ^[106]	29
Figure 2.2	Angular distribution of $b\bar{b}$ pair production in pp collisions at $\sqrt{s} = 14\text{TeV}$ ^[110]	30
Figure 2.3	An overview of the LHCb detector in Run 1&2 ^[111]	31
Figure 2.4	Top left: the LHCb VELO vacuum tank. Top right: the silicon sensors and readout hybrids. Bottom: the VELO sensors along z and cross-section of a VELO sensor in the xy plane. The detector is shown in its closed position ^[112]	32
Figure 2.5	Left: VELO tracking efficiency in data and simulation from 2011 as a function of the number of reconstructed tracks in the event. Right: IP resolution as a function of momentum ^[112]	33
Figure 2.6	Left: the scheme of the LHCb dipole magnet. Right: the magnetic field intensity as a function of z ^[113]	33
Figure 2.7	A layout of the third TT detection layer ^[113]	34
Figure 2.8	A layout of IT detector ^[113]	35
Figure 2.9	A layout of the OT detector ^[114]	35
Figure 2.10	An overview of the various track types and y -axis magnetic field intensity as a function of the z coordinate ^[111]	37
Figure 2.11	An overview of the RICH 1 (left) & 2 (right) detectors ^[113]	38
Figure 2.12	Cherenkov angle vs. particle momentum for the RICH radiators ^[113]	38
Figure 2.13	An overview of the calorimeter system ^[115]	40
Figure 2.14	An overview of the muon system ^[113]	41
Figure 2.15	An overview of the LHCb trigger system in Run 2 ^[116]	42
Figure 2.16	Some typical hadron signals obtained with LHCb high level triggers in a LHC proton-lead fill in 2016.....	43
Figure 2.17	LHCb integrated luminosity versus time during the 8.16 TeV pPb data-taking in 2016.....	44
Figure 2.18	The LHCb event display of a high multiplicity proton-lead event.....	44
Figure 2.19	LHCb data processing applications and data flow.....	45

LIST OF FIGURES AND TABLES

Figure 2.20	The event multiplicity (nVeloClusters) distributions in the 'Sim09e' proton-lead simulations. The left plot is for the pPb (forward) configuration, while the right plot is for the Pbp (backward) configuration.	47
Figure 2.21	The nVeloClusters distributions in 'Sim09k' proton-lead simulations and comparisons to the real data. The left plot is for the pPb (forward) configuration, while the right plot is for the Pbp (backward) configuration.	47
Figure 3.1	D mesons decay topology.....	49
Figure 3.2	Invariant mass distributions in a mass window around the $\phi(1020)$ peak of the K^-K^+ in D_s^+ decays from real data and MC simulations. The Lorentzian function fit results and parameters are shown as well for data and MC comparison.....	54
Figure 3.3	PV nTracks distributions for different nPV values in an event, for the forward configuration.....	56
Figure 3.4	PV nTracks distribution in different PVZ intervals. The left is for forward configuration, and the right is for backward configuration.	56
Figure 3.5	PV nTracks distributions in minimum bias events, compared to those in D_s^+ or D^+ event. The left is for forward configuration, and the right is for backward configuration.....	57
Figure 4.1	Mass fit to extract the D_s^+ inclusive signal in a typical p_T and y^* interval. (left figure is Fwd, right figure is Bwd)	59
Figure 4.2	Mass fit to extract the D^+ inclusive signal in a typical p_T and y^* interval. (left figure is Fwd, right figure is Bwd)	59
Figure 4.3	The inclusive D_s^+ signal yields in different p_T and y^* intervals. (left figure is Fwd, right figure is Bwd)	60
Figure 4.4	The inclusive D^+ signal yields in different p_T and y^* intervals. (left figure is Fwd, right figure is Bwd)	60
Figure 4.5	$\log_{10}\chi_{IP}^2$ fit to extract the D_s^+ prompt signal in a typical p_T and y^* interval. (left figure is Fwd, right figure is Bwd.)	61
Figure 4.6	$\log_{10}\chi_{IP}^2$ fit to extract the D^+ prompt signal in a typical p_T and y^* interval. (left figure is Fwd, right figure is Bwd.)	62
Figure 4.7	The prompt D_s^+ signal yields in different p_T and y^* intervals. (left figure is Fwd, right figure is Bwd)	62

LIST OF FIGURES AND TABLES

Figure 4.8	The prompt D^+ signal yields in different p_T and y^* intervals. (left figure is Fwd, right figure is Bwd)	62
Figure 4.9	The prompt fraction of D_s^+ in different p_T and y^* intervals. (left figure is Fwd, right figure is Bwd)	63
Figure 4.10	The prompt fraction of D^+ in different p_T and y^* intervals. (left figure is Fwd, right figure is Bwd)	63
Figure 4.11	The prompt D_s^+ (D^+) yield as a function of p_T , y^* and PV nTracks. Only the statistical uncertainties are shown here.....	64
Figure 5.1	The geometrical acceptance efficiency, ϵ_{acc} , as a function of p_T and y^* of prompt D_s^+ (up), D^+ (down) meson for Fwd (left) and Bwd (right) configurations. Only the statistical uncertainties are shown here.....	66
Figure 5.2	The ratio of the geometrical acceptance efficiency (D^+/D_s^+) as a function of p_T and y^* (2D) for Fwd (left) and Bwd (right) configurations. Only the statistical uncertainties are shown here.....	67
Figure 5.3	The ratio of geometrical acceptance efficiency (D^+/D_s^+) as a function of p_T , y^* and PV nTracks (3D) for Fwd (up) and Bwd (down) configurations. Only the statistical uncertainties are shown here.	68
Figure 5.4	The mass distribution of truth unmatched D_s^+ (up), D^+ (down) mesons for Fwd (left) and Bwd (right) simulation.	69
Figure 5.5	The tracking efficiency correction factor table for Fwd (left) and Bwd (right) configuration.....	69
Figure 5.6	The distribution of nVeloClusters in pPb data, simulation and weighted simulation. Fwd on the left and Bwd on the right.	70
Figure 5.7	The tracking efficiency, $\epsilon_{rec\&sel}$, as a function of p_T and y^* of prompt D_s^+ (up), D^+ (down) meson for Fwd (left) and Bwd (right) configurations, multiplicity taken into consideration. Only the statistical uncertainties are shown here.	71
Figure 5.8	The ratio of $\epsilon_{rec\&sel}$ (D^+/D_s^+) as a function of p_T and y^* for Fwd (left) and Bwd (right) configurations, multiplicity taken into consideration. Only the statistical uncertainties are shown here.....	72
Figure 5.9	The ratio of $\epsilon_{rec\&sel}$ (D^+/D_s^+) as a function of p_T , y^* and PV nTracks for Fwd (up) and Bwd (down) configurations, multiplicity taken into consideration. Only the statistical uncertainties are shown here.	73
Figure 5.10	The Data/MC DLL variables distribution ^[134]	74

LIST OF FIGURES AND TABLES

Figure 5.11	Decay channels are used in PID calibration samples ^[135]	74
Figure 5.12	The PID efficiency, ϵ_{PID} , as a function of p_{T} and y^* of prompt D_s^+ (up), D^+ (down) meson for Fwd (left) and Bwd (right) configurations. Only the statistical uncertainties are shown here.	75
Figure 5.13	The ratio of $\epsilon_{\text{PID}} (D^+/D_s^+)$ as a function of p_{T} and y^* for Fwd (left) and Bwd (right) configurations, multiplicity taken into consideration. Only the statistical uncertainties are shown here.	75
Figure 5.14	The ratio of $\epsilon_{\text{PID}} (D^+/D_s^+)$ as a function of p_{T} , y^* and PV nTracks for Fwd (up) and Bwd (down) configurations, multiplicity taken into consideration. Only the statistical uncertainties are shown here.	76
Figure 5.15	The trigger efficiency, ϵ_{tri} , as a function of p_{T} and y^* of prompt D_s^+ (up), D^+ (down) meson for Fwd (left) and Bwd (right) configurations. Only the statistical uncertainties are shown here.	77
Figure 5.16	The ratio of $\epsilon_{\text{tri}} (D^+/D_s^+)$ as a function of p_{T} and y^* for Fwd (left) and Bwd (right) configurations, multiplicity taken into consideration. Only the statistical uncertainties are shown here.	77
Figure 5.17	The ratio of $\epsilon_{\text{tri}} (D^+/D_s^+)$ as a function of p_{T} , y^* and PV nTracks for Fwd (up) and Bwd (down) configurations, multiplicity taken into consideration. Only the statistical uncertainties are shown here.	78
Figure 5.18	The total efficiency, ϵ_{tot} , as a function of p_{T} and y^* of prompt D_s^+ (up), D^+ (down) meson for Fwd (left) and Bwd (right) configurations.	79
Figure 5.19	The ratio of $\epsilon_{\text{tot}} (D^+/D_s^+)$ as a function of p_{T} and y^* for Fwd (left) and Bwd (right) configurations. Only the statistical uncertainties are shown here..	79
Figure 5.20	The ratio of $\epsilon_{\text{tot}} (D^+/D_s^+)$ as a function of p_{T} , y^* and PV nTracks for Fwd (up) and Bwd (down) configurations. Only the statistical uncertainties are shown here.....	80
Figure 6.1	Mis-ID mass spectrum shape	81
Figure 6.2	Relative systematic uncertainties of $M(D_s^+)$ (up) and $M(D^+)$ (down) fit as a function of p_{T} and y^* (display with decimal). Left for Fwd and Right for Bwd.	82
Figure 6.3	Relative systematic uncertainties of $\log_{10}\chi_{\text{IP}}^2$ fit as a function of p_{T} and y^* (display with decimal). Fwd(left) ,Bwd(right) , D_s^+ (up) , D^+ (down).	83
Figure 6.4	Relative systematic uncertainties from mass fit as a function of p_{T} and y^* and PV nTracks. (a) is forward D_s^+ , (b) is backward D_s^+ , (c) is forward D^+ , (d) is backward D^+	86

LIST OF FIGURES AND TABLES

Figure 6.5	Relative systematic uncertainties from $\log_{10}\chi_{IP}^2$ fit as a function of p_T and y^* and PV nTracks. (a) is forward D_s^+ , (b) is backward D_s^+ , (c) is forward D^+ , (d) is backward D^+	87
Figure 6.6	Relative systematic uncertainties from tracking table as a function of p_T and y^* (display with decimal). Fwd(left) ,Bwd(right) , D_s^+ (up) , D^+ (down).	88
Figure 6.7	The relative systematic uncertainties from ratio of $\epsilon_{rec\&sel} (D^+/D_s^+)$ as a function of p_T and y^* (display with decimal). Left for Fwd and Right for Bwd.	88
Figure 6.8	The relative systematic uncertainties from ratio of $\epsilon_{rec\&sel} (D^+/D_s^+)$ as a function of p_T and y^* and PV nTracks. Up for Fwd and Down for Bwd.....	89
Figure 6.9	Relative systematic uncertainties from PID table as a function of p_T and y^* (display with decimal). Fwd(left) ,Bwd(right) , D_s^+ (up) , D^+ (down).	90
Figure 6.10	The relative systematic uncertainties from ratio of $\epsilon_{PID} (D^+/D_s^+)$ as a function of p_T and y^* (display with decimal). Left for Fwd and Right for Bwd.	90
Figure 6.11	The relative systematic uncertainties from ratio of $\epsilon_{PID} (D^+/D_s^+)$ as a function of p_T and y^* and PV nTracks. Up for Fwd and Down for Bwd.	91
Figure 6.12	The relative systematic uncertainties from multiplicity correction as a function of p_T and y^* (display with decimal). Fwd(left) ,Bwd(right) , D_s^+ (up) , D^+ (down).....	92
Figure 6.13	Relative systematic uncertainties from trigger efficiencies as a function of p_T and y^* (display with decimal). Left for Fwd and Right for Bwd.	92
Figure 7.1	Double differential cross-sections of prompt D_s^+ (up) and D^+ (down) in pPb collisions at $\sqrt{s_{NN}} = 8.16$ TeV in the forward (left) and backward (right) rapidity regions. The vertical bar and the vertical box on each data point represent statistical uncertainty and systematic uncertainty respectively.	94
Figure 7.2	Differential cross-section of prompt D_s^+ mesons in pPb collisions at $\sqrt{s_{NN}} = 8.16$ TeV as a function of p_T (left) and y^* (right) in the forward and backward regions. The vertical bar and the vertical box on each data point represent statistical uncertainty and systematic uncertainty respectively.	95
Figure 7.3	Differential cross-section of prompt D^+ mesons in pPb collisions at $\sqrt{s_{NN}} = 8.16$ TeV as a function of p_T (left) and y^* (right) in the forward and backward regions. The vertical bar and the vertical box on each data point represent statistical uncertainty and systematic uncertainty respectively.	95

LIST OF FIGURES AND TABLES

Figure 7.4 The typical interpolation results for D_s^+ (left) and D^+ (right) cross-sections in pp collisions at $\sqrt{s}=8.16$ TeV with a power-law function and a linear function. The black data points are LHCb result at $\sqrt{s}=5$ and 13 TeV. 96

Figure 7.5 Nuclear modification factor $R_{p\text{Pb}}$ as a function of p_T for prompt D_s^+ mesons in the (left) forward data and (right) backward data, integrated over the common rapidity ranges with the pp reference. The vertical bar and the vertical box on each data point represent statistical and systematic uncertainty respectively. The coloured bands denote the theoretical calculations using the HELAC-Onia generator, incorporating the nPDFs of EPPS16 (grey) and nCTEQ15 (cyan). The brown box (which looks like a line) represents the CGC1 calculations. 97

Figure 7.6 Nuclear modification factor $R_{p\text{Pb}}$ as a function of rapidity for prompt D_s^+ mesons, integrated over $1 < p_T < 10$ GeV/c. The vertical bar and the vertical box on each data point represent statistical and systematic uncertainty respectively. The coloured bands denote the theoretical calculations using the HELAC-Onia generator, incorporating the nPDFs of EPPS16 (grey) and nCTEQ15 (cyan). The brown box at forward rapidities represents the CGC1 calculations. 98

Figure 7.7 Nuclear modification factor $R_{p\text{Pb}}$ as a function of p_T for prompt D^+ mesons in the (left) forward data and (right) backward data, integrated over the common rapidity ranges with the pp reference. The vertical bar and the vertical box on each data point represent statistical and systematic uncertainty respectively. The coloured bands denote the theoretical calculations using the HELAC-Onia generator, incorporating the nPDFs of EPPS16 (grey) and nCTEQ15 (cyan). The brown box (which looks like a line) represents the CGC1 calculations and the red box denotes the CGC2 calculations. 98

Figure 7.8 Nuclear modification factor $R_{p\text{Pb}}$ as a function of rapidity for prompt D^+ mesons, integrated over $1 < p_T < 10$ GeV/c. The vertical bar and the vertical box on each data point represent statistical and systematic uncertainty respectively. The coloured bands denote the theoretical calculations using the HELAC-Onia generator, incorporating the nPDFs of EPPS16 (grey) and nCTEQ15 (cyan). The brown and red boxes at forward rapidities represent the CGC1 and CGC2 calculations, respectively. 99

LIST OF FIGURES AND TABLES

Figure 7.9 Prompt D_s^+ nuclear modification factor R_{pPb} as a function of p_T in different forward y^* bins. The vertical bar and the vertical box on each data point represent statistical and systematic uncertainty respectively. The coloured bands denote the theoretical calculations using the HELAC-Onia generator, incorporating the nPDFs of EPPS16 (grey) and nCTEQ15 (cyan)..... 100

Figure 7.10 Prompt D_s^+ nuclear modification factor R_{pPb} as a function of p_T in different backward y^* bins. The vertical bar and the vertical box on each data point represent statistical and systematic uncertainty respectively. The coloured bands denote the theoretical calculations using the HELAC-Onia generator, incorporating the nPDFs of EPPS16 (grey) and nCTEQ15 (cyan)..... 107

Figure 7.11 Prompt D^+ nuclear modification factor R_{pPb} as a function of p_T in different forward y^* bins. The vertical bar and the vertical box on each data point represent statistical and systematic uncertainty respectively. The coloured bands denote the theoretical calculations using the HELAC-Onia generator, incorporating the nPDFs of EPPS16 (grey) and nCTEQ15 (cyan). The red line represents the CGC2 calculations..... 108

Figure 7.12 Prompt D^+ nuclear modification factor R_{pPb} as a function of p_T in different backward y^* bins. The vertical bar and the vertical box on each data point represent statistical and systematic uncertainty respectively. The coloured bands denote the theoretical calculations using the HELAC-Onia generator, incorporating the nPDFs of EPPS16 (grey) and nCTEQ15 (cyan)..... 109

Figure 7.13 Comparison of the D_s^+ and D^+ nuclear modification factors R_{pPb} versus p_T with the previous D^0 measurements^[142]. 109

Figure 7.14 Comparison of the D_s^+ and D^+ nuclear modification factors R_{pPb} versus y^* with the previous D^0 measurements^[142]. 110

Figure 7.15 ALICE results of nuclear modification factors R_{pPb} of prompt D mesons in pPb collisions at $\sqrt{s_{NN}}=5.02$ TeV^[48]. These figures are taken from Ref. [48]. 110

Figure 7.16 D_s^+ Forward and backward production ratio R_{FB} as a function of p_T (left) and $|y^*|$ (right). The vertical bar and vertical box represent statistical and systematic uncertainty respectively. The coloured bands denote the HELAC-Onia theoretical calculations, incorporating the nPDFs of EPPS16 (gray) and nCTEQ15 (cyan). 112

LIST OF FIGURES AND TABLES

Figure 7.17	D^+ Forward and backward production ratio R_{FB} as a function of p_T (left) and $ y^* $ (right). The vertical bar and vertical box represent statistical and systematic uncertainty respectively. The coloured bands denote the HELAC-Onia theoretical calculations, incorporating the nPDFs of EPPS16 (gray) and nCTEQ15 (cyan).	115
Figure 7.18	The D_s^+/D^+ ratio (including branching fraction) as functions of p_T in different y^* bins in pPb collisions at $\sqrt{s_{NN}}=8.16$ TeV. The error bars mark statistical uncertainties and the red boxes mark uncorrelated systematic uncertainties, the blue boxes mark correlated systematic uncertainties. The coloured bands mark the HELAC-Onia theoretical calculations, incorporating the nPDFs of EPPS16 (gray) and nCTEQ15 (cyan). .	118
Figure 7.19	ALICE results of the prompt D -meson relative abundances as a function of p_T in pPb collisions at $\sqrt{s_{NN}}=5.02$ TeV ^[48] . Taken from Ref. [48].	119
Figure 7.20	The D_s^+/D^+ ratio (including branching fractions) as a function of the event multiplicity (the scaled PV nTracks) in different p_T (within 2-6 GeV/c) and y^* bins in the forward and backward pPb collisions at $\sqrt{s_{NN}}=8.16$ TeV.	120
Figure 7.21	The D_s^+/D^+ ratio (including branching fractions) as a function of the event multiplicity (the scaled PV nTracks) in different p_T (within 6-12 GeV/c) and y^* bins in the forward and backward pPb collisions at $\sqrt{s_{NN}}=8.16$ TeV.	121
Figure 7.22	The D_s^+/D^+ ratio (including branching fractions) as a function of the event multiplicity (the scaled PV nTracks) in pPb collisions at $\sqrt{s_{NN}}=8.16$ TeV, integrated over the p_T range of 2-6 GeV/c for the forward and backward collisions.	121
Figure 7.23	The D_s^+/D^+ ratio (including branching fractions) as a function of the event multiplicity (the scaled PV nTracks) in pPb collisions at $\sqrt{s_{NN}}=8.16$ TeV, integrated over the p_T range of 6-12 GeV/c for the forward and backward collisions.	122
Figure 8.1	The ratio of strange hadrons to non-strange hadrons in different systems, predicted by ALICE ^[150]	128
Figure 8.2	Detection area of SMOG ^[152]	129
Table 2.1	Basic information of Monte Carlo simulation sample	46
Table 3.1	Online selections for D_s^+ and D^+ candidates.	53
Table 3.2	Offline selections for D_s^+ candidates	55
Table 3.3	Offline selections for D^+ candidates	55
Table 3.4	Event selections for the multiplicity dependence study	55
Table 6.1	systematic uncertainties summary	85

LIST OF FIGURES AND TABLES

Table 7.1	Double differential cross-section $\frac{d^2\sigma}{dp_T dy^*}$ mb/(GeV/c) for prompt D_s^+ as functions of p_T and y^* in pPb collisions at $\sqrt{s_{NN}} = 8.16$ TeV. The first error is statistical, the second one is the systematic uncertainty that is uncorrelated between bins, and the third one is the correlated systematic error.	101
Table 7.2	Double differential cross-section $\frac{d^2\sigma}{dp_T dy^*}$ mb/(GeV/c) for prompt D^+ as functions of p_T and y^* in pPb collisions at $\sqrt{s_{NN}} = 8.16$ TeV. The first error is statistical, the second one is the systematic uncertainty that is uncorrelated between bins, and the third one is the correlated systematic error.	102
Table 7.3	Differential cross-section $\frac{d\sigma}{dp_T}$ (mb/(GeV/c)) for prompt D_s^+ as a function of p_T at forward ($1.5 < y^* < 4.0$) and backward ($-5.0 < y^* < -2.5$) rapidities in pPb collisions at $\sqrt{s_{NN}} = 8.16$ TeV. The first error is statistical, the second one is the systematic uncertainty that is uncorrelated between bins, and the third one is the correlated systematic error.....	103
Table 7.4	Differential cross-section $\frac{d\sigma}{dp_T}$ (mb/(GeV/c)) for prompt D^+ as a function of p_T at forward ($1.5 < y^* < 4.0$) and backward ($-5.0 < y^* < -2.5$) rapidities in pPb collisions at $\sqrt{s_{NN}} = 8.16$ TeV. The first error is statistical, the second one is the systematic uncertainty that is uncorrelated between bins, and the third one is the correlated systematic error.....	104
Table 7.5	Differential cross-section $\frac{d\sigma}{dy^*}$ (mb) for prompt D_s^+ as a function of y^* ($1 < p_T < 13$ GeV/c) in pPb collisions at $\sqrt{s_{NN}} = 8.16$ TeV. The first error is statistical, the second one is the systematic uncertainty that is uncorrelated between bins, and the third one is the correlated systematic error.	105
Table 7.6	Differential cross-section $\frac{d\sigma}{dy^*}$ (mb) for prompt D^+ as a function of y^* ($1 < p_T < 14$ GeV/c) in pPb collisions at $\sqrt{s_{NN}} = 8.16$ TeV. The first error is statistical, the second one is the systematic uncertainty that is uncorrelated between bins, and the third one is the correlated systematic error.	106
Table 7.7	Nuclear modification factor R_{pPb} for prompt D_s^+ mesons as a function of p_T forward rapidity regions, integrated over the common rapidity region of $2.0 < y^* < 4.0$ with pp reference. The first and second errors are statistical and systematic uncertainties, respectively.	106
Table 7.8	Nuclear modification factor R_{pPb} for prompt D_s^+ mesons as a function of p_T backward rapidity regions, integrated over common rapidity region of $2.5 < y^* < 4.5$ with pp reference. The first and second errors are statistical and systematic uncertainties, respectively.	107

LIST OF FIGURES AND TABLES

Table 7.9	Nuclear modification factor R_{pPb} for prompt D_s^+ mesons as a function of y^* , integrated over $1 < p_T < 10 \text{ GeV}/c$. The first and second errors are statistical and systematic uncertainties, respectively.	108
Table 7.10	Nuclear modification factor R_{pPb} for prompt D^+ mesons as a function of p_T forward rapidity regions, integrated over common rapidity region of $2.0 < y^* < 4.0$ with pp reference. The first and second errors are statistical and systematic uncertainties, respectively.	111
Table 7.11	Nuclear modification factor R_{pPb} for prompt D^+ mesons as a function of p_T backward rapidity regions, integrated over common rapidity region of $2.5 < y^* < 4.5$ with pp reference. The first and second errors are statistical and systematic uncertainties, respectively.	111
Table 7.12	Nuclear modification factor R_{pPb} for prompt D^+ mesons as a function of y^* , integrated over $1 < p_T < 10 \text{ GeV}/c$. The first and second errors are statistical and systematic uncertainties, respectively.	112
Table 7.13	Nuclear modification factor R_{pPb} for prompt D_s^+ mesons in bins of p_T and y^* . The first and second errors are statistical and systematic uncertainties, respectively.	113
Table 7.14	Nuclear modification factor R_{pPb} for prompt D^+ mesons in bins of p_T and y^* . The first and second errors are statistical and systematic uncertainties, respectively.	114
Table 7.15	D_s^+ Forward and backward production ratio R_{FB} as a function of p_T and $ y^* $. Integrated over common p_T and y^* range : $1 < p_T < 13 \text{ GeV}/c$ for $2.5 < y^* < 3.0$, $1 < p_T < 11 \text{ GeV}/c$ for $3.0 < y^* < 3.5$, $1 < p_T < 7 \text{ GeV}/c$ for $3.5 < y^* < 4.0$. The first and second errors are statistical and systematic uncertainty respectively.	115
Table 7.16	D^+ Forward and backward production ratio R_{FB} a function of p_T and $ y^* $. Integrated over common p_T and y^* range : $1 < p_T < 14 \text{ GeV}/c$ for $2.5 < y^* < 3.0$, $1 < p_T < 11 \text{ GeV}/c$ for $3.0 < y^* < 3.5$, $1 < p_T < 8 \text{ GeV}/c$ for $3.5 < y^* < 4.0$. The first and second errors are statistical and systematic uncertainty respectively.	116
Table 7.17	The D_s^+/D^+ ratio (including branching fractions) as a function of p_T in different y^* bins in pPb collisions at $\sqrt{s_{NN}}=8.16 \text{ TeV}$, for the forward (upper) and backward (lower) rapidity regions. The first error is statistical uncertainty, the second is the component of the systematic uncertainty that is uncorrelated between bins and the third is the correlated component.	123

LIST OF FIGURES AND TABLES

Table 7.18 The D_s^+/D^+ ratio (including branching fractions) as functions of p_T (within 2-6 GeV/c), y^* and PV nTracks for the forward (upper) and backward (lower) pPb collisions at $\sqrt{s_{NN}}=8.16$ TeV. The first error is statistical uncertainty, the second error is the component of the systematic uncertainty that is uncorrelated between bins and the third is the correlated component. 124

Table 7.19 The D_s^+/D^+ ratio (including branching fractions) as functions of p_T (within 6-12 GeV/c), y^* and PV nTracks for the forward (upper) and backward (lower) pPb collisions at $\sqrt{s_{NN}}=8.16$ TeV. The first error is statistical uncertainty, the second error is the component of the systematic uncertainty that is uncorrelated between bins and the third is the correlated component. 125

LIST OF SYMBOLS AND ACRONYMS

SM	标准模型 (Standard Model)
QCD	量子色动力学 (Quantum ChromoDynamics)
QED	量子电动力学 (Quantum ElectroDynamics)
QGP	夸克胶子等离子体 (Quark-Gluon Plasma)
CERN	欧洲核子研究中心 (European Organization for Nuclear Research)
LEP	大型正负电子对撞机 (large Electron-Positron collider)
LHC	大型强子对撞机 (Large Hadron Collider)
ALICE	大型离子对撞机实验 (A Large Ion Collider Experiment)
CMS	紧凑型缪子螺线管 (Compact Muon Solenoid)
LHCb	大型强子对撞机底物理实验 (Large Hadron Collider beauty)
ATLAS	环形 LHC 装置 (A Toroidal LHC Apparatus)
RHIC	相对论性重离子对撞机 (Relativistic Heavy Ion Collider)
LINAC	直线加速器 (LINear ACcelerator)
PSB	质子同步加速器助推器 (Proton Synchrotron Booster)
CGC	色玻璃凝聚 (Colour Glass Condensate)
CNM	冷核物质 (Cold Nuclear Matter)
nPDFs	核部分子分布函数 (Nuclear parton distribution functions)
FF	碎裂函数 (Fragmentation Function)
MC	蒙特卡罗 (Monte Carlo)
PV	主顶点 (Primary Vertices)
VELO	顶点探测器 (VErtex LOcator)
RICH	环形切伦科夫探测器 (Ring Imaging Cherenkov detector)
SPD	闪烁体探测器 (Scintillating Pad Detector)
ECAL	电磁量能器 (Electromagnetic CALorimeter)
HCAL	强子量能器 (Hadronic CALorimeter)
GEM	气体电子倍增管 (Gas Electron Multiplier)
MWPC	多丝正比室 (Multi-Wire Proportional Chambers)
L0	硬件触发 (hardware trigger)
HLT	高级软件触发 (High Level software stage Trigger)
EFF	事例筛选器 (Event Filter Farm)
IP	碰撞参数 (Impact Parameter)
PID	粒子鉴别 (Particle IDentification)

LIST OF SYMBOLS AND ACRONYMS

BKGCAT	本底分类 (BacKGround CATegories)
DLL	似然函数的对数变化值 (Delta Log Likelihood)

CHAPTER 1 INTRODUCTION

1.1 Standard Model and quantum chromodynamics

The Standard Model (SM) is a theory of fundamental microscopic interactions that successfully describes most of the known phenomena in elementary particle physics^[1]. It addresses three of the four fundamental interactions, namely, the electromagnetic, weak and strong interactions. The structure of the SM is a renormalizable quantum gauge field theory based on a local gauge symmetry of the type $SU(3) \otimes SU(2) \otimes U(1)$, where $SU(3)$ is the gauge symmetry for the strong force between the color charges and $SU(2) \otimes U(1)$ is for the unified weak and electromagnetic interactions between the electro-weak charges.

The elementary particles in the SM are shown in Fig. 1.1. There are three generations of quarks (u, d, c, s, t, b) and leptons ($e, \nu_e, \mu, \nu_\mu, \tau, \nu_\tau$) which are basic building blocks of matter. They are spin- $\frac{1}{2}$ fermions and interact with each other through the mediation of Yang-Mills gauge fields. The quarks carry both color and electro-weak charges, while the leptons have only electro-weak charges. In addition, there are spin-1 force carriers (gauge bosons). The gluons mediate strong interactions between the particles carrying color charge, and the photons mediate electromagnetic interactions between the particles carrying electric charge, while the W^\pm and Z^0 mediate weak interactions between the particles carrying weak charge. Photon and gluons are massless but W^\pm and Z^0 have large masses. This indicates the electroweak gauge symmetry has been broken. The spontaneous breaking of the electroweak gauge symmetry can be explained by the Higgs mechanism which predicted the existence of Higgs boson (spin-zero)^[2]. The Higgs boson was finally discovered at LHC in 2012^[3-4], which completed the Standard-Model jigsaw.

Quantum chromodynamics (QCD)^[5] is the theory describing strong interactions, and it is also an $SU(3)$ group with non-abelian gauge symmetry. The QCD Lagrangian can be written as

$$\mathcal{L}_{\text{QCD}} = \sum_f \bar{q}_i^f \left(i\gamma_\mu D_{ij}^\mu - m_f \delta_{ij} \right) q_j^f - \frac{1}{4} G_a^{\mu\nu} G_{\mu\nu}^a, \quad (1.1)$$

where q_i^f is a quark field with flavour f (flavor is the index for different quarks), mass m_f , and color charge i . The covariant derivative D_{ij}^μ is written in terms of the gluon fields G_a^μ

The Standard Model of Particle Physics

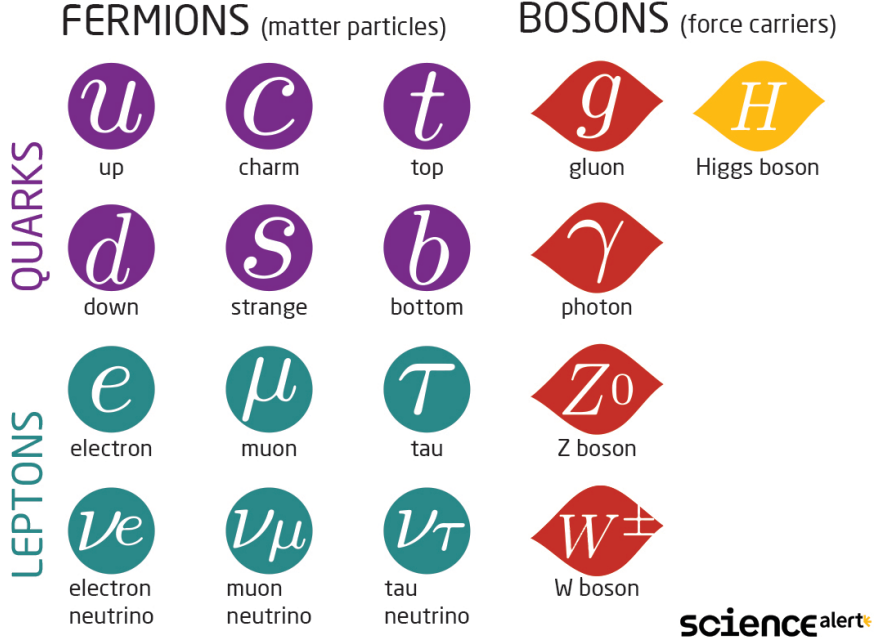


Figure 1.1 Elementary particles in the Standard Model

(a runs from 1 to 8) and the strong coupling constant g_s as,

$$D_{ij}^\mu = \partial^\mu \delta_{ij} - ig_s \left(\frac{\lambda_{ij}^a}{2} \right) G_a^\mu, \quad (1.2)$$

where λ_{ij}^a are the Gell-Mann matrices. The second term of Eq. 1.1 describes the kinematics and the dynamics of the gluons with the gluon strength tensor defined as

$$G_{\mu\nu}^a = \partial_\mu G_\nu^a - \partial_\nu G_\mu^a + ig_s f_{abc} G_\mu^b G_\nu^c, \quad (1.3)$$

where f_{abc} are the structure constants of SU(3). The third term of Eq. 1.3 distinguishes QCD from QED, giving rise to triple and quartic gluon self-interactions. These self-interactions lead to anti-screening in color interaction. The unrenormalized constants in the Lagrangian need to be redefined (renormalization scheme) to ensure that the observables are finite when the ultraviolet cut off is removed. The observables do not depend on renormalization scheme and renormalization scale μ . The coupling constant $\alpha_s = g_s^2/(4\pi)$ is the only fundamental parameter in QCD besides quark masses. It depends on the renormalization scheme and renormalization scale μ . The coupling constant satisfies the renormalization group equation (RGE) :

$$\mu^2 \frac{d\alpha_s}{d\mu^2} = \beta(\alpha_s) = -(b_0\alpha_s^2 + b_1\alpha_s^3 + b_2\alpha_s^4 + \dots) \quad (1.4)$$

where $b_0, b_1, b_2 \dots$ correspond to one loop, two loops, three loops ... contributions. In the

one loop approximation, α_s can be expressed as

$$\alpha_s(\mu^2) = \frac{\alpha_s(\mu_0^2)}{1 + b_0 \alpha_s(\mu_0^2) \ln(\mu^2/\mu_0^2)}. \quad (1.5)$$

When μ is the scale of the momentum transfer Q in a given process, $\alpha_s(Q^2)$ indicates the effective strength of the strong interaction in this process. Equation 1.5 shows that α_s is not constant but depends on the momentum transfer, Q ^[6]. In experiments, α_s can not be measured directly, but only indirectly through physical processes, such as the total cross-section for $e^+e^- \rightarrow$ hadrons at high energies. A summary of measurements of α_s as a function of the energy scale Q is shown in Fig. 1.2.

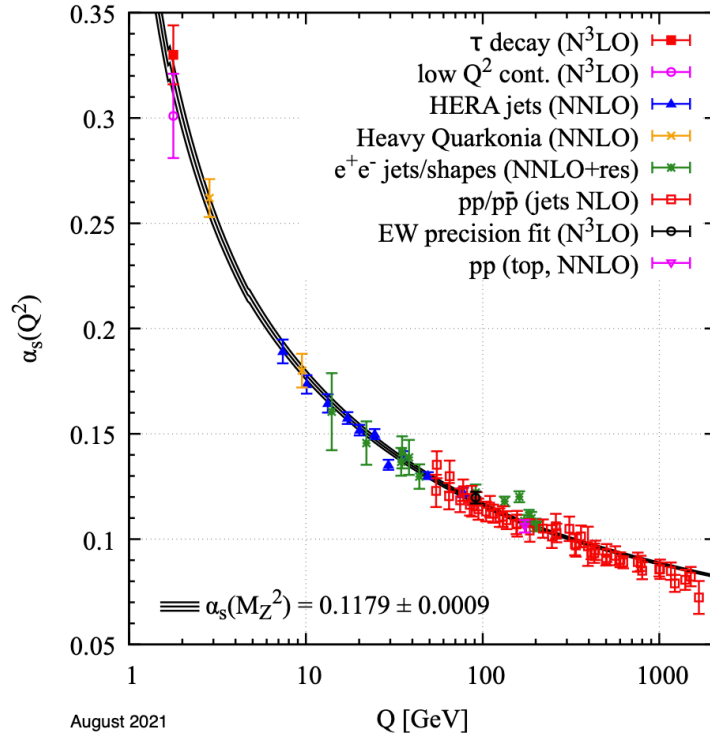


Figure 1.2 Summary of measurements of α_s as a function of the energy scale Q ^[7]

The running of the coupling constant α_s as a function of Q can be related to two of the core phenomena of strong interactions: asymptotic freedom and color confinement. At large Q , the coupling constant is small, and the interaction between quarks/gluons becomes weaker. This is a unique property of gauge theories based on a non-abelian group of $SU(3)$, and is known as asymptotic freedom. A perturbative expansion in term of α_s (perturbative QCD) can be applied to calculate these QCD processes. At small Q (below about a few hundred MeV), the interaction between quarks/gluons becomes stronger, and free quarks or gluons cannot exist alone but instead combine into bound states

(hadrons) in which their color charge is “hidden”. It is known as “color confinement”. In phenomenology, the interaction potential between color charges increases linearly with the distance between the charges. If one tries to separate the quark and the antiquark in a meson, the interaction energy will keep increasing until new $q\bar{q}$ pairs are pulled out from the vacuum and combined with the existing quarks to form new color-neutral mesons. These low energy QCD processes are non-perturbative, but can be calculated numerically with lattice QCD (LQCD)^[8].

1.2 Deconfinement and Quark–Gluon Plasma

Due to the asymptotic freedom feature of QCD, quarks and gluons should no longer be confined in hadrons at an arbitrarily high temperature or baryon density. Therefore, it is expected that there should be a phase transition from the ordinary hadronic matter to the deconfined matter with quarks and gluons as basic constituents, which is called quark-gluon plasma (QGP). The most intuitive feature of the deconfinement QCD phase transition is that the release of many new degrees of freedom will lead to a rapid increase in energy density around the critical temperature T_c . Lattice QCD calculations indeed predict such rapid change in various thermodynamic quantities at a temperature of $T_c \sim 155$ MeV, as shown in Fig. 1.3. At lower temperature ($T < 150$ MeV), the lattice QCD results are well described by the hadron resonance gas model (HRG)^[9], which assumes non-interacting hadrons and resonances as the fundamental constituents. The thermodynamic quantities change rapidly at $T_c \sim 155$ MeV, then gradually approach the ideal gas limit (assuming free quarks and gluons as constituents) at higher temperatures. Lattice calculations indicate that the transition from hadronic gas to quark-gluon plasma is a smooth crossover within a range of temperature around $T_c \sim 155$ MeV^[10-11], depicted by the yellow band in Fig. 1.3.

Figure 1.4 shows the current knowledge of the QCD phase diagram in the plane of temperature (T) and baryon chemical potential (μ_B). The μ_B is closely related to the net-baryon number density of the system. The ordinary nuclear matter is located at approximately $T \sim 0$ and baryon chemical potential $\mu_B \sim 1$ GeV. The lattice QCD prediction for the crossover in Fig. 1.3 is corresponding to the case of zero baryon chemical potential. The matter could be in the QGP phase with nearly zero μ_B in the early Universe (about 10^{-5} seconds after the big bang), and then hadronize into hadron gas after a smooth crossover. At small but finite baryon chemical potential (or net baryon density), the transi-

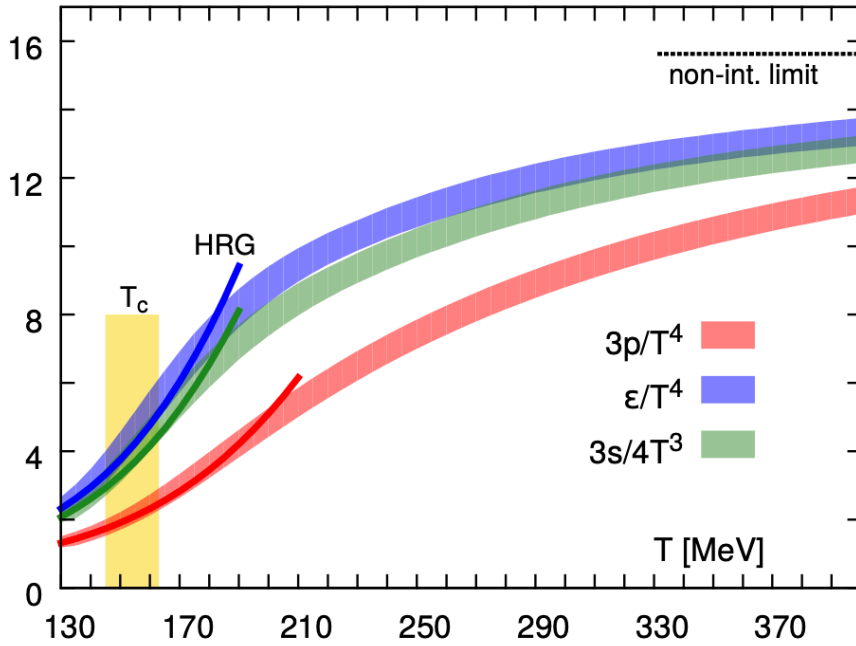


Figure 1.3 The normalized pressure, energy density, and entropy density as a function of the temperature from lattice QCD calculations ((2+1)-flavor) at zero net baryon density. The predictions of the hadron resonance gas (HRG) model are also shown with same color lines. This horizontal dotted line represents the ideal gas (or Stefan-Boltzmann) limit, which is the limit without interaction. The vertical yellow band indicates the crossover temperature region. This figure is taken from Ref. [10]

tion from hadrons gas to QGP is also a crossover. But at larger baryon chemical potential, QCD theories predict a first order phase transition from the hadron phase to QGP phase, and the end point of the first order phase transition is called the QCD critical point^[12]. At higher baryon density and lower temperature, cold dense quark matter is expected to be a color superconductor which could exist in the core of neutron stars or quark stars.

1.3 Relativistic heavy ion collisions

In order to fully understand the mechanism of color confinement and the QCD behaviour in the non-perturbative regime, it was proposed in 1970s to study the QCD phase transition with heavy ion collision experiments. In these experiments, heavy nuclei (like lead ions) are accelerated to relativistic speed and then collide with each other. The large kinetic energy carried by the incident nuclei will be deposited in the collision zone which has a typical size of 10 fm. The vacuum there is then quickly heated up to above T_c , then the deconfinement phase transition will happen, and quark-gluon plasma will be formed in a short time period of a few fm/c before it cools down and hadronizes again.

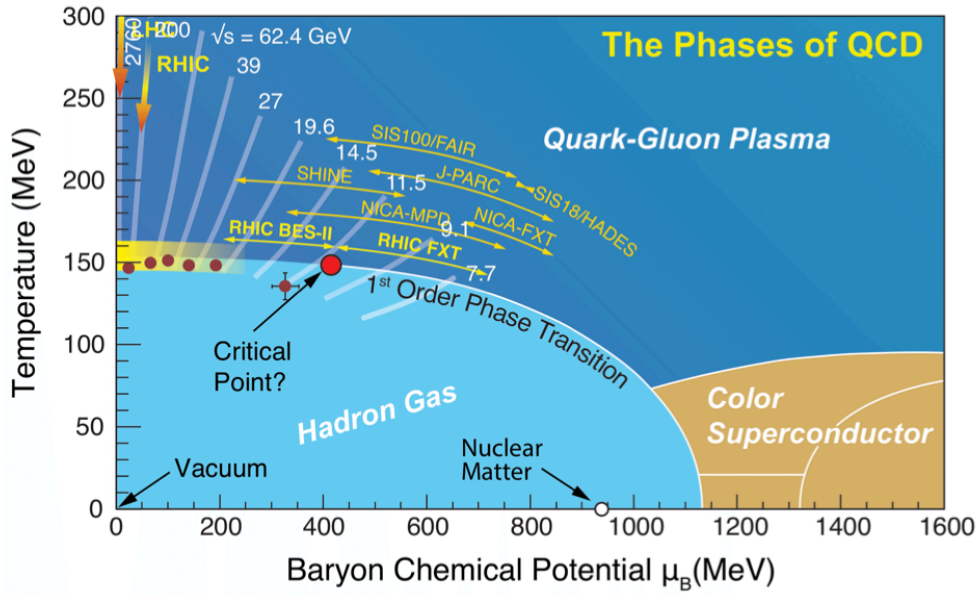


Figure 1.4 A sketch of the current understanding of the QCD phase diagram as a function of temperature and the baryon chemical potential. This figure is taken from Ref. [13]

Since early 1980s, several accelerator facilities around the world conducted their scientific programs of relativistic heavy ion collisions in order to create QGP, to study its properties, and to study the QCD phase structure:

- **Bevatron** (Billions of eV Synchrotron) : From 1954 to 1993 at Lawrence Berkeley National Laboratory, U.S.
- **AGS** (Alternating Gradient Synchrotron) : Since 1960 at Brookhaven National Laboratory, U.S. Now used as injector for RHIC.
- **SPS** (Super Proton Synchrotron) : Since 1976 at CERN. Now the injector for the LHC.
- **SIS-18** (Schwer-Ionen-Synchrotron) : Since 2001 at GSI.
- **RHIC** (Relativistic Heavy Ion Collider) : Since 2000 at Brookhaven National Laboratory, U.S.
- **LHC** (Large Hadron Collider) : Since 2009 at CERN.

Bevatron, AGS, SIS-18 and SPS are fixed target experiments. At these configurations the nucleons are stopped in the collision region, hence the baryon density is high ($\mu_B = 200\text{--}500$ MeV), which is named stopping regime. Some experimental hints of QGP formation were observed in the 158A GeV Pb-Pb collisions at the CERN SPS^[14-18]. Then came collider mode, the Au-Au collision at $\sqrt{s_{NN}} = 200$ GeV at RHIC and the Pb-Pb collision at $\sqrt{s_{NN}} = 5.5$ TeV at LHC allow to explore the QCD phase diagram in the region of μ_B close to zero, which is named Bjorken regime. RHIC claims that QGP has

been created in its Au-Au collision in 2004^[19]. The research direction of ultra-relativistic heavy ion collisions has then shifted to measuring quantitatively the QGP properties^[20-22]. RHIC also conducts a beam energy scan and fixed-target program to study the QCD phase structure at finite or high baryon chemical potential, in particular, to look for the QCD critical point. This is also the main goal for future heavy ion facilities at FAIR, NICA, J-PARC and HIAF. This thesis will focus on the ultra high energy heavy ion collisions at the LHC.

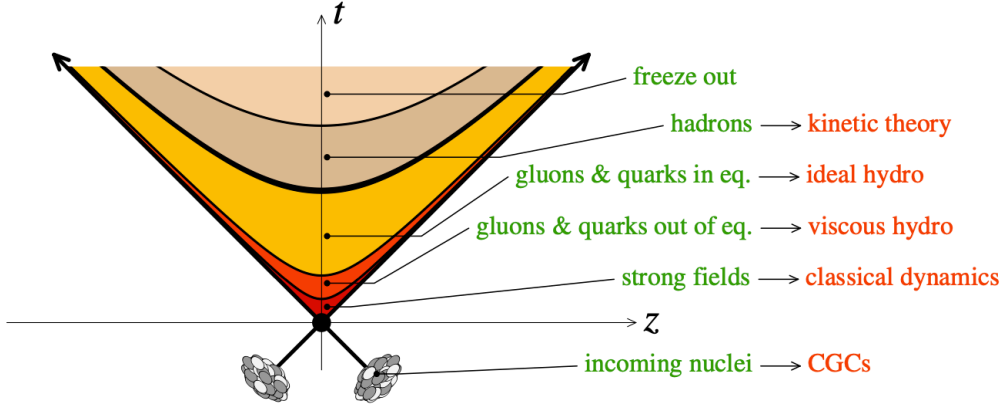


Figure 1.5 The main evolution stages of heavy ion collisions^[23]

The space-time evolution of relativistic heavy ion collisions is a very complex process. The main stages of a relativistic heavy ion collision in Bjorken scenario are shown in Fig. 1.5:

- Before the collision, and in the center-of-mass frame, the two incoming nuclei became disk-shaped due to longitudinal Lorentz contraction. These disks are full of partons (mainly gluons) carrying only a small part of the parent nucleons momentum but relatively large transverse momenta. These partons are weakly coupled according to the asymptotic freedom of QCD, which is known as the color glass condensate^[24] (CGC).
- These two nuclei collide with each other at $\tau (\equiv \sqrt{t^2 - z^2}) = 0$ and the interactions start developing. Hard processes, which have relatively large transferred momentum ($Q > 10$ GeV), mainly occur in this stage. They occur faster due to uncertainty principle. These processes will produce ‘hard particles’, such as heavy quarks.
- At $\tau \sim 0.2$ fm/c, corresponding to the ‘semi-hard’ processes ($Q \sim 1$ GeV). A large number of the partons originally inside the colliding nuclei are released by the collision. Most of the hadrons captured in the detectors are produced by the fragmentation and hadronization of partons released at this stage. These partons form a relatively dense medium, with an average energy density several times larger

than that of normal nuclear matter.

- At $\tau = 1 \text{ fm}/c$, the dense partonic matter rapidly approaches towards thermal equilibrium. Such a rapid thermalization represents that the partons are strongly coupled. The outcome of this thermalization process is QGP. When quarks and gluons reach local thermal equilibrium, the partonic medium also evolves from viscous fluid to ideal fluid. Then, QGP keeps expanding and cooling down. Finally, These colored quarks and gluons are trapped in colorless hadrons by hadronization ($\tau = 10 \text{ fm}/c$). This is the phase transition from QGP to hadron gas. Then the hot and relatively dense hadron gas keeps expanding and cooling, with local equilibrium still preserved.
- At $\tau = 20 \text{ fm}/c$, the density of the hadron gas becomes so low that the interactions between hadrons stop. The hadrons then undergo free streaming until they reach the detectors. This transition from a fluid state to a system of free particles is called freeze-out.

Although QGP cannot be directly detected in heavy ion collisions, the existence of QGP stage during the evolution results in many novel experimental phenomena in the final state of heavy ion collisions. They are usually called “QGP signatures”, such as the strangeness enhancement represented by ratios of yields between strange hadrons and non-strange hadrons, the significant energy loss of jet or heavy flavors in hot medium represented by nuclear modification factor, R_{AA} , and the large collective motion represented by the elliptic flow, $v_2(p_T)$.

1.4 Strangeness enhancement

In 1982, J. Rafelski and B. Müller predicted the enhancement of strange particles production due to the creation of QGP in relativistic AA collisions^[25-26] for the following reasons:

- In the case of pure hadron gas, strange quarks confined in hadrons and have to be pair produced due to strangeness conservation. This makes the energy threshold higher than 500 MeV.
- In contrast, in QGP, strange quarks are no longer bound in hadrons. Due to the restoration of the chiral symmetry, the mass of strange quark decreases to $100 \text{ MeV}/c^2$ ^[27], which is lower than the QGP temperature.
- High density gluons and quarks in QGP lead to a large strangeness production via

gluon fusion and light quarks annihilation, as shown in Fig. 1.6.

- The equilibration time of partonic reactions are much shorter than the time of hadronic reactions, which results in easier production of multi-strange particles.

This phenomenon was first observed by the NA35, WA97, and NA57 Collaborations in the 1990s^[16,28-29] and also confirmed at RHIC^[30] and LHC^[31]. The hyperon-to-pion ratios as a function of $\langle N_{\text{part}} \rangle$, for AA and pp collisions at LHC and RHIC energies, are shown in Figure 1.7. These hyperon-to-pion ratio is higher in AA collisions than in pp collisions, and increases with multiplicity. The slope of Ω/π is slightly larger than that of Ξ/π indicates that the more strange quarks contained in a hadron, the stronger its enhancement is. Therefore, the strangeness enhancement was once considered as a QGP signature.

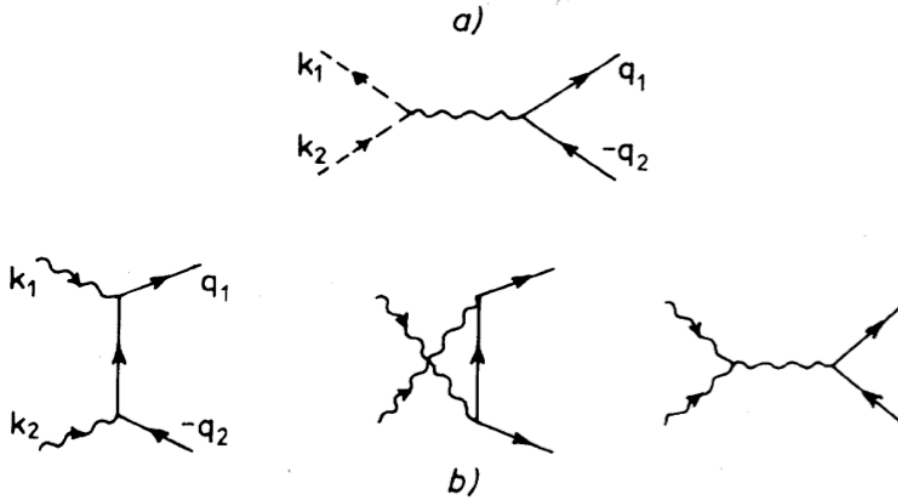


Figure 1.6 The lowest order QCD diagrams for $s\bar{s}$ production^[25]

1.5 Open heavy flavor in heavy ion collisions

Open heavy flavor hadrons, which contain at least one charm or beauty quark and other lighter quarks (u, d, s) as constituents, are sensitive probes to characterizing QGP for the following reasons^[32]:

- Since heavy quarks are so heavy that their thermal productions in QGP created at LHC and RHIC energies are negligible. They originate almost entirely from the initial collision and their productions can be calculated by perturbative QCD.
- The heavy quarks was produced earlier than the formation of QGP and experienced the whole QGP evolution process. They scatters frequently with the dense partons in

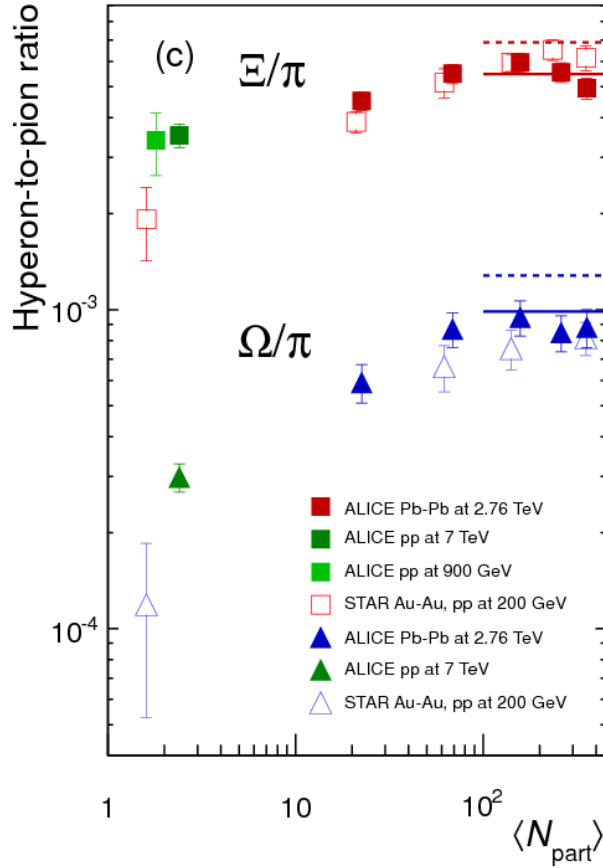


Figure 1.7 Hyperon-to-pion ratios as a function of $\langle N_{\text{part}} \rangle$, for AA and pp collisions at LHC and RHIC energies^[31]

the hot medium, loses their energies, and even gets thermalized with QGP. Heavy flavor hadrons can be produced through the recombination of heavy quarks with light quarks during the QGP evolution till the QGP hadronization.

- The earlier produced heavy flavor hadrons can survive in the QGP phase due to the larger binding energy compared with light hadrons. Because different heavy flavor hadrons have different binding energies, their survival temperatures are different. Therefore, heavy flavor hadrons carry QGP information of different stages. For example, the b hadrons carry the information of the early stage of QGP, while the c hadrons are more sensitive to the late stage of QGP.

1.5.1 Open heavy flavor production

Heavy quarks are produced in the hard scattering processes with large momentum transfers, due to the large heavy quark masses ($m_c \approx 1.3 \text{ GeV}/c^2$, $m_b \approx 4.2 \text{ GeV}/c^2$). The strong coupling constant is weak on these energy scales. The cross-section of the $c\bar{c}$ pair

production in two-parton scatterings, $\sigma_{ij \rightarrow c\bar{c}}$, can be calculated by perturbative QCD. At leading order (LO), There are two processes contributing to the heavy quarks pair production in perturbative QCD: the quark-antiquark annihilation and the gluon fusion^[33]. Then heavy quarks will undergo hadronization to form heavy flavor hadrons. Since hadronization is a process with low energy scale and hence large coupling constant, it can only be constrained by experimental data or calculated with phenomenological methods.

The production cross-section of open heavy flavor hadrons in pp collisions can be obtained from the elementary heavy quark-antiquark production cross-section by applying the factorisation theorem:

$$\sigma_{pp \rightarrow H_c + X} = \sum_{i,j=q,\bar{q},g} f(x_i, Q^2) \otimes f(x_j, Q^2) \otimes \sigma_{ij \rightarrow c\bar{c}} \otimes D(z_c, Q^2) \quad (1.6)$$

where $f(x_i, Q^2)$ is the parton distribution function (PDF), describing the probability to find a parton i with momentum fraction x_i and momentum scale Q^2 in the colliding proton, as shown in Fig. 1.8, and $D(z_c, Q^2)$ is the fragmentation function (FF), which describes the probability that the charm quark fragments to the hadron H_c , carrying a fraction z_c of the original quark momentum. The PDFs are parametrised using measurements of deep-inelastic scattering^[34-35] and obey the Dokshitzer-Gribov-Lipatov-Altarelli-Parisi (DGLAP) equations^[36]. The FFs are supposed to be universal and can be measured in e^+e^- collisions^[37-38]. This is how the fragmentation mechanism of heavy flavor hadronization is handled. Later, the heavy quark hadronization mechanism in QGP medium will also be introduced.

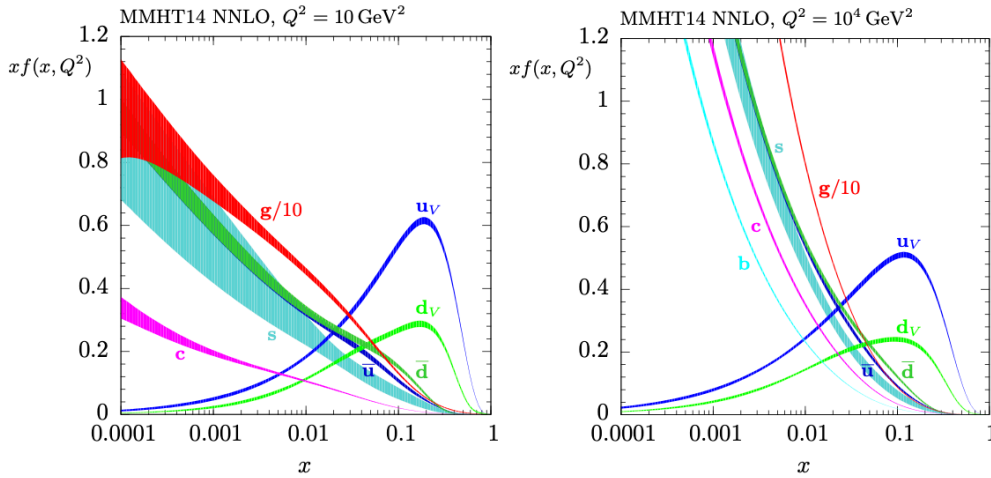


Figure 1.8 The parton distribution functions at $Q^2 = 10 \text{ GeV}^2$ and $Q^2 = 10^4 \text{ GeV}^2$ (MMHT2014 NNLO), with associated 68% confidence-level uncertainty bands^[39].

In relativistic heavy ion collisions, the production of heavy flavor hadrons is more complicated than that in pp collisions. It cannot be simply regarded as the superposition of nucleon-nucleon collisions, because it is also affected by various cold nuclear matter effects and hot nuclear matter effects.

1.5.2 Hot nuclear matter effects

The hard partons (including heavy quarks) produced in the early stage of relativistic heavy ion collisions play an important role in studying the transport properties of QGP. During these partons passing through QGP, the interactions between hard partons and the colored medium by inelastic (gluon radiation) and elastic (scattering) processes which lead to significant parton energy loss. What is observed is the softening of hadron p_T distributions (“jet quenching”). This phenomenon is predicted by Bjorken in the early 1980s^[40] and was confirmed by RHIC^[41], quantified by nuclear modification factor, R_{AA} ,

$$R_{AA} = \frac{1}{\langle T_{AA} \rangle} \frac{dN_{AA}}{dp_T} / \frac{d\sigma_{pp}}{dp_T} \quad (1.7)$$

where $\langle T_{AA} \rangle$ is the nuclear overlap function defined as $\langle N_{\text{coll}} \rangle / \sigma_{\text{inel}}^{\text{NN}}$, $\sigma_{\text{inel}}^{\text{NN}}$ is the inelastic nucleon–nucleon cross-section and $\langle N_{\text{coll}} \rangle$ is the average number of binary nucleon-nucleon collisions occurring in a single nucleus-nucleus (AA) collision, can be calculated with the Glauber model^[42]. If the AA collision were a simple superposition of pp collisions, the ratio R_{AA} would be unity.

Both the light and heavy quarks will lose energy when traversing QGP, but the mechanism is slightly different. As a recent result shown in Fig. 1.9, the averaged D meson nuclear modification factors in central Pb-Pb collisions are measured by ALICE^[43]. The R_{AA} of D mesons is larger than that of light-flavour particles at low p_T . It should be noted that due to the strong radial flow at LHC energy, the light-flavour particles can also be produced from soft processes. However this soft component does not exist in D -meson production. The R_{AA} of D mesons is similar to that of light-flavour particles at very large p_T , because the effects from radial flow and the difference in the hadronisation mechanisms become negligible there.

For quantitative understanding of the parton energy loss in high p_T . The R_{AA} and the elliptic flow of prompt D mesons and pions are compared with three theoretical models in Fig. 1.10. These models provide a fair description of both the R_{AA} and the elliptic flow v_2 of D mesons and pions at high p_T . This indicates that the dependence of radiative energy loss on the colour charge and the quark mass of the hard-scattered partons has been

properly handled in these calculations.

Figure 1.11 shows that the R_{AA} of high p_T D mesons increases from central to peripheral collisions and eventually becomes close to unity in p Pb collision, where QGP is not expected to be formed due to small system size. The R_{AA} of p Pb collision deviates slightly from unity indicates that heavy flavor production and momentum distributions may be influenced by cold nuclear matter (CNM) effects. Precisely measuring heavy flavor production in p Pb collisions can constrain the contribution of cold nuclear matter effects and provide a baseline for studying the hot nuclear matter effects in AA collisions.

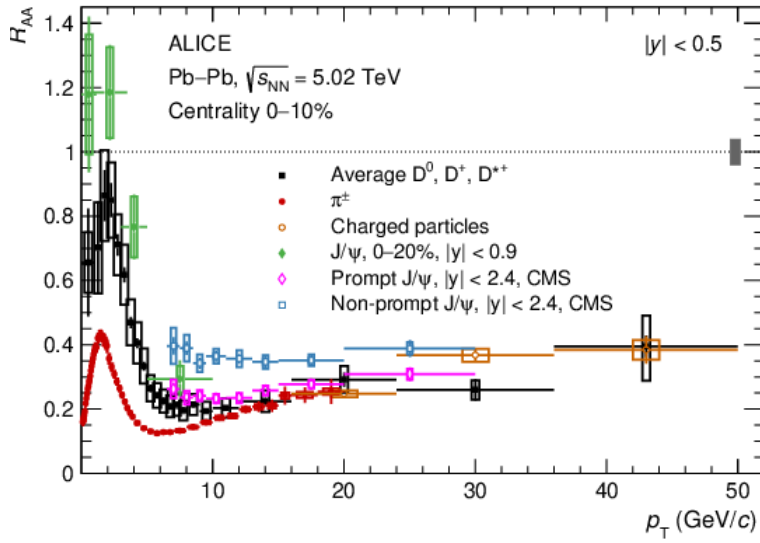


Figure 1.9 The nuclear modification factors, R_{AA} , of prompt D -mesons in the 0–10% centrality class compared to those of charged pions, charged particles, inclusive J/ψ measured by ALICE, and of prompt and non-prompt J/ψ from CMS. This figure is taken from Ref. [43].

1.5.3 Cold nuclear matter effects

The CNM effects include initial state effects and final state effects, such as nuclear shadowing, parton saturation, multiple scattering of partons, nuclear absorption and isospin effects. The CNM effects can be studied by measuring the nuclear modification factor, R_{pPb} . In addition, due to the asymmetry of the p Pb collision, the forward-backward production ratio (R_{FB}) can also be used to characterize CNM effects, which is defined as:

$$R_{FB}(p_T, y_{cms}) = \frac{d^2\sigma_{pPb}(p_T, +|y_{cms}|)/dp_T dy_{cms}}{d^2\sigma_{PbP}(p_T, -|y_{cms}|)/dp_T dy_{cms}}, \quad (1.8)$$

where y_{cms} is the rapidity in the nucleon-nucleon centre-of-mass system. Any deviation from unity of R_{pPb} or R_{FB} suggests the existence of CNM effects.

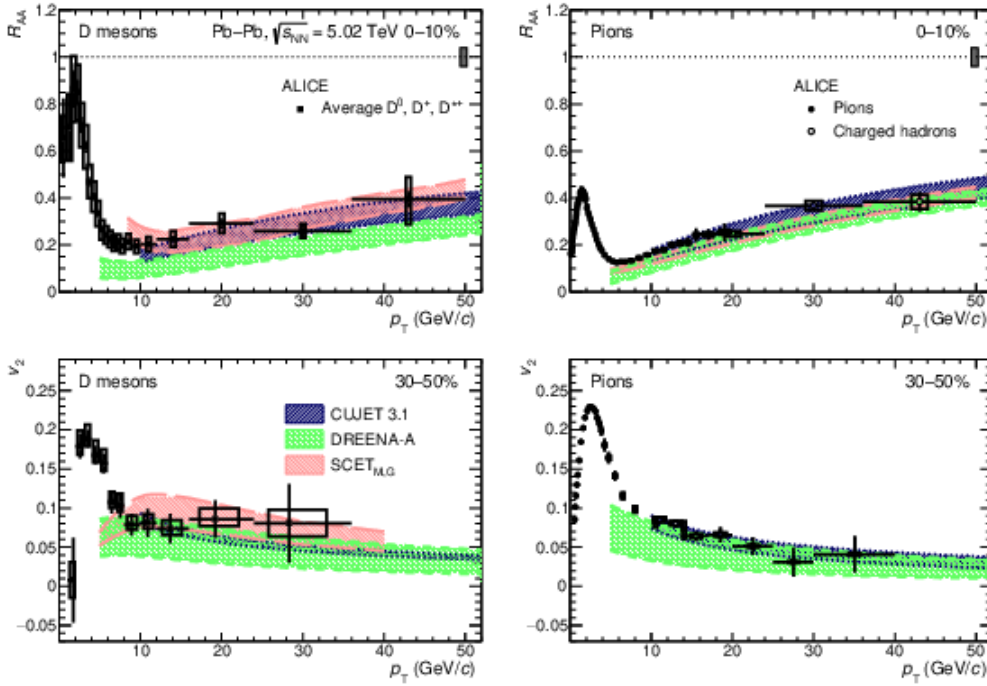


Figure 1.10 The R_{AA} and the elliptic flow of prompt D mesons^[43] and pions as a function of p_T , and compared with predictions from the models based on pQCD calculations (CUJET3.1^[44], DREENA-A^[45], SCET_{M,G}^[46]).

1.5.3.1 Nuclear parton distribution functions

The first CNM effect is related to the modifications of the parton distribution functions in nuclei^[49] (nPDFs). In p Pb collisions, one of the PDFs used in Eq. 1.6 should be replaced by the nucleus PDF (nPDF):

$$f_i^{\text{Pb}}(x, Q^2) = 82f_i^{p/\text{Pb}}(x, Q^2) + 126f_i^{n/\text{Pb}}(x, Q^2) \quad (1.9)$$

where $f_i^{p/\text{Pb}}$ ($f_i^{n/\text{Pb}}$) are the PDFs of a bound proton (neutron). The deep inelastic scattering experiments have shown that the bound nucleon PDFs are not the same as those of a free proton, which are modified in a complex way. This modification of PDFs is quantified by the nuclear modification:

$$R_i^{\text{Pb}}(x, Q^2) = \frac{f_i^{p/\text{Pb}}(x, Q^2)}{f_i^p(x, Q^2)} \quad (1.10)$$

A typical form of such modifications is shown in Fig. 1.12. In this function, four different behaviors of $R_i^{\text{Pb}}(x, Q^2)$ can be distinguished^[50], which correspond to:

- For $x \gtrsim 0.8$: This is the Fermi motion region. $R_i^{\text{Pb}}(x, Q^2) > 1$. Partons in the nucleus are more likely to have higher momentum fractions^[51].
- For $0.3 \lesssim x \lesssim 0.8$: This is the EMC region. $R_i^{\text{Pb}}(x, Q^2) < 1$, reaches the min-

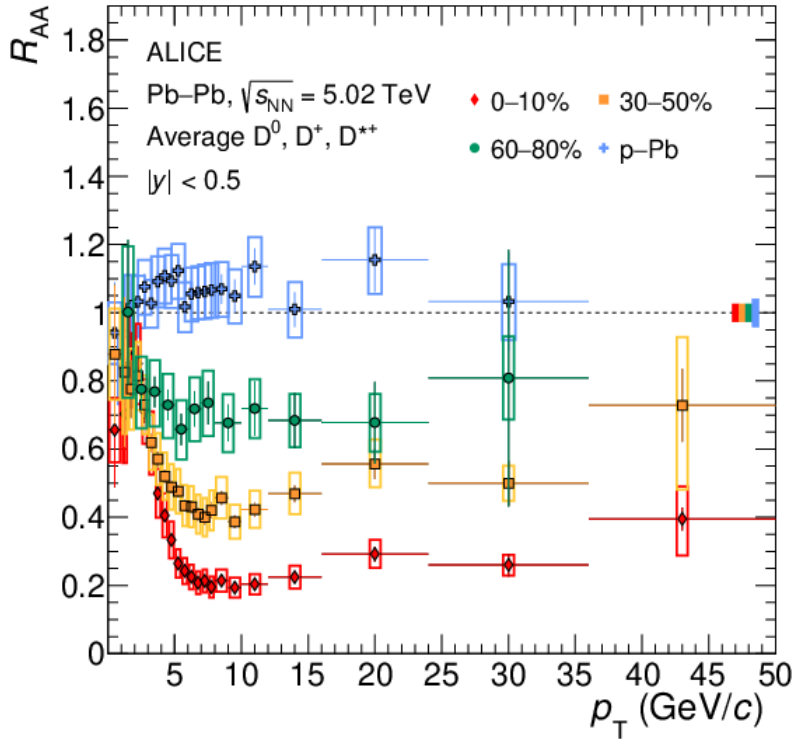


Figure 1.11 The prompt D-meson R_{AA} as a function of p_T measured in Pb–Pb collisions at $\sqrt{s_{NN}} = 5.02$ TeV in different centrality class (0–10%, 30–50%^[43], 60–80%^[47]), compared to that in p –Pb collisions^[48]

imum value around 0.6. The origin of the EMC effect may be attributed to non-perturbative effects^[52].

- For $0.1 \lesssim x \lesssim 0.3$: This is the anti-shadowing region. $R_i^{\text{Pb}}(x, Q^2) > 1$. It is produced by the coherence of multiscattering quark nuclear processes^[53].
- For $x \lesssim 0.1$: This is the shadowing region. $R_i^{\text{Pb}}(x, Q^2) < 1$, increases with increasing x and increases with increasing Q^2 . The usual explanation for the origin of shadowing is multiple scattering, from which many models have been developed^[54-56].

At LHC energies, most of the partons that produce heavy flavor come from the shadowing and anti-shadowing region.

Since nPDFs is non-perturbative phenomena, experimental inputs are crucial. So the first task is to connect the final-state particle kinematics, rapidity y and transverse momentum p_T , with the (x, Q^2) . In a $2 \rightarrow 2$ process, the final particle momentum fraction x is^[50],

$$x \approx \frac{2m_T}{\sqrt{s_{NN}}} e^{-y} \quad (1.11)$$

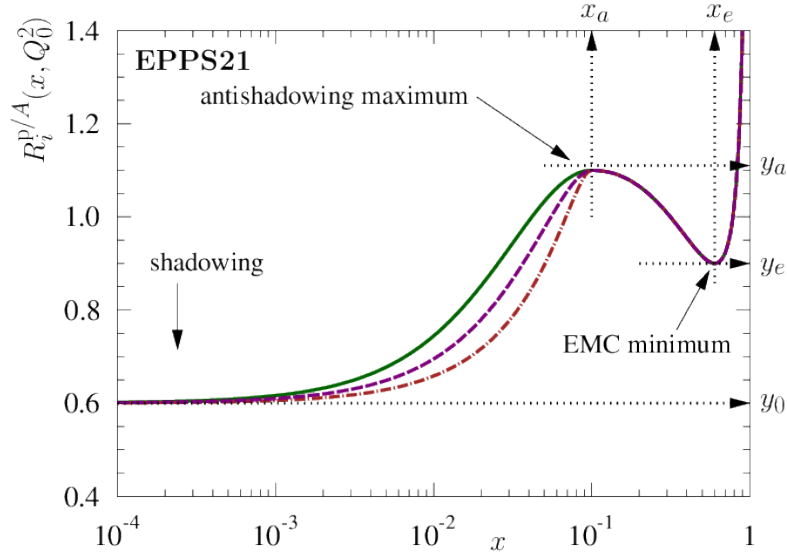


Figure 1.12 A typical modification of parton distribution functions in nucleus^[57]

where $m_T = \sqrt{m^2 + p_T^2}$ is the transverse mass of the final particle. Equation 1.11 shows that one can probe smaller x region in higher $\sqrt{s_{NN}}$ and more forward y .

The latest EPPS21^[57], which is a global analysis of collinearly factorized nPDFs at next-to-leading order in perturbative QCD, significantly improved the constraint on gluon distributions at small and intermediate values of the momentum fraction x compare with EPPS16^[58], shown in the left panel of Fig. 1.13. Many recent measurements from p Pb collisions at LHC have been included for the constraint: 5 TeV dijet (CMS)^[59] and 5 TeV D-meson (LHCb)^[60], as well as 8.16 TeV W^\pm (CMS)^[61]. The right panel of Fig. 1.13 shows the (x, Q^2) regions probed by these data.

This thesis will use open charm mesons (D mesons : $D_s^+ = c\bar{s}, D^+ = c\bar{d}$) as a probe to the CNM effects in $\sqrt{s_{NN}}=8.16$ TeV p Pb collisions and compare with the QCD calculations based on EPPS16^[58], nCTEQ15^[62]. Because of the larger collision energy and the forward coverage of the LHCb detector, the smaller x region can be reached in this study, as shown in Fig. 1.14.

1.5.3.2 Parton saturation and color glass condensate

As shown in Fig. 1.8, the gluon density increases strongly at low values of x , which implies a high gluon fusion probability. This leads to the break-down of perturbation QCD even for a small coupling constant, by strong non-linear effects. Meanwhile, the partons density cannot increase forever as x becomes smaller, otherwise it will cause the cross-section of deep inelastic scattering at fixed Q^2 to increase to unacceptably large value. This

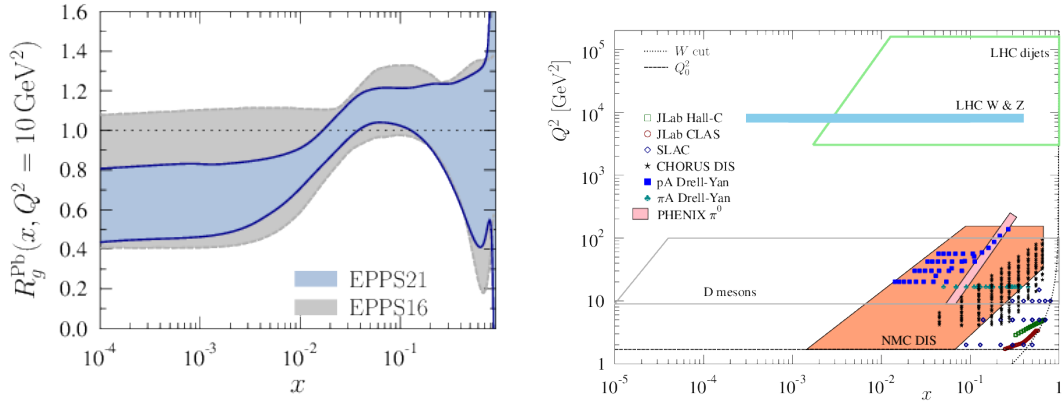


Figure 1.13 (left) $R_g^{\text{Pb}}(x, Q^2)$ calculated by EPPS16 and EPPS21. (right) The data used in EPPS21 displayed on the (x, Q^2) plane.

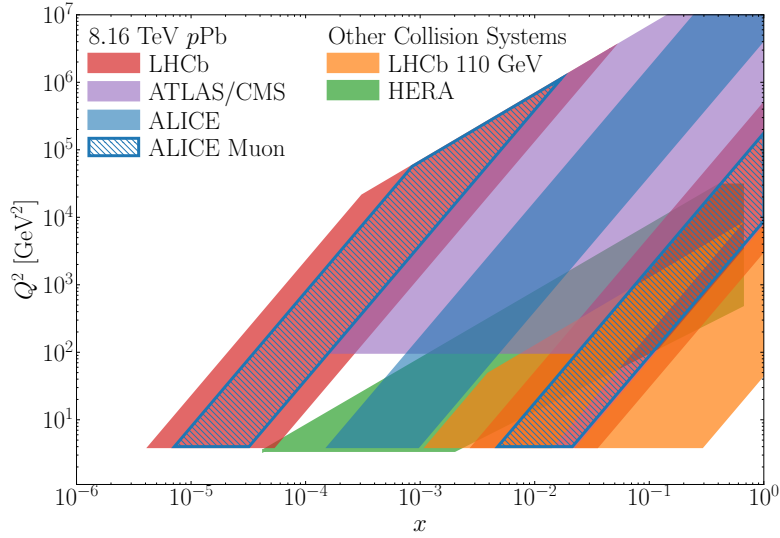


Figure 1.14 The (x, Q^2) coverage of several experiments.

phenomenon is parton saturation^[63]. This phenomenon can be described by an effective field theory, which called the color glass condensate^[24] (CGC). This “color” represents gluons carry color charges; “glass” represents gluons with small x are distributed randomly on the nucleus transverse disk; “condensate” represents gluon density is very high and saturated.

Figure 1.15 show the phase–diagram for QCD evolution. In the Bjorken limit, which corresponds to the case of $Q^2 \rightarrow \infty$ at fixed x , the parton number increases but density decreases. The evolution of this process is described by DGLAP^[64] (Dokshitzer-Gribov-Lipatov-Altarelli-Parisi) equations. On the way to approaching Regge-Gribov limit, corresponds to $x \rightarrow 0$ at fixed Q^2 , the gluon density in a proton rises very fast. The evolution of this process is described by the BFKL^[65] (Balitsky-Fadin-Kuraev-

Lipatov) equation. When x becomes smaller, gluon recombination will prevent the growth of gluon density until saturation. The evolution of this process is described by the BK^[66] (Balitsky-Kovchegov) or JIMWLK^[67] (Jalilian-Marian-Iancu-McLerran-Weigert-Leonidov-Kovner) equations. Equation 1.12 gives the relationship between Q_s and x when gluon is saturated,

$$Q_s^2 \propto (1/x)^\lambda. \quad (1.12)$$

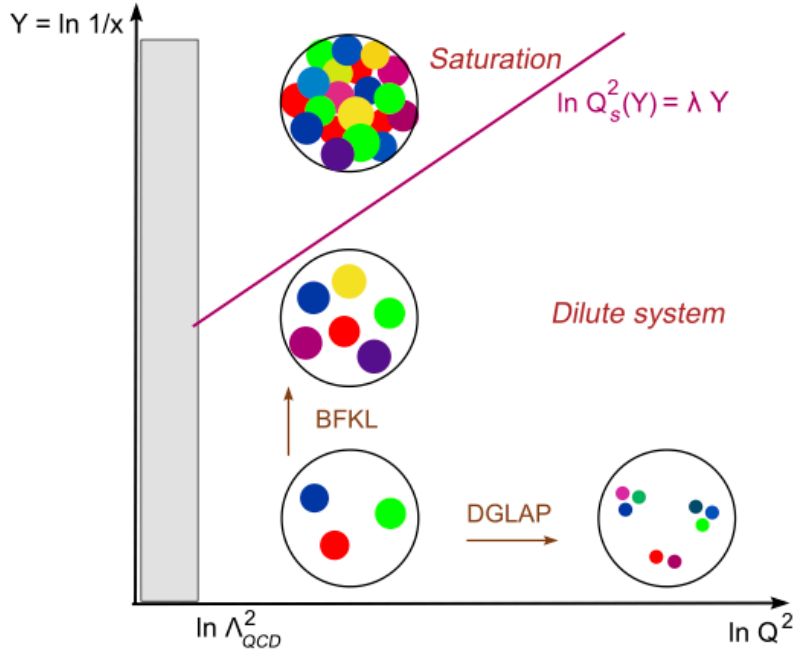


Figure 1.15 The phase-diagram for QCD evolution^[68].

Proton-lead collisions which are collisions between a dilute nucleon and dense nucleons can be studied in the CGC framework. For lead nucleus ($A \sim 200$) at LHC energy ($x \sim 10^{-4}$), the saturation momentum Q_s^2 is about 2-4 GeV² as shown in Fig. 1.16. The CGC successfully predict a suppression of D mesons production in forward pPb collisions relative to pp ^[69], supporting a strong shadowing at very low x .

1.5.3.3 Cronin effect

Another important CNM effect that contributes to the modification of the D mesons production in pPb collisions compared to that in pp collisions is the Cronin enhancement, which was first observed in the fixed-target proton-nucleus (H_2 , D_2 , Be, Ti and W) collision at Fermilab^[71]. It describes an enhancement of the inclusive hadron production at intermediate p_T ($2 < p_T < 6 \text{ GeV}/c$), eventually lead to an increase of the nuclear

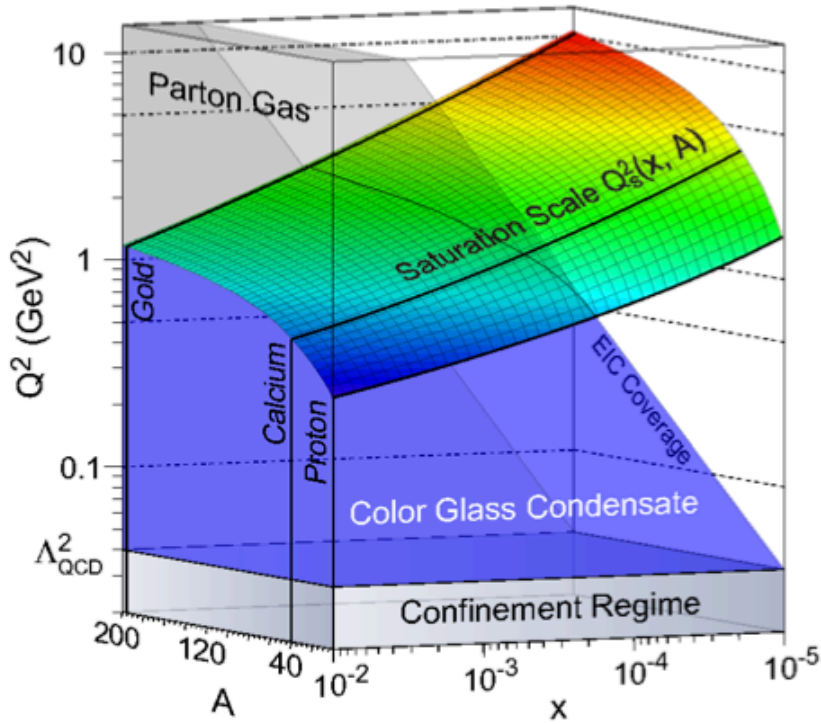


Figure 1.16 Saturation momentum as a function of momentum fraction x and atomic number A ^[70].

modification factor above unity.

The interpretation of this effect is based on the multiple interactions in the large x region and partons re-scattering^[72-73]. These interactions transfer transverse momentum to the partons, which led to p_T broadening for the hadrons produced in hard scatterings, such as heavy flavor hadrons. Relevant theoretical calculations^[74] have successfully explained the open heavy flavor enhancement in backward pA collisions at LHC^[75] and RHIC^[76].

1.5.4 Heavy flavor hadronisation

There are two kinds of hadronisation mechanisms in medium. One is the heavy flavor hadronisation via fragmentation into lower-momentum hadrons, the other is that they can recombine with other quarks to form higher-momentum hadrons.

In ep/ee collisions, the clean environment allows to study the fragmentation functions of heavy flavor. The fragmentation fractions represent the probabilities of a quark to hadronize into a given hadron. Figure 1.17 shows charm quark fragmentation fraction in different experiments. The fragmentation fraction in ep and ee are compatible within uncertainties, but different from the ones measured in pp . This is also an important evidence that the Parton-to-hadron fragmentation universality hypothesis (the independence

of the collision system) is invalid.

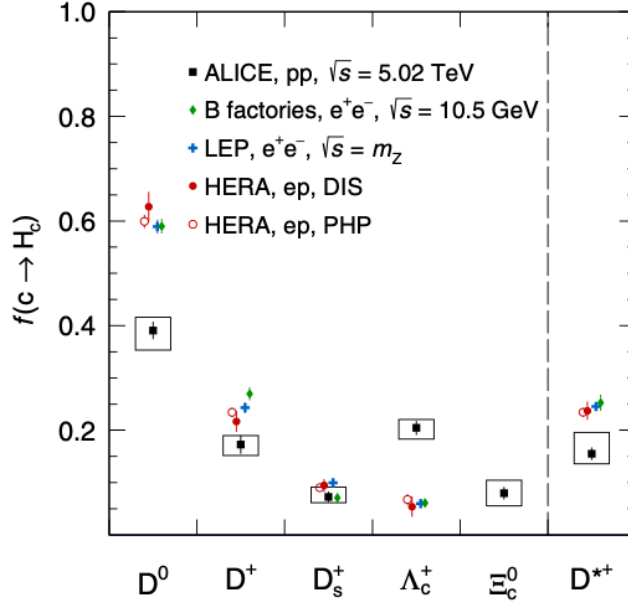


Figure 1.17 Charm quark fragmentation into charm hadrons measured in different collisions and energies^[77].

In QGP medium, the high p_T heavy flavor quark hadronisation is still dominated by fragmentation mechanism. But the low p_T heavy flavor quarks can be hadronized through the recombination with low momentum light quarks which is copious in QGP^[78-81]. Due to the larger binding energy, the heavy flavor quarks will preferentially recombine with s quarks instead of u, d quarks^[82]. This leads to the enhancement of strange heavy flavor hadrons compared with non-strange heavy flavor hadrons. The strange charm meson D_s^+ is a sensitive probe of the recombination (coalescence) mechanism. If recombination mechanism contributes to its production, the D_s^+/D^+ production ratio is expected to be larger in heavy ion collisions compared to pp collisions, also due to the enhanced strangeness production in QGP.

Recently, the enhancement of D_s^+/D^0 was observed in PbPb collisions at $\sqrt{s_{NN}} = 5.02$ TeV at ALICE^[83] and in AuAu collisions at $\sqrt{s_{NN}} = 200$ GeV at STAR^[84]. Figure 1.18 shows the results of ALICE. The top row shows the D_s^+/D^0 yield ratios in 0–10% (left panel) and 30–50% (middle panel) centrality regions compared to pp collision at the same energy^[85] (right panel) and to theoretical calculations. The D_s^+/D^0 ratios in PbPb collisions divided by those results in pp collisions are shown in the bottom row of the same figure. In the $2 < p_T < 8$ GeV/ c region, the D_s^+/D^0 ratios in PbPb collisions are higher than those in pp collisions (2.3σ for 0–10% centrality and 2.4σ for 30–50% centrality). This result is also consistent with the previous $\sqrt{s_{NN}} = 5.02$ TeV PbPb results of AL-

ICE^[47]. Figure 1.19 shows the results of STAR. The enhancement of the D_s^+/D^0 ratio was also observed in $\sqrt{s_{NN}} = 200$ GeV AuAu collisions^[84]. These results indicate that the recombination mechanism plays an important role in charm hadronization in heavy ion collisions.

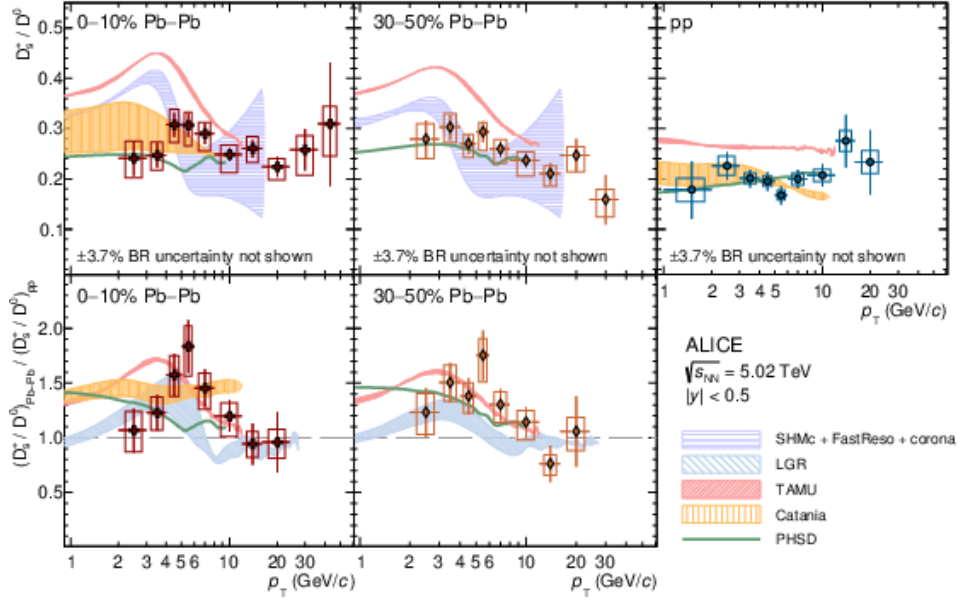


Figure 1.18 Top: D_s^+/D^0 ratios as a function of p_T in 0–10% (left panel) and 30–50% (middle panel) centrality classes in PbPb collisions at $\sqrt{s_{NN}} = 5.02$ TeV and in pp collisions (right panel) at the same centre-of-mass energy. Bottom: D_s^+/D^0 ratios in PbPb collisions divided by those in pp collisions, in 0–10% (left panel) and 30–50% (right panel) centrality classes, compared with theoretical calculations^[83].

1.6 Strangeness enhancement in small system

In recent years, some QGP signatures that were originally observed in heavy ion collisions have also been seen in high-multiplicity pp or pA collisions (also known as small system). In 2017, strangeness enhancement was observed in high-multiplicity pp ^[87] and pPb ^[88–89] collisions. As shown in Fig. 1.20, the ratio of the yields of (multi-)strange hadrons to those of non-strange hadrons (pions) increases significantly with the event charged particle multiplicity in small systems, and gradually approaches the values in PbPb collisions, where a QGP is formed. This enhancement are more pronounced for multi-strange hadrons which have larger strangeness contents. Although the origin of the strangeness enhancement in small system is still under debate, this may indicate that a common underlying physics mechanism which gradually compensates the strangeness suppression in fragmentation.

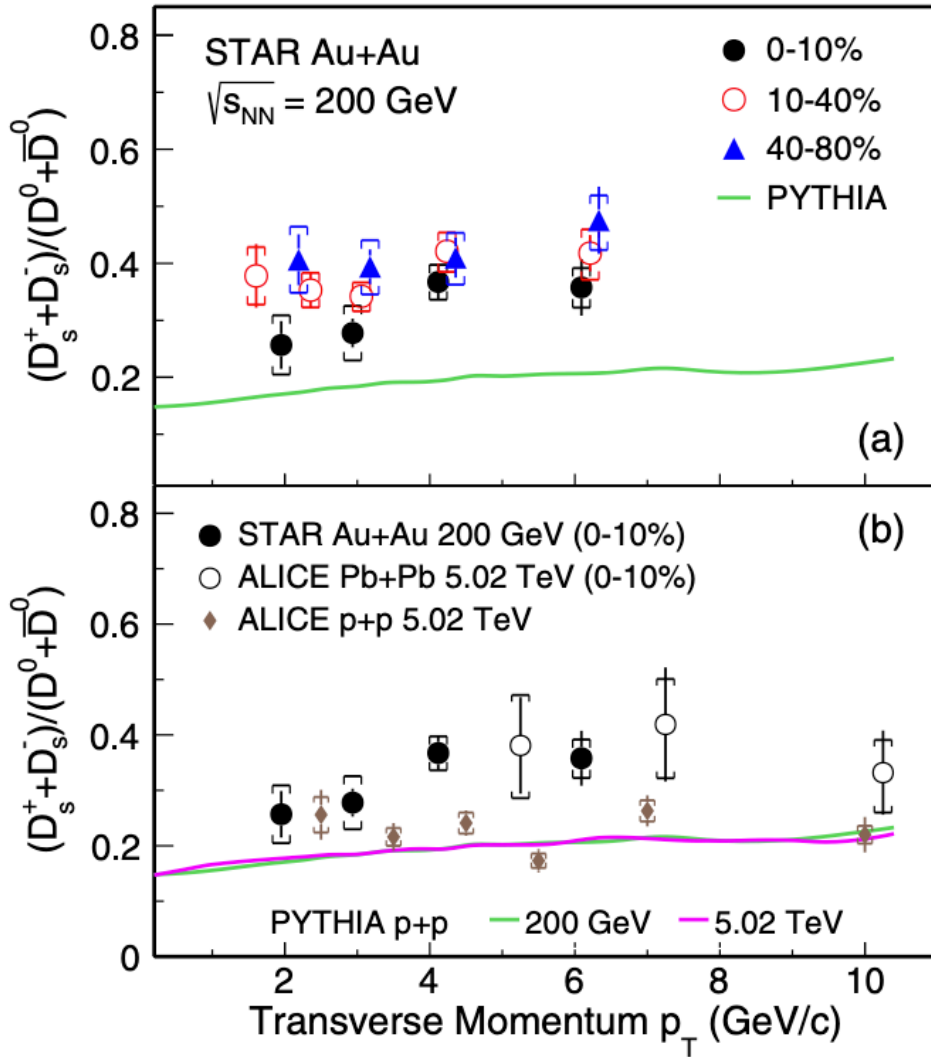


Figure 1.19 Top: D_s^+/D^0 ratios as a function of p_T in various centrality classes in AuAu collisions at $\sqrt{s_{NN}} = 200$ GeV^[84], compared to a PYTHIA simulation for pp collisions at the same energy. Bottom: STAR results of D_s^+/D^0 ratios as a function of p_T in AuAu collisions at $\sqrt{s_{NN}} = 200$ GeV^[84], compared to ALICE results in PbPb^[43] and pp ^[86] collisions at $\sqrt{s_{NN}} = 5.02$ TeV, as well as to the PYTHIA simulations for pp collisions at the same energies.

Next, several theoretical models to understand strangeness enhancement in small system are introduced. The first one is the dynamical core–corona initialisation (DCCI) model^[93-95]. The (multi) strange over non-strange ratio that gradually increases in the small system and eventually saturates into the large system is interpreted as a continuous change of the hadron production mechanism from string fragmentation to the QGP formation. The DCCI model combines two mechanisms through the core-corona structure. The ‘core’ hadronization from QGP, which represents the fluids under local thermal and chemical equilibrium. While the ‘corona’ hadronization by string fragmentation, which represents the system composed of non-equilibrated partons traversing the fluids or the

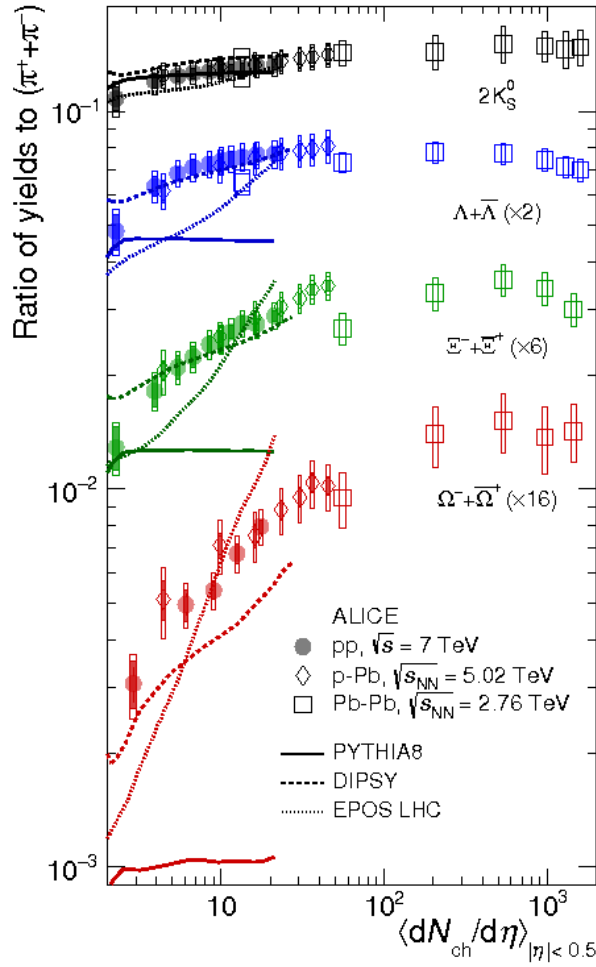


Figure 1.20 The ratios of strange hadron yields to pions as a function of multiplicity (p_T integrated) from pp , pPb and $PbPb$ collisions at LHC energies. The data is compared with theoretical calculations^[90-92]. This figure is taken from Ref. [87].

vacuum. The fraction of core-corona represents the evolution from small systems to large systems. This model successfully reproduces the strangeness enhancement in small systems as shown in Fig. 1.21 and strongly indicate the formation of proton-sized droplets of QGP in high multiplicity small colliding systems.

The other attempt is the rope hadronization model^[96-97], which does not assume a formation of QGP. This model is based on the Lund string model^[98-99] where the confined colour field between a $q\bar{q}$ pair is modelled as a semi-classical string with tension $\kappa = 1$ GeV/fm. The string will break into smaller pieces and form a new pair $q\bar{q}$, when the energy

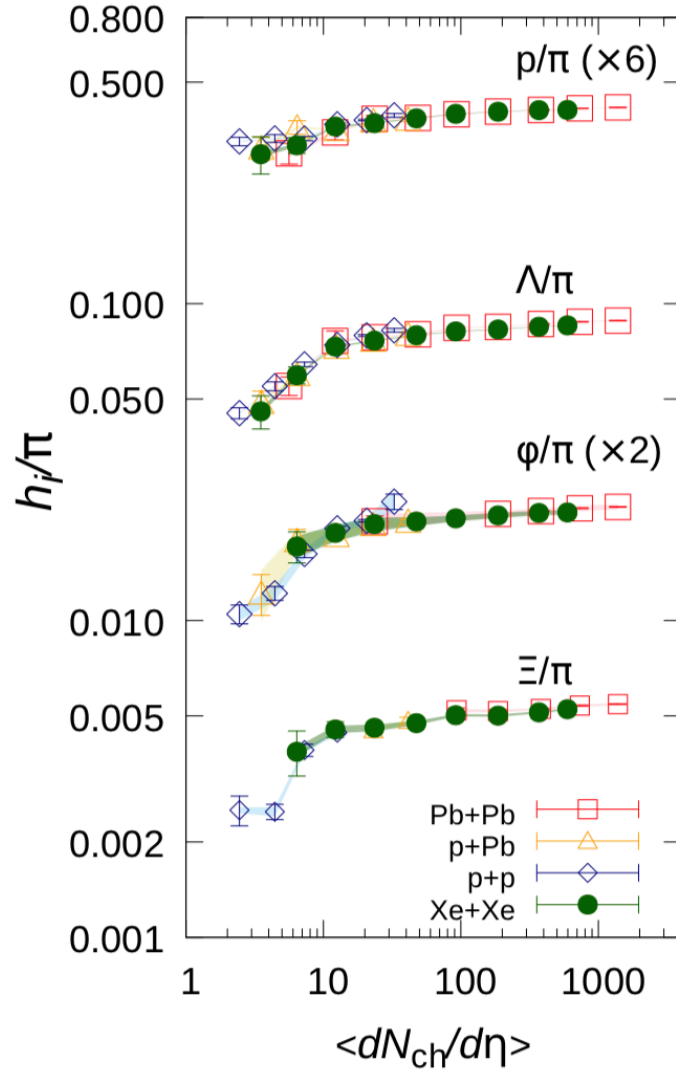


Figure 1.21 Strange hadrons over non-strange hadrons yield ratios as a function of charged particle multiplicity in different collision systems^[95].

is sufficient. The probability of string breaking follows the Schwinger equation^[100]:

$$\frac{d\mathcal{P}}{dp_{\perp}} \propto \kappa \exp\left(-\frac{\pi m_{\perp}^2}{\kappa}\right). \quad (1.13)$$

The above equation shows that the production of s quarks is suppressed compared with u , d quarks due to a larger mass threshold. But this is limited to the strings fragment independently with each other. When the quark pairs density is high enough, the overlapping colored strings act coherently to form a stronger color rope as shown in Fig. 1.22. This color rope would then hadronize with a higher effective string tension κ which leads to strange hadrons enhancement. In 2018, the rope hadronization model is embedded to PYTHIA8^[101], Angantyr^[102] and reproduced enhanced production of strange and multi-

strange hadrons in small system as shown in Fig. 1.23.

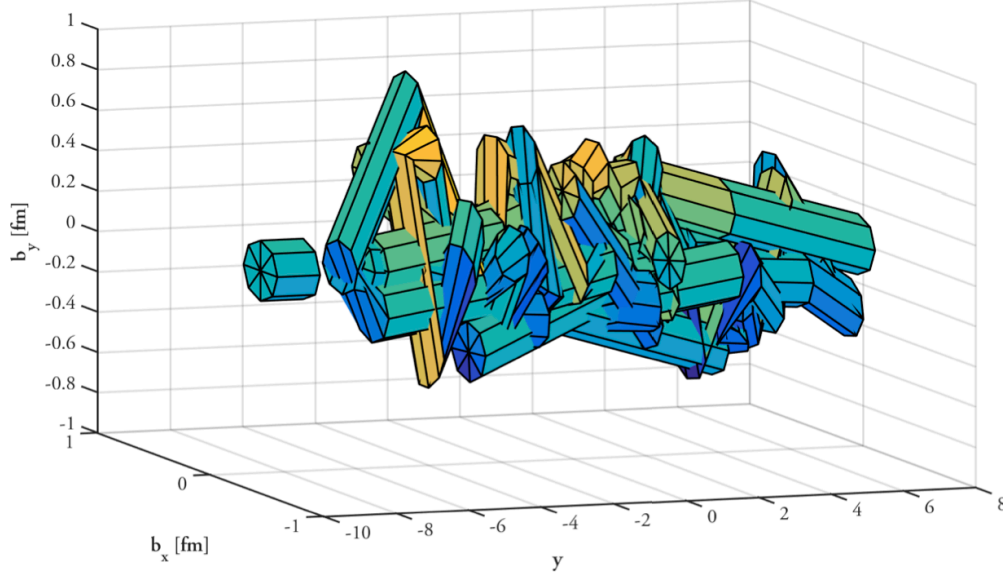


Figure 1.22 Strings overlap with each other in a simulated pp collisions. This figure is taken from Ref. [97].

In the future, the measurement of strangeness enhancement in small system will focus on very high-multiplicity events in pp collision and check if multi-strange hadron to pion ratios will reach saturation (towards Pb-Pb values) or continue to increase.

In view of the fact that s quarks can be copiously produced in small systems (pp , pPb), the strangeness enhancement in hadronisation of heavy flavor quarks is also expected to be observed. Indeed, the recent LHCb measurement on B_s^0/B^0 ratios at low p_T ($p_T < 6$ GeV/ c) in pp collisions seems hint an increasing trend with the event multiplicity, as shown in Fig. 1.24^[104]. While the data shows no significant multiplicity dependence at higher p_T ranges. This is qualitatively consistent with the emergence of quark coalescence as an additional hadronization mechanism for heavy quarks in high-multiplicity collisions. Relevant measurements have also been done from ALICE, but their D_s^+/D^+ ratios in pPb collisions do not show a significant dependence on charged-particle multiplicity due to the limitation of statistics, as shown in Fig. 1.25^[48].

1.7 Thesis scope

This thesis will measure the double differential cross-sections of the prompt D_s^+ and D^+ produced in pPb collisions at $\sqrt{s_{NN}} = 8.16$ TeV taken by the LHCb detector, covering the forward rapidity range of $1.5 < y < 4.0$ and the backward rapidity range of $-5.0 <$

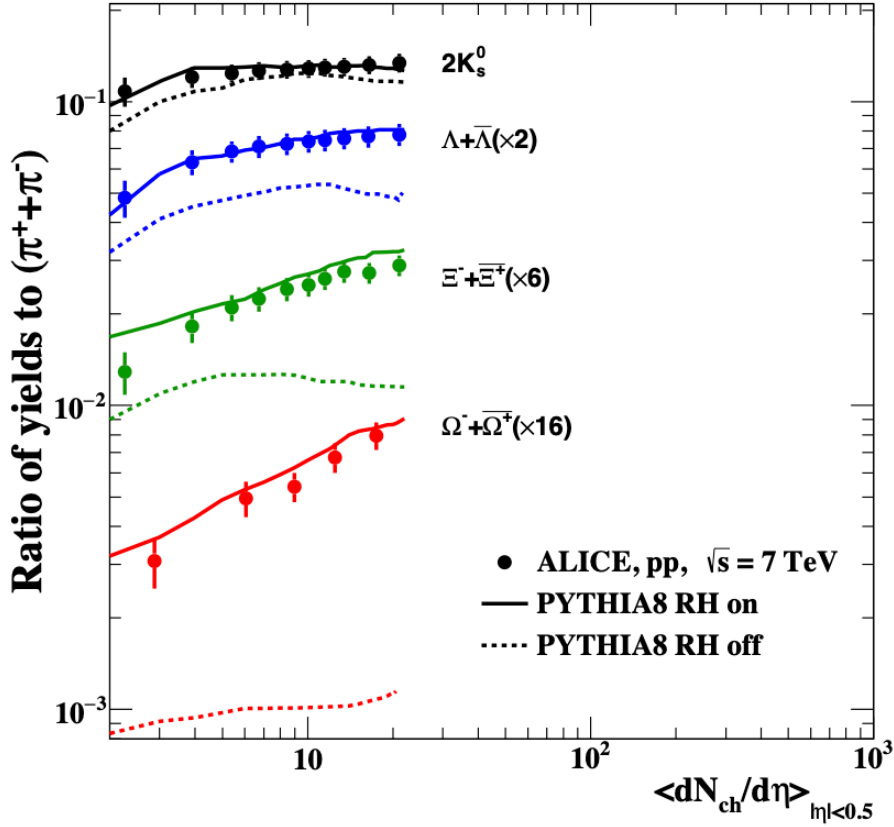


Figure 1.23 Ratio of yield of strange hadrons to pions as a function of multiplicity at mid-rapidity from PYTHIA8 with and without rope hadronization, and compared to ALICE data^[103]

$y < -2.5$, and the transverse momentum range of $1 < p_T < 13 \text{ GeV}/c$. Based on these results, the nuclear modification factor and the forward-backward ratio will be calculated and compared with theoretical calculations, and the influence of cold nuclear matter effects on the open charm meson production will be discussed.

In addition, the D_s^+/D^+ cross-section ratio will be measured as a function of event multiplicity in different transverse momentum intervals in $p\text{Pb}$ collisions. The contribution of recombination mechanism in different p_T intervals will be studied, in order to find whether there is strangeness enhancement in charm hadronisation in small system. Although it will not end the debate on whether QGP is formed in small systems, this thesis aims to provide a more complete and clear experimental perspective for answering this question.

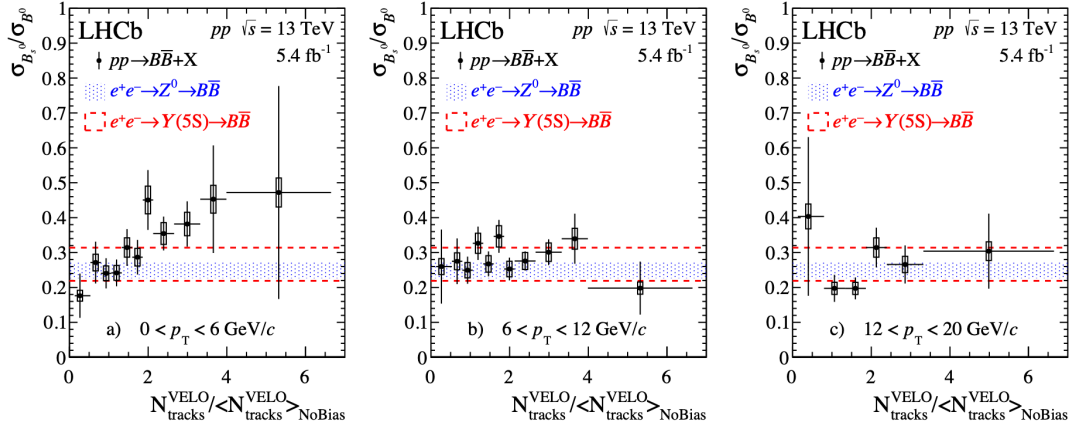


Figure 1.24 B_s^0/B^0 ratios as a function of normalized event multiplicity in different p_T ranges in pp collisions at $\sqrt{s} = 13$ TeV^[104].

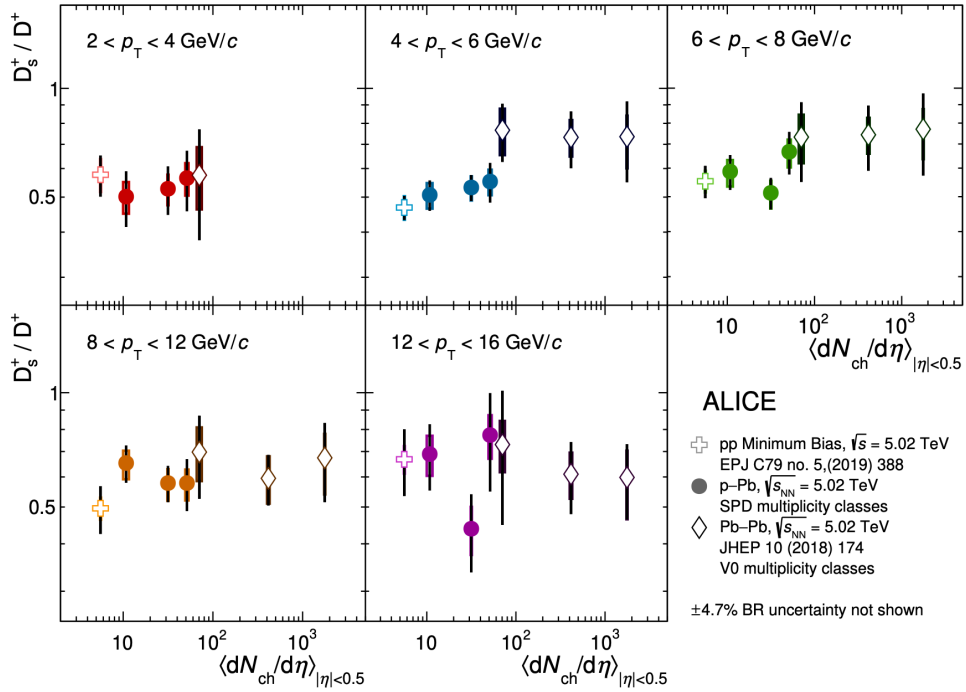


Figure 1.25 D_s^+/D^+ ratios as a function of the event charged particle multiplicity in pp , pPb and $PbPb$ collisions at 5 TeV^[48].

CHAPTER 2 THE LHCb EXPERIMENT

2.1 The Large Hadron Collider

The Large Hadron Collider (LHC) is a circular hadron accelerator and collider. This machine is installed in the 26.7 km tunnel previously used for the Large Electron Positron Collider (LEP). It is located on the Swiss French border and lies between 45 m and 170 m below the surface. A more detailed description can be found here^[105].

The LHC aims to perform hadronic collisions at very high energies. A schematic layout of the LHC is shown in Fig. 2.1. In the standard configuration, the proton beam is boosted through LINear ACcelerator 4 (LINAC 4), Proton Synchrotron Booster (PSB), Proton Synchrotron (PS) and Super Proton Synchrotron (SPS) sequentially. The beam energy reaches 450 GeV at SPS. Then the beams are injected into the separated pipes of the LHC in opposite directions. The beams are guided by the superconducting magnets and boosted by the radiofrequency cavities to reach TeV energy level. In order to produce a magnetic field around 8.33 T, these magnets are put inside superfluid helium at 1.9 K. In addition, ultra-high vacuum should also be maintained in the pipes where the beams travel. The maximum laboratory energy per proton is 7 TeV. The centre of mass energy of the colliding proton pairs is up to 14 TeV. Besides protons, the LHC can also operate with beams of heavy ions, such as lead. The acceleration process of lead is similar to the protons. Except that they started at LINAC 3 and then injected at the Low Energy Ion Ring (LEIR) and then to the PS. This allows us to combine a proton beam with a lead beam to perform proton-lead collisions.

The proton or ions in the beams are distributed in small packages, named bunches, and are organised along the LHC pipes. There are about 2800 bunches in each beam, but not all the bunches are filled with proton or ions (empty bunches). The plan of the filled or empty bunches inside the LHC is called as filling scheme. During the four-year Run 2 period, the integrated luminosity is about 150 fb^{-1} , which is much higher than Run 1. In the proton run, the bunch spacing can be up to 25 ns, with $\sim 10^{11}$ protons per bunch, the peak instantaneous luminosity is about $10^{34} \text{ cm}^{-2} \text{ s}^{-1}$. In the lead run, the bunch spacing is 75 ns, with $\sim 10^7$ ions per bunch, the peak instantaneous luminosity is about $10^{27} \text{ cm}^{-2} \text{ s}^{-1}$.

There are four large experiments located in LHC: ATLAS (A Toroidal LHC Appa-

ratus), CMS (Compact Muon Solenoid), ALICE (A Large Ion Collider Experiment) and LHCb (Large Hadron Collider beauty).

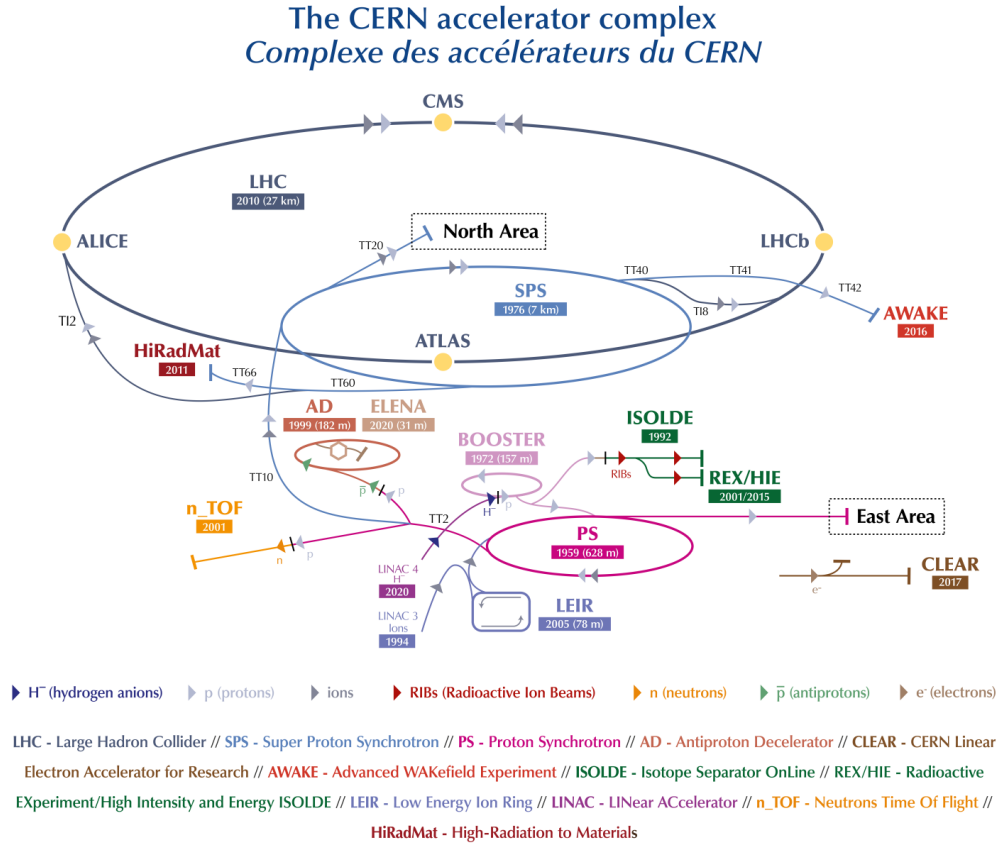


Figure 2.1 Schematic layout of the CERN accelerator complex^[106].

2.2 The LHCb experiment

The original physics goals of LHCb are to study CP violation, rare decays of beauty and charm hadrons, flavour symmetry breaking and to search for new particles. In these fields, many important results have been made, such as the discovery of pentaquark^[107], the first observation of CP violation in the charm decays^[108] or the recent evidence for the breaking of lepton universality in beauty-quark decays^[109]. Additionally, LHCb has also been involved in some interesting physics programs, such as the study of heavy ion collisions, which is also the main topic of this thesis.

The LHCb detector is a single-arm forward spectrometer. “Single-arm” means that most devices are located on one side of the collision point. “Forward” refers to the geometric acceptance of the detector. The angular coverage is from 10 to 300 mrad in the horizontal plane and from 10 to 250 mrad in the vertical plane without considering mag-

netic field bending. The LHCb forward coverage is significantly different from other experiments at the LHC. The purpose of this design is that the $b\bar{b}$ pair has higher density in the forward. The production process of $b\bar{b}$ pair in pp collision is simulated by PYTHIA8, including $\bar{q}q \rightarrow \bar{b}b$, $gg \rightarrow \bar{b}b$, $\bar{q}q \rightarrow \bar{b}bg$ (where $q \neq b$), $\bar{b}b \rightarrow \bar{b}b$, $gg \rightarrow \bar{b}bg$ processes. The five flavors (u, d, s, c, b) are considered in parton distribution functions. Figure 2.2 shows that most $b\bar{b}$ pair (27%) are distributed in the narrow cone angle.

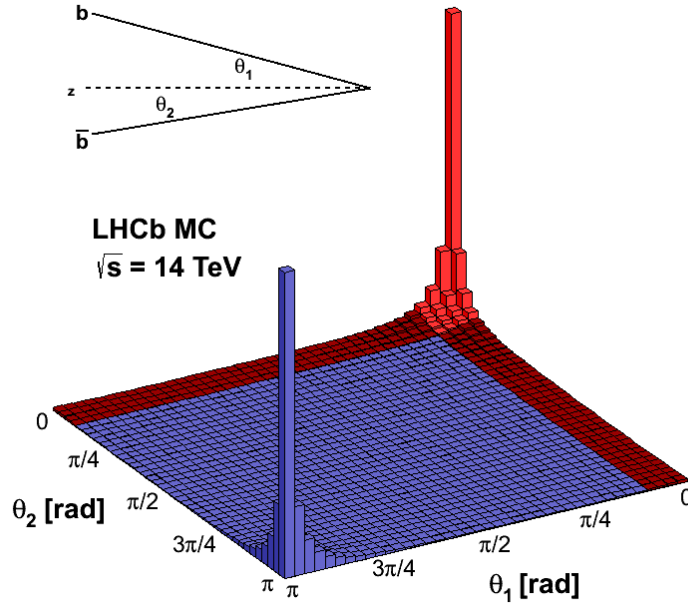


Figure 2.2 Angular distribution of $b\bar{b}$ pair production in pp collisions at $\sqrt{s} = 14\text{TeV}$ ^[110].

In order to reconstruct B -hadrons, the detector needs to have good vertex resolution, for primary vertices (PV) where B -hadrons are produced and secondary vertices (SV) where B -hadrons decay. The mean flight distance of B -hadrons are ~ 10 mm. In addition, a good resolution of mass, lifetime, angular variables are also required. The sub-detectors of LHCb are designed to achieve these goals.

Figure 2.3 shows an overview of the LHCb in Run 1&2, containing the definition of coordinate system (x - y - z axis). The sub-detectors from left to right are: VERtEX LOCator (VELO), Ring Imaging Cherenkov detector 1 (RICH1), Tracker Turicensis (TT), magnet, three tracking stations (T1, T2, T3), RICH2, muon station (M1), Electromagnetic Calorimeter (ECAL) and Hadronic Calorimeter (HCAL), and rest of the muon system stations (M2, M3, M4 and M5).

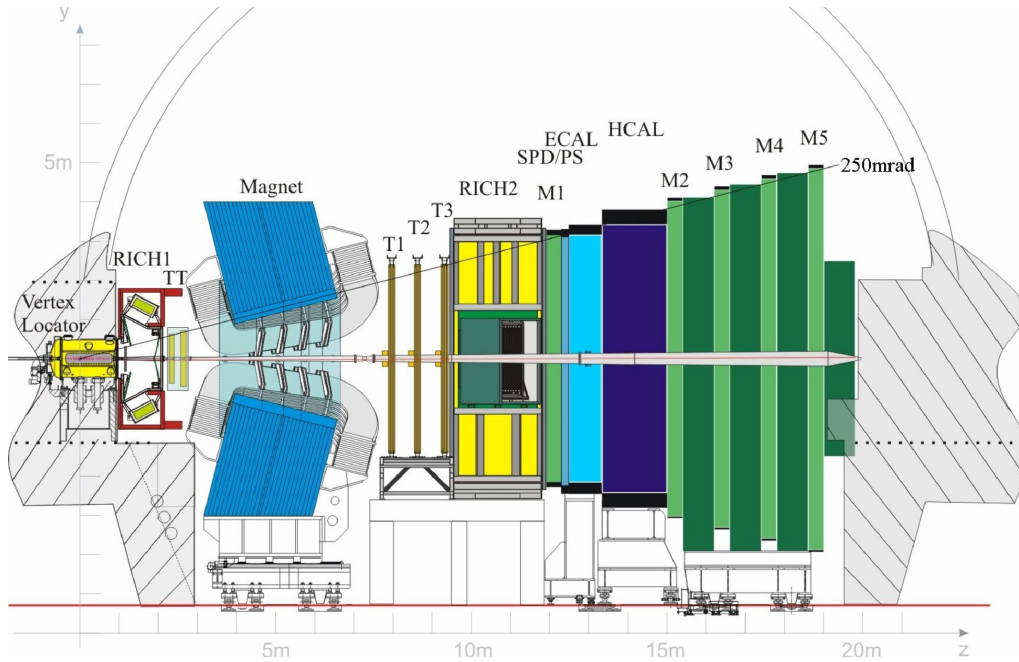


Figure 2.3 An overview of the LHCb detector in Run 1&2^[111].

2.2.1 Tracking system

The main components of LHCb tracking are silicon micro-strip detectors and straw tube drift chambers, including the following sub-detectors : VELO, TT (Tracker Turicensis), IT (Inner Tracker) and OT (Outer Tracker). It provides a high-precision reconstruction of charged tracks and interaction vertices. Combined with dipole magnets, the tracking system can also provide precise measurement of the particle momentum.

2.2.1.1 Vertex locator

The Vertex Locator (VELO) is a silicon microstrip detector, located at most upstream of the detector, surrounding the beam collision region. The VELO aims to accurately measure the track of charged particles. These tracks can be used to reconstruct primary vertex and secondary vertex. The high tracking precision also allows accurate measurements of the lifetimes and the impact parameters of particles. More than this, these tracks can be used as seeds for the downstream detector to reconstruct the complete track.

The VELO consists of 21 silicon modules. Each module contains two semicircular microstrips silicon sensors, known as R and ϕ sensors. These two sensors with different structures are used to measure the two-dimensional hit position. The R sensor records the radial impact position, and the ϕ sensor provides azimuth information. These silicon modules are arranged along the beam as shown in Fig. 2.4. The radius of each sensor is about 42 mm and the thickness is around 300 μm . For easy operation and modification,

these sensors are placed in two retractable halves. When testing beam, the beam focusing and other parameters are not very stable. To avoid interference to the beam and radiation damage to the sensor, the two VELO halves are separated. After the beam focusing is stable, the two VELO halves are closed to cover full azimuthal angular. At this time, the sensors are only 7 mm away from the LHC beams. The geometry of VELO ensures that tracks within the LHCb acceptance can leave footprints on it.

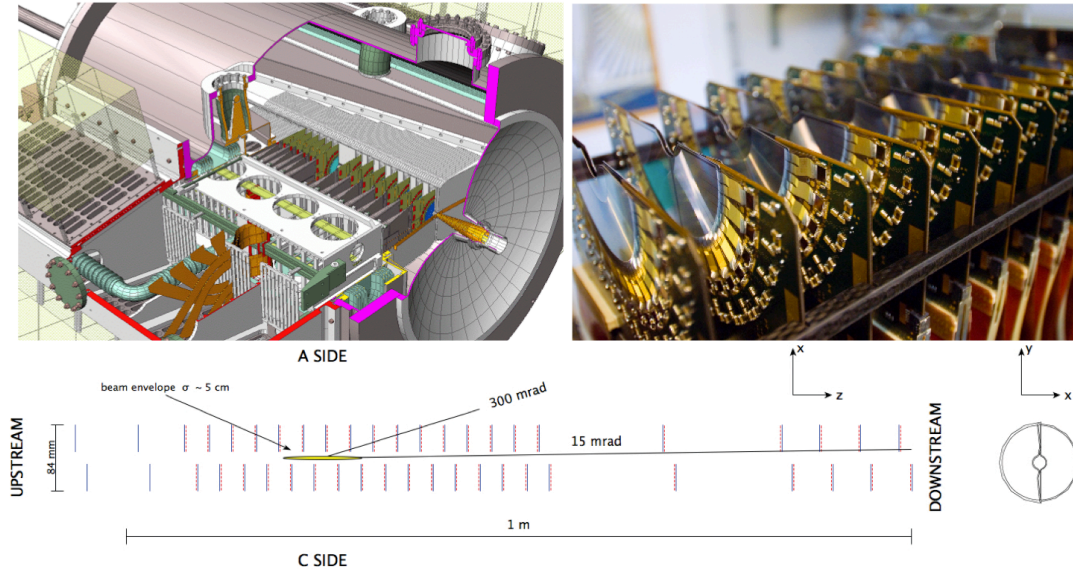


Figure 2.4 Top left: the LHCb VELO vacuum tank. Top right: the silicon sensors and readout hybrids. Bottom: the VELO sensors along z and cross-section of a VELO sensor in the xy plane. The detector is shown in its closed position^[112].

A typical efficiency for VELO track is 98% as shown in the left of Fig. 2.5. On the basis of VELO track, we can reconstruct PV. The resolution of PV is $10 \sim 35 \mu\text{m}$ in the transverse plane and $50 \sim 300 \mu\text{m}$ along the beam axis, depending on the number of tracks used for PV reconstruction. The impact parameter (IP), which is the distance between a track and its closest PV, is often used to separate particle produced in the PV and those decayed from beauty or charm. The IP resolution as a function of track momentum is shown in the right of Fig. 2.5. The above discussion is based on pp collisions. For proton-lead configuration, the detector occupancy reaches higher values, so the performance is expected to decline.

2.2.1.2 Magnet dipole

LHCb dipole magnets produce an integrated magnetic field of about 4 Tm. The total weight of the dipole is 1600 tons and it operates at room temperature. The main magnetic field is along the y -axis, and the non-uniformity is about 1%. It can bend charged particles

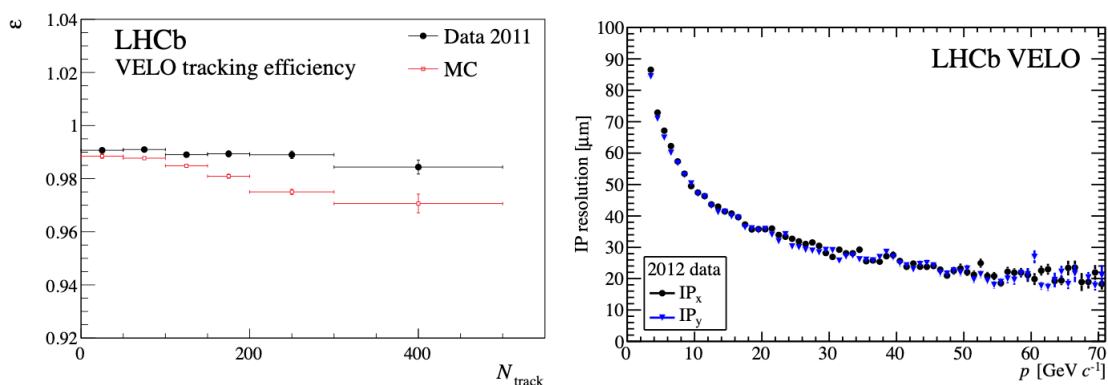


Figure 2.5 Left: VELO tracking efficiency in data and simulation from 2011 as a function of the number of reconstructed tracks in the event. Right: IP resolution as a function of momentum^[112].

on the x - z plane, and accurately measure the momentum of charged particles in combination with the upstream and downstream track systems. Low momentum charged particles will deviate greatly when passing through the magnetic field and will not be accepted by downstream detectors. Therefore, only detectors placed upstream of the dipoles can be used to find them. Most high momentum particles are bent by magnets and can be detected in downstream trackers. The relative accuracy of measurement of momentum and magnetic field strength is 0.5% and 0.01% respectively. In order to avoid systematic uncertainty caused by asymmetry of magnetic field, The magnetic field polarity is reversed frequently during data-taking.

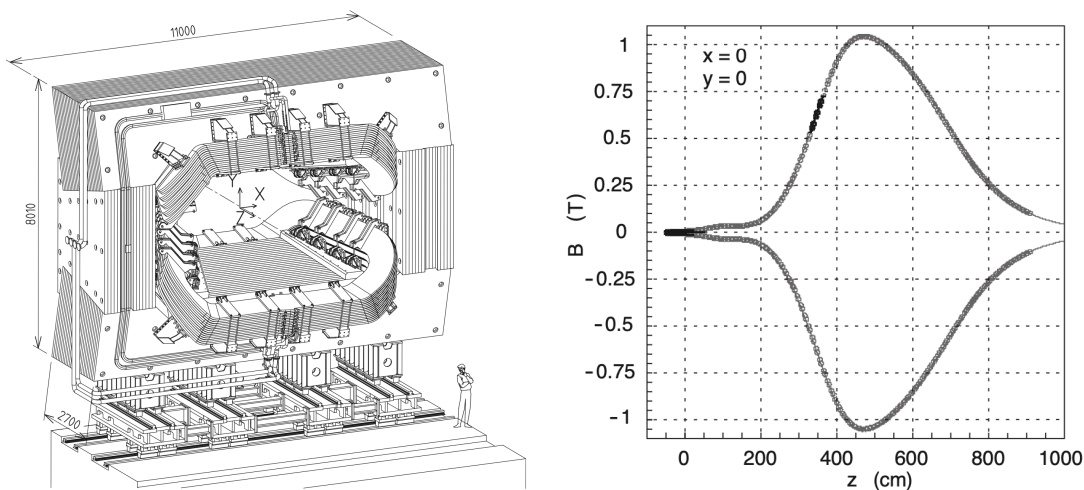


Figure 2.6 Left: the scheme of the LHCb dipole magnet. Right: the magnetic field intensity as a function of z ^[113].

2.2.1.3 Silicon Tracker

The silicon tracker consists of the Tracker Turicensis (TT) and the Inner Tracker (IT). Both TT and IT use silicon microstrip sensors.

The TT is placed at the upstream of the magnet. It is made up of four detection layers with an x - u - v - x arrangements. Each layer is composed of many sensor units. The sensor unit is 9.64 cm wide, 9.44 cm long and 500 μm thick. There is an angle in the sensor arrangement direction between layers to ensure that 3D information of hit can be reconstructed. The first and last layers (x layers) are vertical, the middle two layers (u and v layers) are rotated with an angle of -5° and 5° respectively. A typical TT hit reconstruction efficiency is 99.7%, and the resolution is about 50 μm . A layout of the v -layer of the TT detector is shown in Fig. 2.7.

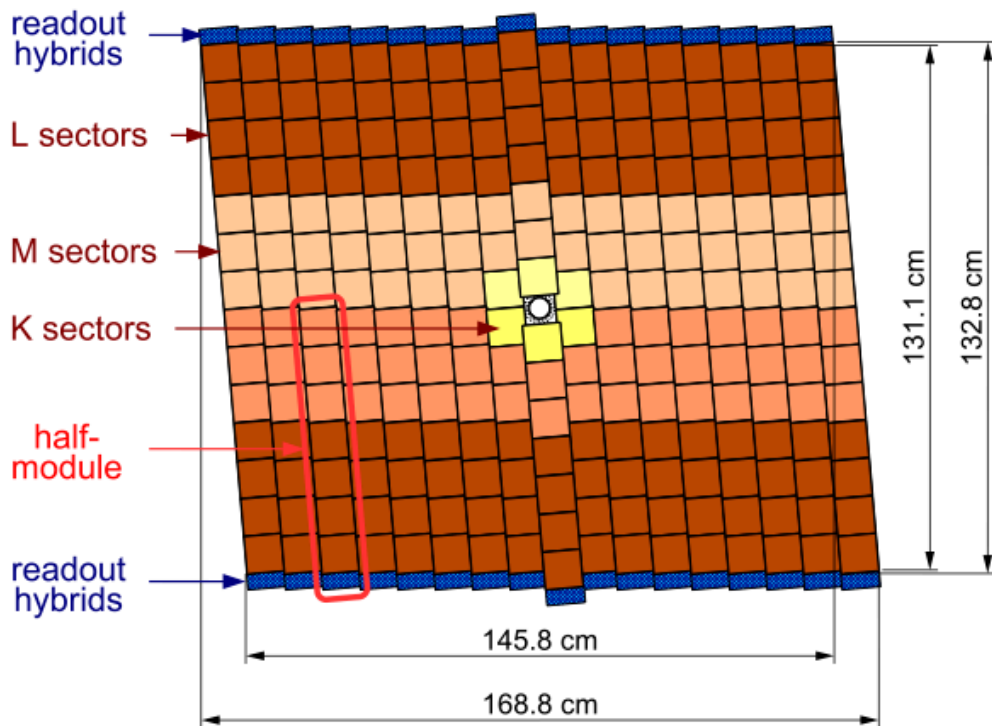


Figure 2.7 A layout of the third TT detection layer^[113].

The IT is next to the magnet and located downstream, is part of T stations. It is made up of four detector boxes that are arranged around the beam pipe. Each detector box contains four detection layers and each detection layer consists of seven detector modules as shown in Fig. 2.8. A typical IT hit reconstruction efficiency is 99.8%, and the resolution is about 50 μm .

2.2.1.4 Outer tracker

The OT is a drift-time detector, covers the largest fraction in T stations (including T1, T2 and T3), designed to track charged particles and accurately measure their momentum.

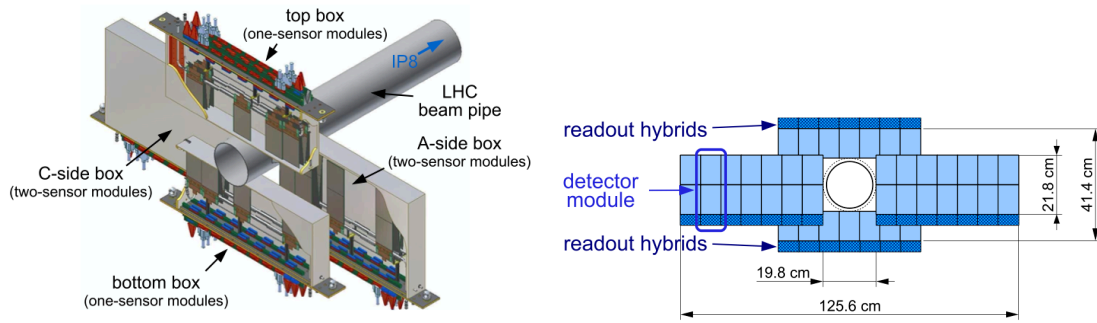


Figure 2.8 A layout of IT detector^[113].

It is composed of two staggered layers straw-tube drift chambers and is filled with mixture gas of argon (70%), carbon dioxide (28.5%) and oxygen (1.5%) as shown in Fig. 2.9. Charged particles passing the straw-tubes will ionise the gas along their track. The ionisation electrons will drift to the wire located at the centre of the straw. The drift time is proportional to the distance of the particle track to the wire. A typical OT hit reconstruction efficiency is 99.3%, and the resolution is about 200 μm .

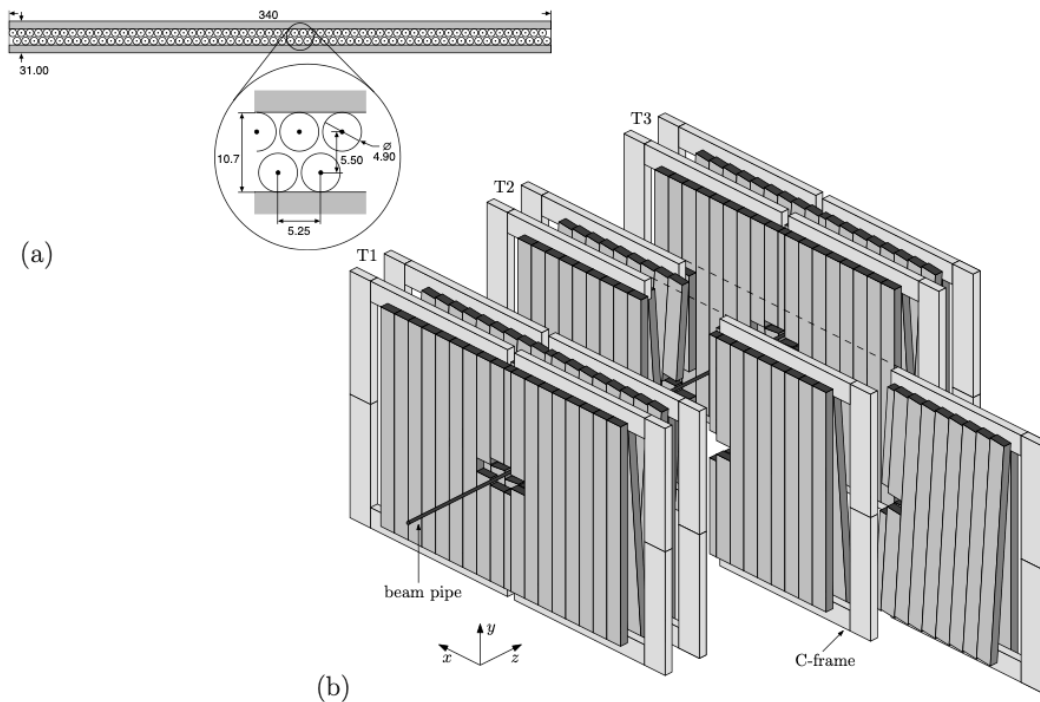


Figure 2.9 A layout of the OT detector^[114].

2.2.1.5 Track reconstruction

These sub-detectors constitute the LHCb track system, which collect hits and combine them into tracks in different ways. According to these different ways, tracks are classified into several types: Long tracks, Upstream tracks, Downstream tracks, VELO tracks,

T tracks as shown in Fig. 2.10.

- VELO tracks, which only have hits in the VELO and will not leave hits in TT. Some VELO tracks can even point backward (backward tracks).
- Upstream tracks, which only have hits in the VELO and TT. These tracks usually have low momentum, so they fly out of the detector after being deflected by the magnetic field.
- T tracks, which have hits in the T stations.
- Downstream tracks, which have hits in TT and the T stations. Since these tracks have no VELO hits, they may be long-lived particles that decay after flying out of the VELO, such as K_s^0 and Λ .
- Long tracks, which have hits in the VELO and the T stations. It may also have hits in TT. It has the best position and momentum resolution, so it is widely used in physical analysis.

If the particles are reconstructed into different track types multiple times, only the tracks that are most suitable for physical analysis are retained. Therefore, the long tracks has priority over any other track type, the upstream tracks has priority over the VELO tracks, and the downstream track has priority over the T tracks.

The reconstruction of long tracks begins with the search of VELO tracks. The advantage of this is that there is no magnetic field in VELO, which forms straight tracks. The two algorithms promote these VELO tracks to long tracks. The first algorithm is called forward tracking, which combines the VELO tracks with the hits of three T stations. For a given VELO track and a single hit at one of the T stations, the momentum is fixed. If other T stations hits can match the momentum direction, we can determine the long tracks. In the second algorithm, it is called track matching. The VELO tracks is combined with the T tracks to match long tracks. The T tracks and VELO tracks are found by an independent track search algorithm. If hits compatible with a long tracks are found in TT, they will be added to the long tracks to improve the momentum resolution and serve as the identification of the fake tracks.

In this thesis, the open charm meson decays are reconstructed using three long tracks. When studying the multiplicity dependence of open charm meson productions, VELO tracks are used to characterize the event multiplicity.

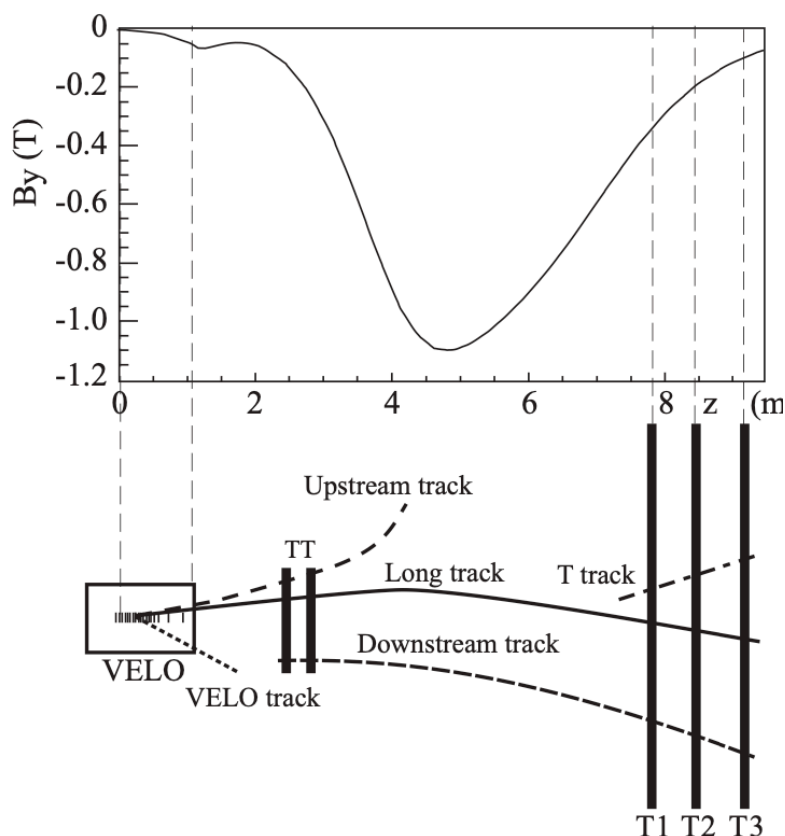


Figure 2.10 An overview of the various track types and y -axis magnetic field intensity as a function of the z coordinate^[111].

2.2.2 Particle identification system

Particle identification in LHCb consists of the RICH system, the calorimeter system and the muon system. All the information from these systems are integrated in a combined likelihood to maximise the identification efficiency. The particles that can be identified are: γ , e , μ , π^\pm , K^\pm and $p\bar{p}$. The efficiency fluctuates between 90 – 100%. In this thesis, the efficiencies are calculated using calibration samples, since the LHCb simulation estimates those quantities poorly.

2.2.2.1 RICH system

The RICH system consists of RICH 1 and RICH 2 as shown in Fig. 2.11. The primary purpose of the RICH system is the identification of charged hadrons (π , K , p), and assist in identification of charged leptons (e , μ). RICH works by producing Cherenkov light rings when particles pass through a radiator gas with a specific refractive index n . By measuring the Cherenkov angle θ_c , we can obtain the velocity of particles through $\cos\theta_c = \frac{1}{n\beta}$. Combined with the momentum measured by the tracking system, we can get the particle

mass.

The RICH 1 contains aerogel and fluorobutane (C_4F_{10}) gas radiators, covering the full LHCb acceptance of 25-300 mrad and low momentum region 1–60 GeV/c. The RICH 2 contains (CF_4) gas radiators, covering the limited LHCb acceptance of 15-120 mrad and high momentum region. The Cherenkov angle as function of the particle momentum for each radiator are shown in Fig. 2.12.

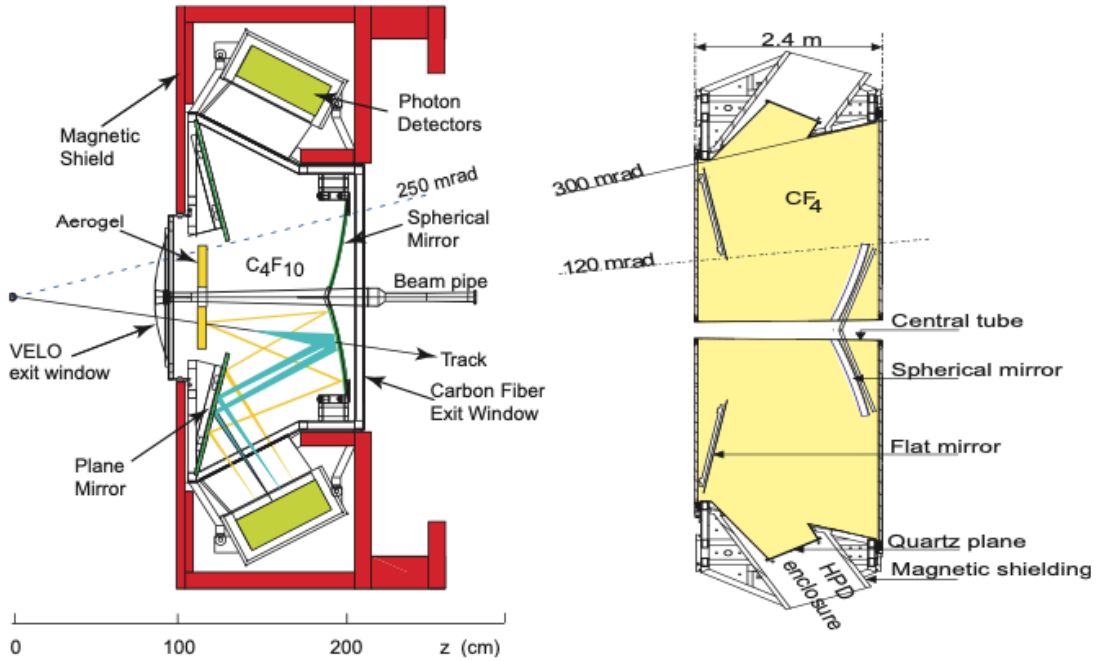


Figure 2.11 An overview of the RICH 1 (left) & 2 (right) detectors^[113].

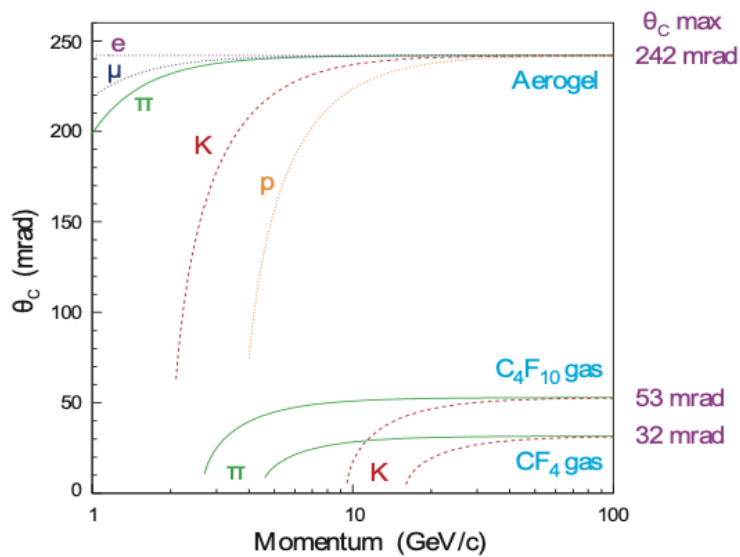


Figure 2.12 Cherenkov angle vs. particle momentum for the RICH radiators^[113].

2.2.2.2 Calorimeter system

The calorimeter system has four parts, namely Scintillating Pad Detector (SPD), Pre-Shower Detector (PrS), Electromagnetic Calorimeter (ECal) and Hadron Calorimeter (HCal). All these detectors are designed with a higher granularity in the inner region, and a lower granularity in the outer region. An overview of the LHCb calorimeter system is shown in Fig. 2.13. The primary purpose of the calorimeters is to identify photons, electrons and π^0 candidates, and provides necessary inputs for hardware trigger L0 by measuring the deposited transverse energy.

SPD and PrS are two walls of scintillator pads separated by a 15mm lead. The SPD measures charged track multiplicity and identify electrons and photons. Then, the energy is measured in a PrS cell. ECAL is placed next to the PrS and is designed to measure transverse energy. The total depth of 42 cm corresponds to 25 electron radiation lengths to ensure the full containment of the high energy electromagnetic showers and to get better energy and transverse energy resolution. The ECAL energy is also used to determine centrality in heavy ions collisions. HCal is placed next to the ECAL, and measure the transverse energy of hadrons. In addition, the thickness of 5.6 interaction lengths also containing most hadronic showers before the muon chambers.

2.2.2.3 Muon system

The muon system is composed of five stations M1-M5 placed along the beam pipe. The M1 station is located downstream the RICH2 station to improve the transverse momentum resolution in the trigger. The M2-M5 are located downstream the calorimeters and are interleaved with iron absorbers to select penetrating muons. A gas electron multiplier (GEM) is used in the inner region of station M1 due to particle rate exceeds safety limits for ageing. The rest uses multi-wire proportional chambers (MWPC). The layout of the muon stations is shown in Fig. 2.14.

Tracks reconstructed in the tracking system are extrapolated to the muon chambers, and if there are associated hits in all the five stations, the track is identified as a muon candidate. This is very critical for studying of quarkonia, rare decays and CP violation.

2.2.2.4 Combined particle identification performance

The PID information obtained separately from these sub-detectors is combined to provide more powerful variables. Two different methods are used. In the first method, a

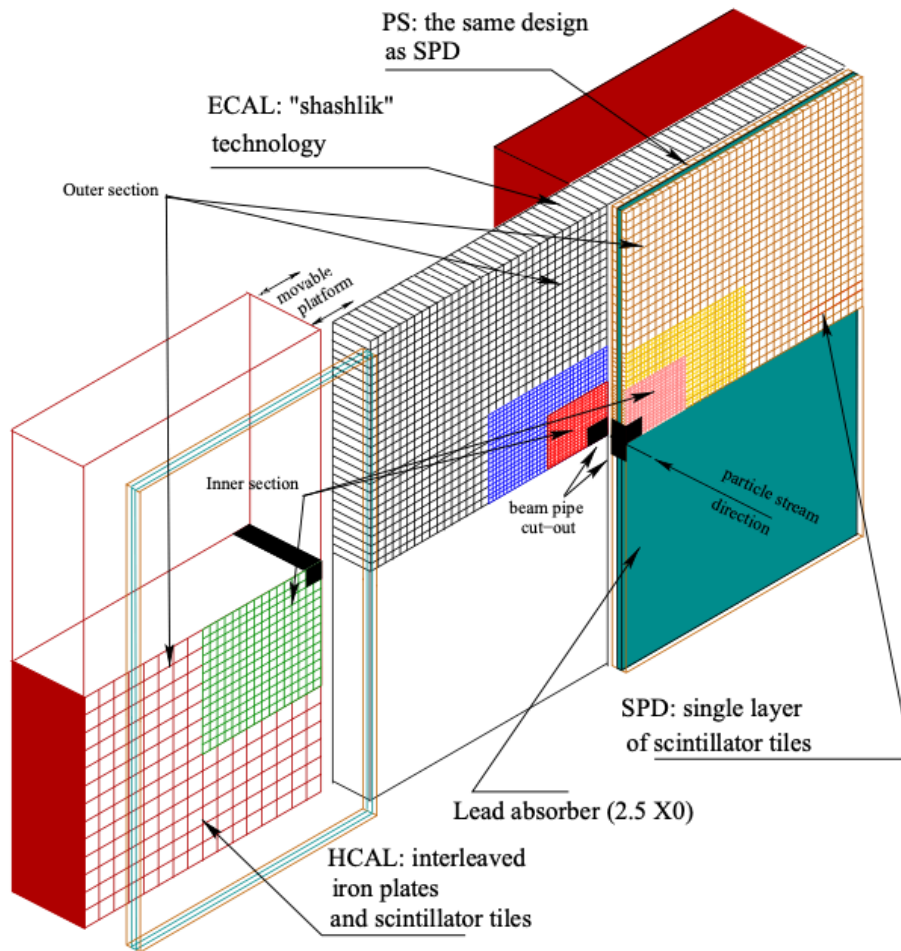


Figure 2.13 An overview of the calorimeter system^[115].

combined delta log likelihood is constructed to describe the relative possibility of a PID hypothesis to particle X , compared with a pion hypothesis. The likelihood information from each sub-system is simply added linearly. In the second method, a multivariate technique is used to consider correlations between the detector systems.

2.2.3 Trigger system

The nominal bunch crossing frequency of pp (pPb) collisions in the LHC is 40 MHz (2 MHz). It greatly exceeds the limitation of bandwidth and storage capacity of LHCb, so it needs to focus on the reconstruction of particles containing c and b quarks. The LHCb trigger consists of two levels: hardware trigger (L0) and High Level software stage Trigger (HLT). The final event rate is reduced to 10kHz. The trigger data flow in Run 2 is shown in Fig. 2.15.

The L0 trigger is based on the calorimeter system and muon system. The L0-

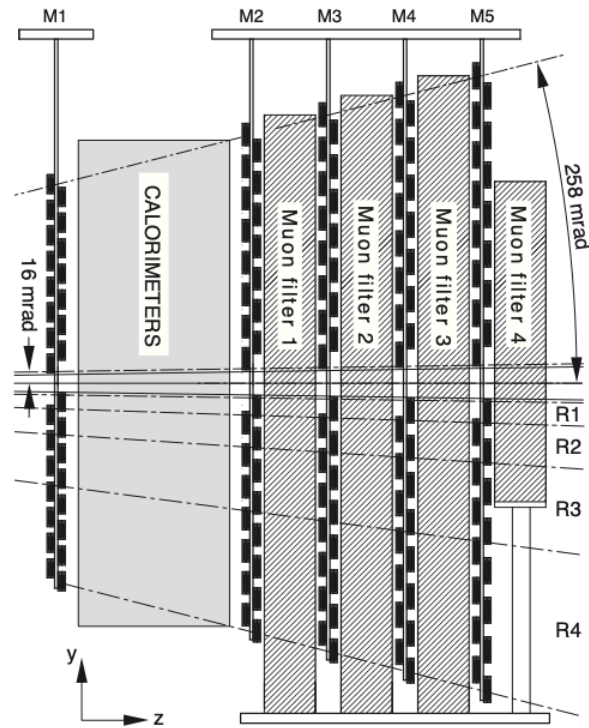


Figure 2.14 An overview of the muon system^[113].

calorimeter trigger system use transverse energy deposited by particles in SPD, PS, ECAL and HCAL. The transverse energy of each candidate is compared to the threshold and events containing at least one candidate above threshold fire this trigger. The L0-muon system looks for straight-line tracks in the five muon stations. The track direction is used to estimate the transverse momentum of a muon candidate. This trigger is fired if the largest transverse momentum above the threshold or the largest and second largest transverse momentum above the threshold. Besides, A maximum number of SPD hits is required in most L0 trigger lines to reduce the complexity of events. L0 trigger has a fixed $4 \mu\text{s}$ delay to decide whether to keep the event.

The HLT is a software trigger performed by Event Filter Farm (EFF). It is divided into HLT1 and HLT2. In HLT1, partial event reconstruction is performed. Events selected by the HLT1 can be used to align and calibrate the detector. In HLT2, the event rate is sufficiently low to allow full event reconstruction. This allows us to more finely select the desired physics events. In Run 2, HLT2 provides two different data streams for physical analysis, including full stream, which saves the complete original information of the selected event, and turbo stream, which saves some information of the selected event to reduce the size of event and allow a higher event rate. This thesis is based on data in the turbo stream.

The HLT is configured by a 32 bit value, named Trigger Configuration Key (TCK). Each run has one unique TCK that defines the sequence of algorithms and selections.

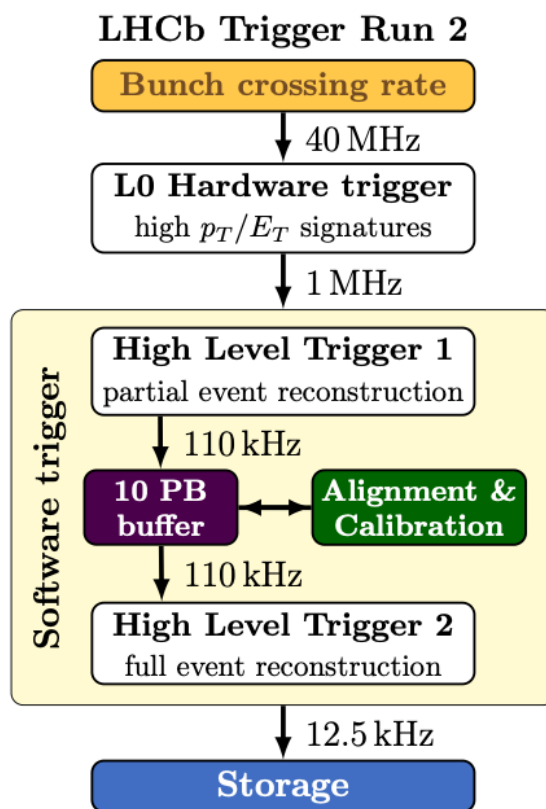


Figure 2.15 An overview of the LHCb trigger system in Run 2^[116].

2.3 Datasets

2.3.1 Proton-lead data

The data samples used for this analysis are proton-lead collisions, collected by LHCb detector during 2016. This dataset corresponds to LHC fills in the range of [5519,5573]. There are approximately 540 lead bunches and 684 proton bunches in total, and 260 colliding bunches per fill for LHCb. During online data taking, the status of the detector/trigger needs to be monitored at all times. Figure 2.16 shows some typical hadron signals obtained with the LHCb high level triggers in a LHC proton-lead fill, indicating the excellent detector and HLT performance.

In order to access both the proton and the lead fragmentation regions, data were taken in two different configurations. In the forward configuration, or pPb , the proton beam points towards the LHCb arm, whereas in the backward configuration, or PbP , the lead beam does. The integrated luminosity of forward and backward is $12.18 \pm 0.32 \text{ nb}^{-1}$ and

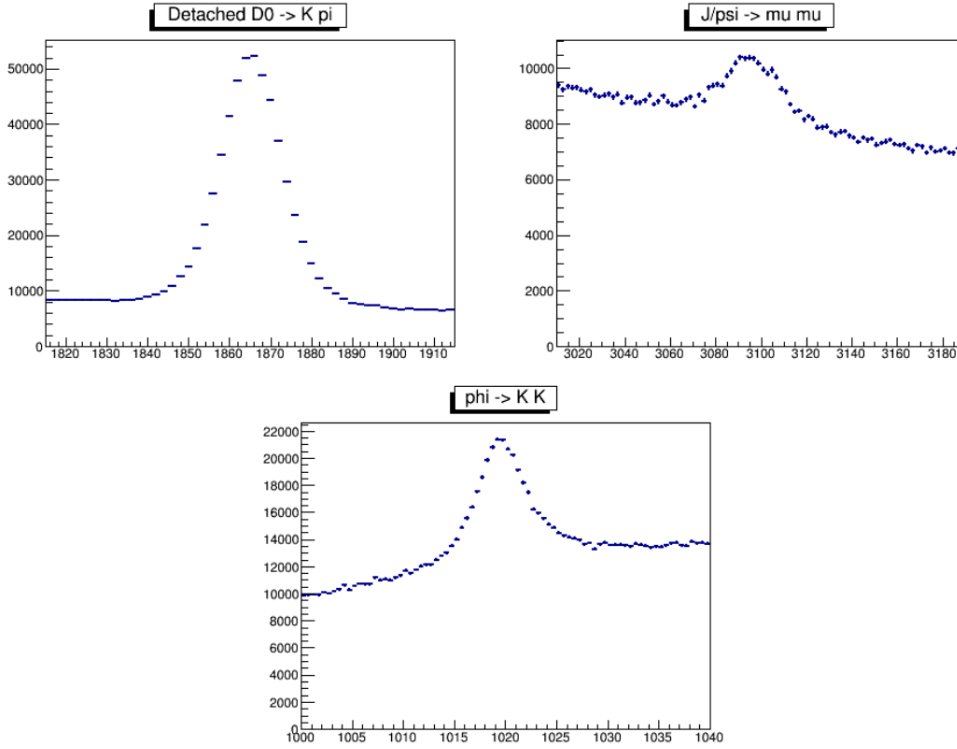


Figure 2.16 Some typical hadron signals obtained with LHCb high level triggers in a LHC proton-lead fill in 2016.

$18.57 \pm 0.46 \text{ nb}^{-1}$ respectively. Figure 2.17 shows the increase of integrated luminosity as a function of time. For both configurations, the polarity of the magnet was pointing downwards (MagDown).

The energy per nucleon of the lead beam and the proton beam was 2.56 TeV and 6.50 TeV, respectively, which means an energy in the nucleon-nucleon centre-of-mass system of $\sqrt{s_{NN}} = 8.16 \text{ TeV}$. The centre-of-mass frame does not coincide with the laboratory frame due to the asymmetry of the collision, with a constant boost of $\delta y = 0.5 \log(A_{Pb}/Z_{Pb}) = 0.465$ in the direction of the proton beam. The rapidity coverage in the centre-of-mass system is $[1.5, 4]$ in the forward configuration and $[-5.0, -2.5]$ in the backward configuration. The forward-backward production ratio $R_{FB}(p_T, y) \equiv \frac{d^2\sigma_{pPb}(p_T, +|y|)/dp_T dy}{d^2\sigma_{pPb}(p_T, -|y|)/dp_T dy}$ can be measured in a common $|y|$ range of $[2.5, 4]$, independently of the pp cross-section at the same energy. This is a unique measurement of the LHCb detector for open heavy flavor hadrons^[117].

In 2016 proton-lead data taking, the L0 TCKs are 0x1621 and 0x1622. These L0 TCKs reduce the event rate to 400 kHz. The HLT1 TCKs are 0x11431621 and 0x11441621. The latter was used in the last part of the backward run (fills from 5562 to 5573) and has some tunings for the high multiplicity lines. These HLT1 TCKs fur-

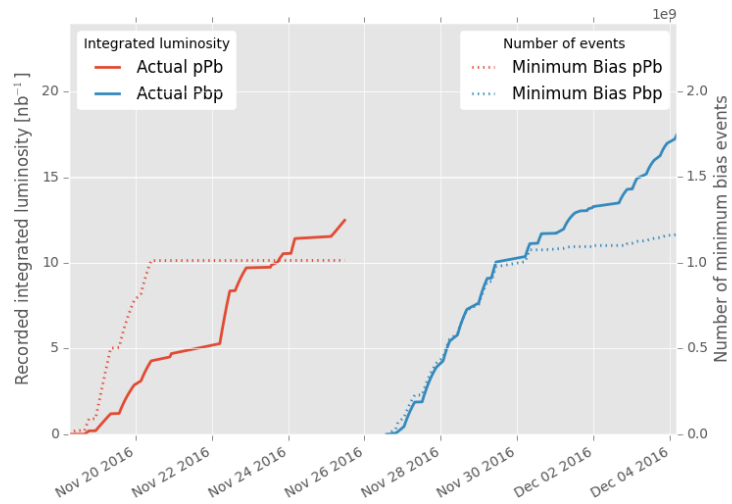


Figure 2.17 LHCb integrated luminosity versus time during the 8.16 TeV pPb data-taking in 2016.

then reduce the event rate to 10-20 kHz. For HLT2, most of the data have been taken with the TCK 0x21461621, where the **Hlt2HighVeloMultTurbo** line is prescaled by a factor of 0.01. The very early runs of forward configuration have been taken with the HLT2 TCK 0x21421621, where the main difference is that the **Hlt2HighVeloMultTurbo** line was not prescaled and was not requesting a single PV. In fill 5523 (pPb) and fills 5562-5573 (PbP), the data was processed with the HLT2 TCK 0x21451621 where the **Hlt2HighVeloMultTurbo** prescale factor is 1. These two HLT2 TCKs allow to collect more high multiplicity events. In these TCKs, the HLT2 is almost pass through and keeps 10-20 kHz event rate from HLT1^[118]. A typical high multiplicity proton-lead event display is shown in Fig. 2.18. Particles identified as pions (orange), kaons (red), protons (magenta), electrons (blue) or muons (green) are shown in different colours^[119].

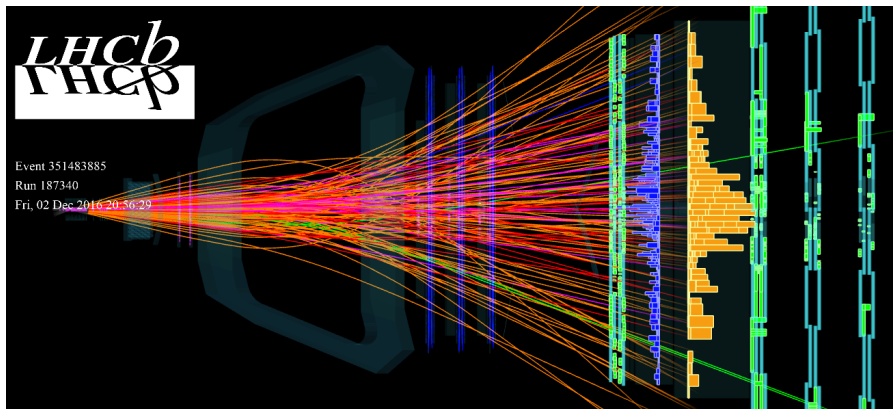


Figure 2.18 The LHCb event display of a high multiplicity proton-lead event.

2.3.2 LHCb simulation and proton-lead Monte Carlo data

Monte Carlo (MC) simulation plays an important role in high energy physics experiments. Before the experiment, it can be used to develop trigger, reconstruction and physics analysis programs. It can also be used to evaluate the radiation environment and its impact on aging maintenance during the experiment. After the experiment, it can provide efficiency, purity values for physics analysis. The LHCb Monte Carlo simulation is based on a collection of different software packages, each specialized in a given domain, working together as shown in Fig. 2.19.

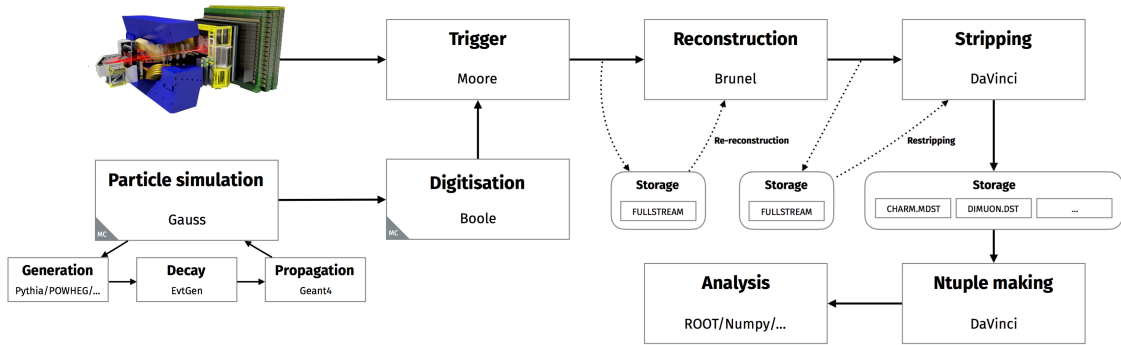


Figure 2.19 LHCb data processing applications and data flow.

LHCb simulation starts with the Gauss framework^[120]. Gauss is responsible for describing how the collision occurred (pp , pPb ...). Firstly, Beam Tool is used to set the particle type and particle energy of the collision beam. Then, Pile-Up Tool determines the number of interactions per event. Followed by the generator, it is used to describe the specific physical process of collision, and contains many physical models. The proton-proton collisions are usually generated with the PYTHIA8^[101], while proton-ion collisions are usually generated with EPOS-LHC^[121]. Then, these generated hadrons are transferred to EvtGen^[122] to decay. LHCb users can use DecFiles^[123] to customise the particle decay, such as custom phase space and correct angular correlations. Another important function of DecFiles is to describe only the events that contain specific particles. This will greatly improve the simulation efficiency for some rare decays. Finally, the simulation of the physical process experienced by particles when passing through the detector is delegated to the GEANT4^[124]. The hits, tracks and other information fed back from GEANT4 are recorded as Monte Carlo truth. There are two types Gauss output: generator-only mode (.gen format) and full simulation mode (.sim format).

The output of Gauss is passed to Boole framework^[120]. Boole provides the response of the LHCb detector and digitization to the simulated physics events. Then, the output

can be triggered by Moore framework as real data taking. And then Brunel framework is responsible for the event reconstruction. The output files (.dst format) contain all reconstructed information which are bulky for physical analysis. The DaVinci software application is used for the stripping, and also provides tools to select event. The output files (.root format) can be directly used for analysis in ROOT analysis framework.

The MC simulation samples for 2016 pPb and PbP have been produced with the official LHCb tune for these data-taking periods. The MC events are generated by mixing a simulated minimum-bias event and a simulated signal event. The minimum bias component is modeled with EPOS-LHC and the signal component is modeled with PYTHIA 8. The digitization, detector settings, reconstruction and selection are same as the real data. There were two iterations for the 2016 pPb/PbP simulation data productions. In the first version (called 'Sim09e'), the simulated event multiplicity (represented by the total number of VELO clusters for example) shows significant difference with that of real data, as shown in Fig. 2.20. In particular, it has much more low multiplicity events than the data, but lack of statistics for high multiplicity events. This issue largely affected the estimation of reconstruction efficiency in this analysis, as the efficiency has significant dependence on the event multiplicity. In the second version (called 'Sim09k'), the simulated event multiplicity has been greatly improved by manually piling-up multiple minimum bias EPOS events in the same collision vertex. Although there is still difference in event multiplicity distributions between the improved simulation and the real data, it can be completely resolved by applying weights on the simulated events according to their event multiplicity to make its distribution match the real data, as shown in Fig. 2.21. Hence, the 'Sim09k' simulation samples are used in this thesis. The author of this thesis has made a lot of contributions to this improvement, which is also an embodiment of innovation.

Table 2.1 Basic information of Monte Carlo simulation sample

Configuration	Magnet polarity	Beam Energy (GeV)	Simulation version	Statistics ($\times 10^6$)
forward	magnet-down	6500GeV (proton)-2560GeV (lead)	Sim09e	4
backward	magnet-down	2560GeV (lead)-6500GeV (proton)	Sim09e	4
forward	magnet-down	6500GeV (proton)-2560GeV (lead)	Sim09k	20
backward	magnet-down	2560GeV (lead)-6500GeV (proton)	Sim09k	20

2.3.3 Data Preservation

As a member of the LHCb collaboration, all data and related simulations can be found on this website : <https://lhcb-portal-dirac.cern.ch/DIRAC/>. The data and simulation used

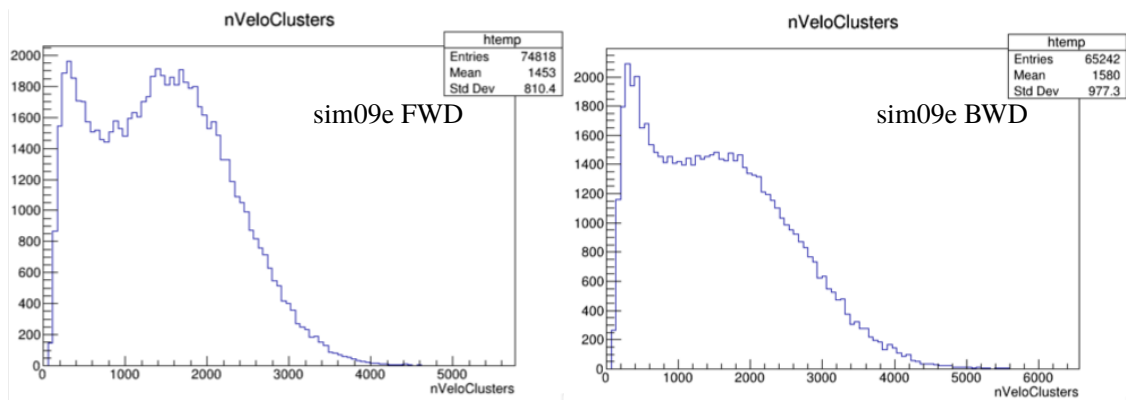


Figure 2.20 The event multiplicity ($nVeloClusters$) distributions in the 'Sim09e' proton-lead simulations. The left plot is for the pPb (forward) configuration, while the right plot is for the PbP (backward) configuration.

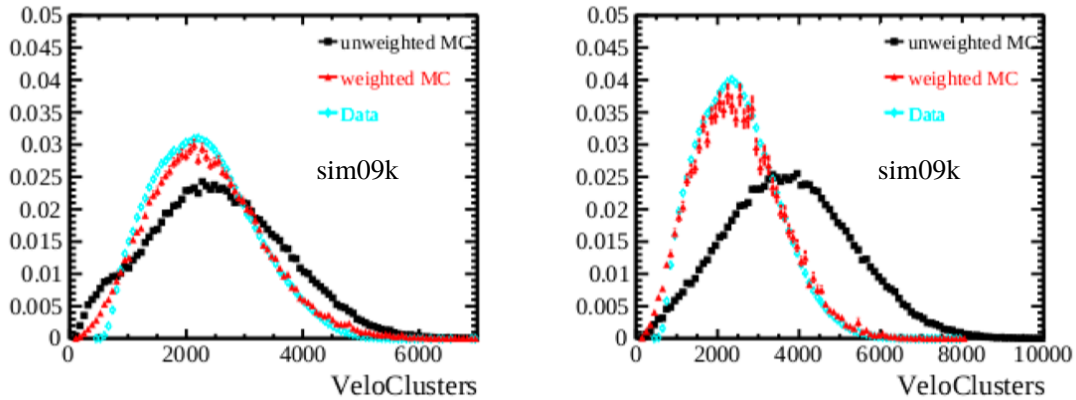


Figure 2.21 The $nVeloClusters$ distributions in 'Sim09k' proton-lead simulations and comparisons to the real data. The left plot is for the pPb (forward) configuration, while the right plot is for the PbP (backward) configuration.

in this thesis are stored in `lxfplus : /eos/lhcb/wg/IonPhysics/analyses/DsDp-pPb-8TeV`. The code used for this analysis was also uploaded to gitlab : <https://gitlab.cern.ch/lhcb-ift/dsdp-ppb-8tev>.

CHAPTER 3 ANALYSIS STRATEGY AND SELECTIONS

This thesis will measure the cross-sections, the nuclear modification factor, the forward-backward ratio and the cross-section ratios for open charm mesons (D_s^+ , D^+) based on p Pb data collected at LHCb in 2016. This chapter will introduce the general analysis strategy and the signal selections.

3.1 Analysis strategy

The D_s^+ (D^+) mesons, composed by a charm quark and a strange (down) antiquark, cannot be detected directly because of their short lifetimes. They are reconstructed with the final-state hadrons of their decays. The decay channels used in this thesis are $D_s^\pm \rightarrow K^\mp K^\pm \pi^\pm$ and $D^\pm \rightarrow K^\mp \pi^\pm \pi^\pm$.

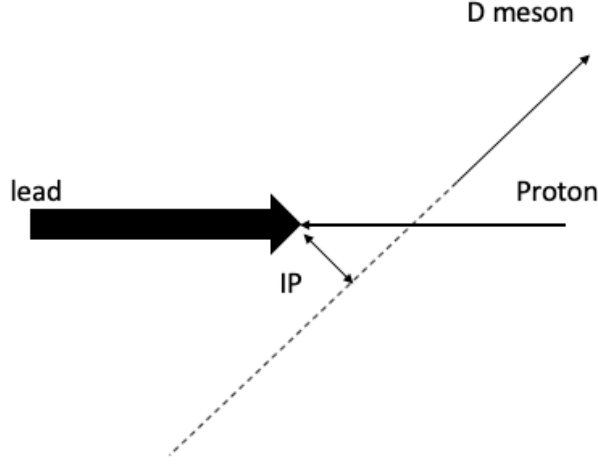
The inclusive D_s^+ (D^+) yields are composed of two contributions: the prompt D_s^+ (D^+) which is produced from the primary interaction vertex (PV) directly, and the non-prompt D_s^+ (D^+) which is produced from the decay of b -hadrons. These two components can be distinguished topologically, thanks to the excellent vertex resolution of the LHCb tracking system. The impact parameter (IP), which is defined as the minimum distance between the back-propagated D_s^+ (D^+) track and the PV (see Fig. 3.1), is powerful in discriminating the prompt from the non-prompt components. It is clear that a D -meson with a smaller impact parameter is more likely to originate from the PV. In practice, the IP-related selections have been optimized to reduce the combinatorial backgrounds and the non-prompt contributions but to keep as many as possible the prompt contributions, which are the major interests of this thesis.

The double differential cross-section for prompt D_s^+ (D^+) production in a given (p_T, y^*) bin is defined as:

$$\frac{d^2\sigma}{dp_T dy^*} = \frac{N(D_s^\pm \rightarrow K^\mp K^\pm \pi^\pm)}{\mathcal{L} \times \epsilon_{\text{tot}} \times \mathcal{B}(D_s^\pm \rightarrow K^\mp K^\pm \pi^\pm) \times \Delta p_T \times \Delta y^*}, \quad (3.1)$$

$$\frac{d^2\sigma}{dp_T dy^*} = \frac{N(D^\pm \rightarrow K^\mp \pi^\pm \pi^\pm)}{\mathcal{L} \times \epsilon_{\text{tot}} \times \mathcal{B}(D^\pm \rightarrow K^\mp \pi^\pm \pi^\pm) \times \Delta p_T \times \Delta y^*}. \quad (3.2)$$

The quantity y^* is the rapidity defined in the nucleon-nucleon centre-of-mass frame. The centre-of-mass frame does not coincide with the laboratory frame due to the asymmetry


 Figure 3.1 *D* mesons decay topology.

of the collision, so y^* is shifted by a constant value with respect to the rapidity in the laboratory frame:

$$y^* = y - \delta y, \quad (3.3)$$

where $\delta y = 0.5 \log(A_{\text{Pb}}/Z_{\text{Pb}}) = 0.465$ ^[125]. The direction of proton beam is defined as the positive z -axis. The other quantities are defined as the following:

- N is the number of prompt signals reconstructed with the specified decay channel.
- \mathcal{L} is the integrated luminosity and is determined for the forward and backward configurations separately in the way as described in Ref. [126]. $\mathcal{L}_{\text{Fwd}} = 0.01218 \pm 0.00032 \text{ pb}^{-1}$ for the forward configuration, and $\mathcal{L}_{\text{Bwd}} = 0.01857 \pm 0.00046 \text{ pb}^{-1}$ for the backward configuration.
- ϵ_{tot} is the total efficiency for the reconstruction of signal channels in each (p_{T}, y^*) bin.
- \mathcal{B} is the branching fraction. $\mathcal{B}(D_s^\pm \rightarrow K^\mp K^\pm \pi^\pm) = (2.24 \pm 0.13)\%$ with the $K^+ K^-$ invariant mass in the range of $1000 < m(K^+ K^-) < 1040 \text{ MeV}/c^2$ ^[127]. $\mathcal{B}(D^\pm \rightarrow K^\pm \pi^\mp \pi^\pm) = (9.38 \pm 0.16)\%$ obtained from the PDG^[128].
- $\Delta p_{\text{T}} = 1 \text{ GeV}/c$ is the bin width of the transverse momentum, with the full measured p_{T} range of $[1, 13] \text{ GeV}/c$.
- $\Delta y^* = 0.5$ is the bin width of the rapidity. The forward and backward rapidity coverage are $1.5 < y^* < 4.0$ and $-5.0 < y^* < -2.5$, respectively.

The nuclear modification factor is defined as the ratio of cross-section in $p\text{Pb}$ collisions to that in pp collisions at the same energy, normalized by the number of nucleons in

Pb nucleus ($A = 208$),

$$R_{p\text{Pb}}(p_T, y^*) = \frac{1}{A} \frac{d^2\sigma_{p\text{Pb}}(p_T, y^*)/dp_T dy^*}{d^2\sigma_{pp}(p_T, y^*)/dp_T dy^*}. \quad (3.4)$$

The forward-backward production ratio is defined as

$$R_{\text{FB}}(p_T, y^*) = \frac{d^2\sigma_{p\text{Pb}}(p_T, +|y^*|)/dp_T dy^*}{d^2\sigma_{p\text{Pb}}(p_T, -|y^*|)/dp_T dy^*}, \quad (3.5)$$

which is calculated for a common rapidity range of $2.5 < |y^*| < 4.0$. These two variables are also studied in bins of p_T and y^* integrated over y^* and p_T respectively.

The D_s^+/D^+ production ratio is measured as functions of p_T, y^* and event multiplicity (represented by PV nTracks in this measurement), defined as

$$R_{D_s^+/D^+}(p_T, y^*, \text{PV nTracks}) = \frac{N(D_s^\pm \rightarrow K^\mp K^\pm \pi^\pm)}{N(D^\pm \rightarrow K^\mp \pi^\pm \pi^\pm)} \times \frac{B(D^\pm \rightarrow K^\mp \pi^\pm \pi^\pm)}{B(D_s^\pm \rightarrow K^\mp K^\pm \pi^\pm)} \times \frac{\epsilon_{D^+}}{\epsilon_{D_s^+}} \quad (3.6)$$

The PV nTracks is the number of tracks used in reconstructing the primary vertex (PV) where the D -mesons originates. This 3D binning scheme focuses more on the event multiplicity dimension and ensures that the statistics in each bin is roughly comparable. The 3D binning scheme is defined as the following:

- Forward configuration
 - PV nTracks : [10, 60, 80, 100, 120, 140, 200]
 - p_T : [2, 4, 6, 8, 12]
 - y^* : [1.8, 2.3, 2.8, 3.3]
- Backward configuration
 - PV nTracks : [10, 60, 80, 100, 120, 140, 180, 250]
 - p_T : [2, 4, 6, 8, 12]
 - y^* : [-2.8, -3.3, -3.8, -4.3]

3.2 Selection criteria

Due to the large number of final state particles in proton-lead collisions, there are a lot of backgrounds in the D_s^+/D^+ reconstructions. But there are many significant differences between a background and a signal, such as the lifetime, the invariant mass, and the decay topology related variables. Certain selection criteria can be applied on these quantities, to remove most of the backgrounds and hence improve the signal significance, and also to save disk space and analysis time. There are three stages of selections applied in the signal reconstructions: online selections, offline selections and event selections .

3.2.1 Online selections

The online event selection is implemented in the trigger, which consists of hardware and software stages. The hardware trigger is based on information from the muon systems and the calorimeter. The software stage (Turbo lines in HLT) is based on the full event reconstruction and the subsequent signal reconstructions/selections.

At the L0 level, the TCK of L0 trigger are 0x1621 and 0x1622. This step is mainly realized by calorimeter. Specifically, it requires hits in SPD and energy deposited in calorimeter. More detailed description can be found here^[129].

The TCK of HLT1 trigger are 0x11431621 and 0x11441621. The underlying HLT1 lines are either **Hlt1TrackMVA** or **Hlt1TwoTrackMVA**. **Hlt1TrackMVA** requires a long track reconstructed, restrict the $p(> 5000 \text{ MeV})$ and $p_T (> 500 \text{ MeV})$ of the tracks, and away from other PV in the same collision. **Hlt1TwoTrackMVA** requires a pair of long tracks reconstructed. In addition to meeting the same requirements as **Hlt1TrackMVA**, these two tracks also require that the combined candidate have large p_T and good-quality vertex. More detailed description is here^[130].

The HLT2 turbo lines used for D_s^+ and D^+ analyses are **Hlt2CharmHadDs2KKPi_XSecTurbo** and **Hlt2CharmHadDpm2KPiPi_XsecTurbo** respectively. Both of them are included in HLT2 TCK 0x21461621 and use **Hlt2CharmHadSharedDetachedDpmChildKFilter** and **Hlt2CharmHadSharedDetachedDpmChildpiFilter** as input turbo lines which put constraints on K and π daughters.

The variables and corresponding online selection criteria used in HLT2 are listed below:

- Primary vertex (PV). Each event contains at least one primary vertex which is reconstructed with at least five tracks in the VELO detector.
- Momentum (p) and transverse momentum (p_T). Each track must have at least 1 GeV/ c momentum and 200 MeV/ c transverse momentum. At least two of the three tracks constituting the signal (D_s^+, D^+) have transverse momentum higher than 400 MeV/ c . The transverse momentum of at least one track is higher than 1000 MeV/ c .
- $\chi^2/\text{ndf}(\text{track})$, is the ratio of the fit goodness to the fit degrees of freedom for the decay product track. The track is expected to have a good fit quality: $\chi^2/\text{ndf}(\text{track}) < 3$.
- $\chi^2/\text{ndf}(\text{vtx})$, is the ratio of the fit goodness to the fit degrees of freedom for the

decay vertex of the signal (D_s^+, D^+). The signal is expected to have a good vertex fit quality: $\chi^2/\text{ndf}(\text{vtx}) < 25$.

- $\text{DLL}_{K\pi}$, which is the log likelihood difference between the K and π hypothesis, is used to perform particle identification (PID). The higher the value, the more likely the particle is kaon, otherwise it is more likely to be pion. The kaon candidates are required to have $\text{DLL}_{K\pi}(K) > 5$. The pion candidates are required to have $\text{DLL}_{K\pi}(\pi) < 5$.
- χ_{IP}^2 , is the difference in fitting χ^2 for a particular PV reconstructed with and without one decay product track of the signal (D_s^+, D^+) in consideration. The IP represents impact parameter. The higher the value is, the more likely the track is not from this PV. χ_{IP}^2 of all decay product tracks should be greater than 4. χ_{IP}^2 of at least two tracks should be greater than 10. χ_{IP}^2 of at least one track should be greater than 50.
- Direction angle, is the angle between the signal's momentum and its flight direction (from the best PV to the signal decay vertex). The higher this value is, the more likely the decay vertex is randomly combined fake vertex. The direction angle of signal (D_s^+, D^+) should be less than 34.6 mrad.
- Invariant mass. The invariant mass of signal (D_s^+, D^+) is required to be within the corresponding mass window in order to reduce the background.
- Lifetime, is the decay time of a signal in its rest frame. A lower limit of 0.15 ps is set for D_s^+ and D^+ signals in order to remove combinatorial background.

All the online selection criteria are listed in Tab. 3.1.

3.2.2 Offline selections

In addition to the online selections, some tighter offline selections are also applied to reduce background further and to achieve better signal significance. The offline selections are listed in Tabs. 3.2 and 3.3. Some particular selections are explained as the following:

- ProbNNghost. ProbNN is a neural network classifier, which requires the total probability of all categories to be 1. The ProbNN X is the probability of the candidate to be a particle X . As long as less than 70% hits of a track can match a real final state particle hits, it will be classified as ghost track. Here, all tracks are required to have ProbNNghost < 0.3 to suppress ghost tracks which contribute most of the background.
- Invariant mass. The invariant mass windows of D_s^+ and D^+ are further tightened. For D_s^+ , in order to further reduce background, the invariant mass of its decay prod-

Table 3.1 Online selections for D_s^+ and D^+ candidates

Quantity	Selections
p_T (track)	$> 200 \text{ MeV}/c$
$\chi^2/\text{ndf}(\text{track})$	< 3
$p(\text{track})$	$> 1 \text{ GeV}/c$
$\text{DLL}_{K\pi}(K)$	> 5
$\text{DLL}_{K\pi}(\pi)$	< 5
p_T (at least two tracks)	$> 400 \text{ MeV}/c$
p_T (at least one track)	$> 1000 \text{ MeV}/c$
$\chi_{\text{IP}}^2(\text{all tracks})$	> 4
$\chi_{\text{IP}}^2(\text{at least two tracks})$	> 10
$\chi_{\text{IP}}^2(\text{at least one track})$	> 50
Direction angle	$< 34.6 \text{ mrad}$
$\chi^2/\text{ndf}(\text{vtx})$	< 25
Lifetime	$\tau > 0.15 \text{ ps}$
$m(D_s^+)$	$1879 < m(D_s^+) < 2059 \text{ MeV}/c^2$
$m(D^+)$	$1779 < m(D^+) < 1959 \text{ MeV}/c^2$

ucts K^+ and K^- is required to be in a mass window around the $\phi(1020)$ peak mass, $1000 < m(K^- K^+) < 1040 \text{ MeV}/c^2$. Figure 3.2 shows the $K^- K^+$ invariant mass distributions in this mass window for both the real data and MC. The almost consistent data/MC Lorentzian fit parameters show the MC simulation reproduces the data very well. The MC simulation includes both the ϕ resonant decay mode and the non-resonant decay mode. This selection is also applied on the truth MC D_s^+ signals, because it is included in the definition of the D_s^+ branching fraction that used in this analysis.

- Lifetime. An upper limit cut that is far larger than its lifetime is added for D_s^+ in order to remove more background in low rapidity region.

3.2.3 Event selections

When studying the dependence of D_s^+/D^+ cross-section ratio with multiplicity, it is critical to ensure the stability of multiplicity distribution in each event. Therefore, some event selections are needed for this purpose. PV nTracks (the number of tracks used to

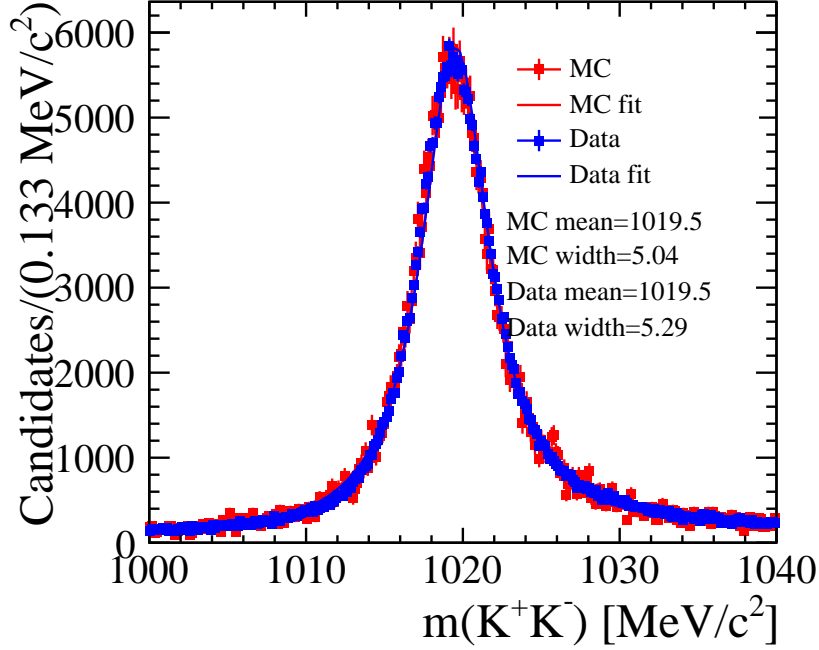


Figure 3.2 Invariant mass distributions in a mass window around the $\phi(1020)$ peak of the $K^- K^+$ in D_s^+ decays from real data and MC simulations. The Lorentzian function fit results and parameters are shown as well for data and MC comparison.

reconstruct the primary vertex) is used to represent the event multiplicity in this analysis. If there is more than one PV in this event, these PV's will interfere with each other and affect the distribution of PV nTracks, as shown in Fig. 3.3. Therefore, each event is required to have only one PV ($nPV = 1$). Besides that, the location of PV (especially in z direction) also affects the distribution of PV nTracks. When the PV just falls on the edge of VELO, some of the tracks are not within the acceptance of VELO. Figure 3.4 shows this effect, and hence the PV z position (PVZ) is required to be within $-20 < PVZ < 80$ mm and $-40 < PVZ < 80$ mm for the forward and backward configurations, respectively. These event selections are listed in Tab. 3.4. As a reference, the PV nTracks distributions in D_s^+, D^+ event are compared with that in minimum bias event where almost no selections are applied. As shown in Fig. 3.5, the PV ntracks of D_s^+ and D^+ event are similar and significantly larger than that of the normal pPb collision event.

Table 3.2 Offline selections for D_s^+ candidates

Quantity	Selections
η	$2 < \eta < 5$
p_T (track)	$> 400 \text{ MeV}/c$
p (track)	$3.2 < p < 100 \text{ GeV}/c$
$\text{DLL}_{K\pi}(\pi^+)$	< 0
$\text{ProbNNghost}(K/\pi)$	< 0.3
$m(D_s^+)$	$1889 < m(D_s^+) < 2049 \text{ MeV}/c^2$
$m(K^- K^+)_\phi$	$1000 < m(K^- K^+)_\phi < 1040 \text{ MeV}/c^2$
Lifetime	$\tau < 10 \text{ ps}$

 Table 3.3 Offline selections for D^+ candidates

Quantity	Selections
η	$2 < \eta < 5$
p_T (track)	$> 400 \text{ MeV}/c$
p (track)	$3.2 < p < 100 \text{ GeV}/c$
$\text{DLL}_{K\pi}(\pi^+)$	< 0
$\text{ProbNNghost}(K/\pi)$	< 0.3
$\text{DiraAngle}(D^+)$	$< 15 \text{ mrad}$
$m(D^+)$	$1794 < m(D^+) < 1944 \text{ MeV}/c^2$

Table 3.4 Event selections for the multiplicity dependence study

Quantity	Selections
PV z position (PVZ)	$-20 < \text{PVZ} < 80 \text{ mm}$ (forward)
PV z position (PVZ)	$-40 < \text{PVZ} < 80 \text{ mm}$ (backward)
Number of PVs (nPv)	$\text{nPV} = 1$

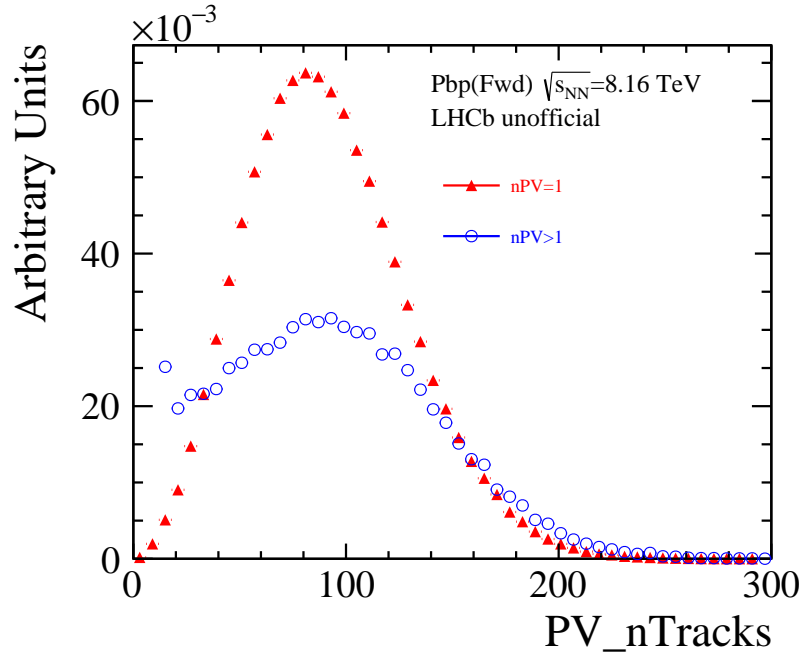


Figure 3.3 PV nTracks distributions for different nPV values in an event, for the forward configuration.

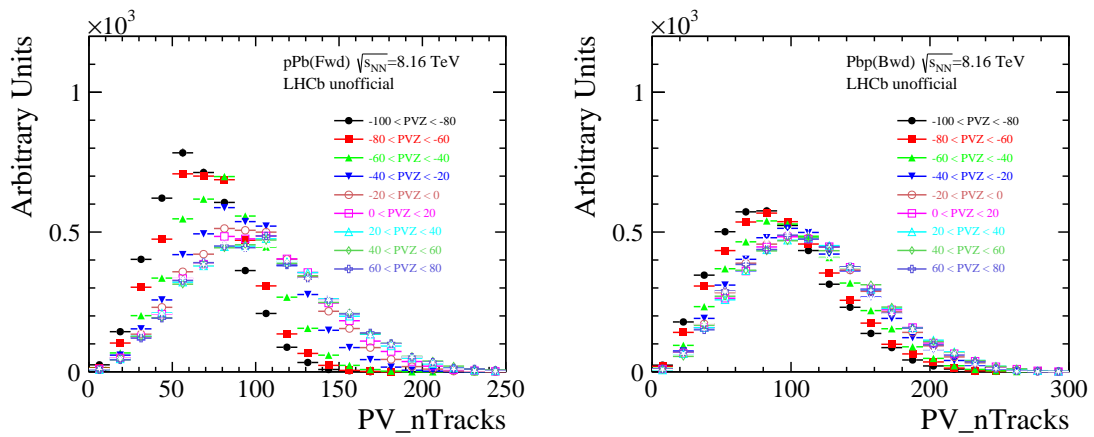


Figure 3.4 PV nTracks distribution in different PVZ intervals. The left is for forward configuration, and the right is for backward configuration.

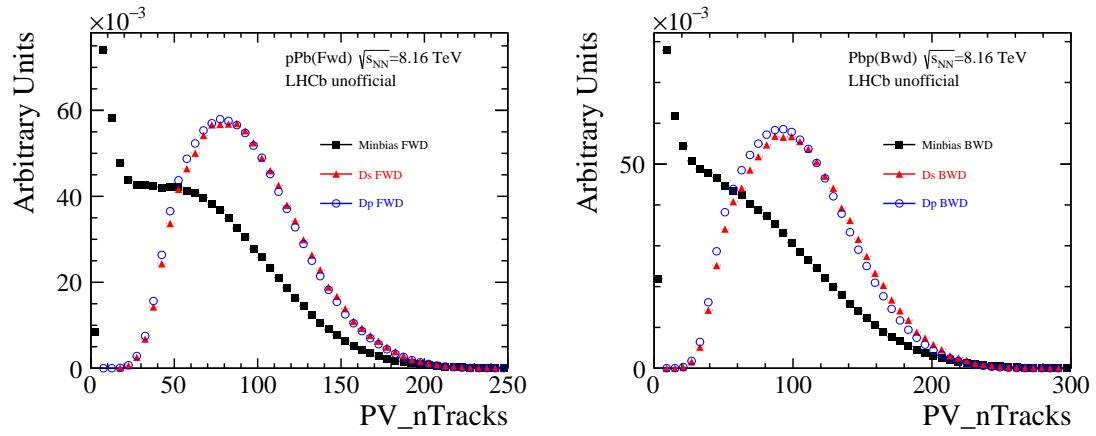


Figure 3.5 PV nTracks distributions in minimum bias events, compared to those in D_s^+ or D^+ event. The left is for forward configuration, and the right is for backward configuration.

CHAPTER 4 SIGNAL YIELD DETERMINATION

After the previous selection, there are some backgrounds in the data sample. They are mainly composed of two components: the combinatorial background and D_s^+ (D^+) signals from b -hadrons decay (non-prompt signal). Simple event selection cannot further remove these background, so the prompt signal is extracted by fitting. For the convenience of discussion, these prompt D_s^+ (D^+) signals and non-prompt D_s^+ (D^+) signals are collectively referred to as inclusive D_s^+ (D^+) signals.

Experience shows that the invariant mass spectrum has a good discrimination on the combinatorial background. The inclusive D_s^+ (D^+) mesons was extracted by fitting the invariant mass distribution of the candidates that passed the online and offline selections. The signal is described by a combination of a Crystal Ball (CB) function plus a Gaussian function as follow Equation 4.1, 4.2.

$$F_{\text{signal}} = f \times F_{\text{CB}} + (1 - f) \times F_{\text{Gauss}} , \quad (4.1)$$

$$F_{\text{CB}}(x; M, \sigma, \alpha, n) = \begin{cases} \frac{\left(\frac{n}{|\alpha|}\right)^n e^{-\frac{1}{2}\alpha^2}}{\left(\frac{n}{|\alpha|} - |\alpha| - \frac{x-M}{\sigma}\right)^n}, & \text{if } \frac{x-M}{\sigma} < -|\alpha| , \\ \exp\left(-\frac{1}{2}\left(\frac{x-M}{\sigma}\right)^2\right), & \text{if } \frac{x-M}{\sigma} \geq -|\alpha| . \end{cases} \quad (4.2)$$

In this probability density function (PDF), the mean and width of the central Gaussian distribution are given by M and σ respectively. The parameter α describes the boundary between the Gaussian and power law component while n describes the order of the power law. The CB function describes the mass peak with a lossy tail on the left. In the case of energy loss by photon emission, the tail should be described by the $1/x$ function, which corresponds to fix $n=1$. The CB and Gaussian function share a common mean value. For Fwd mass fit, the $\alpha(D_s^+)$ is fixed to 2.637, the fraction of CB component $f(D_s^+)$ is fixed to 0.797. For Bwd fit, the $\alpha(D_s^+)$ is fixed to 2.557, the fraction of CB component $f(D_s^+)$ is fixed to 0.792. These values are obtained from kinematically-unbinned mass fits (data). The two variables aren't fixed in the D^+ mass fit because of the larger statistics.

A linear function is used to describe the shape of combinatorial background. Some typical mass fits are displayed in Figures 4.1, 4.2. The blue line represents the total fit function and the red dashed line represents the combinatorial background. All mass fits are shown in Appendix C.

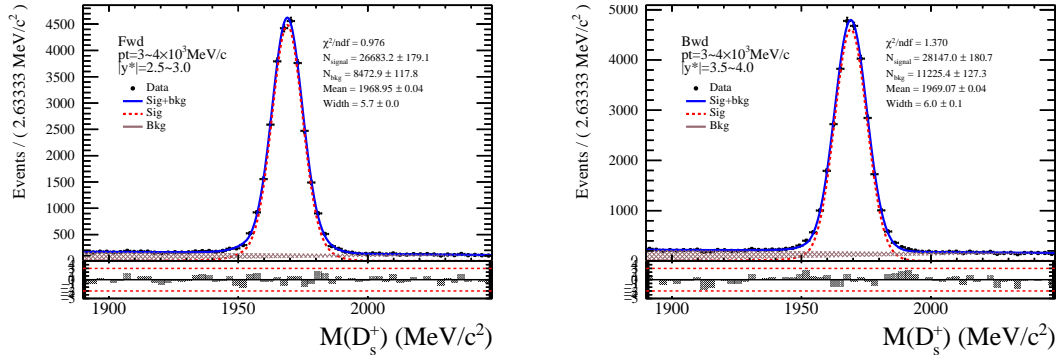


Figure 4.1 Mass fit to extract the D_s^+ inclusive signal in a typical p_T and y^* interval. (left figure is Fwd, right figure is Bwd)

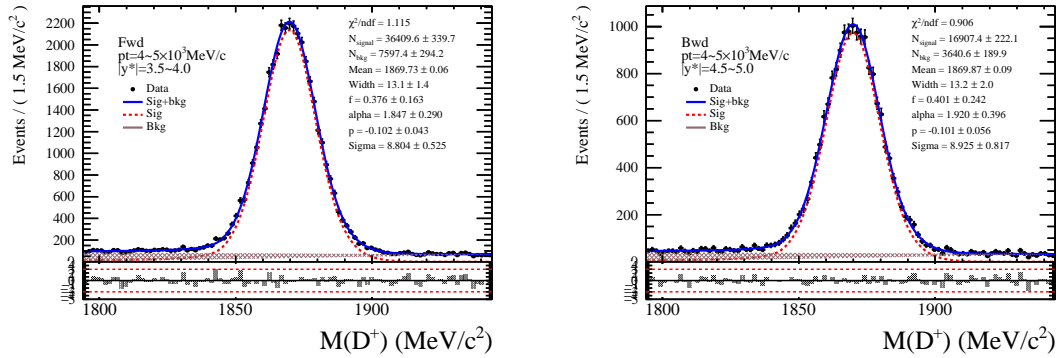


Figure 4.2 Mass fit to extract the D^+ inclusive signal in a typical p_T and y^* interval. (left figure is Fwd, right figure is Bwd)

The inclusive D_s^+ (D^+) yields in different kinematic bins are shown in Figure 4.3, 4.4 and listed in Tables B.1, B.2, B.3, B.4 in Appendix B. In these bins at the kinematic edge, the fitting fails due to low statistics, and the setting is null.

The prompt D_s^+ (D^+) mesons was extracted by fitting the $\log_{10}\chi_{\text{IP}}^2$ distribution, where χ_{IP}^2 is defined as the difference in the vertex-fit χ^2 of a given PV reconstructed with and without the D_s^+ (D^+) candidate under consideration. On average, the prompt D_s^+ (D^+) mesons have a smaller IP (impact parameter) than non-prompt D_s^+ (D^+) mesons due to the flight distance of B hadrons. The χ_{IP}^2 is almost positively correlated with IP. Thus prompt D_s^+ (D^+) mesons can be discriminated through this method. The combinatorial background was statistically subtracted by sPlot technique^[131] using invariant mass as variable. So the $\log_{10}\chi_{\text{IP}}^2$ distribution of weighted data contains only prompt and non-prompt D_s^+ (D^+). The shape of prompt and non-prompt components were described by Bukin function as follows Equation 4.3.

To obtain a better result, we fit $\log_{10}\chi_{\text{IP}}^2$ in a narrower mass window. The inclusive D_s^+ (D^+) mesons yield is fixed by the mass fit. The parameters ϵ , ρ_L and ρ_R of the non-prompt

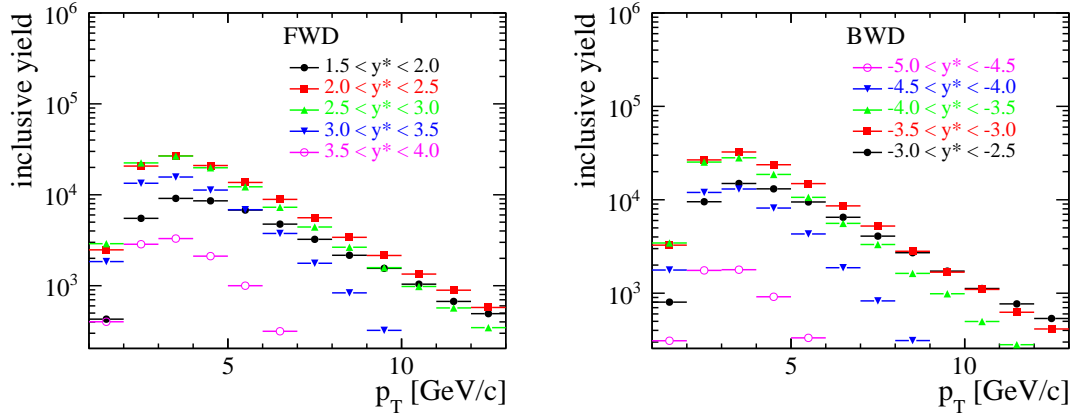


Figure 4.3 The inclusive D_s^+ signal yields in different p_T and y^* intervals. (left figure is Fwd, right figure is Bwd)

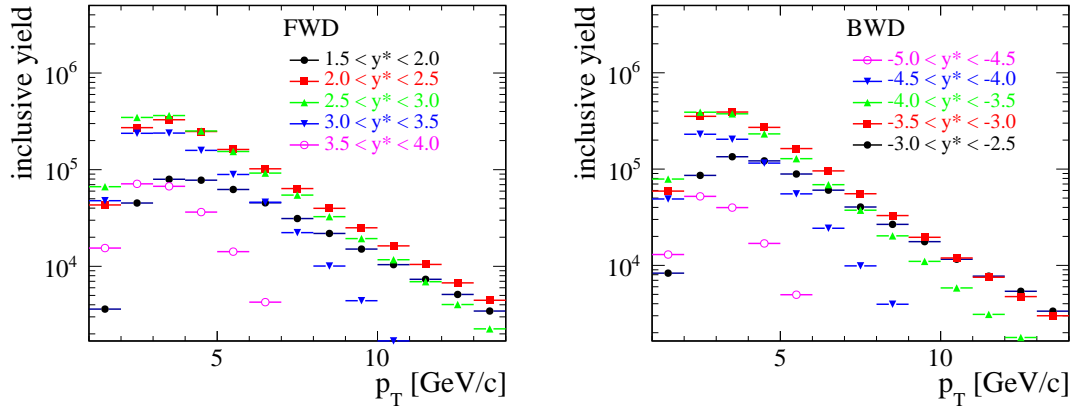


Figure 4.4 The inclusive D^+ signal yields in different p_T and y^* intervals. (left figure is Fwd, right figure is Bwd)

component are fixed from simulation. Some typical fits are displayed in Figures 4.5, 4.6. The red line represents the prompt component and the green dashed line represents non-prompt component. The prompt D_s^+ (D^+) yields in different kinematic bins are shown in Figure 4.7, 4.8. For comparison, the prompt-fraction is calculated (prompt/(prompt+non-prompt)) and shown in Figure 4.9, 4.10. In general, The prompt fraction of D^+ is larger than that of D_s^+ .

All $\log_{10}\chi^2_{\text{IP}}$ fits are shown in Appendix D. The numerical results of fractions are included in Tables B.7, B.8, B.9, B.10 in Appendix B.

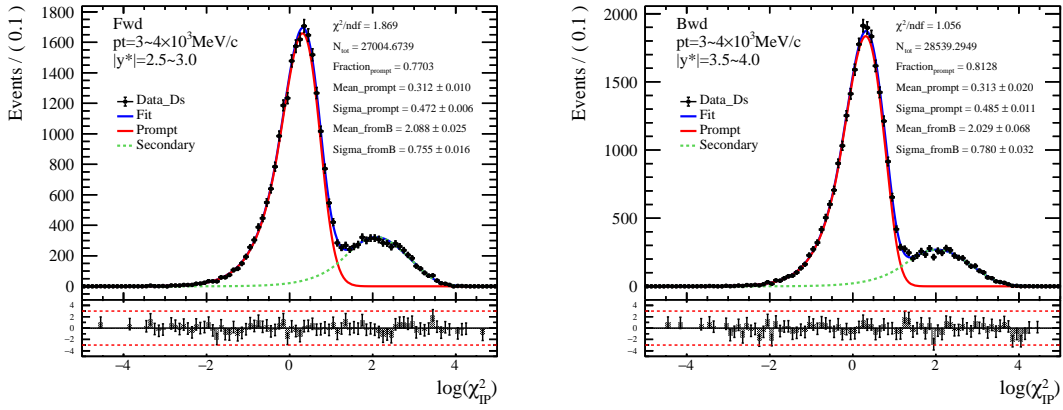


Figure 4.5 $\log_{10}\chi_{\text{IP}}^2$ fit to extract the D_s^+ prompt signal in a typical p_T and y^* interval. (left figure is Fwd, right figure is Bwd.)

$$\mathcal{P}(x; \mu, \sigma, \epsilon, \rho_L, \rho_R) = \begin{cases} \exp\left\{ \frac{(x-x_1)\epsilon\sqrt{\epsilon^2+1}\sqrt{2\ln 2}}{\sigma(\sqrt{\epsilon^2+1}-\epsilon)^2 \ln(\sqrt{\epsilon^2+1}+\epsilon)} + \rho_L \left(\frac{x-x_1}{\mu-x_1}\right)^2 - \ln 2 \right\} & x \leq x_1, \\ \exp\left\{ -\left[\frac{\ln\left(1+2\epsilon\sqrt{\epsilon^2+1}\frac{x-\mu}{\sigma\sqrt{2\ln 2}}\right)}{\ln(1+2\epsilon^2-2\epsilon\sqrt{\epsilon^2+1})} \right]^2 \times \ln 2 \right\} & x_1 < x < x_2, \\ \exp\left\{ \frac{(x-x_2)\epsilon\sqrt{\epsilon^2+1}\sqrt{2\ln 2}}{\sigma(\sqrt{\epsilon^2+1}-\epsilon)^2 \ln(\sqrt{\epsilon^2+1}+\epsilon)} + \rho_R \left(\frac{x-x_2}{\mu-x_2}\right)^2 - \ln 2 \right\} & x \geq x_2. \end{cases} \quad (4.3)$$

$$x_1 = \mu + \sigma\sqrt{2\ln 2} \left(\frac{\epsilon}{\sqrt{\epsilon^2+1}} - 1 \right), \quad x_2 = \mu + \sigma\sqrt{2\ln 2} \left(\frac{\epsilon}{\sqrt{\epsilon^2+1}} + 1 \right).$$

When studying D_s^+/D^+ production ratio as a function of p_T, y^* and PV nTracks, the basic method is the same as before, except refit in 3D intervals. In addition, parameters are no longer fixed in the mass and $\log_{10}\chi_{\text{IP}}^2$ fits except n of CB function since there are enough statistics in these bins. The prompt D_s^+ (D^+) 3D distributions are shown in Figure 4.11. The numerical results are summarized in Tables B.5, B.6, B.11, B.12, B.13, B.14 in Appendix B.

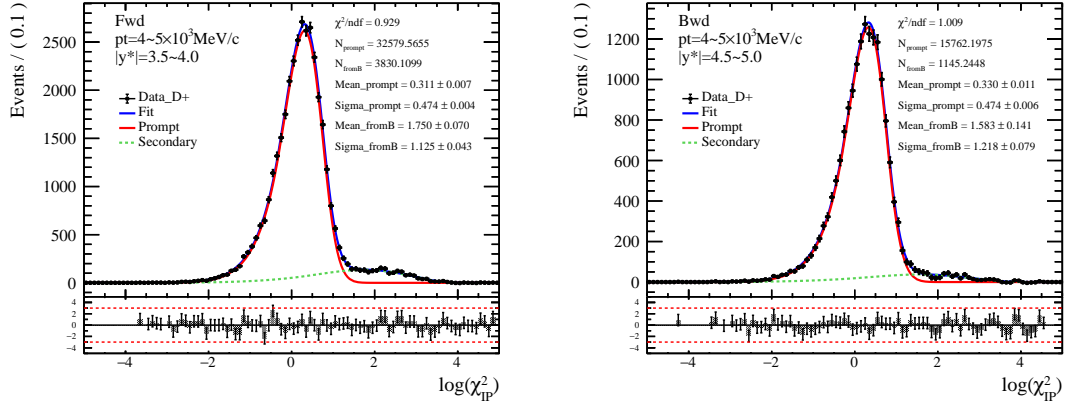


Figure 4.6 $\log_{10}\chi_{IP}^2$ fit to extract the D^+ prompt signal in a typical p_T and y^* interval. (left figure is Fwd, right figure is Bwd.)

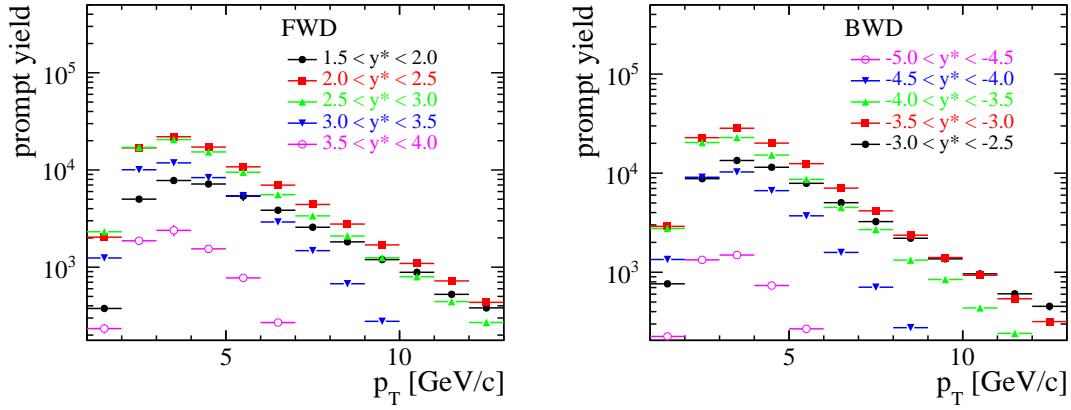


Figure 4.7 The prompt D_s^+ signal yields in different p_T and y^* intervals. (left figure is Fwd, right figure is Bwd)

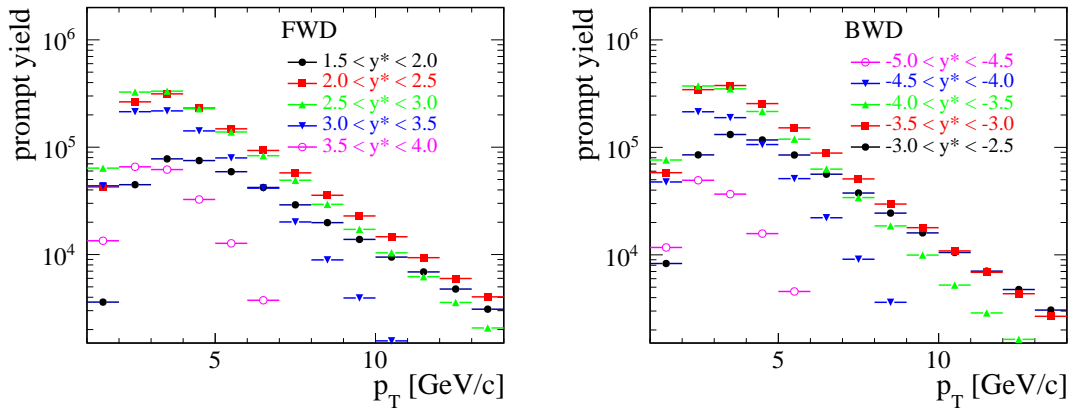


Figure 4.8 The prompt D^+ signal yields in different p_T and y^* intervals. (left figure is Fwd, right figure is Bwd)

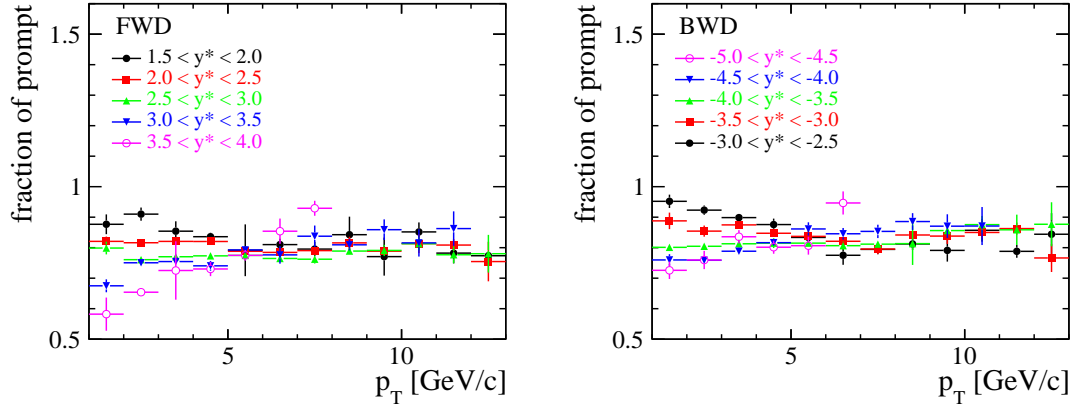


Figure 4.9 The prompt fraction of D_s^+ in different p_T and y^* intervals. (left figure is Fwd, right figure is Bwd)

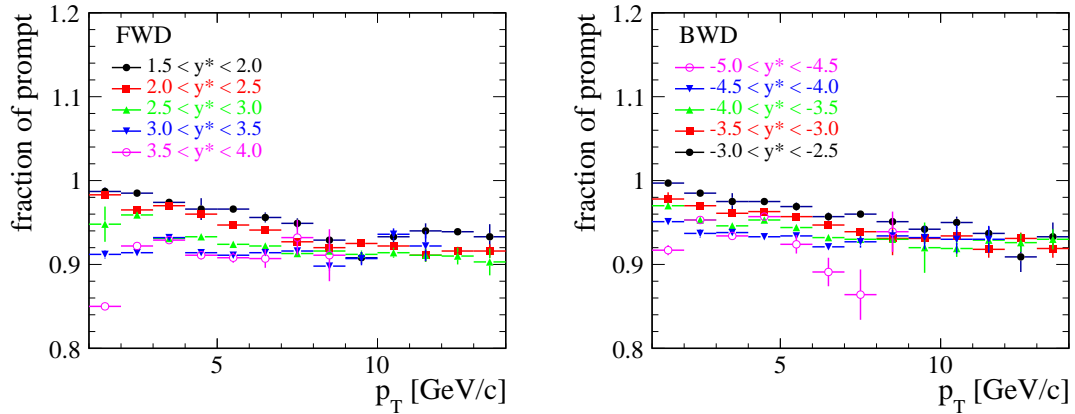


Figure 4.10 The prompt fraction of D^+ in different p_T and y^* intervals. (left figure is Fwd, right figure is Bwd)

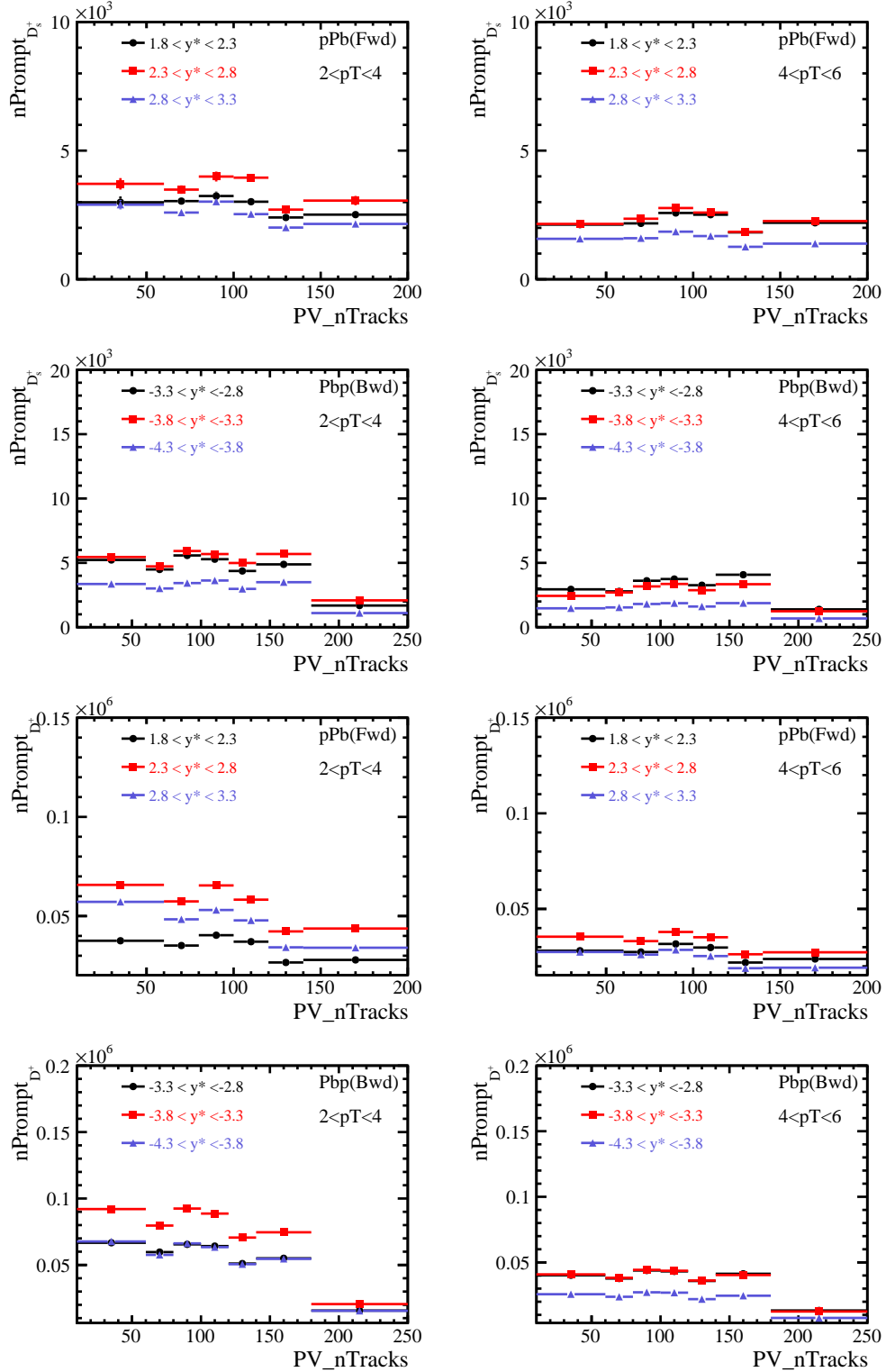


Figure 4.11 The prompt D_s^+ (D^+) yield as a function of p_T , y^* and PV nTracks. Only the statistical uncertainties are shown here.

CHAPTER 5 EFFICIENCIES CORRECTION

After the collision, not all the generated D_s^+ and D^+ signals can be detected. First, not all signals can be accepted by the detector since LHCb is a forward detector, even if the high density production area is in the forward. This is the geometrical acceptance efficiency, ϵ_{acc} . Secondly, even if signals are accepted by the detector, they may not be reconstructed by the tracking system (Section 2.2.1) and then passed the online and offline selections (without PID selections). This is the reconstruction and selection efficiency, $\epsilon_{\text{rec\&sel}}$. Then, the decay products of the signals may not be correctly recognized by the particle identification system (Section 2.2.2), the PID efficiency, ϵ_{PID} . Finally, the signals may not be triggered by the trigger system (Section 2.2.3) and saved, trigger efficiency, ϵ_{tri} . The total efficiency is obtained by multiplying these four parts:

$$\epsilon_{\text{tot}} = \epsilon_{\text{acc}} \times \epsilon_{\text{rec\&sel}} \times \epsilon_{\text{PID}} \times \epsilon_{\text{tri}}. \quad (5.1)$$

These efficiencies cannot be obtained directly from the data, but are estimated by LHCb Monte Carlo simulation samples (Section 2.3.2).

5.1 Geometrical acceptance efficiency

The geometrical acceptance efficiency, ϵ_{acc} , is estimated by generator level Monte Carlo which only contains the basic information of particle generation and decay (energy, momentum) without detector simulation. The Gauss option files are almost same as the official Monte Carlo to restore the real data collection situation as much as possible. We use Pythia8^[132] as the generator instead of EPOS.

The ϵ_{acc} of D_s^+ is defined as:

$$\epsilon_{\text{acc}} = \frac{D_s^+ \text{ with } K^- K^+ \pi^+ \text{ in LHCb acceptance}}{\text{Generated } D_s^+ \text{ with } K^- K^+ \pi^+}. \quad (5.2)$$

The ϵ_{acc} of D^+ is defined as:

$$\epsilon_{\text{acc}} = \frac{D^+ \text{ with } K^- \pi^+ \pi^+ \text{ in LHCb acceptance}}{\text{Generated } D^+ \text{ with } K^- \pi^+ \pi^+}. \quad (5.3)$$

We assume the geometrical acceptance efficiency is independent with multiplicity. Both Fwd and Bwd geometrical acceptance efficiencies are measured. The ϵ_{acc} results are shown in Figure 5.1. The results are summarized in Tables A.1, A.2, A.5, A.6 in Appendix A. The ratio of geometrical acceptance efficiencies (D^+/D_s^+) are shown in Figures 5.2, 5.3.

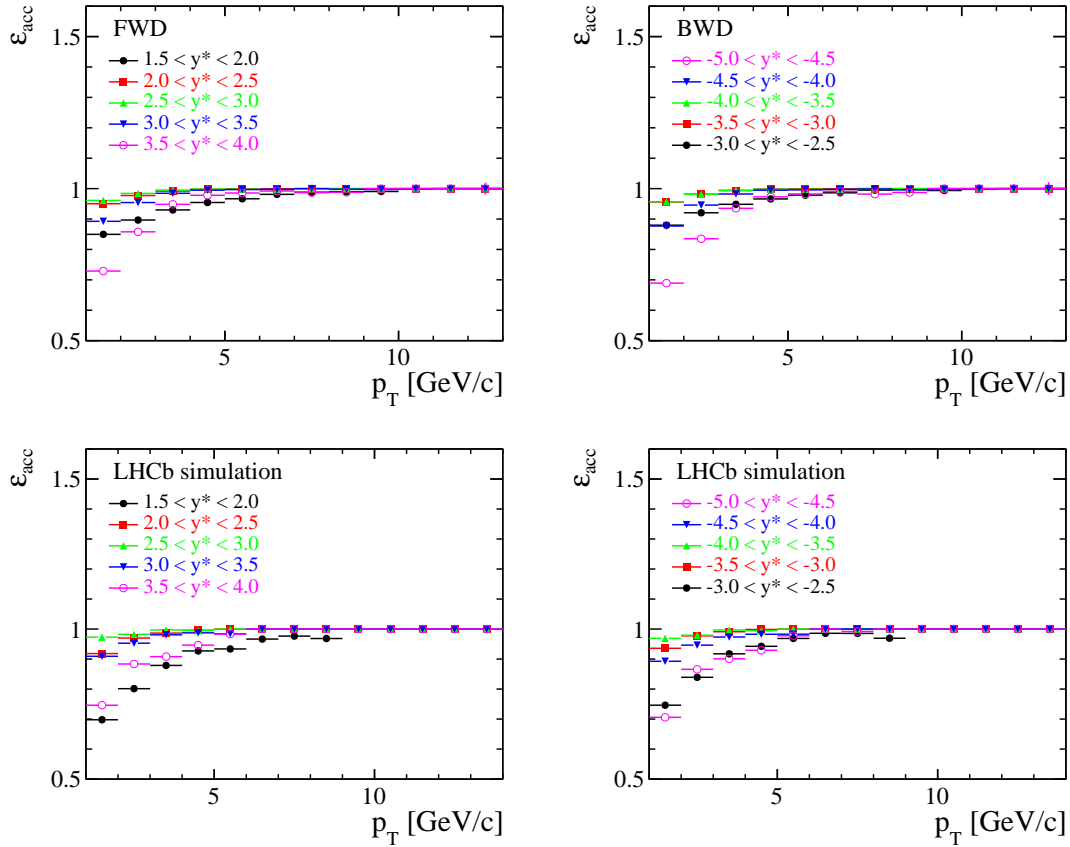


Figure 5.1 The geometrical acceptance efficiency, ϵ_{acc} , as a function of p_T and y^* of prompt D_s^+ (up), D^+ (down) meson for Fwd (left) and Bwd (right) configurations. Only the statistical uncertainties are shown here.

The results are summarized in Tables A.9, A.10 in Appendix A.

5.2 Reconstruction and selection efficiency

The D_s^+ reconstruction and selection efficiency is defined as

$$\epsilon_{\text{rec\&sel}} = \frac{\sum D_s^+ \text{ in acceptance, reconstructed and selected}}{D_s^+ \text{ with } K^+ K^- \pi^+ \text{ in LHCb acceptance}}. \quad (5.4)$$

The D^+ reconstruction and selection efficiency is defined as

$$\epsilon_{\text{rec\&sel}} = \frac{\sum D^+ \text{ in acceptance, reconstructed and selected}}{D^+ \text{ with } K^- \pi^+ \pi^+ \text{ in LHCb acceptance}}. \quad (5.5)$$

This efficiency is estimated with official Monte Carlo include detector simulation. It includes two parts: the efficiency of reconstructing the three long tracks (contain hits in the VELO, TT and tracking stations) and the refinement of the signals. The selections are listed in the Table 3.2, 3.3 without PID requirements. There are several corrections that must be considered due to the difference between data and simulation. For example,

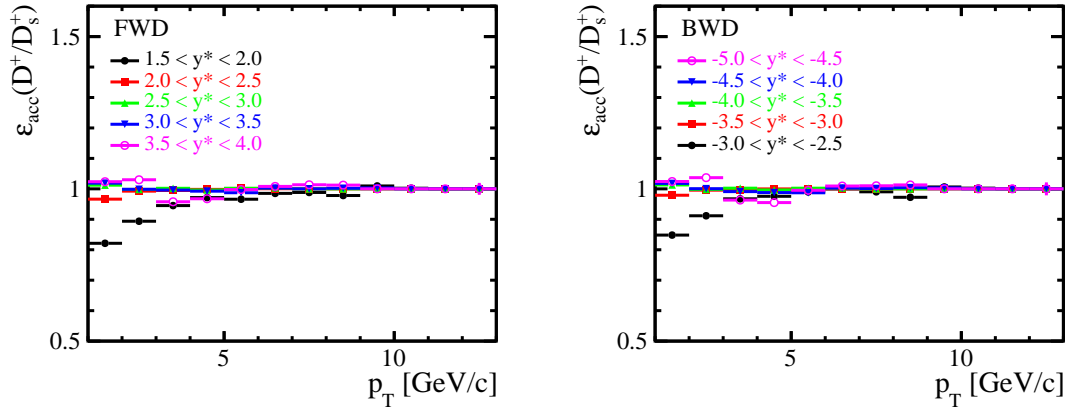


Figure 5.2 The ratio of the geometrical acceptance efficiency (D^+/D_s^+) as a function of p_T and y^* (2D) for Fwd (left) and Bwd (right) configurations. Only the statistical uncertainties are shown here.

the track reconstruction efficiency cannot be perfectly simulated^[133]. Next, I will discuss these corrections in detail.

5.2.1 Truth matching

The signals in the simulation are picked out by truth matching requirements which include particle ID requirements and BKG CAT requirements, but the truth matching algorithm occasionally flags the signal track as a ghost. This effect can be seen by plotting the mass distribution of events which passed the selection where at least one track did not satisfy the correct truth-matching requirements. A peak around the D_s^+ mass can be seen in Figure 5.4. A Crystal Ball signal and a linear background is used to fit the mass spectrum. The ratio of D_s^+ candidates in this peak over truth matched D_s^+ signals is the truth match inefficiency. Since the fraction of not truth matched D_s^+ meson is small, this correction is performed for unbinned simulation samples. The D_s^+ fit gives a fraction of 3.36% for Fwd and 2.71% for Bwd. The same method applied to the D^+ gives a fraction of 2.23% for Fwd and 2.17% for Bwd.

5.2.2 Tracking correction

As mentioned before, the reconstruction efficiency cannot be perfectly simulated. A correction factor, $w_{\text{tracking}} = \epsilon_{\text{tracking}}^{\text{data}} / \epsilon_{\text{tracking}}^{\text{MC}}$, need to be considered. This correction factor is given as a function of momentum (p) and pseudo-rapidity (η) as shown in Figure 5.5. The calibration is performed using a tag-and-probe method with detached $J/\psi \rightarrow \mu^+ \mu^-$ and $K_s^0 \rightarrow \pi^+ \pi^-$ decays constructed in the Turbo stream in both data and simulation.

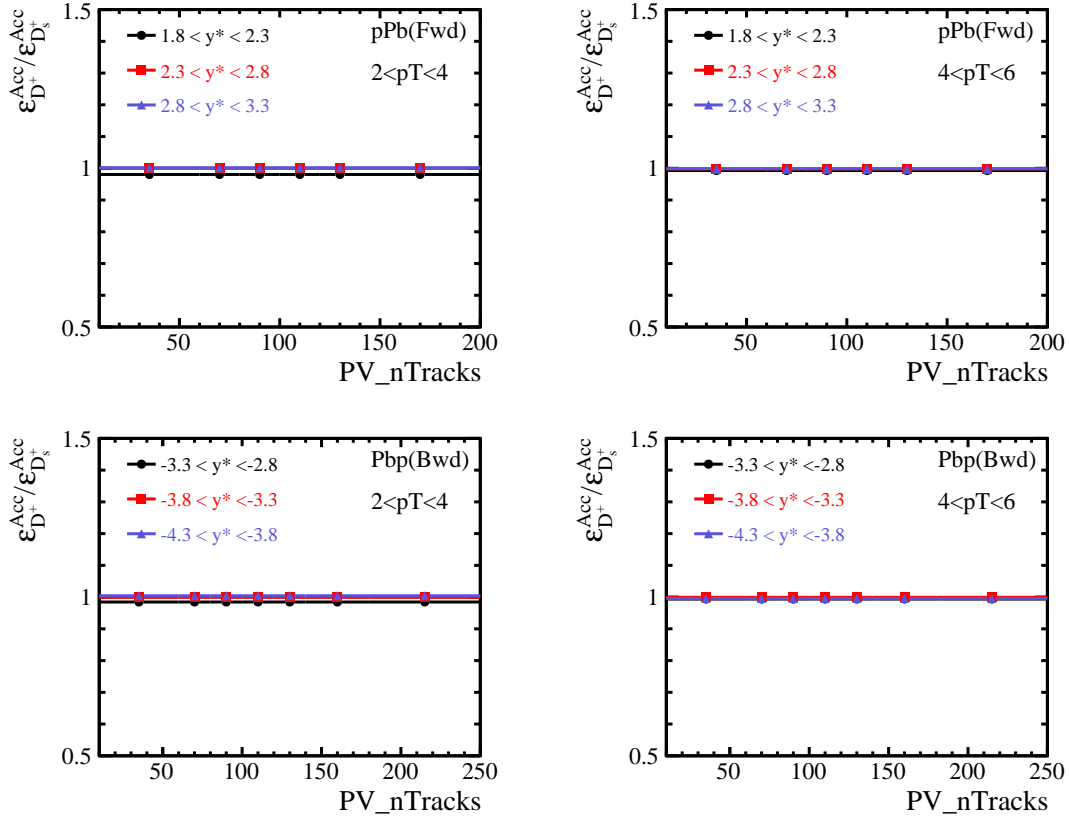


Figure 5.3 The ratio of geometrical acceptance efficiency (D^+/D_s^+) as a function of p_T , y^* and PV nTracks (3D) for Fwd (up) and Bwd (down) configurations. Only the statistical uncertainties are shown here.

The uncertainty quoted in the table are considered as systematic. To take the correction factor into account, the definition of $\epsilon_{\text{rec\&sel}}$ is modified to:

$$\epsilon_{\text{rec\&sel}} = \frac{\sum_{D_s^+ \text{ reconstructed and selected}} w_i(p_{K^-}, \eta_{K^-}) \times w_i(p_{K^+}, \eta_{K^+}) \times w_i(p_{\pi^+}, \eta_{\pi^+})}{D_s^+ \text{ with } K^- K^+ \pi^+ \text{ in LHCb acceptance}}. \quad (5.6)$$

$$\epsilon_{\text{rec\&sel}} = \frac{\sum_{D^+ \text{ reconstructed and selected}} w_i(p_{K^-}, \eta_{K^-}) \times w_i(p_{\pi^+}, \eta_{\pi^+}) \times w_i(p_{\pi^+}, \eta_{\pi^+})}{D^+ \text{ with } K^- \pi^+ \pi^+ \text{ in LHCb acceptance}}. \quad (5.7)$$

where ω_i is the correction factor for track A with momentum, p_A , and pseudorapidity, η_A .

5.2.3 Multiplicity

The LHCb reconstruction efficiency also depends on the multiplicity (clusters, hits, tracks..). The reconstruction efficiency of very low multiplicity and very high multiplicity events is very low. As mention in Section 2.3.2, multiplicity simulation has never been a simple thing in $p\text{Pb}$ collisions. We can now simulate high multiplicity events by modifying the pile up number, but the multiplicity distribution in simulation is slightly different from

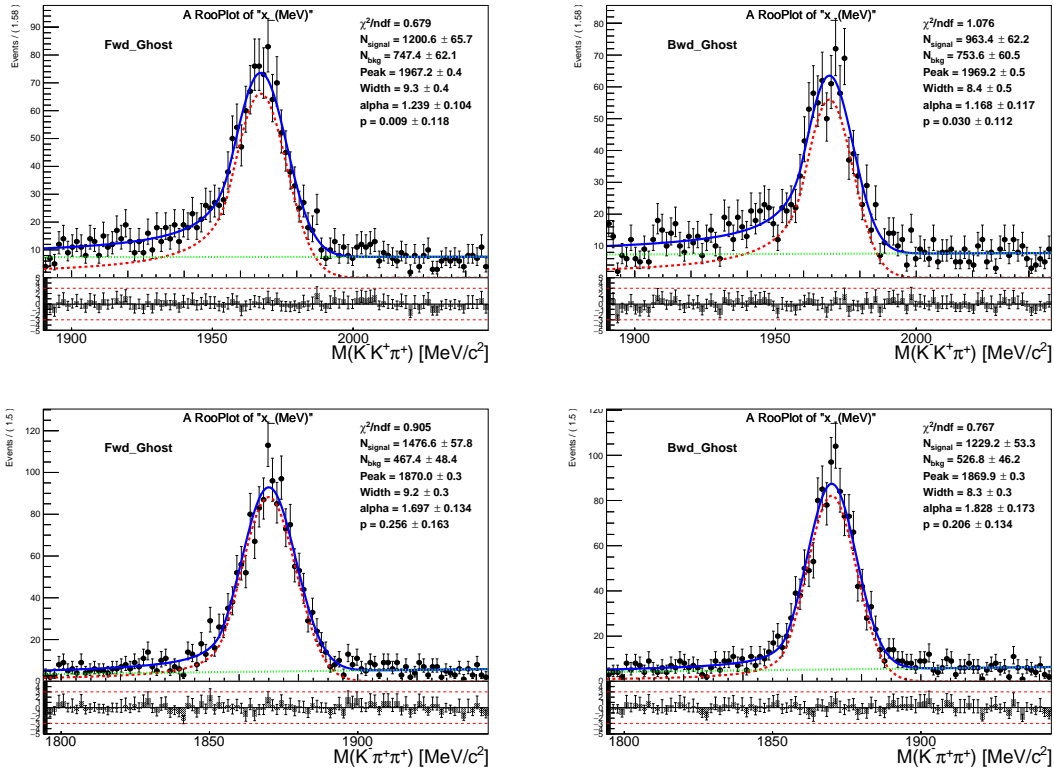


Figure 5.4 The mass distribution of truth unmatched D_s^+ (up), D^+ (down) mesons for Fwd (left) and Bwd (right) simulation.

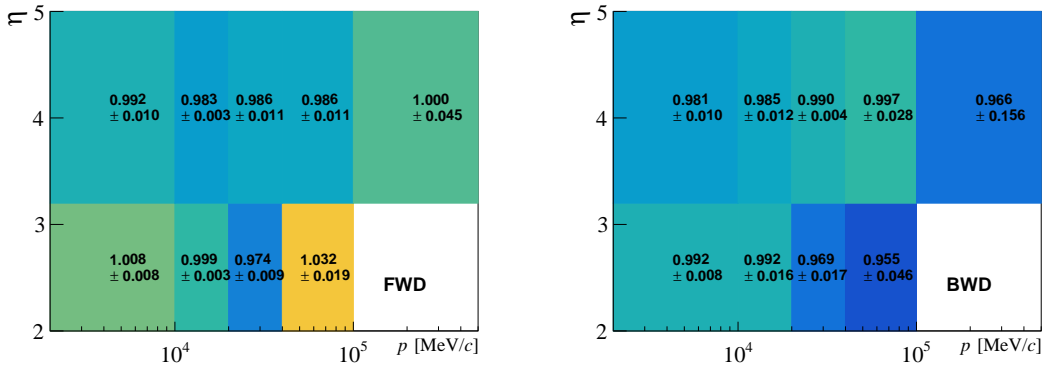


Figure 5.5 The tracking efficiency correction factor table for Fwd (left) and Bwd (right) configuration.

that in data. We use nVeloCluster, nDownstreamTracks, nLongTracks and nSPDHits to correct the simulation and shown in Figure 5.6. Other variables perform well, except nSPDHits. Finally, we use nVeloClusters to define correction factor, $w(\text{nVeloClusters}) = \frac{f_{\text{nVeloClusters distribution}}^{\text{data}}}{f_{\text{nVeloClusters distribution}}^{\text{MC}}}$.

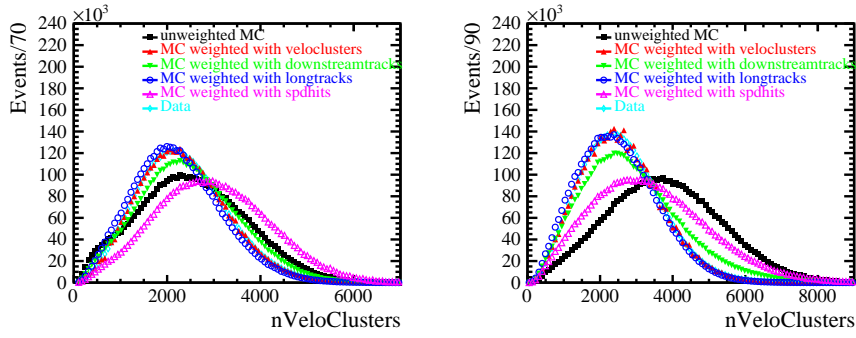


Figure 5.6 The distribution of nVeloClusters in p Pb data, simulation and weighted simulation. Fwd on the left and Bwd on the right.

To consider the correction, Equations 5.6 and 5.7 are modified as:

$$\epsilon_{\text{rec\&sel}} = \frac{\sum_{D_s^+ \text{ rec\&sel}} w_i(p_{K^-}, \eta_{K^-}) \times w_i(p_{K^+}, \eta_{K^+}) \times w_i(p_{\pi^+}, \eta_{\pi^+}) \times w_i(\text{nVeloClusters})}{\sum D_s^+ \text{ with } K^-K^+\pi^+ \text{ in LHCb acceptance} \times w_i(\text{nVeloClusters})}. \quad (5.8)$$

$$\epsilon_{\text{rec\&sel}} = \frac{\sum_{D^+ \text{ rec\&sel}} w_i(p_{K^-}, \eta_{K^-}) \times w_i(p_{\pi^+}, \eta_{\pi^+}) \times w_i(p_{\pi^+}, \eta_{\pi^+}) \times w_i(\text{nVeloClusters})}{\sum D^+ \text{ with } K^-\pi^+\pi^+ \text{ in LHCb acceptance} \times w_i(\text{nVeloClusters})}. \quad (5.9)$$

The $\epsilon_{\text{rec\&sel}}$ as p_T and y^* function results is shown in Figure 5.7. The results are summarized in Table A.13, A.14, A.17, A.18 in Appendix A. The ratio of $\epsilon_{\text{rec\&sel}} (D^+/D_s^+)$ as a function of p_T and y^* (2D) is shown in Figure 5.8. The results are summarized in Table A.21 and A.22 in Appendix A. The ratio of $\epsilon_{\text{rec\&sel}} (D^+/D_s^+)$ as a function of p_T , y^* and PV nTracks (3D) is shown in Figure 5.9. The results are summarized in Table A.23 and A.24 in Appendix A.

5.3 PID efficiency

The particle identification (PID) cuts is not included when considering $\epsilon_{\text{rec\&sel}}$, because the Data/MC agreement for DLL variables (the likelihood information produced by PID system) is poor as shown in Figure 5.10. The best solution is to use calibration samples from data. PID calibration samples contains decay channels with a topology which allows unambiguous identification of one daughter without relying on its PID-related variables. Some typical decay channels are listed in Figure 5.11. Hard (soft) represents to calibration tracks with high (low) p_T .

PIDCalib software package^[136] is the interface between the PID calibration samples and the need of analyst. It provides simple access to calibration samples through a set of scripts, which can study PID selections efficiency as a function of different variables

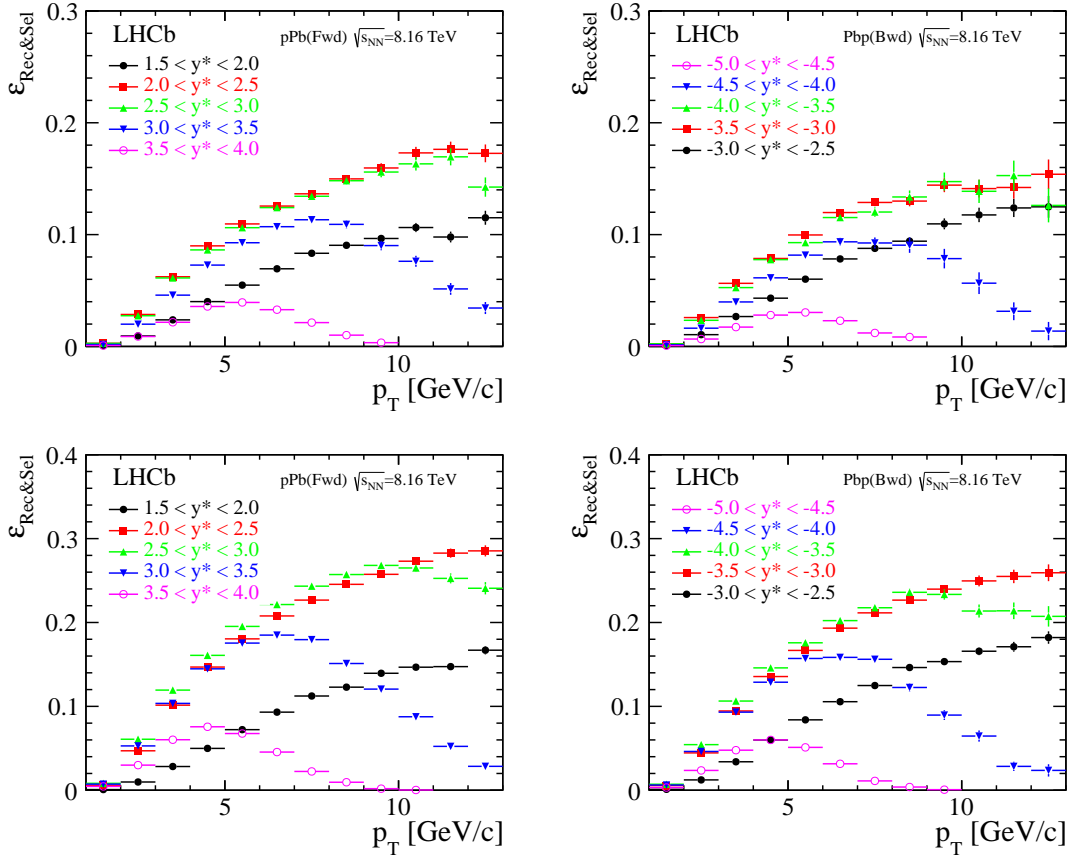


Figure 5.7 The tracking efficiency, $\epsilon_{\text{rec\&sel}}$, as a function of p_T and y^* of prompt D_s^+ (up), D^+ (down) meson for Fwd (left) and Bwd (right) configurations, multiplicity taken into consideration. Only the statistical uncertainties are shown here.

(momentum, pseudorapidity, multiplicity) in different systems (pp , $p\text{Pb}$, PbPb). The PID efficiency, ϵ_{PID} , is defined as the efficiency of the PID selections on the three hadron tracks in the D_s^+ (D^+) selection. The ϵ_{PID} is determined using the single track efficiency in PID calibration samples convolved with the kinematic distribution in MC sample, as the following formula:

$$\epsilon_{\text{PID}}(D^+) = \frac{\sum_{i=1}^N \epsilon_K(p_i^K, \eta_i^K, \text{nVeloClusters}) \epsilon_K(p_i^K, \eta_i^K, \text{nVeloClusters}) \epsilon_\pi(p_i^\pi, \eta_i^\pi, \text{nVeloClusters})}{N} \quad (5.10)$$

$$\epsilon_{\text{PID}}(D_s^+) = \frac{\sum_{i=1}^N \epsilon_K(p_i^K, \eta_i^K, \text{nVeloClusters}) \epsilon_\pi(p_i^\pi, \eta_i^\pi, \text{nVeloClusters}) \epsilon_\pi(p_i^\pi, \eta_i^\pi, \text{nVeloClusters})}{N} \quad (5.11)$$

where N is the sum of the events in the simulation samples used to evaluate the ϵ_{PID} . The PID selections are $\text{DLL}_{K\pi}(K^\pm) > 5$ and $\text{DLL}_{K\pi}(\pi^\pm) < 0$. The PID selections efficiency $\epsilon_K(p_i^K, \eta_i^K, \text{nVeloClusters})$ and $\epsilon_\pi(p_i^\pi, \eta_i^\pi, \text{nVeloClusters})$ as functions of p , η

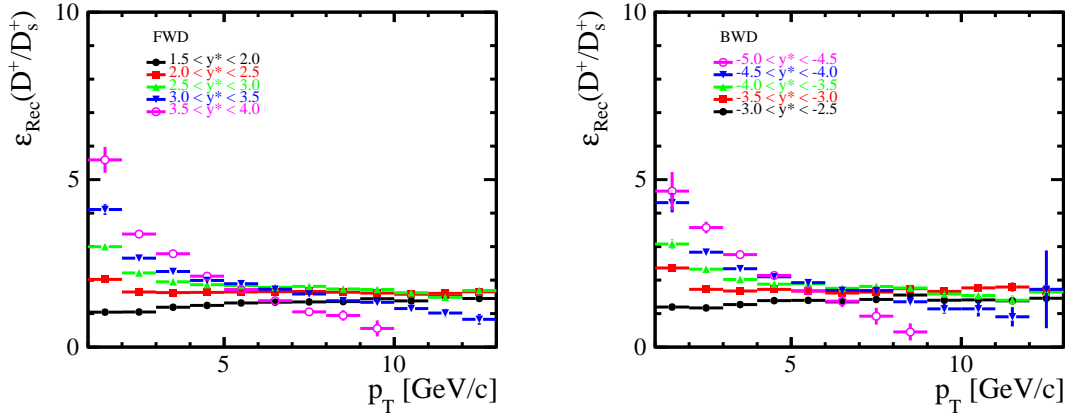


Figure 5.8 The ratio of $\epsilon_{\text{rec\&sel}}(D^+/D_s^+)$ as a function of p_T and y^* for Fwd (left) and Bwd (right) configurations, multiplicity taken into consideration. Only the statistical uncertainties are shown here.

and nVeloClusters are performed by the PIDCalib package. Due to the low statistics at high multiplicity, we use pp PID calibration sample taken in 2016 and $p\text{Pb}$ PID calibration sample taken in 2016 as input.

The ϵ_{PID} results is shown in Figure 5.12. The results are summarized in Table A.25, A.26, A.29, A.30 in Appendix A. The ratio of $\epsilon_{\text{PID}}(D^+/D_s^+)$ as a function of p_T and y^* (2D) is shown in Figure 5.13. The results are summarized in Table A.33 and A.34 in Appendix A. The ratio of $\epsilon_{\text{PID}}(D^+/D_s^+)$ as a function of p_T , y^* and PV nTracks (3D) is shown in Figure 5.14. The results are summarized in Table A.35 and A.36 in Appendix A.

5.4 Trigger efficiency

The High Level software stage Trigger 2 (HLT2) has been included in online and offline selections, so only the efficiency of High Level software stage Trigger 1 (HLT1) needs to be considered. The trigger efficiency, ϵ_{tri} is defined as:

$$\epsilon_{\text{tri}}(p_T, y^*) \equiv \frac{\text{TOS of HLT1 in bin } (p_T, y^*)}{\text{selected signal in bin } (p_T, y^*)},$$

where TOS is trigger on signal. Specifically, it refers to $(\text{Hlt1TrackMVADecision_TOS} == 1 || \text{Hlt1TwoTrackMVADecision_TOS} == 1)$.

The ϵ_{tri} is almost one due to the loose selections, although the ϵ_{tri} of the kinematic edge decreases. The ϵ_{tri} results is shown in Figure 5.15. The results are summarized in Table A.37, A.38, A.41, A.42 in Appendix A. The ratio of $\epsilon_{\text{tri}}(D^+/D_s^+)$ as a function of p_T and y^* (2D) is shown in Figure 5.16. The results are summarized in Table A.45 and A.46

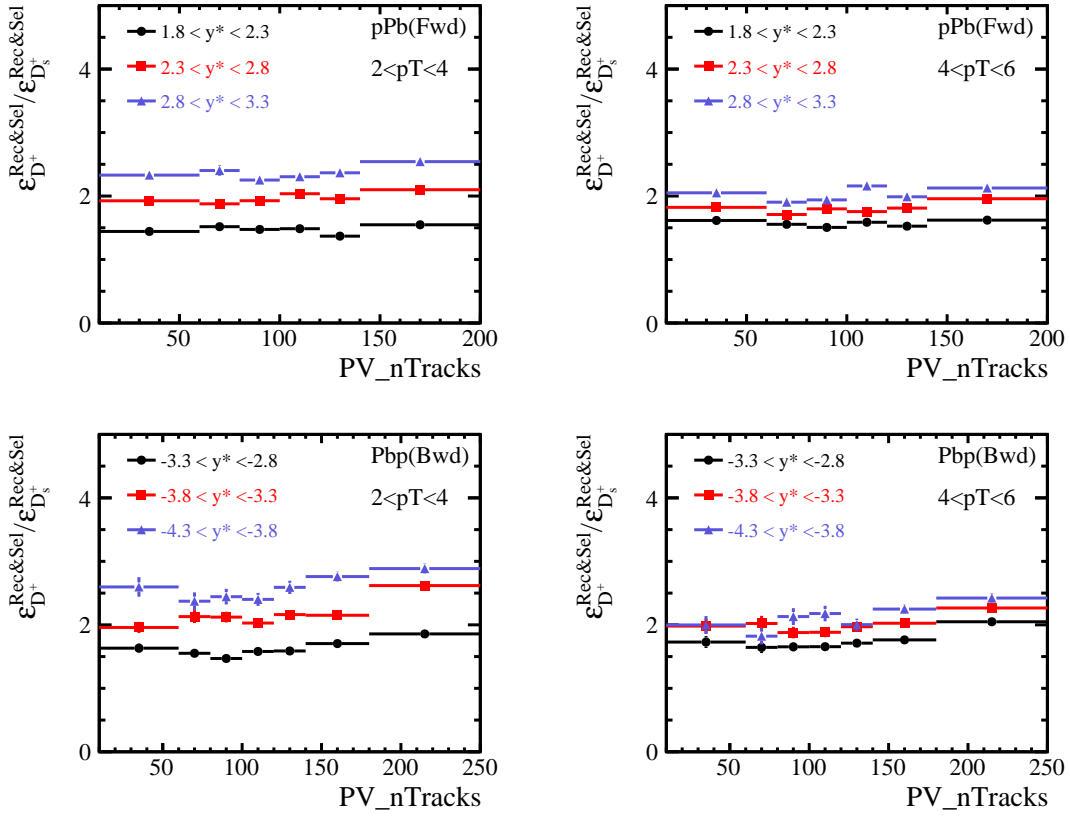


Figure 5.9 The ratio of $\epsilon_{\text{rec\&sel}}(D^+/D_s^+)$ as a function of p_T , y^* and PV nTracks for Fwd (up) and Bwd (down) configurations, multiplicity taken into consideration. Only the statistical uncertainties are shown here.

in Appendix A. The ratio of $\epsilon_{\text{tri}}(D^+/D_s^+)$ as a function of p_T , y^* and PV nTracks (3D) is shown in Figure 5.17. The results are summarized in Table A.47 and A.48 in Appendix A.

5.5 Total efficiency

The total efficiencies are obtained directly from the multiplication of the efficiencies above as given by Equation 5.1. The result is plotted on the Figure 5.18, in which the corrections from truth matching and multiplicity are also included. The uncertainties are due to simulation sample size, which are uncorrelated between bins. The ratio of total efficiency are shown in Figure 5.19 5.20.

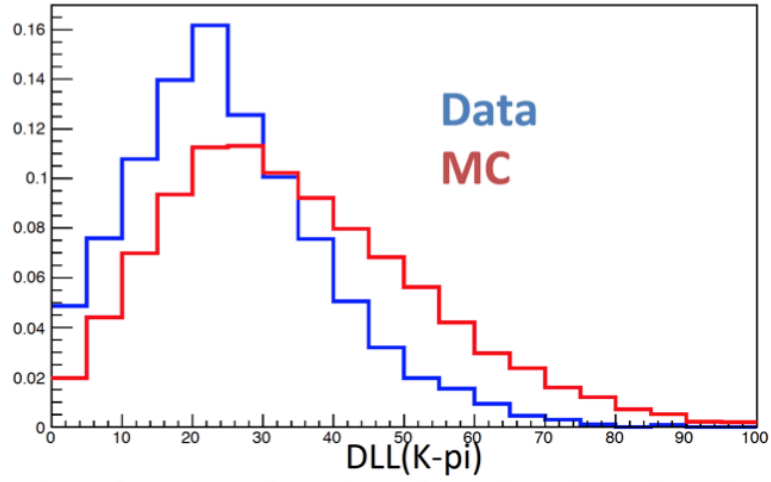


Figure 5.10 The Data/MC DLL variables distribution^[134]

Species	Soft	Hard
e^\pm	—	$J/\psi \rightarrow e^+e^-$
μ^\pm	$D_s^+ \rightarrow \mu^+\mu^-\pi^+$	$J/\psi \rightarrow \mu^+\mu^-$
π^\pm	$K_s^0 \rightarrow \pi^+\pi^-$	$D^* \rightarrow D^0\pi^+, D^0 \rightarrow K^-\pi^+$
K^\pm	$D_s^+ \rightarrow K^+K^-\pi^+$	$D^* \rightarrow D^0\pi^+, D^0 \rightarrow K^-\pi^+$
p^\pm	$\Lambda^0 \rightarrow p\pi^-$	$\Lambda^0 \rightarrow p\pi^-, \Lambda_c^+ \rightarrow pK^-\pi^+$

Figure 5.11 Decay channels are used in PID calibration samples^[135]

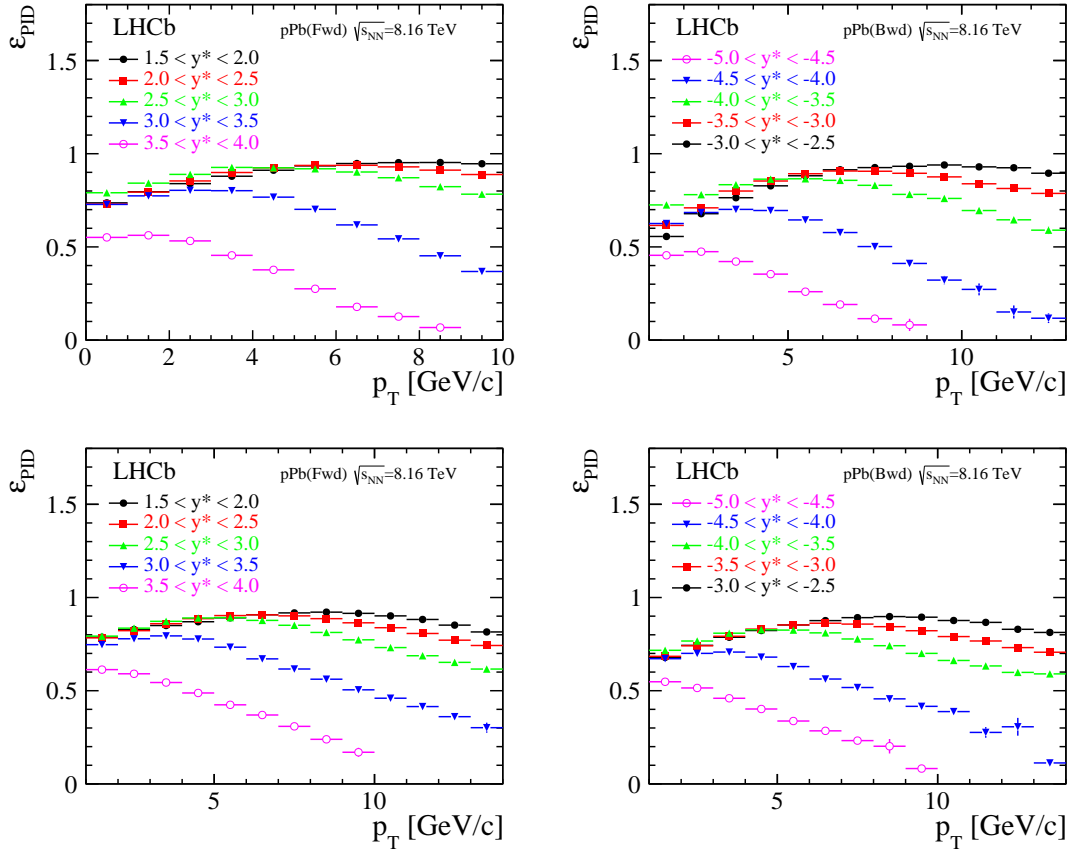


Figure 5.12 The PID efficiency, ϵ_{PID} , as a function of p_T and y^* of prompt D_s^+ (up), D^+ (down) meson for Fwd (left) and Bwd (right) configurations. Only the statistical uncertainties are shown here.

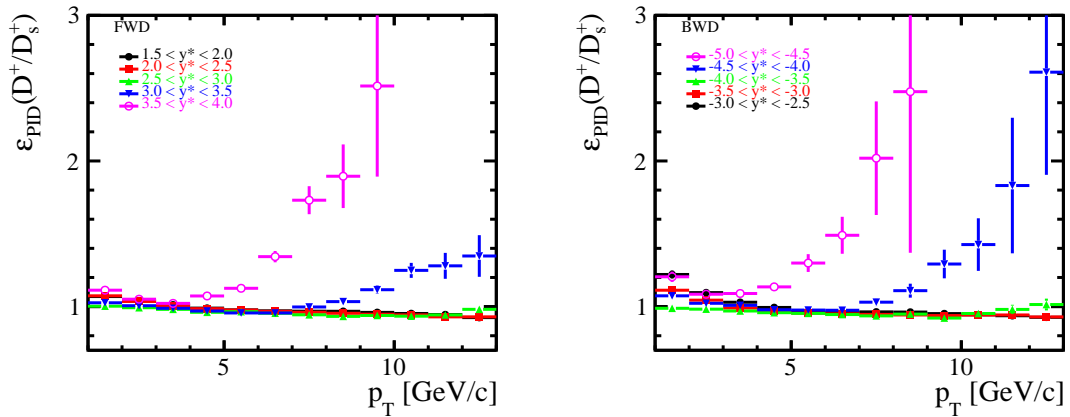


Figure 5.13 The ratio of $\epsilon_{\text{PID}}(D^+/D_s^+)$ as a function of p_T and y^* for Fwd (left) and Bwd (right) configurations, multiplicity taken into consideration. Only the statistical uncertainties are shown here.

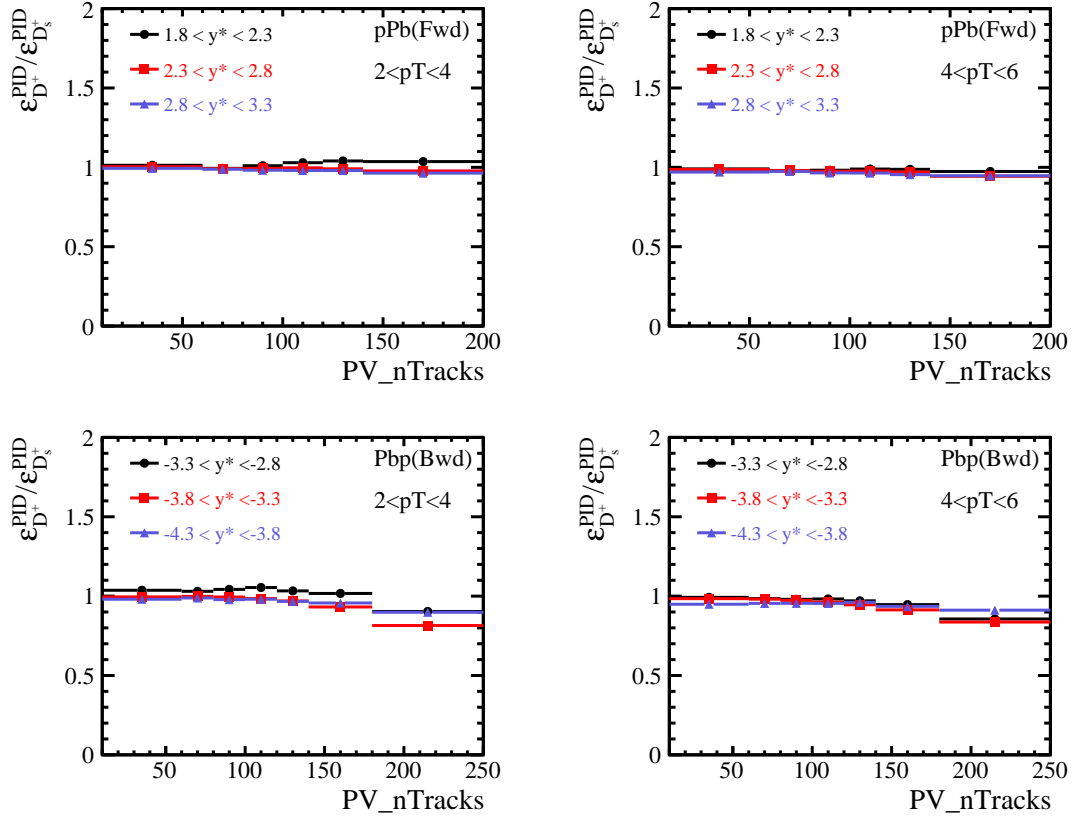


Figure 5.14 The ratio of $\epsilon_{\text{PID}}(D^+/D_s^+)$ as a function of p_T , y^* and PV nTracks for Fwd (up) and Bwd (down) configurations, multiplicity taken into consideration. Only the statistical uncertainties are shown here.

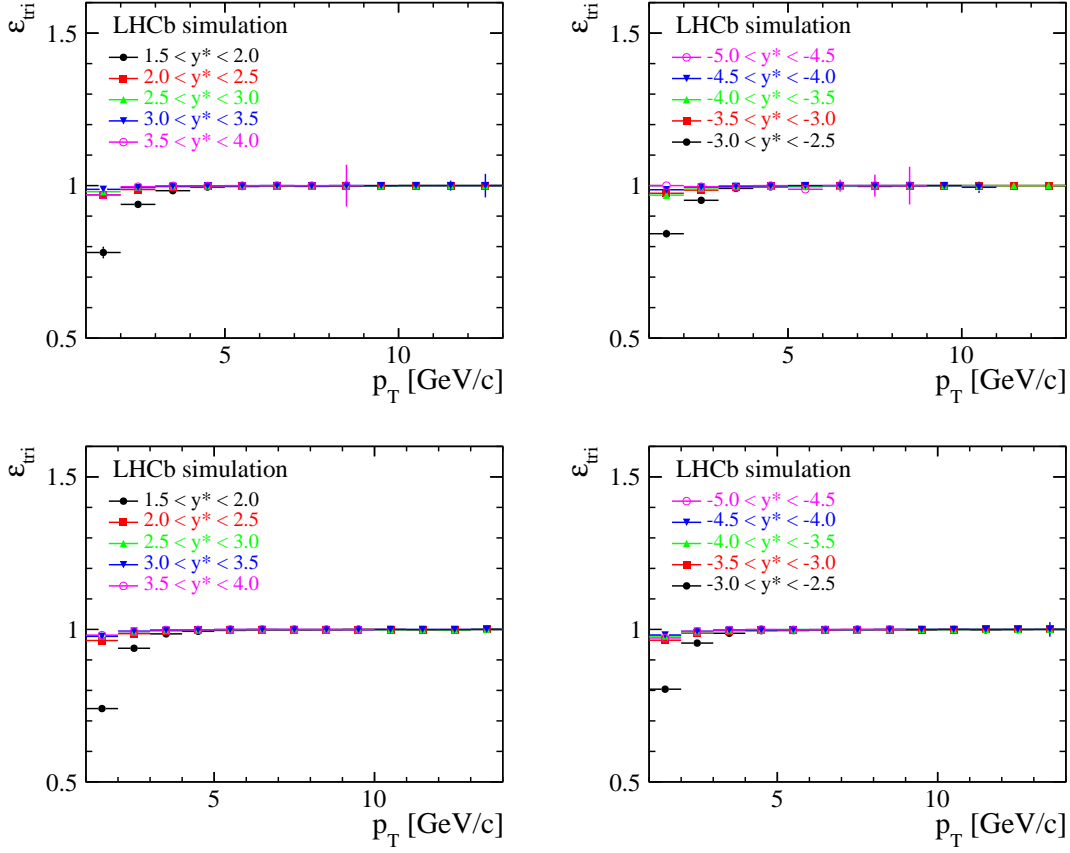


Figure 5.15 The trigger efficiency, ϵ_{tri} , as a function of p_T and y^* of prompt D_s^+ (up), D^+ (down) meson for Fwd (left) and Bwd (right) configurations. Only the statistical uncertainties are shown here.

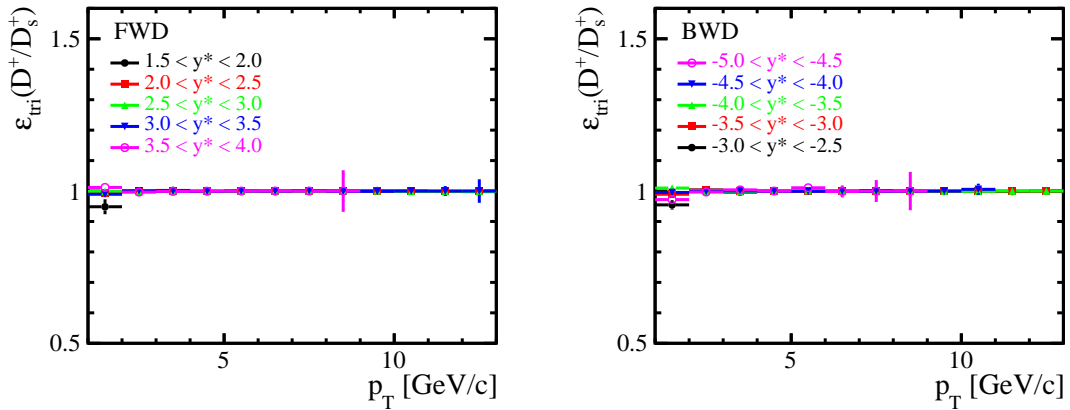


Figure 5.16 The ratio of $\epsilon_{\text{tri}}(D^+/D_s^+)$ as a function of p_T and y^* for Fwd (left) and Bwd (right) configurations, multiplicity taken into consideration. Only the statistical uncertainties are shown here.

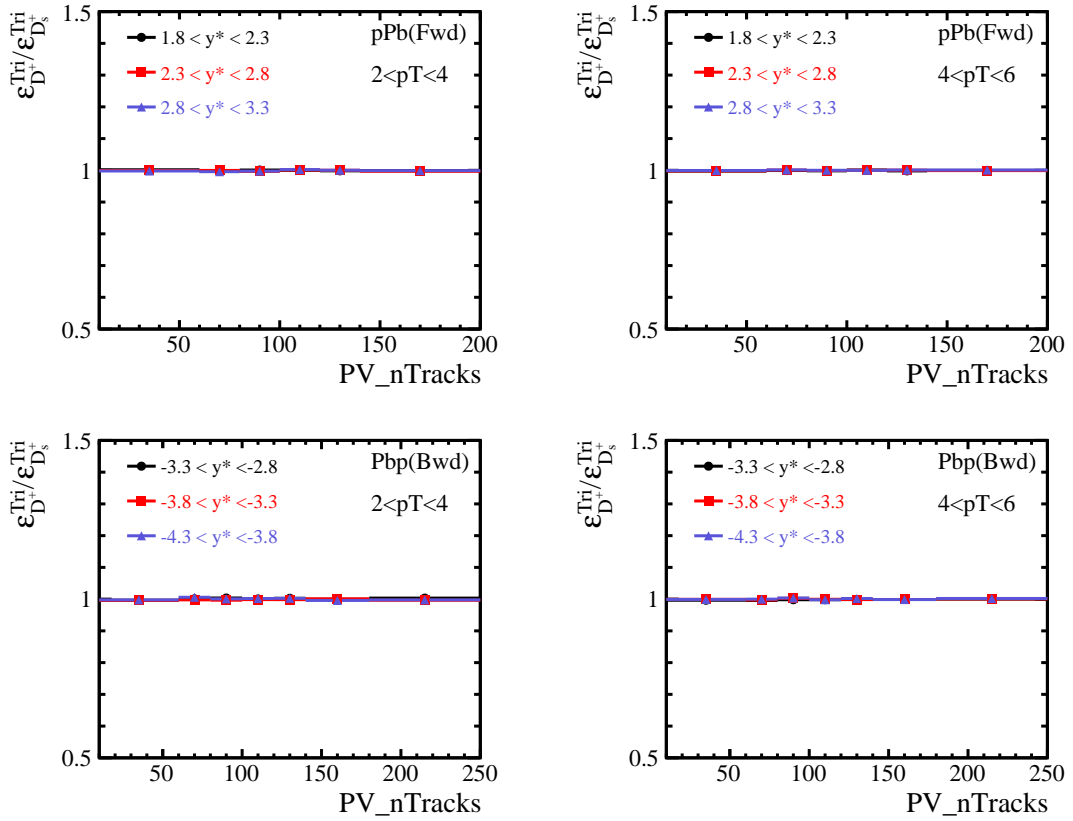


Figure 5.17 The ratio of $\epsilon_{\text{tri}}(D^+/D_s^+)$ as a function of p_T , y^* and PV nTracks for Fwd (up) and Bwd (down) configurations, multiplicity taken into consideration. Only the statistical uncertainties are shown here.

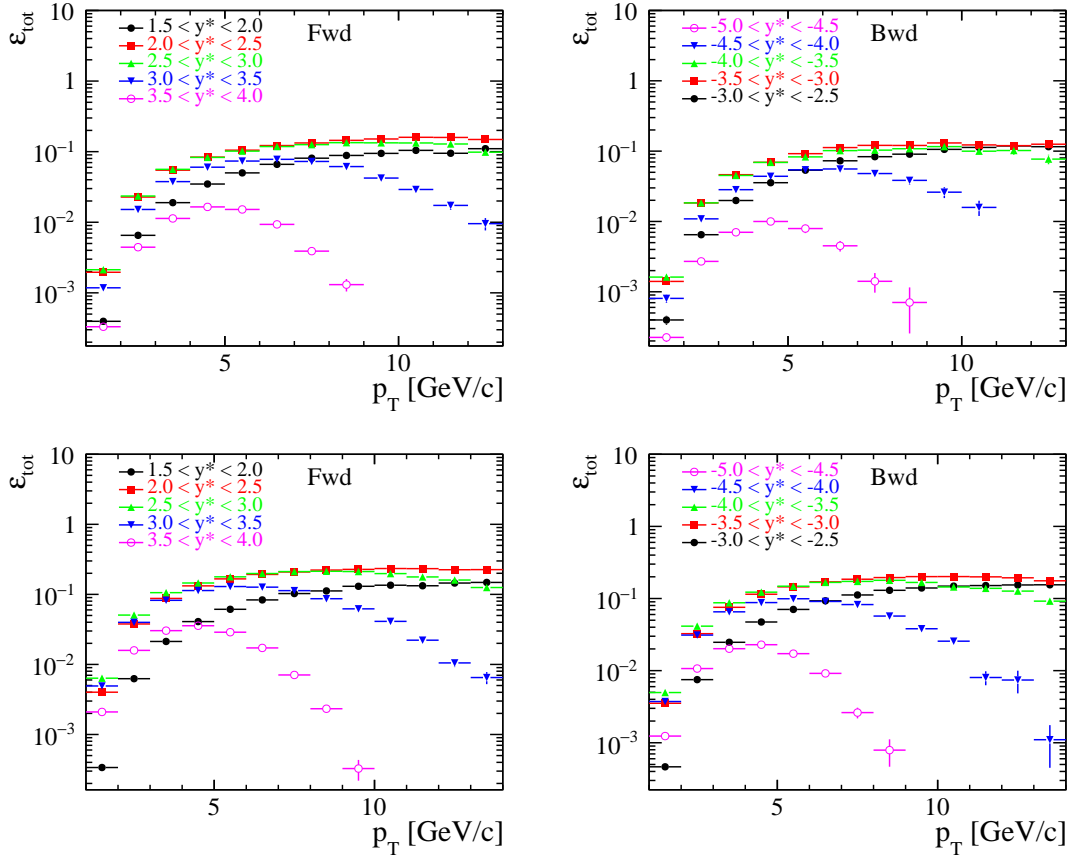


Figure 5.18 The total efficiency, ϵ_{tot} , as a function of p_T and y^* of prompt D_s^+ (up), D^+ (down) meson for Fwd (left) and Bwd (right) configurations.

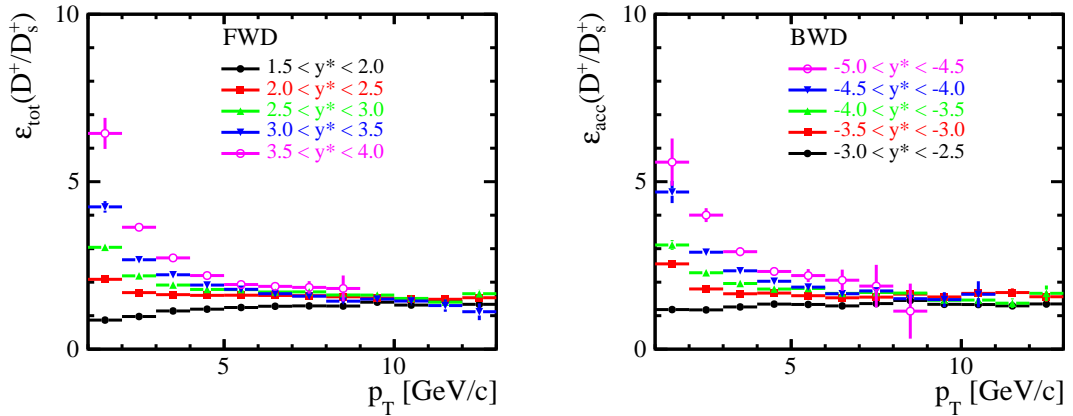


Figure 5.19 The ratio of $\epsilon_{\text{tot}}(D^+/D_s^+)$ as a function of p_T and y^* for Fwd (left) and Bwd (right) configurations. Only the statistical uncertainties are shown here.

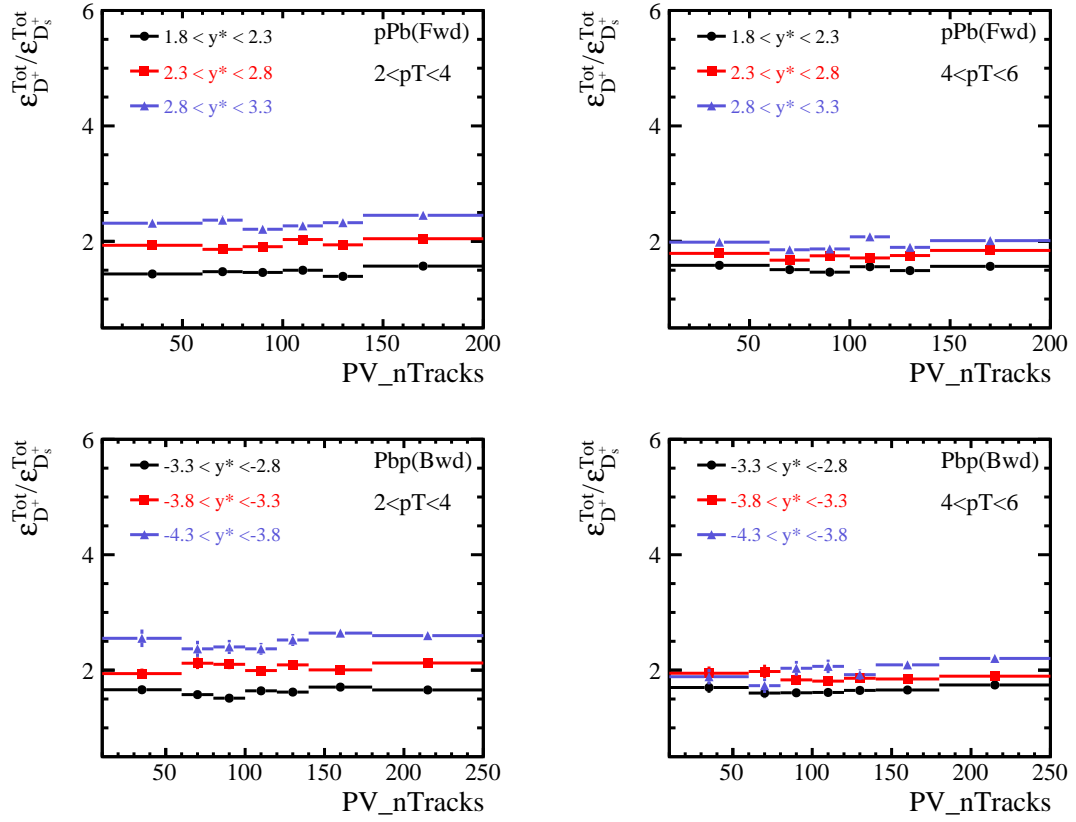


Figure 5.20 The ratio of $\epsilon_{\text{tot}}(D^+/D_s^+)$ as a function of p_T , y^* and PV nTracks for Fwd (up) and Bwd (down) configurations. Only the statistical uncertainties are shown here.

CHAPTER 6 SYSTEMATIC UNCERTAINTIES

In this chapter, we will discuss the systematic uncertainties on the measurement of D_s^+ (D^+). Since the analysis strategy is the same, the source of systematic uncertainties are also the same. These can be roughly divided into two categories : uncorrelated systematic uncertainties between bins and correlated systematic uncertainties between bins.

6.1 Signal yield determination

The prompt D_s^+ (D^+) signal yields are determined through a two steps fit, so the systematical uncertainties are estimated separately.

For the mass fit, the raw yield is related to the fit function used to describe the shape of the D_s^+ (D^+) invariant mass distribution. We replace the Gaussian function with a Crystal Ball function to add a second Crystal Ball to fit the inclusive component. Besides, the uncertainties from mis-ID $D_s^+ \rightarrow K^- K^+ \pi^+$ in $D^+ \rightarrow K^- \pi^+ \pi^+$ and vice versa are also considered. This reason is due to the wrong particle identification between K and π , resulting in mutual pollution between the two decay channels. The shape of mis-ID mass spectrum was obtained from Monte Carlo simulation, and shown in Figure 6.1. The impact of this part is about 0.1%. The systematic uncertainties from mass fit are shown in Figure 6.2. The systematic uncertainty of this part is not very large.

For the $\log_{10}\chi_{\text{IP}}^2$ fit, the ρ_L, ρ_R and ϵ for the non-prompt component are fixed. Their

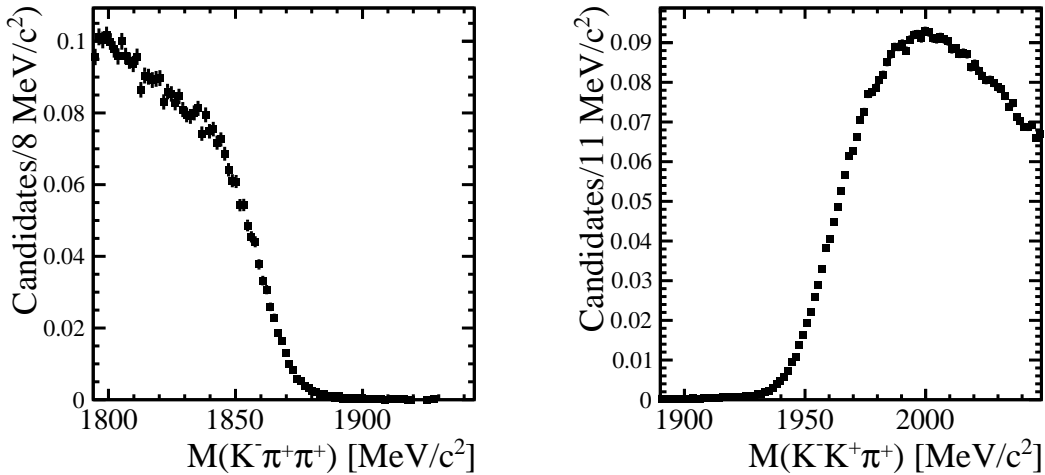


Figure 6.1 Mis-ID mass spectrum shape

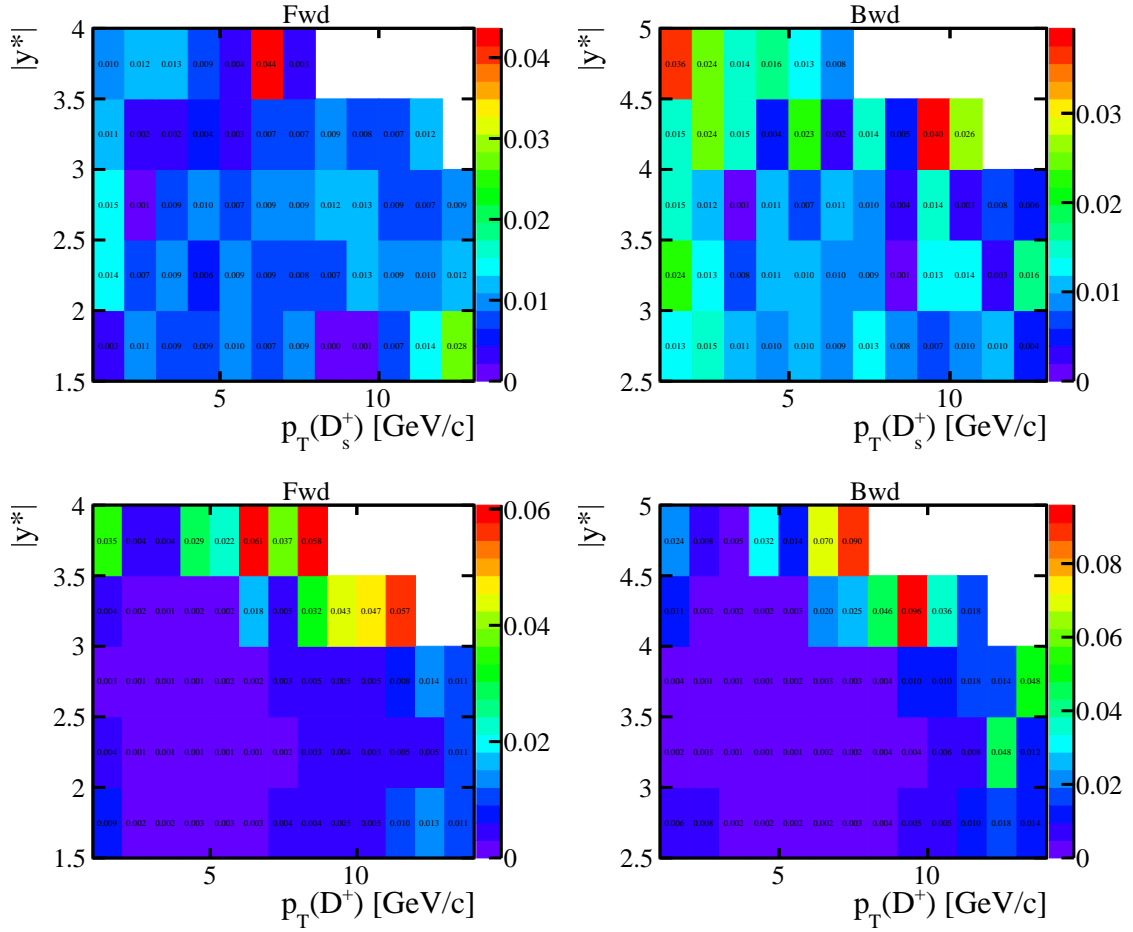


Figure 6.2 Relative systematic uncertainties of $M(D_s^+)(\text{up})$ and $M(D^+)(\text{down})$ fit as a function of p_T and y^* (display with decimal). Left for Fwd and Right for Bwd.

effects are also considered by shifting the values to one sigma away from the mean value. The results are shown in Figure 6.3. In low p_T and low y^* bins, the systematic uncertainties are larger than others, because the prompt component and the non-prompt component can't be distinguished in these bins. The systematic uncertainties in both steps are considered uncorrelated between Fwd and Bwd.

When studying the D_s^+/D^+ production ratio as function of p_T , y^* and PV nTracks, we use the same method but a different fit model. For the mass fit, we replace the linear function with an exponential function to fit the background component. For the $\log_{10}\chi_{\text{IP}}^2$ fit, we replace the Bukin function with an AGE function, shown in equation 6.1, to fit the prompt component. The results are shown in Figures 6.4 6.5.

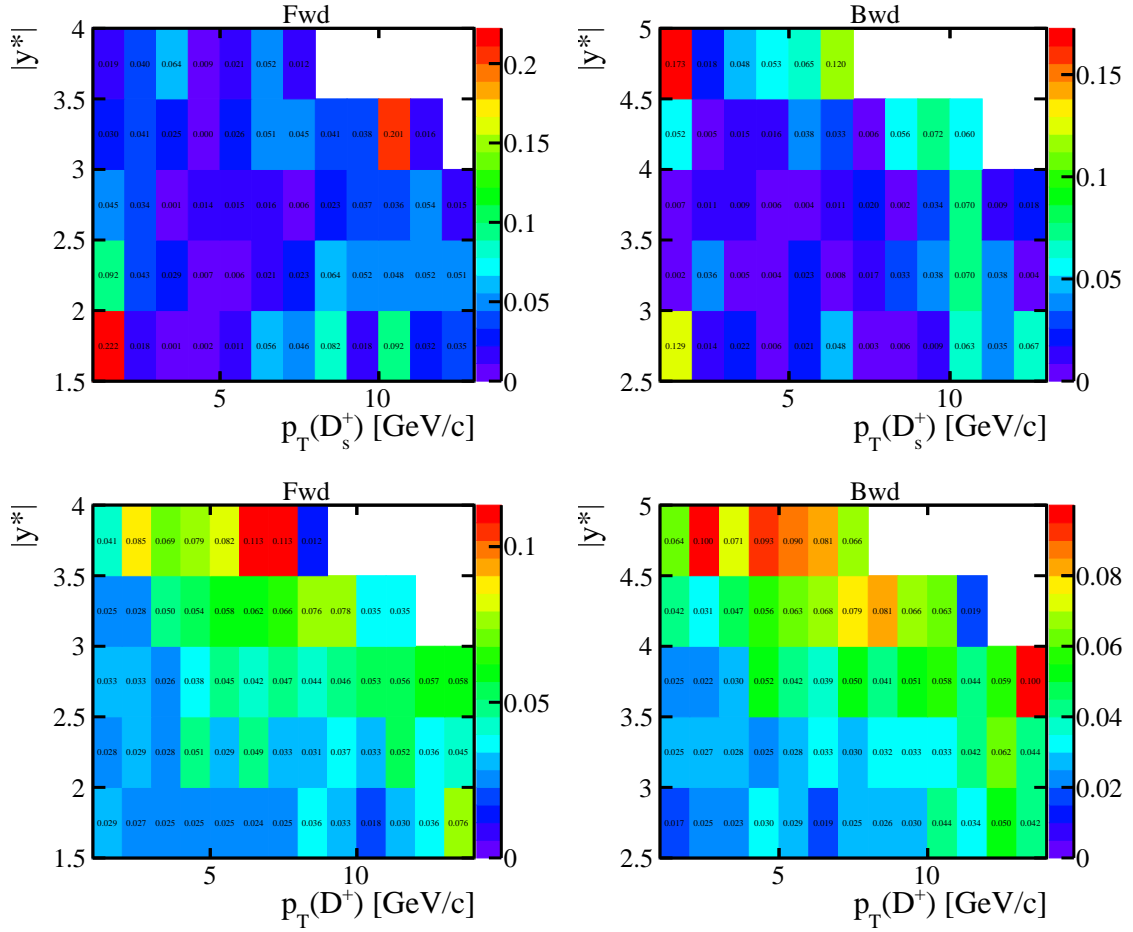


Figure 6.3 Relative systematic uncertainties of $\log_{10}\chi_{IP}^2$ fit as a function of p_T and y^* (display with decimal). Fwd(left) ,Bwd(right) , D_s^+ (up) , D^+ (down).

$$f_{AGE}(x; \mu, \sigma, \epsilon, \rho_L, \rho_R) = \begin{cases} e^{\frac{\rho_L^2}{2} + \rho_L \cdot \frac{x-\mu}{(1-\epsilon)\sigma}} & x < \mu - (\rho_L \cdot \sigma \cdot (1-\epsilon)) \\ e^{-\left(\frac{x-\mu}{\sqrt{2}\cdot\sigma\cdot(1-\epsilon)}\right)^2} & \mu - (\rho_L \cdot \sigma \cdot (1-\epsilon)) \leq x < \mu \\ e^{-\left(\frac{x-\mu}{\sqrt{2}\cdot\sigma\cdot(1+\epsilon)}\right)^2} & \mu \leq x < \mu + (\rho_R \cdot \sigma \cdot (1+\epsilon)) \\ e^{\frac{\rho_R^2}{2} - \rho_R \cdot \frac{x-\mu}{(1+\epsilon)\sigma}} & x \geq \mu + (\rho_R \cdot \sigma \cdot (1+\epsilon)) \end{cases} \quad (6.1)$$

6.2 Efficiencies

The main sources of systematic uncertainties in $\epsilon_{\text{rec\&sel}}$ is the tracking correction factor w_{tracking} . As shown in the Figure 5.5, tracking correction factor is not a fixed value. The uncertainty in the tracking correction factor may propagate into $\epsilon_{\text{rec\&sel}}$. To study this effect, 500 toy Monte Carlo of tracking tables are generated from Gaussian distributions,

of which μ is the mean value and σ the error bar for each bin. These tables are used to measure the efficiencies, and the standard deviation of the efficiency for each bin is used as the systematic uncertainty. The result is shown in Figure 6.6. An additional uncertainty of 1.1%(1.4%) is assigned to the $K(\pi)$ due to the hadronic interactions of these particles with the detector. This uncertainty is dominated by the uncertainty on the material budget and full correlation between kaons and pions is assumed^[137]. Total uncertainty are 3.9% for D^+ , 3.6% for D_s^+ . Besides, the methods with different event multiplicity variables introduce uncertainties at the level of 0.8% per track^[138] and 2.4% on total for this analysis.

When study D_s^+/D^+ ratio, the relative systematic uncertainties from tracking table can be offset partially. The reason is that D_s^+ and D^+ use same tracking table, and they all decay to three final hadrons. When study multiplicity dependence, PVZ distribution bias in MC and data introduces 1%(fwd) and 0.5%(bwd) global systematic uncertainty. The result is shown in Figure 6.7,6.8.

For PID efficiencies, the uncertainties mainly comes from the PIDCalib. The same method (toy Monte Carlo) as estimate tracking table uncertainties is used. The 500 toy Monte Carlo of PIDCalib tables are generated to measure the ϵ_{PID} , and the standard deviation of the efficiency for each bin is used as the systematic uncertainty. This uncertainty is shown in Figure 6.9.

When study D_s^+/D^+ ratio, the relative systematic uncertainties from PIDCalib can be offset partially. The reason is that D_s^+ and D^+ use same binning scheme and input samples are used in PIDCalib. The results are shown in Figure 6.10,6.11.

For the multiplicity corrections, three different variables(nVeloClusters, nLongTracks, nDownstreamTracks) are applied for weighting as shown in the Figure 5.6. The standard deviation for the three efficiency tables are taken as the systematic uncertainties, which is determined in different kinematic bins. The Data/MC multiplicity difference in the forward is less than backward, so the systematic uncertainty is also less than backward. The results are shown in Figure 6.12.

For the trigger efficiencies, the TISTOS method is used to estimate trigger efficiencies and the difference is taken as the uncertainty. The TISTOS method determines the trigger efficiency using data driven techniques^[139]. The TOS (trigger on signal) is $(\text{Hlt1TrackMVADecision_TOS} == 1 | | \text{Hlt1TwoTrackMVADecision_TOS} == 1)$. The TIS (trigger independent of signal) is $(\text{Hlt1Phys_TIS} == 1)$. We apply TIS as denomina-

Table 6.1 systematic uncertainties summary

Source	Relative uncertainty (%)	
<i>Correlated between bins</i>	Fwd	Bwd
Tracking and multiplicity correction	0.1-5.0	0.1-5.0
PID	0.1-10.0	0.1-10.0
Luminosity	2.6	2.5
Hadronic interactions (D_s^+)	3.6	3.6
Hadronic interactions (D^+)	3.9	3.9
Branching fraction(D_s^+)	5.8	5.8
Branching fraction(D^+)	1.7	1.7
<i>Uncorrelated between bins</i>	Fwd	Bwd
Mass fit	0.1-3.0	0.1-6.0
$\log_{10}\chi_{IP}^2$ fit	0.1-20.0	0.1-17.0
MC sample size	0.1-14.7	0.1-14.5

tor, TISTOS as numerator. The difference between data and MC is regarded as systematic uncertainty. The result is shown in Figure 6.13 where it can be seen that the systematic uncertainties from the trigger is negligible. We assuming relative systematic uncertainties from ratio of $\epsilon_{tri}(D^+/D_s^+)$ can be offset totally.

6.3 Other systematics

The relative uncertainty of the corresponding luminosity is 2.6% for Fwd and 2.5% for Bwd data sample. The uncertainties from branching fraction $\mathcal{B}(D_s^+ \rightarrow K^+K^-\pi^+)$ with $\phi(1020)$ mass window cut is 5.8%, $\mathcal{B}(D^+ \rightarrow K^-\pi^+\pi^+)$ is 1.7%.

6.4 Summary of systematic uncertainties

The systematic uncertainties are summarized in Table 6.1.

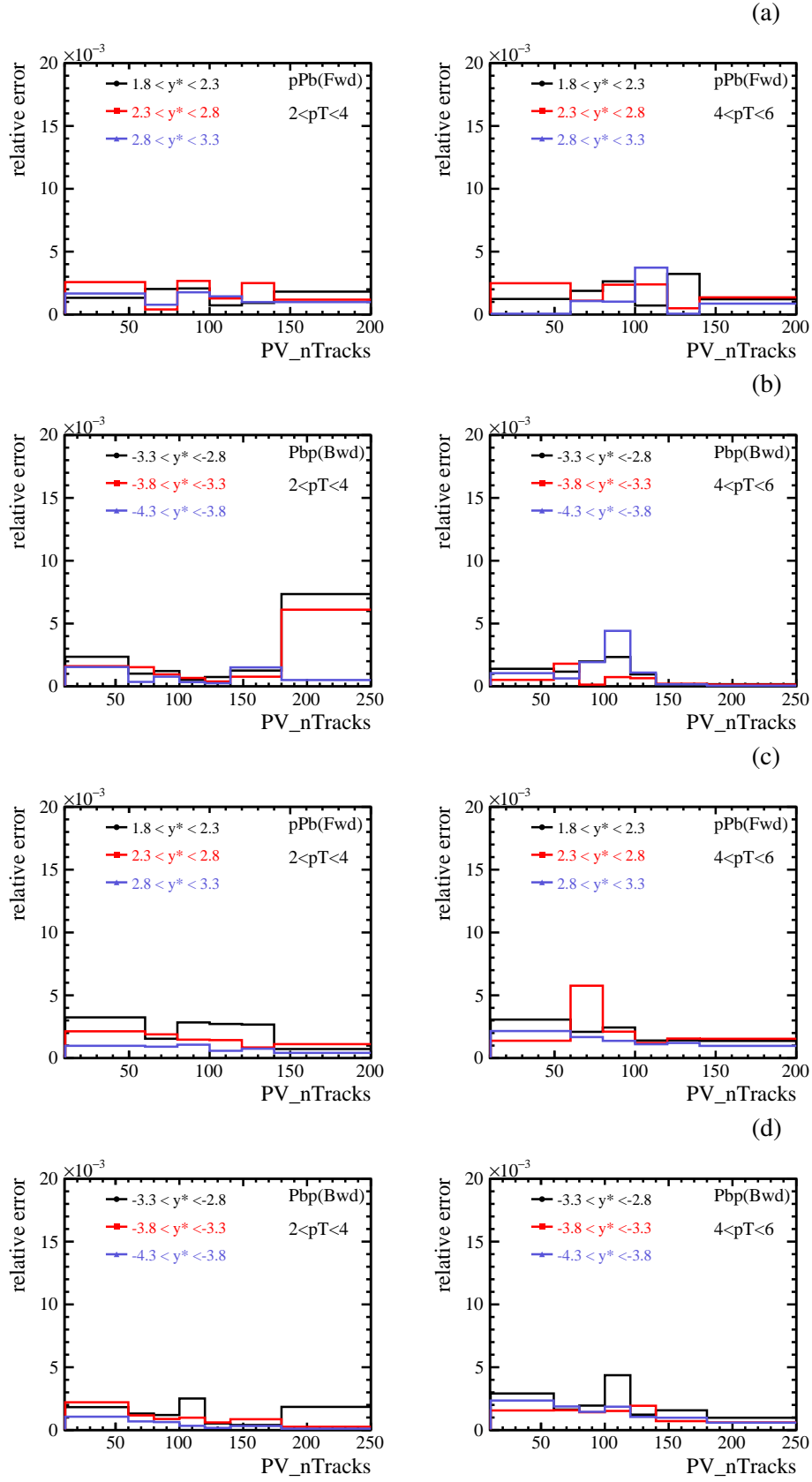


Figure 6.4 Relative systematic uncertainties from mass fit as a function of p_T and y^* and PV nTracks. (a) is forward D_s^+ , (b) is backward D_s^+ , (c) is forward D^+ , (d) is backward D^+ .

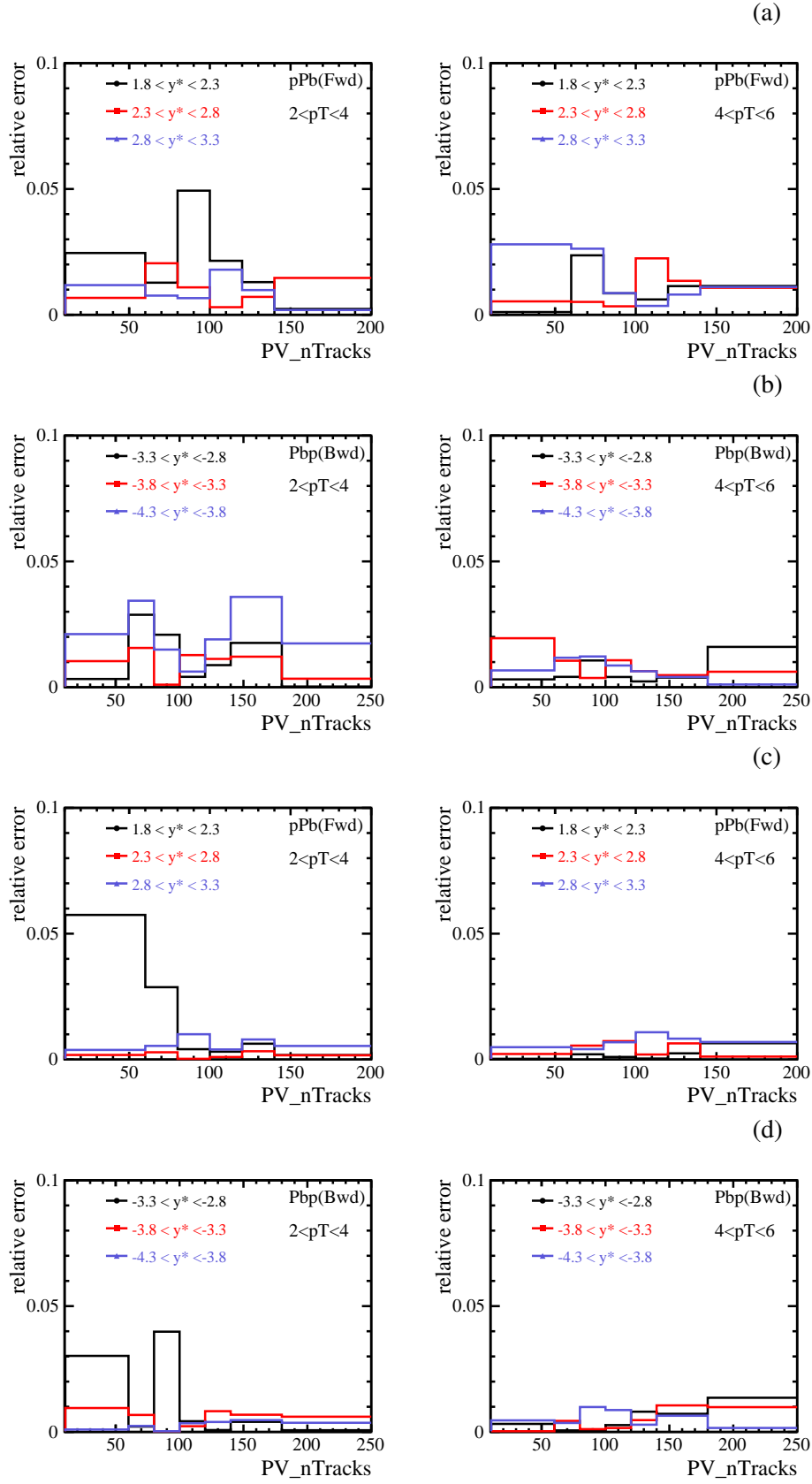


Figure 6.5 Relative systematic uncertainties from $\log_{10}\chi_{\text{IP}}^2$ fit as a function of p_T and y^* and PV nTracks. (a) is forward D_s^+ , (b) is backward D_s^+ , (c) is forward D^+ , (d) is backward D^+ .

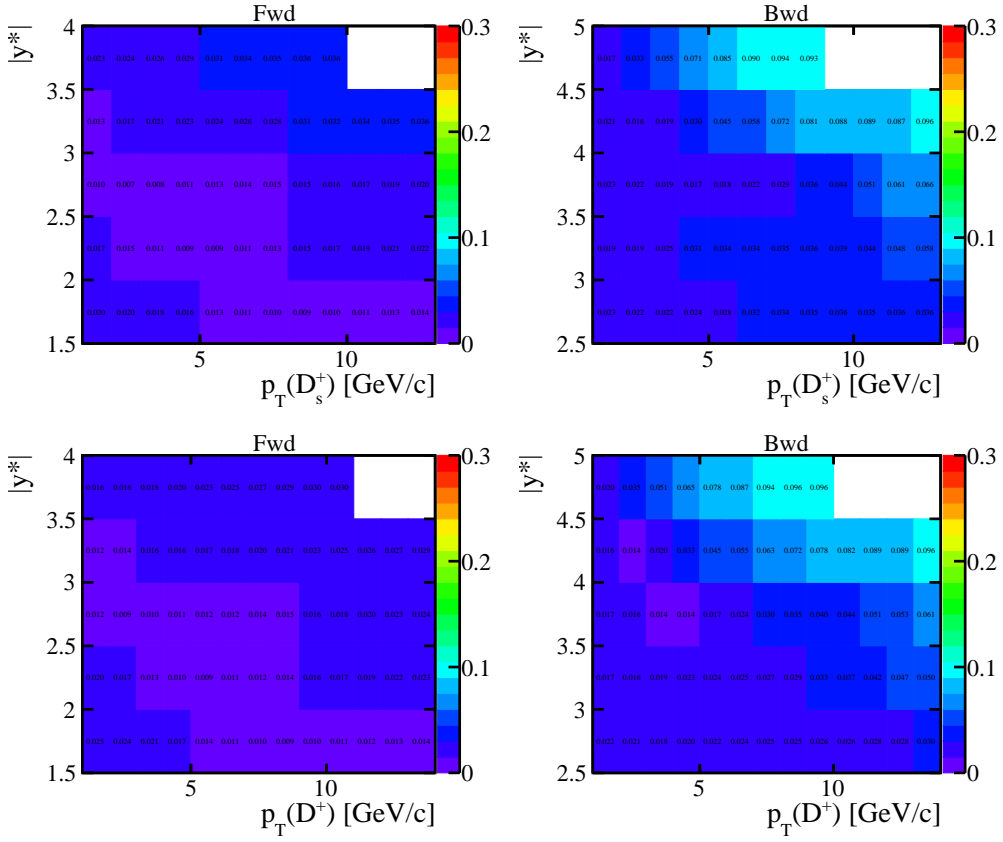


Figure 6.6 Relative systematic uncertainties from tracking table as a function of p_T and y^* (display with decimal). Fwd(left) ,Bwd(right) , D_s^+ (up) , D^+ (down).

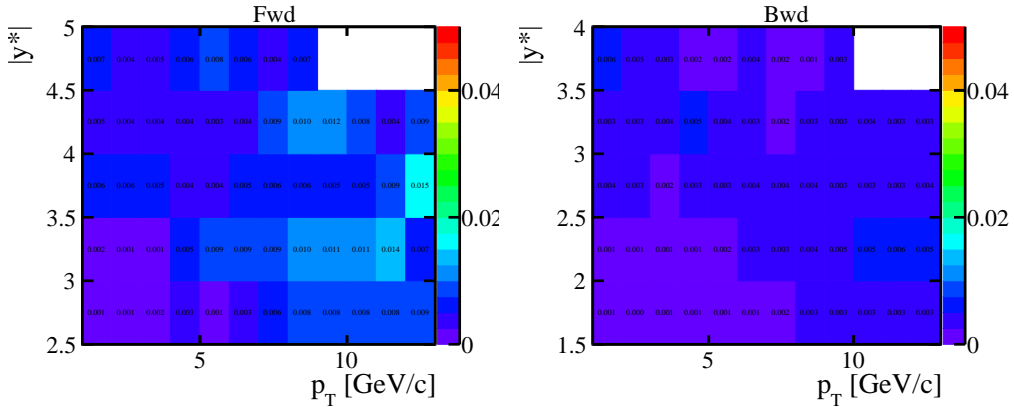


Figure 6.7 The relative systematic uncertainties from ratio of $\epsilon_{\text{rec\&sel}}(D^+/D_s^+)$ as a function of p_T and y^* (display with decimal). Left for Fwd and Right for Bwd.

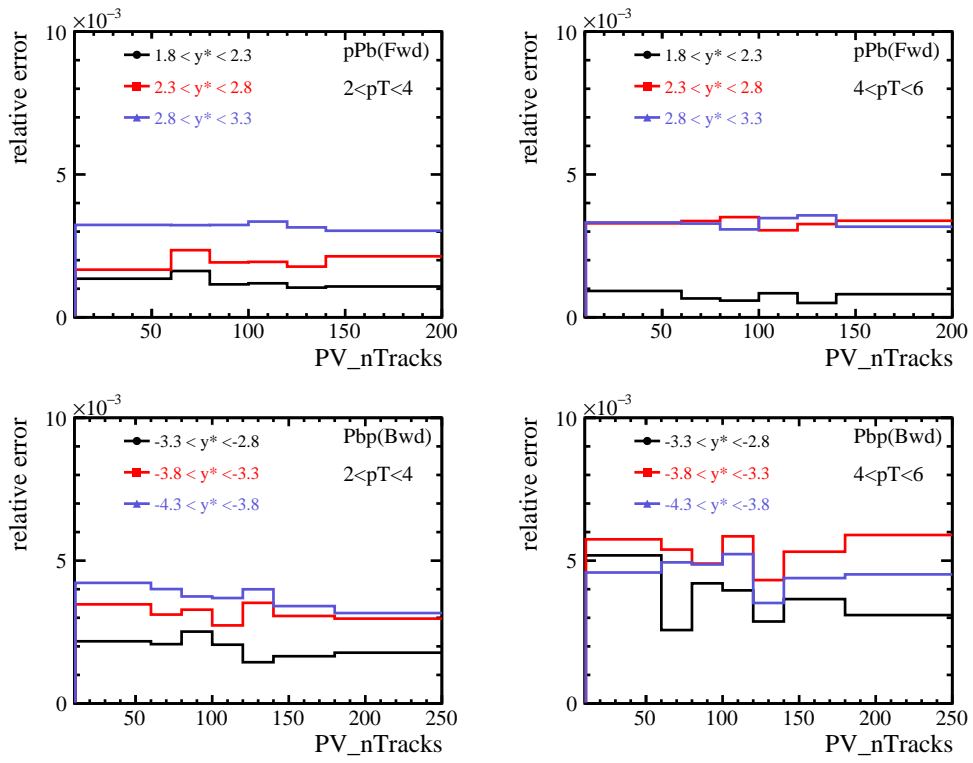


Figure 6.8 The relative systematic uncertainties from ratio of $\epsilon_{\text{rec\&sel}}(D^+/D_s^+)$ as a function of p_T and y^* and PV nTracks. Up for Fwd and Down for Bwd.

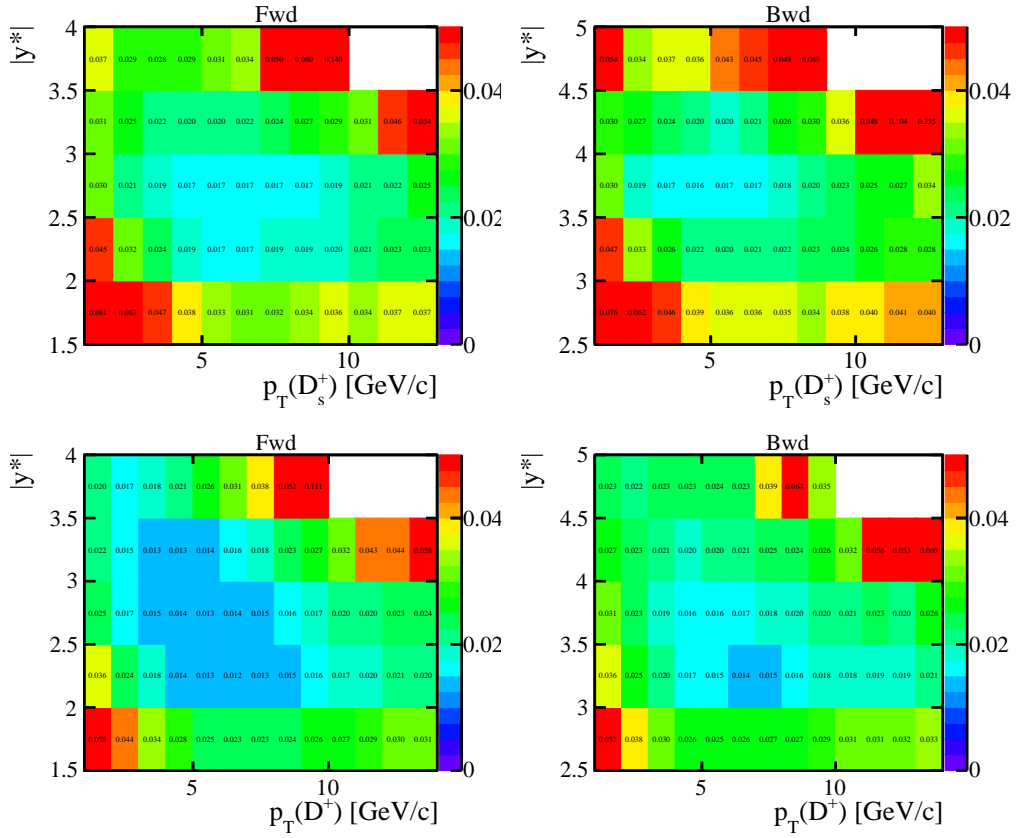


Figure 6.9 Relative systematic uncertainties from PID table as a function of p_T and y^* (display with decimal). Fwd(left), Bwd(right), D_s^+ (up), D^+ (down).

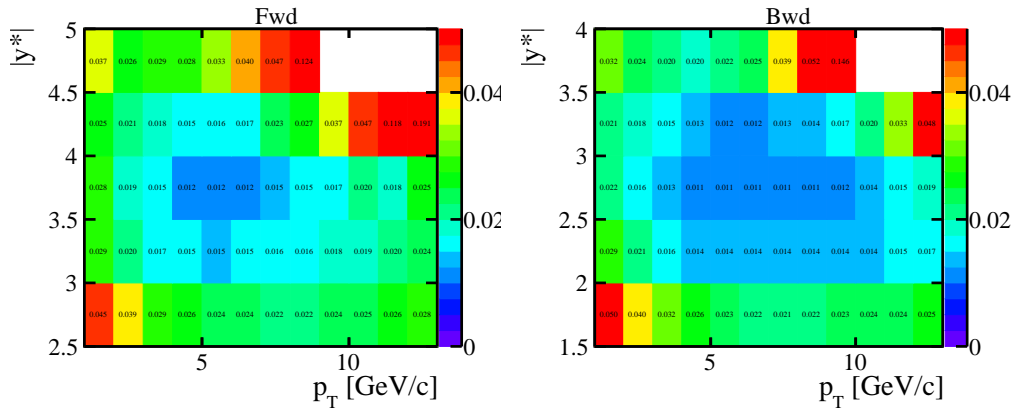


Figure 6.10 The relative systematic uncertainties from ratio of $\epsilon_{\text{PID}}(D^+/D_s^+)$ as a function of p_T and y^* (display with decimal). Left for Fwd and Right for Bwd.

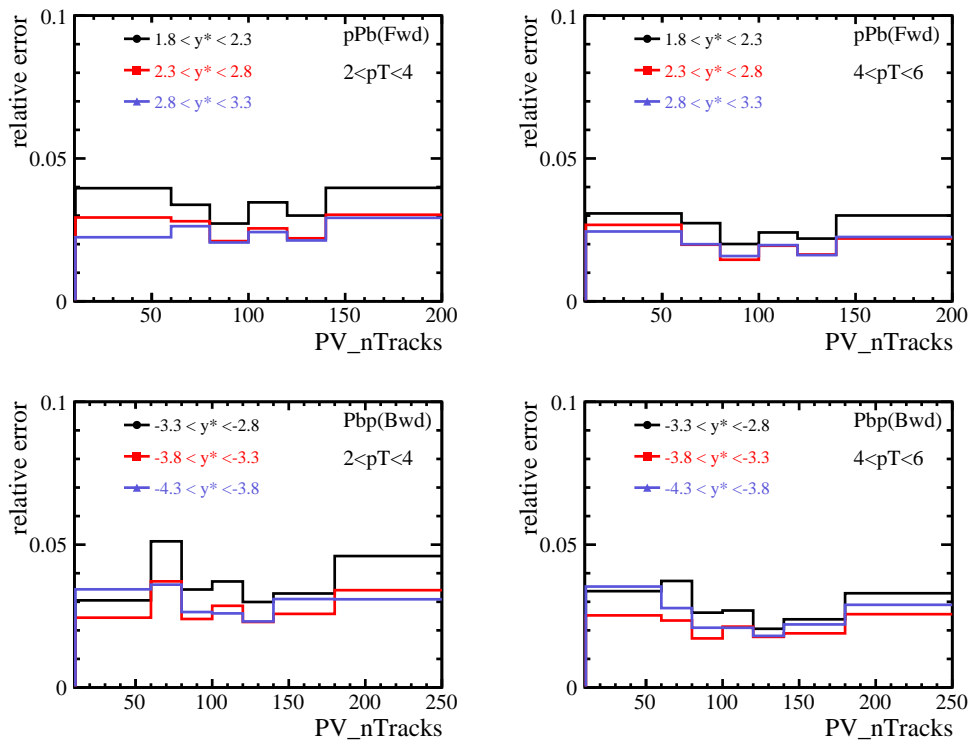


Figure 6.11 The relative systematic uncertainties from ratio of $\epsilon_{PID}(D^+/D_s^+)$ as a function of p_T and y^* and PV nTracks. Up for Fwd and Down for Bwd.

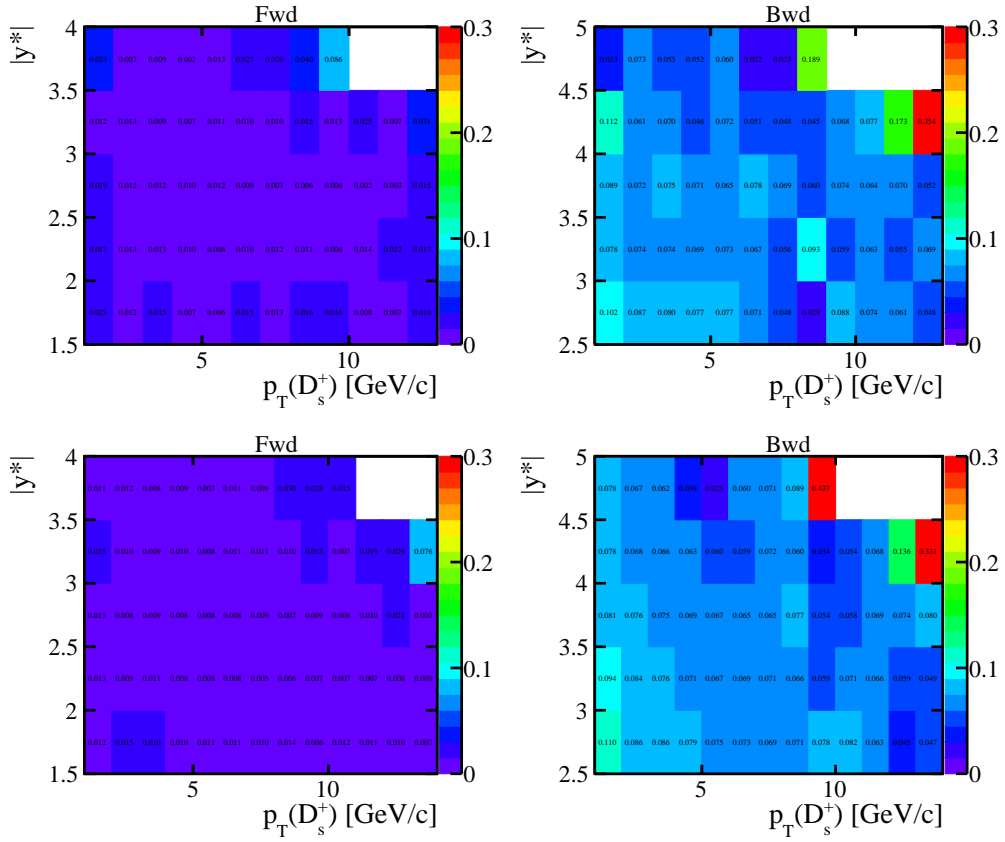


Figure 6.12 The relative systematic uncertainties from multiplicity correction as a function of p_T and y^* (display with decimal). Fwd(left) ,Bwd(right) , D_s^+ (up) , D_s^- (down).

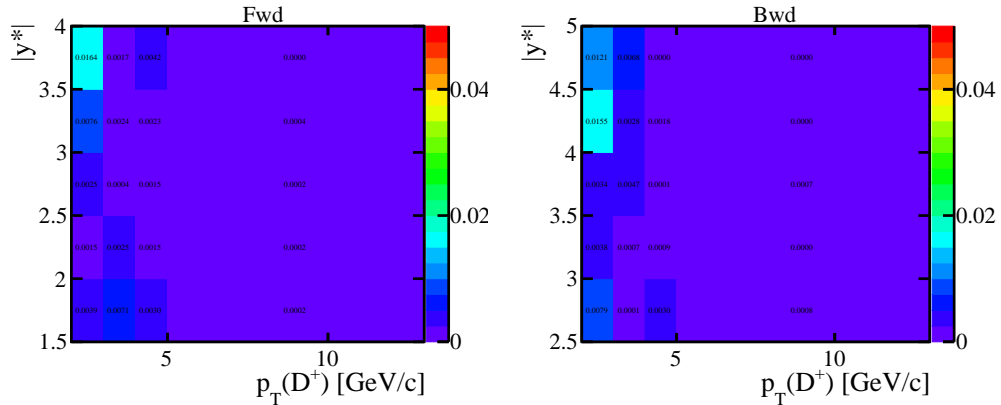


Figure 6.13 Relative systematic uncertainties from trigger efficiencies as a function of p_T and y^* (display with decimal). Left for Fwd and Right for Bwd.

CHAPTER 7 RESULTS AND DISCUSSION

7.1 Production cross-section

The double-differential cross-section of prompt D_s^+ (D^+) mesons can be obtained with Eqs. 3.1 and 3.2. The yields, integrated luminosities, efficiencies and branching fractions have been presented in previous chapters. The measured values of the double-differential cross-section of prompt D_s^+ (D^+) mesons in proton-lead collisions at $\sqrt{s_{\text{NN}}} = 8.16$ TeV in the forward and backward regions as a function of p_{T} and y^* are given in Tabs. 7.1 and 7.2 and shown in Fig. 7.1. The one-dimensional differential prompt D_s^+ (D^+) meson cross-sections as a function of p_{T} or y^* are given in Tabs. 7.3, 7.4, 7.5, and 7.6, and displayed in Figs. 7.2 and 7.3.

The integrated cross-sections of prompt D_s^+ (D^+) meson production in $p\text{Pb}$ collisions at $\sqrt{s_{\text{NN}}} = 8.16$ TeV in the defined forward fiducial regions, summing over all the measured bins, are:

$$\begin{aligned}\sigma(D_s^+)_{\text{forward}}(1 < p_{\text{T}} < 13 \text{ GeV}/c, 1.5 < y^* < 4.0) &= 42.8 \pm 0.3(\text{stat.}) \pm 3.5(\text{syst.}) \text{ mb}, \\ \sigma(D_s^+)_{\text{forward}}(1 < p_{\text{T}} < 13 \text{ GeV}/c, 2.5 < y^* < 4.0) &= 23.7 \pm 0.2(\text{stat.}) \pm 1.8(\text{syst.}) \text{ mb}, \\ \sigma(D^+)_{\text{forward}}(1 < p_{\text{T}} < 14 \text{ GeV}/c, 1.5 < y^* < 4.0) &= 94.0 \pm 0.2(\text{stat.}) \pm 5.0(\text{syst.}) \text{ mb}, \\ \sigma(D^+)_{\text{forward}}(1 < p_{\text{T}} < 14 \text{ GeV}/c, 2.5 < y^* < 4.0) &= 49.7 \pm 0.1(\text{stat.}) \pm 2.5(\text{syst.}) \text{ mb}.\end{aligned}$$

The integrated cross-sections of prompt D_s^+ (D^+) meson production in $p\text{Pb}$ collisions at $\sqrt{s_{\text{NN}}} = 8.16$ TeV in the defined backward fiducial regions, summing over all the measured bins, are:

$$\begin{aligned}\sigma(D_s^+)_{\text{backward}}(1 < p_{\text{T}} < 13 \text{ GeV}/c, -5.0 < y^* < -2.5) &= 43.0 \pm 0.4(\text{stat.}) \pm 4.9(\text{syst.}) \text{ mb}, \\ \sigma(D_s^+)_{\text{backward}}(1 < p_{\text{T}} < 13 \text{ GeV}/c, -4.0 < y^* < -2.5) &= 31.0 \pm 0.3(\text{stat.}) \pm 3.6(\text{syst.}) \text{ mb}, \\ \sigma(D^+)_{\text{backward}}(1 < p_{\text{T}} < 14 \text{ GeV}/c, -5.0 < y^* < -2.5) &= 86.1 \pm 0.2(\text{stat.}) \pm 8.6(\text{syst.}) \text{ mb}, \\ \sigma(D^+)_{\text{backward}}(1 < p_{\text{T}} < 14 \text{ GeV}/c, -4.0 < y^* < -2.5) &= 62.1 \pm 0.1(\text{stat.}) \pm 6.4(\text{syst.}) \text{ mb}.\end{aligned}$$

In the above cross-sections, the first error is statistical and the second one is systematic error.

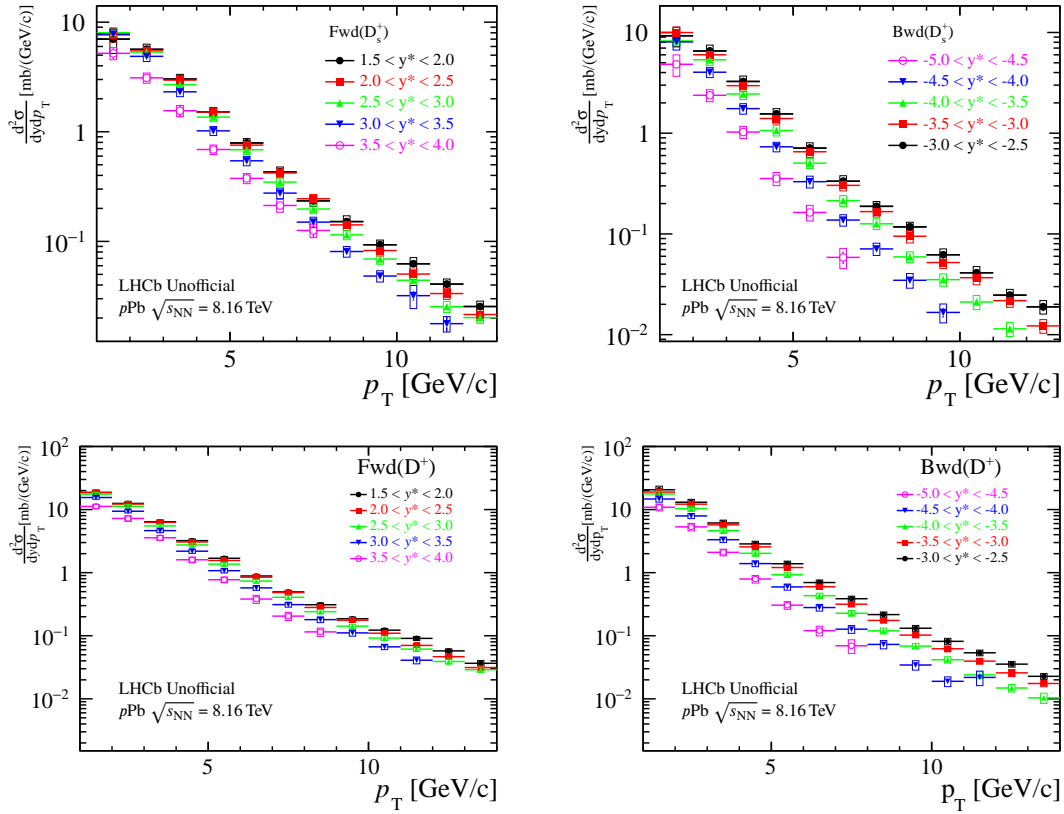


Figure 7.1 Double differential cross-sections of prompt D_s^+ (up) and D^+ (down) in $p\text{Pb}$ collisions at $\sqrt{s_{\text{NN}}} = 8.16$ TeV in the forward (left) and backward (right) rapidity regions. The vertical bar and the vertical box on each data point represent statistical uncertainty and systematic uncertainty respectively.

7.2 Nuclear modification factor

According to Eq. 3.4, the D^+ and D_s^+ production cross-sections in pp collisions at $\sqrt{s} = 8.16$ TeV are needed as reference to calculate the nuclear modification factor $R_{p\text{Pb}}$. Due to the lack of experimental measurements at this particular energy, the reference cross-sections are obtained from the interpolations of the LHCb measurements at $\sqrt{s} = 5$ TeV^[140] and 13 TeV^[141], within a rapidity range of $2.0 < y^* < 4.5$. The D^+ branching fraction used at $\sqrt{s} = 5$ TeV and 13 TeV is 9.13%, while the latest PDG value of 9.38% is used in this thesis. Therefore, the pp cross-sections are re-scaled accordingly to be consistent with this thesis. The default analytical function used for pp cross-section interpolation is the power-law function, as in D^0 measurement^[142].

$$\sigma_{pp} = p_0(\sqrt{s})^{p_1}. \quad (7.1)$$

The typical D_s^+ and D^+ interpolation results are shown in Fig. 7.4, and the full D_s^+ and D^+ interpolation results for each kinematic bin can be found in Appxs. E.1 and E.2 respectively. The uncertainties in the interpolation is calculated with the error propagation

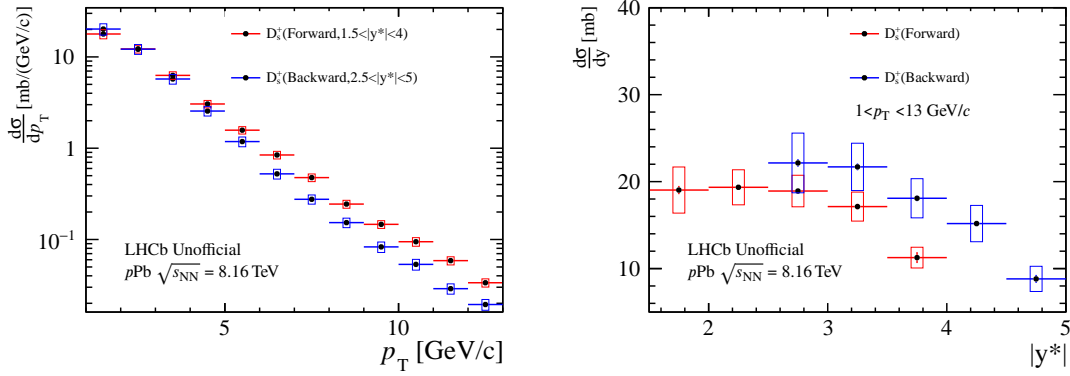


Figure 7.2 Differential cross-section of prompt D_s^+ mesons in $p\text{Pb}$ collisions at $\sqrt{s_{\text{NN}}} = 8.16$ TeV as a function of p_T (left) and y^* (right) in the forward and backward regions. The vertical bar and the vertical box on each data point represent statistical uncertainty and systematic uncertainty respectively.

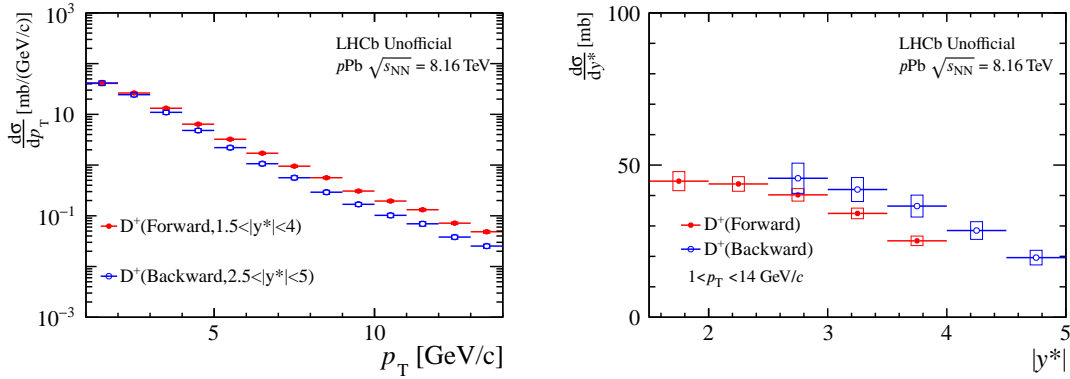


Figure 7.3 Differential cross-section of prompt D^+ mesons in $p\text{Pb}$ collisions at $\sqrt{s_{\text{NN}}} = 8.16$ TeV as a function of p_T (left) and y^* (right) in the forward and backward regions. The vertical bar and the vertical box on each data point represent statistical uncertainty and systematic uncertainty respectively.

formula. Alternatively, the linear function is also considered for the interpolation. The difference with the default interpolation result is taken as an additional systematic uncertainty for $R_{p\text{Pb}}$. The systematic uncertainties from hadronic interaction material budget and branching fraction are correlated between the $\sqrt{s} = 5$ and 13 TeV pp measurements and the $\sqrt{s_{\text{NN}}} = 8.16$ TeV $p\text{Pb}$ measurements. Therefore, they are completely canceled out when calculating $R_{p\text{Pb}}$.

The nuclear modification factors for prompt D_s^+ and D^+ mesons as a function of p_T (y^*) integrated over y^* (p_T) bins are shown in Figs. 7.5, 7.6, 7.7, and 7.8, and the values are listed in Tabs. 7.7, 7.8, 7.9, 7.10, 7.11, and 7.12. The corresponding $R_{p\text{Pb}}$ values for prompt D_s^+ and D^+ mesons as a function of p_T in each y^* bin are also shown in Figs. 7.9, 7.10, 7.11, 7.12 and listed in Tabs. 7.13, 7.14. Both the D_s^+ and D^+ $R_{p\text{Pb}}$ results at forward rapidities show clearly a significant suppression at low p_T , similar to the previous D^0 measurements, confirming the existence of cold nuclear matter effects

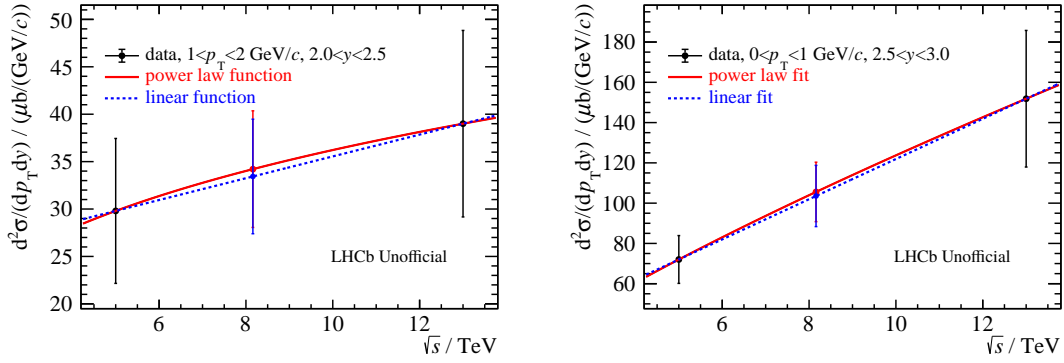


Figure 7.4 The typical interpolation results for D_s^+ (left) and D^+ (right) cross-sections in pp collisions at $\sqrt{s} = 8.16$ TeV with a power-law function and a linear function. The black data points are LHCb result at $\sqrt{s} = 5$ and 13 TeV.

in charm production in proton-lead collisions. In backward rapidities, the R_{pPb} of both particles show a moderate p_T dependence in the measured p_T range, but the overall values slightly increase with the increasing $|y^*|$ to a value close to unity at $y^* = -4.25$.

The R_{pPb} results are compared to the theoretical calculations from the HELAC-Onia generator^{[143] [144]}. It is based on a data-driven parton scattering model. First, the calculation is adjusted according to the cross-section measured in pp collisions at the LHC. Then, the PDFs of nucleon binding in lead nucleus are introduced into the model to calculate the cross-section of pPb collisions, and other cold and hot nuclear matter effects are not considered. The reweighted EPPS16^[58] and nCTEQ15^[62] nPDF sets are used in the calculation. In these new nPDFs, the LHC heavy flavor hadrons results are included by performing Bayesian-reweighting analysis^[145], which greatly reduces the nPDFs uncertainty at low x and hence the uncertainties in the HELAC-Onia calculations. The main uncertainty is determined by the parameterization of nPDFs which corresponds to the 68% confidence band. At forward region, these nPDF theoretical calculations are in good agreement with the data. At backward region, the nPDF calculations can still describe data well at low p_T , but it becomes systematically higher than the data at higher p_T ($p_T > 6$ GeV/c), in particular for D^+ .

In the saturated region (small x), corresponding to $p_T < 5$ GeV/c at forward rapidity, Color Glass Condensate (CGC) theoretical calculations are also included for comparisons. The CGC1^{[146] [69]} calculates D mesons production with the color dipole formalism, the optical Glauber model is used to relate the initial condition of a nucleus with a proton, and does not distinguish D_s^+ and D^+ . The CGC2^[147] calculates D^+ production based on the color dipole formalism and heavy-quark fragmentation function, but can not calculate D_s^+

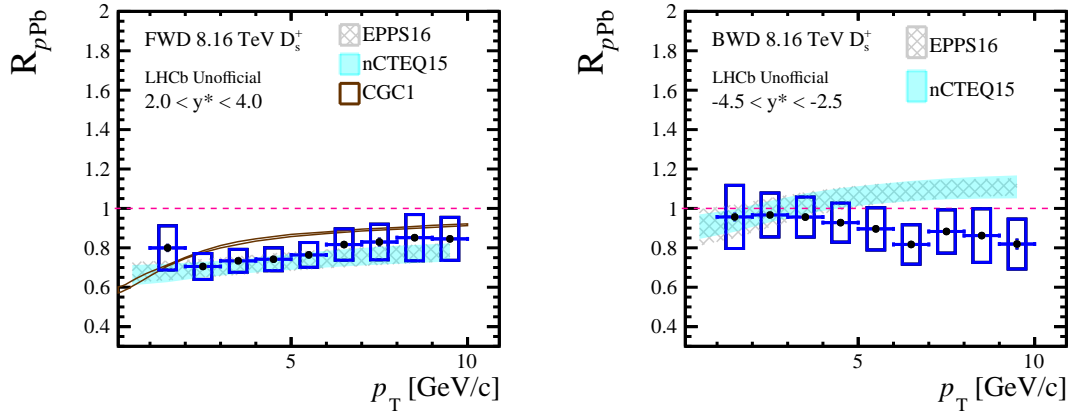


Figure 7.5 Nuclear modification factor R_{pPb} as a function of p_T for prompt D_s^+ mesons in the (left) forward data and (right) backward data, integrated over the common rapidity ranges with the pp reference. The vertical bar and the vertical box on each data point represent statistical and systematic uncertainty respectively. The coloured bands denote the theoretical calculations using the HELAC-Onia generator, incorporating the nPDFs of EPPS16 (grey) and nCTEQ15 (cyan). The brown box (which looks like a line) represents the CGC1 calculations.

yet. In forward rapidity, both the CGC1 and CGC2 calculations are in good agreement with data points within uncertainties. The uncertainty band for CGC1 is very small, since CGC1 only contains the variation of charm quark masses and factorisation scale, which are largely canceled in the ratio of cross-sections versus p_T .

In Figs. 7.13 and 7.14, the D_s^+ and D^+ R_{pPb} results are compared with those of D^0 which have also been measured in pPb collisions at $\sqrt{s_{NN}} = 8.16$ TeV^[142]. These results are almost consistent with each other within uncertainties. The slight difference seen in the forward rapidities in Fig. 7.14 is due to the fact that p_T of D^0 is measured down to 0 GeV/c. These data can also be compared with the R_{pPb} results of D mesons from ALICE (shown in Fig. 7.15^[48]), which is measured in pPb collisions at $\sqrt{s_{NN}} = 5.02$ TeV. It is worth noting that ALICE measures the D meson productions in the central rapidity region, while LHCb measures at the forward/backward rapidity intervals. Nevertheless, the LHCb results seem to be consistent with the ALICE measurements within uncertainties.

7.3 Forward-backward ratio

The forward to backward ratio, R_{FB} , is obtained from Eq. 3.5 which is calculated in the common rapidity region ($2.5 < |y^*| < 4$). Unlike R_{pPb} , R_{FB} does not require pp measurements as a reference, which contributes most of the systematic uncertainty in R_{pPb} . The uncertainties from the branching fraction and tracking efficiencies, PID efficiency are considered fully correlated, while the uncertainties from the signal yield and

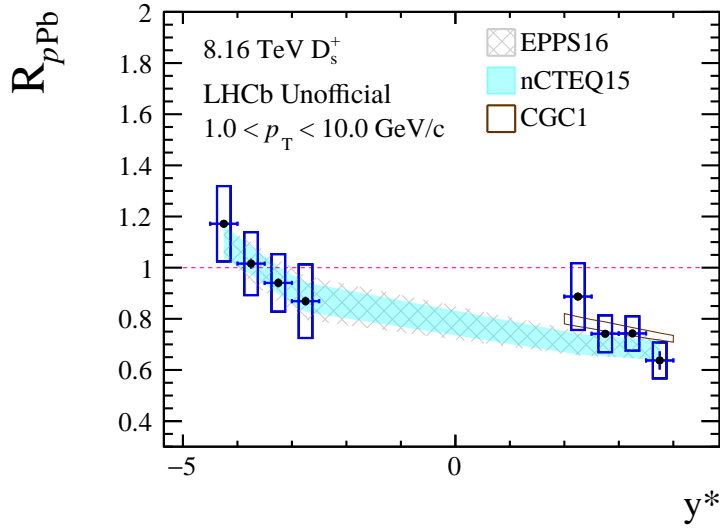


Figure 7.6 Nuclear modification factor R_{pPb} as a function of rapidity for prompt D_s^+ mesons, integrated over $1 < p_T < 10$ GeV/c. The vertical bar and the vertical box on each data point represent statistical and systematic uncertainty respectively. The coloured bands denote the theoretical calculations using the HELAC-Onia generator, incorporating the nPDFs of EPPS16 (grey) and nCTEQ15 (cyan). The brown box at forward rapidities represents the CGC1 calculations.

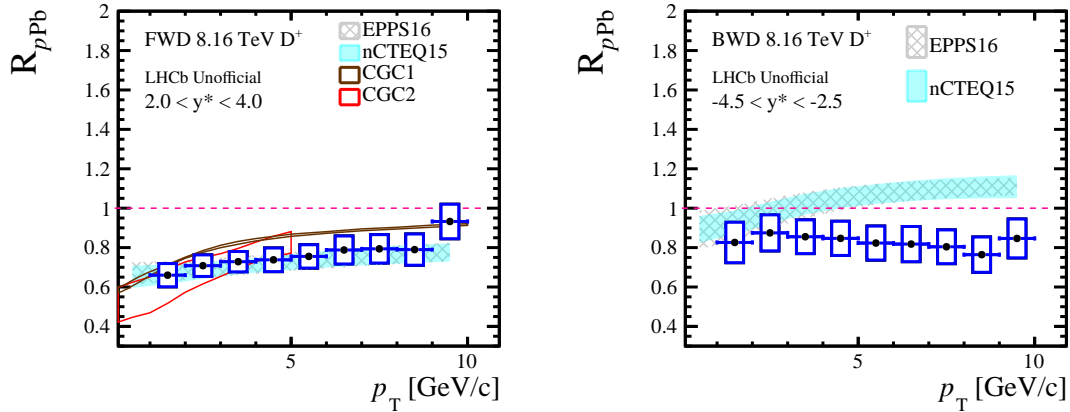


Figure 7.7 Nuclear modification factor R_{pPb} as a function of p_T for prompt D^+ mesons in the (left) forward data and (right) backward data, integrated over the common rapidity ranges with the pp reference. The vertical bar and the vertical box on each data point represent statistical and systematic uncertainty respectively. The coloured bands denote the theoretical calculations using the HELAC-Onia generator, incorporating the nPDFs of EPPS16 (grey) and nCTEQ15 (cyan). The brown box (which looks like a line) represents the CGC1 calculations and the red box denotes the CGC2 calculations.

the simulation sample size are uncorrelated. The values of R_{FB} as a function of p_T ($|y^*|$) are shown in Figs. 7.16 and 7.17 for D_s^+ and D^+ respectively, and listed in Tabs. 7.15 and 7.16. The coloured bands show the HELAC-Onia theoretical calculations, incorporating the nPDFs of EPPS16 and nCTEQ15. In this calculation, the D_s^+ and D_s^- cross-sections in pPb collisions is parameterised using the measured LHC pp data and the nPDFs are used to account for the nuclear matter effects^{[145] [148]}. The uncertainty in the theoretical

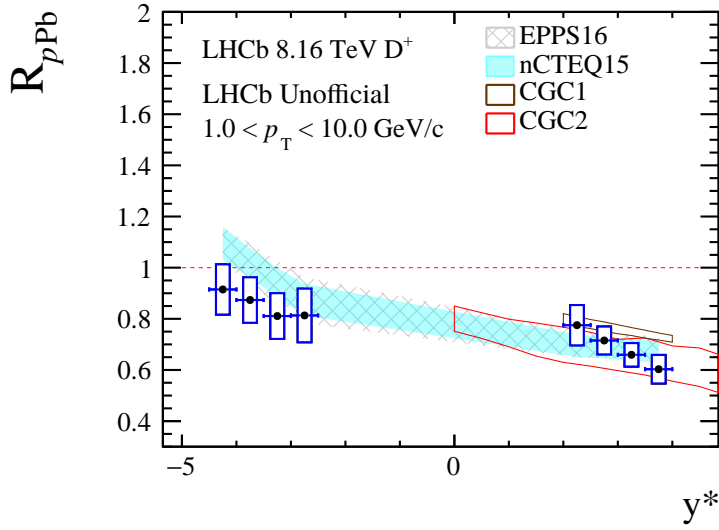


Figure 7.8 Nuclear modification factor R_{pPb} as a function of rapidity for prompt D^+ mesons, integrated over $1 < p_T < 10 \text{ GeV}/c$. The vertical bar and the vertical box on each data point represent statistical and systematic uncertainty respectively. The coloured bands denote the theoretical calculations using the HELAC-Onia generator, incorporating the nPDFs of EPPS16 (grey) and nCTEQ15 (cyan). The brown and red boxes at forward rapidities represent the CGC1 and CGC2 calculations, respectively.

calculation is dominated by the uncertainty of the nPDFs.

In the left of Figs. 7.16 and 7.17, the data points are in good agreement with the theoretical predictions at low p_T and below unity. This suppression at forward rapidity compared to the backward ones (also shown in the right of Figs. 7.16 and 7.17, in particular for $|y^*| > 3.5$) suggests the presence of cold nuclear matter effects. But the data also show a clear rising trend towards high p_T . Since the cross-section of high p_T is small compared to that at low p_T , this difference is not visible in the right of Figs. 7.16 and 7.17. We use $\chi = \sqrt{\frac{(n_{data} - n_{theory})^2}{\sigma_{data}^2 + \sigma_{theory}^2}}$ to test the consistency of data and theory. The overall deviation from EPPS16 by $7.3\sigma(D_s^+)$ and $10.0\sigma(D^+)$. This difference originates from the suppression (compared to the nPDF calculations) at high p_T in R_{pPb} in the backward rapidity region. The underlying physics mechanism which causes this extra high p_T charm hadron suppression at backward rapidity need further theory and experimental investigations.

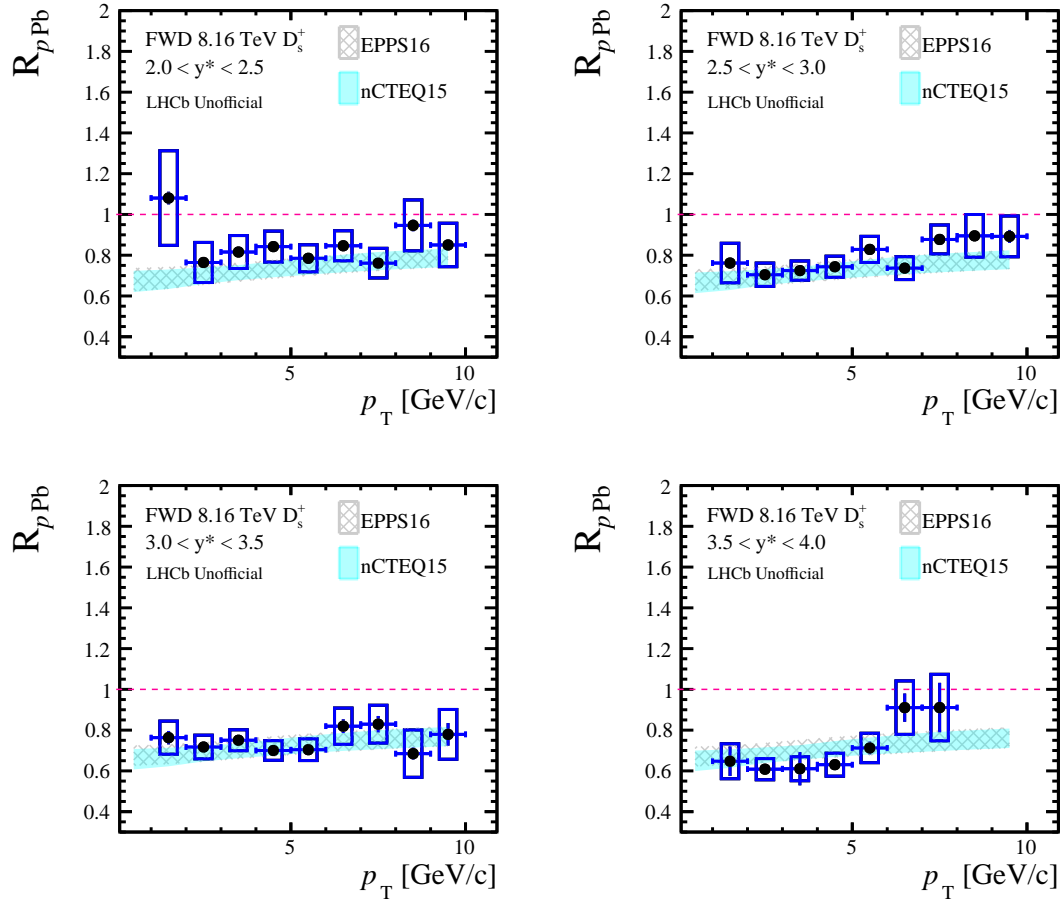


Figure 7.9 Prompt D_s^+ nuclear modification factor R_{pPb} as a function of p_T in different forward y^* bins. The vertical bar and the vertical box on each data point represent statistical and systematic uncertainty respectively. The coloured bands denote the theoretical calculations using the HELAC-Onia generator, incorporating the nPDFs of EPPS16 (grey) and nCTEQ15 (cyan).

Table 7.1 Double differential cross-section $\frac{d^2\sigma}{dp_T dy^*}$ mb/(GeV/c) for prompt D_s^+ as functions of p_T and y^* in pPb collisions at $\sqrt{s_{NN}} = 8.16$ TeV. The first error is statistical, the second one is the systematic uncertainty that is uncorrelated between bins, and the third one is the correlated systematic error.

p_T [GeV/c] y^*	Forward(mb (GeV/c))				
	[1.5, 2]	[2, 2.5]	[2.5, 3]	[3, 3.5]	[3.5, 4]
[1, 2]	7.006 ± 0.422 ± 1.613 ± 0.861	7.658 ± 0.220 ± 0.745 ± 0.775	8.021 ± 0.270 ± 0.441 ± 0.763	7.770 ± 0.334 ± 0.389 ± 0.733	5.197 ± 0.583 ± 0.378 ± 0.536
[2, 3]	5.653 ± 0.156 ± 0.157 ± 0.625	5.464 ± 0.049 ± 0.244 ± 0.520	5.337 ± 0.048 ± 0.187 ± 0.485	4.877 ± 0.073 ± 0.212 ± 0.456	3.105 ± 0.093 ± 0.149 ± 0.296
[3, 4]	3.027 ± 0.120 ± 0.051 ± 0.310	2.961 ± 0.042 ± 0.094 ± 0.273	2.694 ± 0.026 ± 0.034 ± 0.245	2.314 ± 0.032 ± 0.064 ± 0.215	1.556 ± 0.208 ± 0.106 ± 0.149
[4, 5]	1.518 ± 0.029 ± 0.026 ± 0.147	1.514 ± 0.020 ± 0.020 ± 0.137	1.362 ± 0.015 ± 0.030 ± 0.123	1.020 ± 0.024 ± 0.013 ± 0.095	0.689 ± 0.028 ± 0.017 ± 0.066
[5, 6]	0.791 ± 0.085 ± 0.017 ± 0.075	0.755 ± 0.014 ± 0.012 ± 0.068	0.686 ± 0.010 ± 0.014 ± 0.062	0.543 ± 0.011 ± 0.016 ± 0.051	0.376 ± 0.016 ± 0.014 ± 0.037
[6, 7]	0.429 ± 0.012 ± 0.026 ± 0.041	0.421 ± 0.005 ± 0.011 ± 0.038	0.347 ± 0.006 ± 0.008 ± 0.031	0.276 ± 0.011 ± 0.015 ± 0.026	0.213 ± 0.016 ± 0.018 ± 0.022
[7, 8]	0.235 ± 0.008 ± 0.012 ± 0.022	0.245 ± 0.005 ± 0.007 ± 0.022	0.197 ± 0.005 ± 0.004 ± 0.018	0.150 ± 0.007 ± 0.008 ± 0.014	0.126 ± 0.017 ± 0.011 ± 0.014
[8, 9]	0.152 ± 0.011 ± 0.013 ± 0.014	0.141 ± 0.004 ± 0.010 ± 0.013	0.115 ± 0.003 ± 0.004 ± 0.010	0.081 ± 0.004 ± 0.004 ± 0.008	-
[9, 10]	0.093 ± 0.008 ± 0.004 ± 0.009	0.083 ± 0.002 ± 0.005 ± 0.008	0.069 ± 0.002 ± 0.003 ± 0.006	0.048 ± 0.003 ± 0.003 ± 0.005	-
[10, 11]	0.063 ± 0.003 ± 0.006 ± 0.006	0.050 ± 0.002 ± 0.003 ± 0.005	0.044 ± 0.002 ± 0.002 ± 0.004	0.032 ± 0.003 ± 0.007 ± 0.003	-
[11, 12]	0.041 ± 0.002 ± 0.002 ± 0.004	0.033 ± 0.001 ± 0.002 ± 0.003	0.025 ± 0.001 ± 0.002 ± 0.002	0.018 ± 0.003 ± 0.002 ± 0.002	-
[12, 13]	0.025 ± 0.001 ± 0.002 ± 0.002	0.022 ± 0.002 ± 0.002 ± 0.002	0.020 ± 0.002 ± 0.001 ± 0.002	-	-

p_T [GeV/c] y^*	Backward(mb (GeV/c))		
	[-3, -2.5]	[-3.5, -3]	[-4, -3.5]
[1, 2]	9.278 ± 0.410 ± 1.364 ± 1.446	9.981 ± 0.361 ± 0.477 ± 1.269	8.240 ± 0.334 ± 0.392 ± 1.070
[2, 3]	6.553 ± 0.128 ± 0.205 ± 0.913	6.009 ± 0.135 ± 0.244 ± 0.726	5.355 ± 0.054 ± 0.125 ± 0.626
[3, 4]	3.264 ± 0.032 ± 0.101 ± 0.420	2.965 ± 0.071 ± 0.047 ± 0.356	2.449 ± 0.043 ± 0.043 ± 0.289
[4, 5]	1.556 ± 0.037 ± 0.034 ± 0.194	1.399 ± 0.015 ± 0.026 ± 0.165	1.063 ± 0.022 ± 0.022 ± 0.122
[5, 6]	0.712 ± 0.021 ± 0.022 ± 0.089	0.654 ± 0.008 ± 0.020 ± 0.079	0.504 ± 0.007 ± 0.011 ± 0.056
[6, 7]	0.334 ± 0.014 ± 0.018 ± 0.041	0.304 ± 0.004 ± 0.008 ± 0.036	0.214 ± 0.005 ± 0.007 ± 0.026
[7, 8]	0.188 ± 0.005 ± 0.006 ± 0.021	0.167 ± 0.004 ± 0.006 ± 0.019	0.126 ± 0.003 ± 0.005 ± 0.015
[8, 9]	0.117 ± 0.004 ± 0.005 ± 0.012	0.095 ± 0.002 ± 0.005 ± 0.013	0.059 ± 0.005 ± 0.003 ± 0.007
[9, 10]	0.062 ± 0.003 ± 0.003 ± 0.008	0.052 ± 0.002 ± 0.003 ± 0.006	0.035 ± 0.001 ± 0.002 ± 0.004
[10, 11]	0.041 ± 0.002 ± 0.003 ± 0.005	0.037 ± 0.001 ± 0.003 ± 0.004	0.021 ± 0.001 ± 0.002 ± 0.003
[11, 12]	0.025 ± 0.001 ± 0.002 ± 0.003	0.022 ± 0.001 ± 0.002 ± 0.003	0.011 ± 0.001 ± 0.001 ± 0.001
[12, 13]	0.019 ± 0.002 ± 0.002 ± 0.002	0.012 ± 0.001 ± 0.001 ± 0.002	0.008 ± 0.001 ± 0.001 ± 0.001

Table 7.2 Double differential cross-section $\frac{d^2\sigma}{dp_T dy^*}$ mb/(GeV/c) for prompt D^+ as functions of p_T and y^* in pPb collisions at $\sqrt{s_{NN}} = 8.16$ TeV. The first error is statistical, the second one is the systematic uncertainty that is uncorrelated between bins, and the third one is the correlated systematic error.

p_T [GeV/c] y^*	Forward(mb (GeV/c))				
	[1., 5.]	[2., 2.5]	[2.5, 3]	[3., 3.5]	[3.5, 4]
[1, 2]	18.699 ± 0.312 ± 0.901 ± 1.515	18.592 ± 0.096 ± 0.569 ± 1.222	17.575 ± 0.021 ± 0.613 ± 1.025	15.523 ± 0.081 ± 0.444 ± 0.896	11.221 ± 0.110 ± 0.642 ± 0.642
[2, 3]	12.519 ± 0.061 ± 0.373 ± 0.908	12.254 ± 0.025 ± 0.358 ± 0.715	11.278 ± 0.084 ± 0.380 ± 0.611	9.407 ± 0.027 ± 0.265 ± 0.517	7.243 ± 0.035 ± 0.624 ± 0.410
[3, 4]	6.410 ± 0.025 ± 0.174 ± 0.423	6.281 ± 0.014 ± 0.177 ± 0.349	5.504 ± 0.010 ± 0.143 ± 0.295	4.638 ± 0.011 ± 0.235 ± 0.253	3.570 ± 0.021 ± 0.250 ± 0.202
[4, 5]	3.215 ± 0.014 ± 0.087 ± 0.195	3.062 ± 0.005 ± 0.156 ± 0.163	2.747 ± 0.009 ± 0.105 ± 0.147	2.189 ± 0.008 ± 0.118 ± 0.120	1.600 ± 0.014 ± 0.136 ± 0.094
[5, 6]	1.691 ± 0.008 ± 0.048 ± 0.098	1.561 ± 0.005 ± 0.047 ± 0.083	1.363 ± 0.005 ± 0.062 ± 0.073	1.075 ± 0.005 ± 0.063 ± 0.059	0.772 ± 0.009 ± 0.066 ± 0.047
[6, 7]	0.885 ± 0.018 ± 0.024 ± 0.051	0.848 ± 0.004 ± 0.042 ± 0.045	0.735 ± 0.004 ± 0.031 ± 0.040	0.574 ± 0.004 ± 0.037 ± 0.032	0.382 ± 0.015 ± 0.050 ± 0.025
[7, 8]	0.495 ± 0.005 ± 0.015 ± 0.028	0.484 ± 0.003 ± 0.017 ± 0.026	0.407 ± 0.002 ± 0.019 ± 0.022	0.311 ± 0.003 ± 0.021 ± 0.018	0.205 ± 0.008 ± 0.027 ± 0.014
[8, 9]	0.310 ± 0.000 ± 0.013 ± 0.018	0.281 ± 0.002 ± 0.009 ± 0.015	0.241 ± 0.002 ± 0.011 ± 0.013	0.180 ± 0.003 ± 0.015 ± 0.011	0.115 ± 0.010 ± 0.014 ± 0.010
[9, 10]	0.186 ± 0.000 ± 0.007 ± 0.011	0.176 ± 0.001 ± 0.007 ± 0.010	0.142 ± 0.002 ± 0.007 ± 0.008	0.111 ± 0.002 ± 0.010 ± 0.007	—
[10, 11]	0.123 ± 0.002 ± 0.004 ± 0.007	0.110 ± 0.002 ± 0.004 ± 0.006	0.092 ± 0.001 ± 0.005 ± 0.005	0.067 ± 0.002 ± 0.005 ± 0.004	—
[11, 12]	0.091 ± 0.001 ± 0.004 ± 0.005	0.070 ± 0.001 ± 0.004 ± 0.004	0.061 ± 0.001 ± 0.004 ± 0.004	0.041 ± 0.002 ± 0.004 ± 0.003	—
[12, 13]	0.058 ± 0.001 ± 0.003 ± 0.003	0.047 ± 0.001 ± 0.002 ± 0.003	0.039 ± 0.001 ± 0.003 ± 0.002	—	—
[13, 14]	0.037 ± 0.001 ± 0.003 ± 0.002	0.031 ± 0.001 ± 0.002 ± 0.002	0.029 ± 0.001 ± 0.002 ± 0.002	—	—

p_T [GeV/c] y^*	Backward(mb (GeV/c))		
	[-3., -2.5]	[-3.5, -3]	[-4., -3.5]
[1, 2]	20.606 ± 0.226 ± 0.888 ± 2.744	18.952 ± 0.081 ± 0.574 ± 2.150	17.663 ± 0.067 ± 0.517 ± 1.794
[2, 3]	13.065 ± 0.046 ± 0.388 ± 1.415	12.178 ± 0.023 ± 0.342 ± 1.246	10.356 ± 0.018 ± 0.240 ± 0.983
[3, 4]	6.133 ± 0.019 ± 0.158 ± 0.648	5.735 ± 0.010 ± 0.166 ± 0.543	4.620 ± 0.008 ± 0.141 ± 0.427
[4, 5]	2.854 ± 0.010 ± 0.093 ± 0.282	2.564 ± 0.006 ± 0.066 ± 0.233	2.026 ± 0.006 ± 0.106 ± 0.177
[5, 6]	1.385 ± 0.006 ± 0.043 ± 0.132	1.205 ± 0.002 ± 0.035 ± 0.106	0.926 ± 0.005 ± 0.040 ± 0.080
[6, 7]	0.697 ± 0.007 ± 0.016 ± 0.066	0.599 ± 0.001 ± 0.021 ± 0.054	0.432 ± 0.001 ± 0.018 ± 0.037
[7, 8]	0.386 ± 0.009 ± 0.012 ± 0.036	0.316 ± 0.002 ± 0.010 ± 0.029	0.227 ± 0.001 ± 0.012 ± 0.020
[8, 9]	0.216 ± 0.002 ± 0.007 ± 0.020	0.175 ± 0.001 ± 0.006 ± 0.016	0.120 ± 0.001 ± 0.006 ± 0.012
[9, 10]	0.132 ± 0.001 ± 0.005 ± 0.013	0.102 ± 0.001 ± 0.004 ± 0.009	0.069 ± 0.001 ± 0.004 ± 0.006
[10, 11]	0.082 ± 0.001 ± 0.004 ± 0.008	0.062 ± 0.001 ± 0.003 ± 0.006	0.042 ± 0.001 ± 0.003 ± 0.004
[11, 12]	0.054 ± 0.001 ± 0.003 ± 0.005	0.040 ± 0.001 ± 0.002 ± 0.004	0.024 ± 0.001 ± 0.002 ± 0.002
[12, 13]	0.036 ± 0.001 ± 0.002 ± 0.003	0.026 ± 0.000 ± 0.002 ± 0.002	0.015 ± 0.000 ± 0.001 ± 0.002
[13, 14]	0.023 ± 0.000 ± 0.001 ± 0.002	0.018 ± 0.000 ± 0.001 ± 0.002	0.010 ± 0.000 ± 0.001 ± 0.001

Table 7.3 Differential cross-section $\frac{d\sigma}{dp_T}$ (mb/(GeV/c)) for prompt D_s^+ as a function of p_T at forward ($1.5 < y^* < 4.0$) and backward ($-5.0 < y^* < -2.5$) rapidities in p Pb collisions at $\sqrt{s_{NN}} = 8.16$ TeV. The first error is statistical, the second one is the systematic uncertainty that is uncorrelated between bins, and the third one is the correlated systematic error.

Forward	
p_T [GeV/c]	$\frac{d\sigma}{dp_T}$ [mb/(GeV/c)]
[1, 2]	$17.826 \pm 0.433 \pm 0.955 \pm 1.808$
[2, 3]	$12.218 \pm 0.104 \pm 0.216 \pm 1.177$
[3, 4]	$6.276 \pm 0.123 \pm 0.083 \pm 0.592$
[4, 5]	$3.051 \pm 0.027 \pm 0.025 \pm 0.283$
[5, 6]	$1.576 \pm 0.045 \pm 0.017 \pm 0.146$
[6, 7]	$0.843 \pm 0.012 \pm 0.019 \pm 0.079$
[7, 8]	$0.476 \pm 0.011 \pm 0.010 \pm 0.045$
[8, 9]	$0.244 \pm 0.006 \pm 0.009 \pm 0.023$
[9, 10]	$0.147 \pm 0.005 \pm 0.004 \pm 0.014$
[10, 11]	$0.095 \pm 0.003 \pm 0.005 \pm 0.009$
[11, 12]	$0.059 \pm 0.002 \pm 0.002 \pm 0.006$
[12, 13]	$0.034 \pm 0.002 \pm 0.001 \pm 0.003$
Backward	
p_T [GeV/c]	$\frac{d\sigma}{dp_T}$ [mb/(GeV/c)]
[1, 2]	$20.196 \pm 0.421 \pm 0.975 \pm 2.700$
[2, 3]	$12.163 \pm 0.119 \pm 0.196 \pm 1.490$
[3, 4]	$5.729 \pm 0.050 \pm 0.073 \pm 0.694$
[4, 5]	$2.553 \pm 0.025 \pm 0.029 \pm 0.300$
[5, 6]	$1.182 \pm 0.014 \pm 0.020 \pm 0.143$
[6, 7]	$0.524 \pm 0.009 \pm 0.012 \pm 0.063$
[7, 8]	$0.276 \pm 0.004 \pm 0.005 \pm 0.031$
[8, 9]	$0.153 \pm 0.004 \pm 0.004 \pm 0.018$
[9, 10]	$0.083 \pm 0.002 \pm 0.003 \pm 0.011$
[10, 11]	$0.053 \pm 0.002 \pm 0.003 \pm 0.007$
[11, 12]	$0.029 \pm 0.001 \pm 0.001 \pm 0.003$
[12, 13]	$0.019 \pm 0.001 \pm 0.001 \pm 0.002$

CHAPTER 7 RESULTS AND DISCUSSION

Table 7.4 Differential cross-section $\frac{d\sigma}{dp_T}$ (mb/(GeV/c)) for prompt D^+ as a function of p_T at forward ($1.5 < y^* < 4.0$) and backward ($-5.0 < y^* < -2.5$) rapidities in p Pb collisions at $\sqrt{s_{NN}} = 8.16$ TeV. The first error is statistical, the second one is the systematic uncertainty that is uncorrelated between bins, and the third one is the correlated systematic error.

Forward	
p_T [GeV/c]	$\frac{d\sigma}{dp_T}$ [mb/(GeV/c)]
[1, 2]	$40.806 \pm 0.177 \pm 0.728 \pm 2.327$
[2, 3]	$26.351 \pm 0.058 \pm 0.467 \pm 1.356$
[3, 4]	$13.201 \pm 0.019 \pm 0.223 \pm 0.650$
[4, 5]	$6.407 \pm 0.012 \pm 0.137 \pm 0.305$
[5, 6]	$3.231 \pm 0.007 \pm 0.065 \pm 0.153$
[6, 7]	$1.712 \pm 0.012 \pm 0.042 \pm 0.082$
[7, 8]	$0.951 \pm 0.005 \pm 0.022 \pm 0.046$
[8, 9]	$0.563 \pm 0.005 \pm 0.014 \pm 0.029$
[9, 10]	$0.307 \pm 0.001 \pm 0.008 \pm 0.015$
[10, 11]	$0.195 \pm 0.002 \pm 0.004 \pm 0.010$
[11, 12]	$0.132 \pm 0.001 \pm 0.004 \pm 0.007$
[12, 13]	$0.072 \pm 0.001 \pm 0.002 \pm 0.004$
[13, 14]	$0.048 \pm 0.001 \pm 0.002 \pm 0.003$

Backward	
p_T [GeV/c]	$\frac{d\sigma}{dp_T}$ [mb/(GeV/c)]
[1, 2]	$41.403 \pm 0.166 \pm 0.801 \pm 4.415$
[2, 3]	$24.424 \pm 0.032 \pm 0.413 \pm 2.307$
[3, 4]	$10.956 \pm 0.014 \pm 0.174 \pm 1.007$
[4, 5]	$4.814 \pm 0.009 \pm 0.096 \pm 0.422$
[5, 6]	$2.207 \pm 0.005 \pm 0.042 \pm 0.191$
[6, 7]	$1.064 \pm 0.005 \pm 0.020 \pm 0.094$
[7, 8]	$0.563 \pm 0.006 \pm 0.013 \pm 0.051$
[8, 9]	$0.292 \pm 0.002 \pm 0.007 \pm 0.026$
[9, 10]	$0.168 \pm 0.001 \pm 0.004 \pm 0.015$
[10, 11]	$0.102 \pm 0.001 \pm 0.003 \pm 0.010$
[11, 12]	$0.070 \pm 0.001 \pm 0.003 \pm 0.007$
[12, 13]	$0.038 \pm 0.000 \pm 0.002 \pm 0.003$
[13, 14]	$0.025 \pm 0.000 \pm 0.001 \pm 0.002$

Table 7.5 Differential cross-section $\frac{d\sigma}{dy^*}$ (mb) for prompt D_s^+ as a function of y^* ($1 < p_T < 13$ GeV/c) in p Pb collisions at $\sqrt{s_{NN}} = 8.16$ TeV. The first error is statistical, the second one is the systematic uncertainty that is uncorrelated between bins, and the third one is the correlated systematic error.

Forward	
y^*	$\frac{d\sigma}{dy^*}$ [mb]
[1.5, 2.0]	$19.032 \pm 0.474 \pm 1.622 \pm 2.098$
[2.0, 2.5]	$19.347 \pm 0.231 \pm 0.790 \pm 1.854$
[2.5, 3.0]	$18.918 \pm 0.276 \pm 0.482 \pm 1.749$
[3.0, 3.5]	$17.129 \pm 0.344 \pm 0.449 \pm 1.606$
[3.5, 4.0]	$11.262 \pm 0.627 \pm 0.421 \pm 1.117$
Backward	
y^*	$\frac{d\sigma}{dy^*}$ [mb]
[-2.5, -3.0]	$22.148 \pm 0.434 \pm 1.383 \pm 3.142$
[-3.0, -3.5]	$21.695 \pm 0.392 \pm 0.539 \pm 2.667$
[-3.5, -4.0]	$18.086 \pm 0.342 \pm 0.414 \pm 2.214$
[-4.0, -4.5]	$15.176 \pm 0.329 \pm 0.714 \pm 1.962$
[-4.5, -5.0]	$8.814 \pm 0.459 \pm 1.047 \pm 1.002$

Table 7.6 Differential cross-section $\frac{d\sigma}{dy^*}$ (mb) for prompt D^+ as a function of y^* ($1 < p_T < 14$ GeV/c) in pPb collisions at $\sqrt{s_{NN}} = 8.16$ TeV. The first error is statistical, the second one is the systematic uncertainty that is uncorrelated between bins, and the third one is the correlated systematic error.

Forward	
y^*	$\frac{d\sigma}{dy^*}$ [mb]
[1.5, 2.0]	$44.72 \pm 0.32 \pm 1.00 \pm 2.97$
[2.0, 2.5]	$43.80 \pm 0.10 \pm 0.72 \pm 2.29$
[2.5, 3.0]	$40.21 \pm 0.09 \pm 0.75 \pm 1.91$
[3.0, 3.5]	$34.12 \pm 0.09 \pm 0.59 \pm 1.64$
[3.5, 4.0]	$25.11 \pm 0.12 \pm 0.94 \pm 1.24$
Backward	
y^*	$\frac{d\sigma}{dy^*}$ [mb]
[-3.0, -2.5]	$45.67 \pm 0.23 \pm 0.99 \pm 4.87$
[-3.5, -3.0]	$41.97 \pm 0.08 \pm 0.69 \pm 3.87$
[-4.0, -3.5]	$36.53 \pm 0.07 \pm 0.60 \pm 3.55$
[-4.5, -4.0]	$28.50 \pm 0.21 \pm 0.77 \pm 2.80$
[-5.0, -4.5]	$19.59 \pm 0.07 \pm 1.01 \pm 2.18$

Table 7.7 Nuclear modification factor R_{pPb} for prompt D_s^+ mesons as a function of p_T forward rapidity regions, integrated over the common rapidity region of $2.0 < |y^*| < 4.0$ with pp reference. The first and second errors are statistical and systematic uncertainties, respectively.

p_T [GeV/c]	R_{pPb} (Forward)
[1, 2]	$0.800 \pm 0.021 \pm 0.112$
[2, 3]	$0.705 \pm 0.005 \pm 0.066$
[3, 4]	$0.734 \pm 0.017 \pm 0.058$
[4, 5]	$0.742 \pm 0.007 \pm 0.058$
[5, 6]	$0.764 \pm 0.008 \pm 0.063$
[6, 7]	$0.816 \pm 0.014 \pm 0.080$
[7, 8]	$0.829 \pm 0.022 \pm 0.090$
[8, 9]	$0.852 \pm 0.016 \pm 0.117$
[9, 10]	$0.845 \pm 0.019 \pm 0.109$

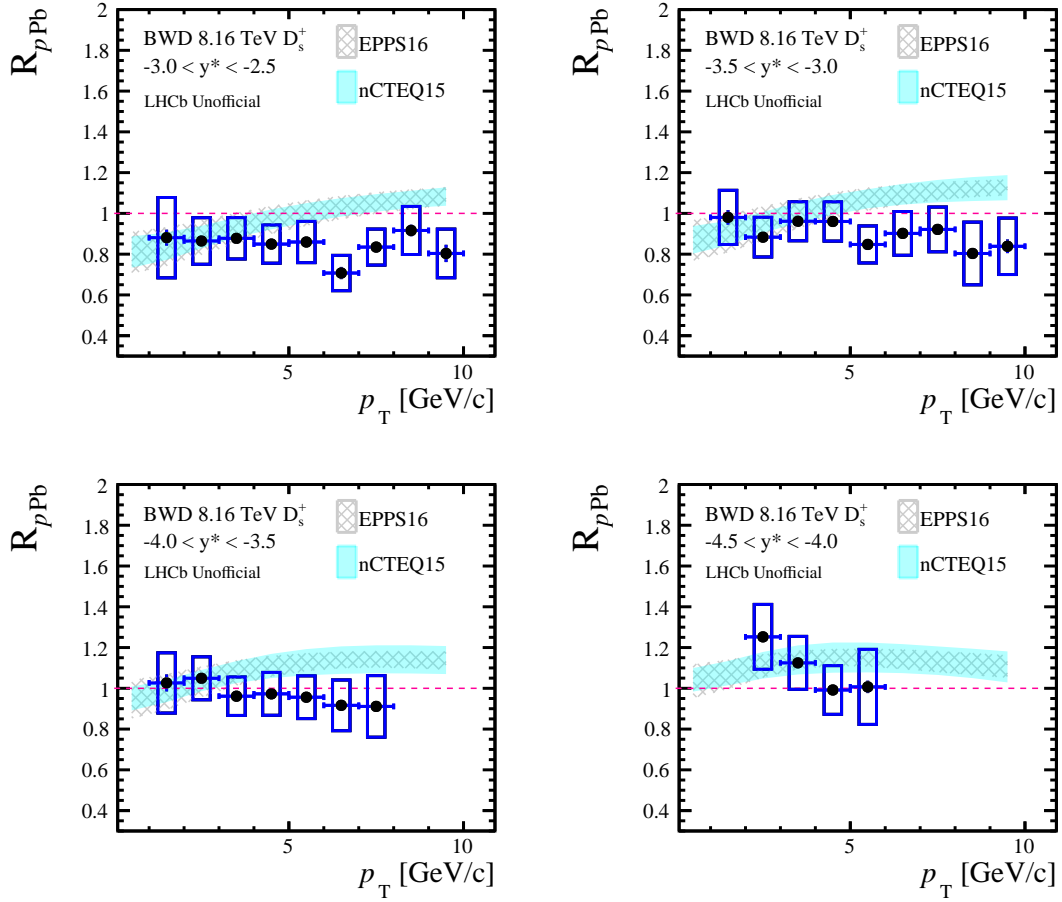


Figure 7.10 Prompt D_s^+ nuclear modification factor R_{pPb} as a function of p_T in different backward y^* bins. The vertical bar and the vertical box on each data point represent statistical and systematic uncertainty respectively. The coloured bands denote the theoretical calculations using the HELAC-Onia generator, incorporating the nPDFs of EPPS16 (grey) and nCTEQ15 (cyan).

Table 7.8 Nuclear modification factor R_{pPb} for prompt D_s^+ mesons as a function of p_T backward rapidity regions, integrated over common rapidity region of $2.5 < |y^*| < 4.5$ with pp reference. The first and second errors are statistical and systematic uncertainties, respectively.

p_T [GeV/c]	$R_{pPb}(\text{Backward})$
[1, 2]	$0.957 \pm 0.022 \pm 0.160$
[2, 3]	$0.967 \pm 0.009 \pm 0.111$
[3, 4]	$0.956 \pm 0.008 \pm 0.101$
[4, 5]	$0.928 \pm 0.009 \pm 0.099$
[5, 6]	$0.896 \pm 0.010 \pm 0.107$
[6, 7]	$0.817 \pm 0.015 \pm 0.100$
[7, 8]	$0.883 \pm 0.013 \pm 0.110$
[8, 9]	$0.862 \pm 0.018 \pm 0.136$
[9, 10]	$0.819 \pm 0.028 \pm 0.127$

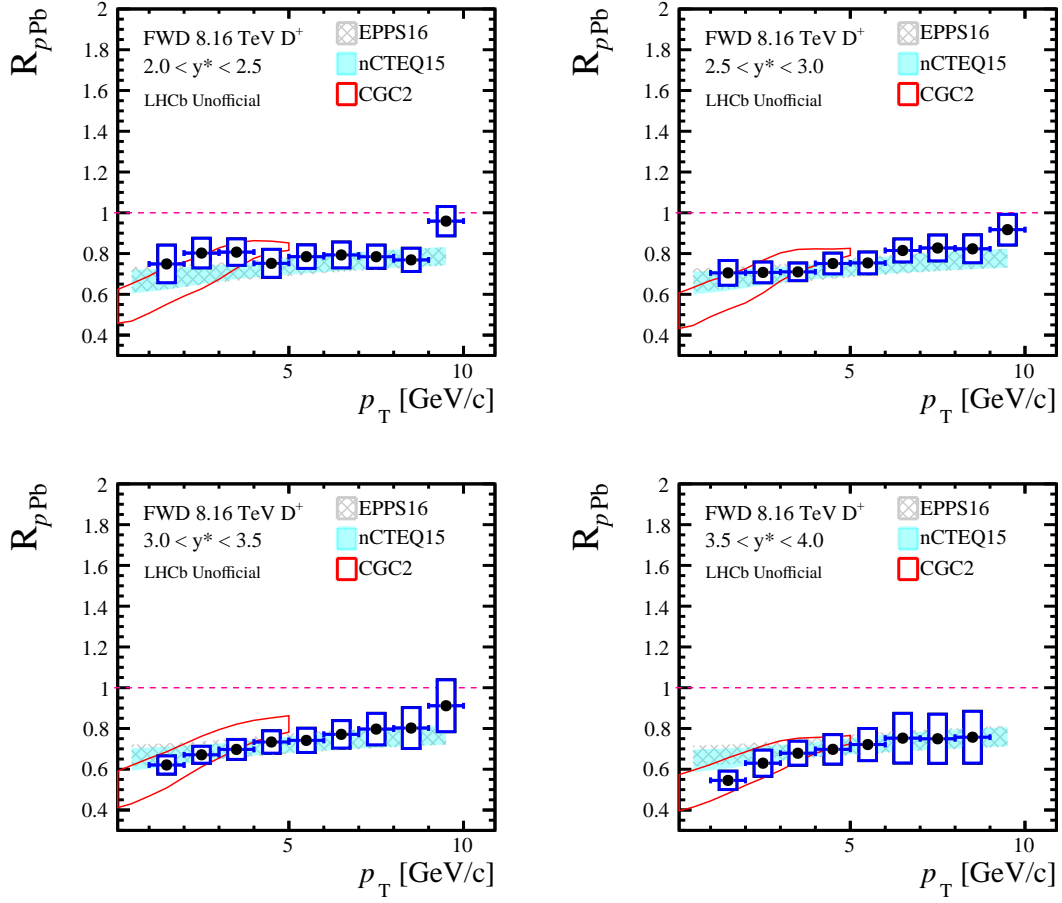


Figure 7.11 Prompt D^+ nuclear modification factor R_{pPb} as a function of p_T in different forward y^* bins. The vertical bar and the vertical box on each data point represent statistical and systematic uncertainty respectively. The coloured bands denote the theoretical calculations using the HELAC-Onia generator, incorporating the nPDFs of EPPS16 (grey) and nCTEQ15 (cyan). The red line represents the CGC2 calculations.

Table 7.9 Nuclear modification factor R_{pPb} for prompt D_s^+ mesons as a function of y^* , integrated over $1 < p_T < 10$ GeV/c. The first and second errors are statistical and systematic uncertainties, respectively.

$ y^* $	R_{pPb}
$[-4.5, -4.0]$	$1.172 \pm 0.012 \pm 0.147$
$[-4.0, -3.5]$	$1.016 \pm 0.019 \pm 0.123$
$[-3.5, -3.0]$	$0.941 \pm 0.017 \pm 0.112$
$[-3.0, -2.5]$	$0.869 \pm 0.017 \pm 0.144$
$[2.0, 2.5]$	$0.887 \pm 0.011 \pm 0.131$
$[2.5, 3.0]$	$0.742 \pm 0.011 \pm 0.072$
$[3.0, 3.5]$	$0.743 \pm 0.015 \pm 0.067$
$[3.5, 4.0]$	$0.637 \pm 0.035 \pm 0.070$

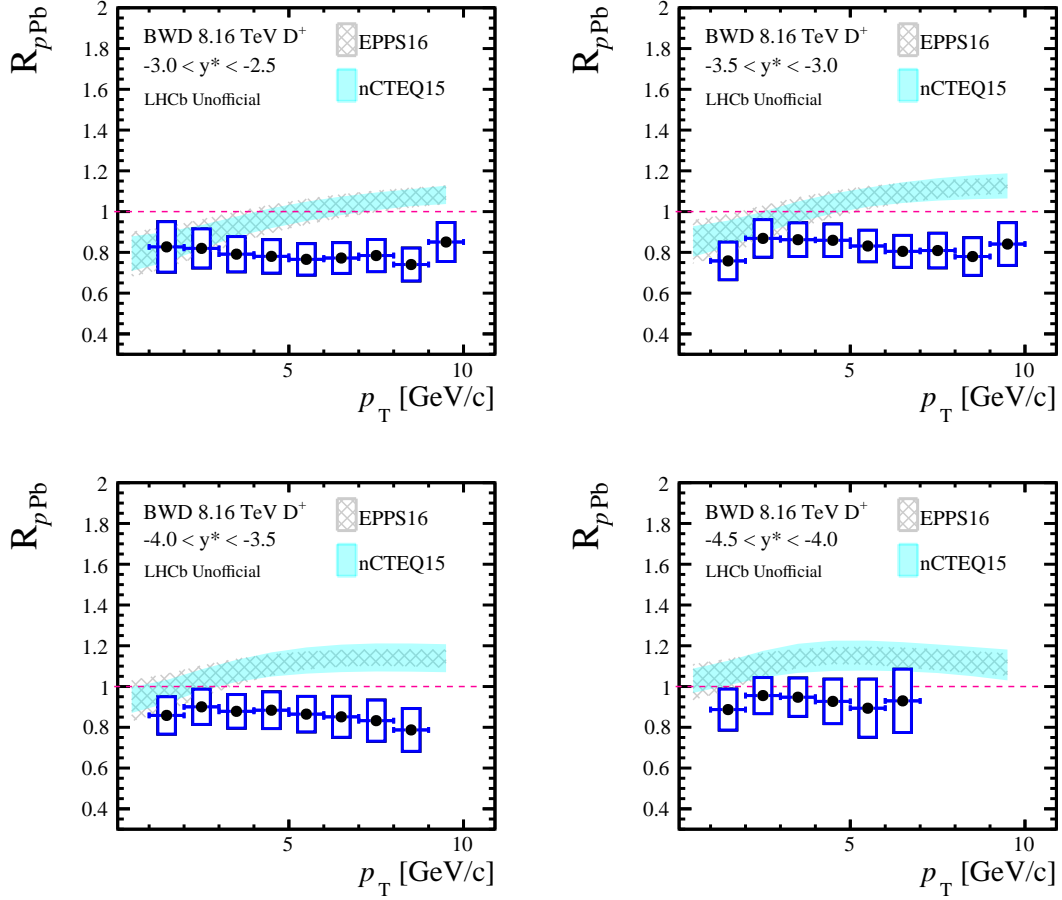


Figure 7.12 Prompt D^+ nuclear modification factor R_{pPb} as a function of p_T in different backward y^* bins. The vertical bar and the vertical box on each data point represent statistical and systematic uncertainty respectively. The coloured bands denote the theoretical calculations using the HELAC-Onia generator, incorporating the nPDFs of EPPS16 (grey) and nCTEQ15 (cyan).

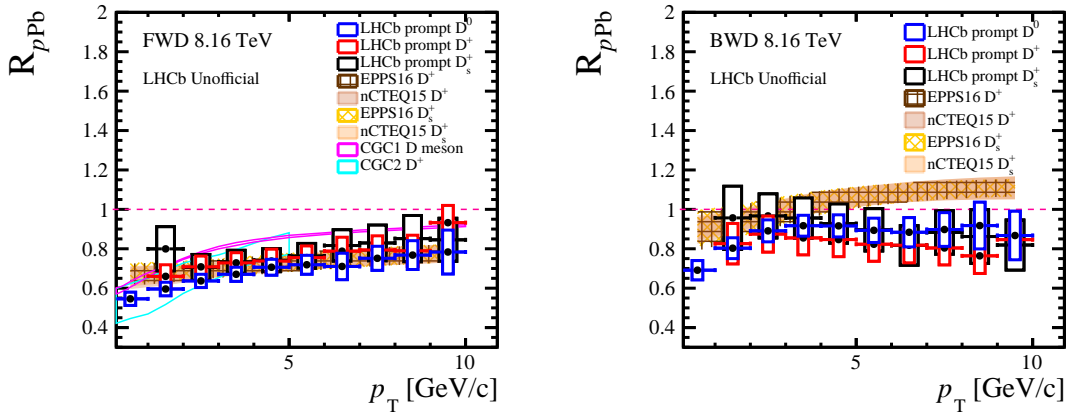


Figure 7.13 Comparison of the D_s^+ and D^+ nuclear modification factors R_{pPb} versus p_T with the previous D^0 measurements^[142].

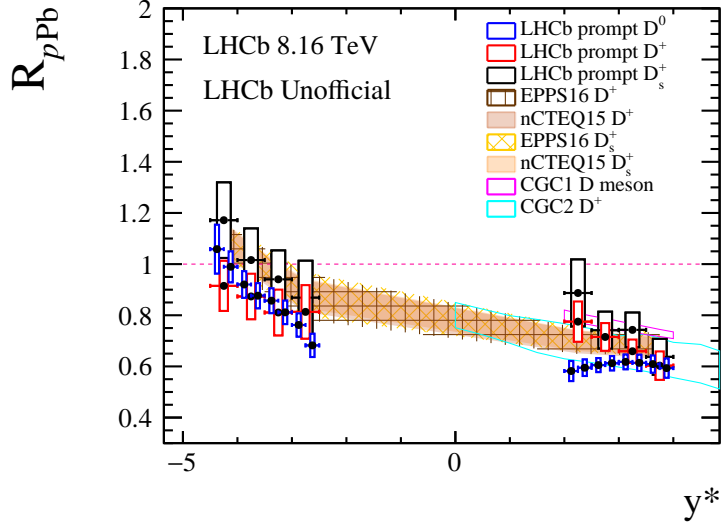


Figure 7.14 Comparison of the D_s^+ and D^+ nuclear modification factors R_{pPb} versus y^* with the previous D^0 measurements^[142].

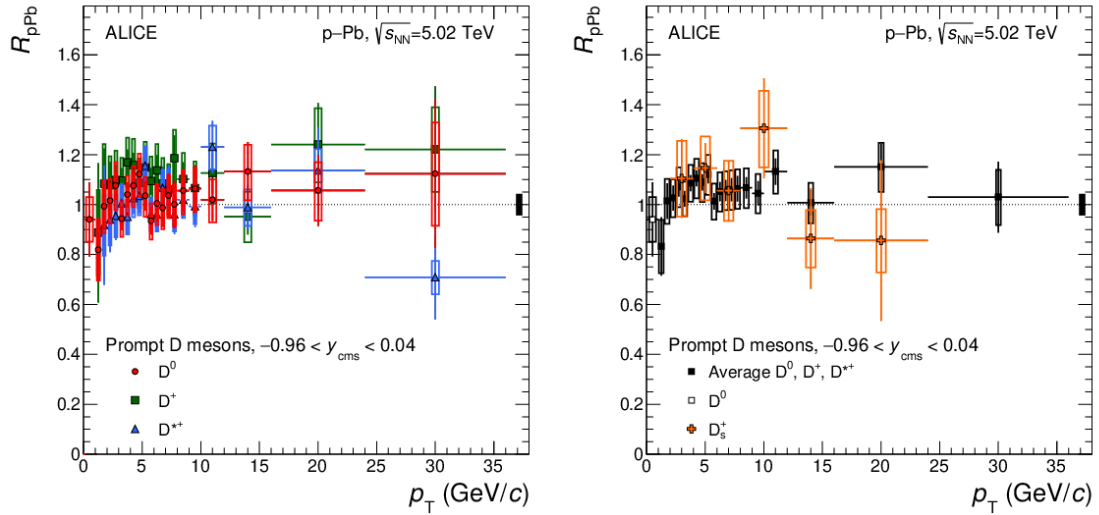


Figure 7.15 ALICE results of nuclear modification factors R_{pPb} of prompt D mesons in pPb collisions at $\sqrt{s_{NN}} = 5.02$ TeV^[48]. These figures are taken from Ref. [48].

Table 7.10 Nuclear modification factor R_{pPb} for prompt D^+ mesons as a function of p_T forward rapidity regions, integrated over common rapidity region of $2.0 < |y^*| < 4.0$ with pp reference. The first and second errors are statistical and systematic uncertainties, respectively.

p_T [GeV/c]	$R_{pPb}(\text{Forward})$
[1, 2]	$0.660 \pm 0.002 \pm 0.059$
[2, 3]	$0.708 \pm 0.002 \pm 0.055$
[3, 4]	$0.728 \pm 0.001 \pm 0.052$
[4, 5]	$0.738 \pm 0.001 \pm 0.060$
[5, 6]	$0.755 \pm 0.002 \pm 0.059$
[6, 7]	$0.788 \pm 0.005 \pm 0.071$
[7, 8]	$0.794 \pm 0.005 \pm 0.072$
[8, 9]	$0.790 \pm 0.010 \pm 0.079$
[9, 10]	$0.932 \pm 0.006 \pm 0.087$

Table 7.11 Nuclear modification factor R_{pPb} for prompt D^+ mesons as a function of p_T backward rapidity regions, integrated over common rapidity region of $2.5 < |y^*| < 4.5$ with pp reference. The first and second errors are statistical and systematic uncertainties, respectively.

p_T [GeV/c]	$R_{pPb}(\text{Backward})$
[1, 2]	$0.826 \pm 0.004 \pm 0.102$
[2, 3]	$0.875 \pm 0.001 \pm 0.091$
[3, 4]	$0.855 \pm 0.001 \pm 0.085$
[4, 5]	$0.847 \pm 0.001 \pm 0.087$
[5, 6]	$0.823 \pm 0.002 \pm 0.086$
[6, 7]	$0.818 \pm 0.003 \pm 0.089$
[7, 8]	$0.804 \pm 0.008 \pm 0.086$
[8, 9]	$0.764 \pm 0.004 \pm 0.089$
[9, 10]	$0.846 \pm 0.005 \pm 0.098$

Table 7.12 Nuclear modification factor R_{pPb} for prompt D^+ mesons as a function of y^* , integrated over $1 < p_T < 10 \text{ GeV}/c$. The first and second errors are statistical and systematic uncertainties, respectively.

$ y^* $	R_{pPb}
$[-4.5, -4.0]$	$0.915 \pm 0.007 \pm 0.098$
$[-4.0, -3.5]$	$0.874 \pm 0.002 \pm 0.089$
$[-3.5, -3.0]$	$0.811 \pm 0.002 \pm 0.089$
$[-3.0, -2.5]$	$0.813 \pm 0.004 \pm 0.105$
$[2.0, 2.5]$	$0.775 \pm 0.002 \pm 0.079$
$[2.5, 3.0]$	$0.715 \pm 0.002 \pm 0.054$
$[3.0, 3.5]$	$0.659 \pm 0.002 \pm 0.046$
$[3.5, 4.0]$	$0.603 \pm 0.003 \pm 0.056$

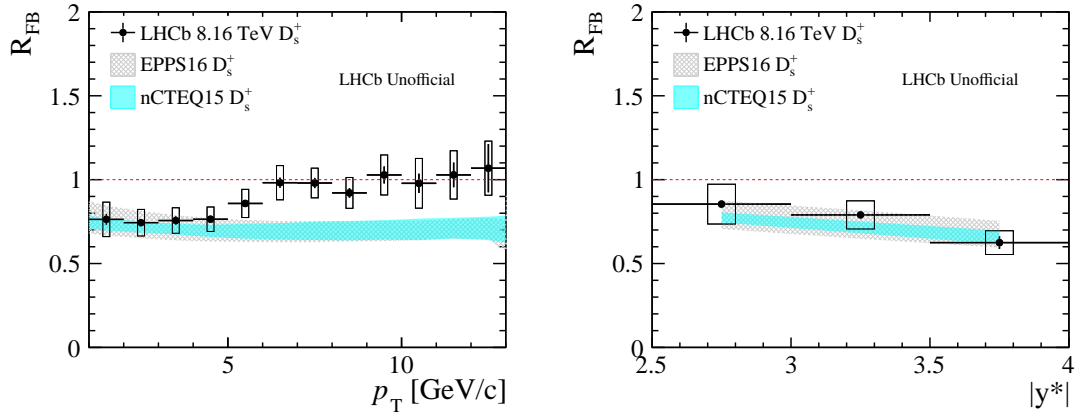


Figure 7.16 D_s^+ Forward and backward production ratio R_{FB} as a function of p_T (left) and $|y^*|$ (right). The vertical bar and vertical box represent statistical and systematic uncertainty respectively. The coloured bands denote the HELAC-Onia theoretical calculations, incorporating the nPDFs of EPPS16 (gray) and nCTEQ15 (cyan).

Table 7.13 Nuclear modification factor $R_{p\text{Pb}}$ for prompt D_s^+ mesons in bins of p_T and y^* . The first and second errors are statistical and systematic uncertainties, respectively.

p_T [GeV/c] y^*	Forward			
	[2, 2.5]	[2.5, 3]	[3, 3.5]	[3.5, 4]
[1, 2]	$1.080 \pm 0.031 \pm 0.232$	$0.762 \pm 0.026 \pm 0.097$	$0.763 \pm 0.033 \pm 0.081$	$0.647 \pm 0.073 \pm 0.086$
[2, 3]	$0.764 \pm 0.007 \pm 0.098$	$0.704 \pm 0.006 \pm 0.057$	$0.717 \pm 0.011 \pm 0.058$	$0.608 \pm 0.018 \pm 0.052$
[3, 4]	$0.816 \pm 0.012 \pm 0.081$	$0.724 \pm 0.007 \pm 0.047$	$0.750 \pm 0.010 \pm 0.051$	$0.611 \pm 0.082 \pm 0.059$
[4, 5]	$0.842 \pm 0.011 \pm 0.076$	$0.743 \pm 0.008 \pm 0.052$	$0.700 \pm 0.017 \pm 0.048$	$0.630 \pm 0.025 \pm 0.056$
[5, 6]	$0.785 \pm 0.015 \pm 0.067$	$0.828 \pm 0.012 \pm 0.064$	$0.704 \pm 0.014 \pm 0.053$	$0.713 \pm 0.031 \pm 0.072$
[6, 7]	$0.846 \pm 0.010 \pm 0.074$	$0.737 \pm 0.013 \pm 0.056$	$0.819 \pm 0.034 \pm 0.089$	$0.910 \pm 0.069 \pm 0.131$
[7, 8]	$0.761 \pm 0.014 \pm 0.073$	$0.877 \pm 0.021 \pm 0.071$	$0.829 \pm 0.040 \pm 0.093$	$0.911 \pm 0.121 \pm 0.163$
[8, 9]	$0.946 \pm 0.029 \pm 0.125$	$0.895 \pm 0.022 \pm 0.105$	$0.685 \pm 0.030 \pm 0.116$	–
[9, 10]	$0.850 \pm 0.019 \pm 0.107$	$0.893 \pm 0.031 \pm 0.100$	$0.779 \pm 0.055 \pm 0.122$	–

p_T [GeV/c] y^*	Backward		
	[-3, -2.5]	[-3.5, -3]	[-4, -3.5]
[1, 2]	$0.881 \pm 0.039 \pm 0.197$	$0.980 \pm 0.035 \pm 0.133$	$1.026 \pm 0.042 \pm 0.148$
[2, 3]	$0.865 \pm 0.017 \pm 0.114$	$0.883 \pm 0.020 \pm 0.097$	$1.049 \pm 0.011 \pm 0.105$
[3, 4]	$0.878 \pm 0.009 \pm 0.102$	$0.961 \pm 0.023 \pm 0.096$	$0.961 \pm 0.017 \pm 0.094$
[4, 5]	$0.849 \pm 0.020 \pm 0.094$	$0.960 \pm 0.011 \pm 0.097$	$0.973 \pm 0.021 \pm 0.105$
[5, 6]	$0.860 \pm 0.026 \pm 0.101$	$0.848 \pm 0.010 \pm 0.091$	$0.956 \pm 0.012 \pm 0.105$
[6, 7]	$0.707 \pm 0.030 \pm 0.087$	$0.902 \pm 0.012 \pm 0.107$	$0.916 \pm 0.020 \pm 0.124$
[7, 8]	$0.835 \pm 0.022 \pm 0.088$	$0.921 \pm 0.023 \pm 0.110$	$0.911 \pm 0.021 \pm 0.151$
[8, 9]	$0.916 \pm 0.029 \pm 0.118$	$0.803 \pm 0.020 \pm 0.154$	–
[9, 10]	$0.804 \pm 0.042 \pm 0.119$	$0.839 \pm 0.033 \pm 0.139$	–

Table 7.14 Nuclear modification factor $R_{p\text{Pb}}$ for prompt D^+ mesons in bins of p_T and y^* . The first and second errors are statistical and systematic uncertainties, respectively.

p_T [GeV/c] y^*	Forward			
	[2, 2.5]	[2.5, 3]	[3, 3.5]	[3.5, 4]
[1, 2]	$0.749 \pm 0.004 \pm 0.092$	$0.705 \pm 0.001 \pm 0.061$	$0.621 \pm 0.003 \pm 0.044$	$0.545 \pm 0.005 \pm 0.045$
[2, 3]	$0.802 \pm 0.002 \pm 0.072$	$0.707 \pm 0.005 \pm 0.050$	$0.671 \pm 0.002 \pm 0.041$	$0.630 \pm 0.003 \pm 0.064$
[3, 4]	$0.807 \pm 0.002 \pm 0.065$	$0.710 \pm 0.001 \pm 0.043$	$0.697 \pm 0.002 \pm 0.049$	$0.679 \pm 0.004 \pm 0.058$
[4, 5]	$0.752 \pm 0.001 \pm 0.068$	$0.751 \pm 0.002 \pm 0.050$	$0.734 \pm 0.003 \pm 0.055$	$0.698 \pm 0.006 \pm 0.072$
[5, 6]	$0.785 \pm 0.002 \pm 0.057$	$0.754 \pm 0.003 \pm 0.053$	$0.742 \pm 0.003 \pm 0.059$	$0.721 \pm 0.008 \pm 0.079$
[6, 7]	$0.793 \pm 0.004 \pm 0.063$	$0.815 \pm 0.005 \pm 0.056$	$0.771 \pm 0.005 \pm 0.067$	$0.753 \pm 0.030 \pm 0.121$
[7, 8]	$0.785 \pm 0.005 \pm 0.056$	$0.827 \pm 0.005 \pm 0.063$	$0.797 \pm 0.008 \pm 0.077$	$0.750 \pm 0.031 \pm 0.120$
[8, 9]	$0.769 \pm 0.005 \pm 0.057$	$0.823 \pm 0.006 \pm 0.068$	$0.802 \pm 0.012 \pm 0.100$	$0.757 \pm 0.066 \pm 0.127$
[9, 10]	$0.959 \pm 0.008 \pm 0.072$	$0.917 \pm 0.010 \pm 0.075$	$0.912 \pm 0.016 \pm 0.127$	–

p_T [GeV/c] y^*	Backward		
	[-3, -2.5]	[-3.5, -3]	[-4, -3.5]
[1, 2]	$0.827 \pm 0.009 \pm 0.124$	$0.758 \pm 0.003 \pm 0.092$	$0.858 \pm 0.003 \pm 0.092$
[2, 3]	$0.820 \pm 0.003 \pm 0.096$	$0.869 \pm 0.002 \pm 0.092$	$0.900 \pm 0.002 \pm 0.086$
[3, 4]	$0.791 \pm 0.002 \pm 0.086$	$0.862 \pm 0.001 \pm 0.082$	$0.878 \pm 0.002 \pm 0.082$
[4, 5]	$0.780 \pm 0.003 \pm 0.082$	$0.859 \pm 0.002 \pm 0.080$	$0.884 \pm 0.003 \pm 0.090$
[5, 6]	$0.766 \pm 0.003 \pm 0.077$	$0.831 \pm 0.002 \pm 0.077$	$0.865 \pm 0.005 \pm 0.087$
[6, 7]	$0.772 \pm 0.008 \pm 0.075$	$0.805 \pm 0.002 \pm 0.078$	$0.851 \pm 0.002 \pm 0.100$
[7, 8]	$0.784 \pm 0.018 \pm 0.079$	$0.809 \pm 0.006 \pm 0.084$	$0.833 \pm 0.005 \pm 0.101$
[8, 9]	$0.740 \pm 0.008 \pm 0.080$	$0.780 \pm 0.004 \pm 0.092$	$0.787 \pm 0.010 \pm 0.105$
[9, 10]	$0.851 \pm 0.005 \pm 0.096$	$0.841 \pm 0.009 \pm 0.105$	–

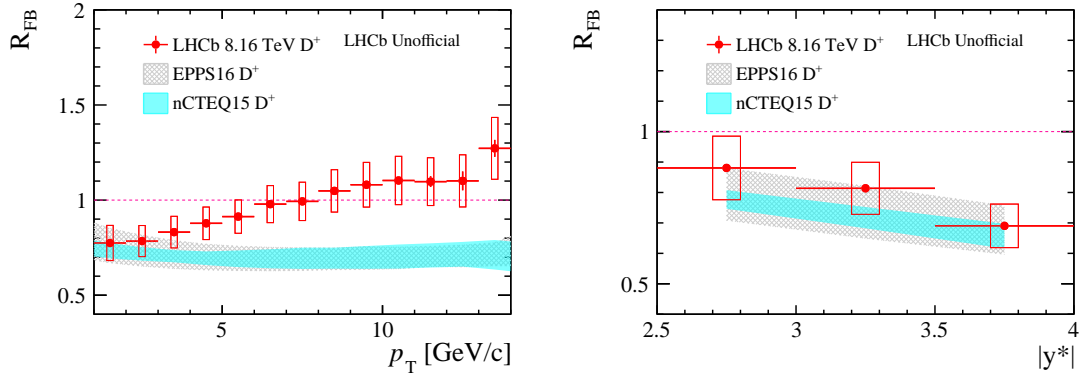


Figure 7.17 D_s^+ Forward and backward production ratio R_{FB} as a function of p_T (left) and $|y^*|$ (right). The vertical bar and vertical box represent statistical and systematic uncertainty respectively. The coloured bands denote the HELAC-Onia theoretical calculations, incorporating the nPDFs of EPPS16 (gray) and nCTEQ15 (cyan).

Table 7.15 D_s^+ Forward and backward production ratio R_{FB} as a function of p_T and $|y^*|$. Integrated over common p_T and y^* range : $1 < p_T < 13$ GeV/c for $2.5 < |y^*| < 3.0$, $1 < p_T < 11$ GeV/c for $3.0 < |y^*| < 3.5$, $1 < p_T < 7$ GeV/c for $3.5 < |y^*| < 4.0$. The first and second errors are statistical and systematic uncertainty respectively.

p_T [GeV/c]	R_{FB}
[1, 2]	$0.763 \pm 0.032 \pm 0.103$
[2, 3]	$0.743 \pm 0.011 \pm 0.079$
[3, 4]	$0.756 \pm 0.026 \pm 0.076$
[4, 5]	$0.764 \pm 0.013 \pm 0.073$
[5, 6]	$0.858 \pm 0.016 \pm 0.084$
[6, 7]	$0.982 \pm 0.030 \pm 0.102$
[7, 8]	$0.980 \pm 0.030 \pm 0.089$
[8, 9]	$0.921 \pm 0.028 \pm 0.092$
[9, 10]	$1.028 \pm 0.051 \pm 0.119$
[10, 11]	$0.978 \pm 0.057 \pm 0.148$
[11, 12]	$1.028 \pm 0.074 \pm 0.144$
[12, 13]	$1.068 \pm 0.144 \pm 0.161$
$ y^* $	R_{FB}
[2.5, 3.0]	$0.854 \pm 0.021 \pm 0.119$
[3.0, 3.5]	$0.790 \pm 0.021 \pm 0.084$
[3.5, 4.0]	$0.625 \pm 0.037 \pm 0.071$

Table 7.16 D^+ Forward and backward production ratio R_{FB} a function of p_{T} and $|y^*|$. Integrated over common p_{T} and y^* range : $1 < p_{\text{T}} < 14 \text{ GeV}/c$ for $2.5 < |y^*| < 3.0$, $1 < p_{\text{T}} < 11 \text{ GeV}/c$ for $3.0 < |y^*| < 3.5$, $1 < p_{\text{T}} < 8 \text{ GeV}/c$ for $3.5 < |y^*| < 4.0$. The first and second errors are statistical and systematic uncertainty respectively.

p_{T} [GeV/c]	R_{FB}
[1, 2]	$0.775 \pm 0.004 \pm 0.092$
[2, 3]	$0.785 \pm 0.003 \pm 0.082$
[3, 4]	$0.832 \pm 0.002 \pm 0.083$
[4, 5]	$0.878 \pm 0.003 \pm 0.086$
[5, 6]	$0.913 \pm 0.004 \pm 0.088$
[6, 7]	$0.979 \pm 0.010 \pm 0.097$
[7, 8]	$0.993 \pm 0.014 \pm 0.101$
[8, 9]	$1.048 \pm 0.022 \pm 0.111$
[9, 10]	$1.081 \pm 0.013 \pm 0.118$
[10, 11]	$1.103 \pm 0.022 \pm 0.127$
[11, 12]	$1.097 \pm 0.028 \pm 0.126$
[12, 13]	$1.101 \pm 0.049 \pm 0.137$
[13, 14]	$1.272 \pm 0.044 \pm 0.163$
$ y^* $	R_{FB}
[2.5, 3.0]	$0.881 \pm 0.005 \pm 0.104$
[3.0, 3.5]	$0.814 \pm 0.003 \pm 0.086$
[3.5, 4.0]	$0.690 \pm 0.004 \pm 0.072$

7.4 D_s^+/D^+ cross-section ratio

The measurement of the relative abundances of the D_s^+ and D^+ in p Pb collisions can provide clue about the modification of the hadronisation mechanism in small system.

The p_T -differential D_s^+/D^+ ratios are shown in Figs. 7.18 and listed in Tab. 7.17. The uncertainties from the luminosity is canceled out due to the same data sample. The uncertainties from K (π) hadronic interactions with the detector, tracking efficiencies and PID efficiency are considered partially correlated, while the uncertainties from the signal yield and the simulation sample size are uncorrelated. The p_T -differential D_s^+/D^+ ratios are compatible in each rapidity intervals and in agreement with the theoretical calculation. This implies that relative abundance does not change and is independent of rapidity. Similarly, it is also consistent with the ALICE results as shown in Fig. 7.19^[48].

The D_s^+/D^+ ratios are also studied in different p_T and rapidity intervals as a function of the PV nTracks. The results are shown in Figs. 7.20 and 7.21 and listed in Tabs. 7.18 and 7.19. In these figures, the x -axis is scaled with the average numbers of PV ntracks in minimum bias events, which are 60.25 and 68.97 for the forward and backward collisions respectively. In order to improve the statistics, we also integrate kinematic bins to obtain the ratios versus multiplicity in low ($2 - 6$ GeV/ c) and high momentum ($6 - 12$ GeV/ c) ranges, shown in Figs. 7.22 and 7.23. To estimate the significance of the rising trend, a linear function is used to fit the data point in these two figures. This line deviates from flat distribution by 7.3σ (forward) and 12.6σ (backward) in the $2 - 6$ GeV/ c p_T range, and by 5.2σ (forward) and 4.9σ (backward) in the $6 - 12$ GeV/ c p_T range. This result is compared horizontally with result of ALICE, as shown in Figs. ???. Our result have more statistics and more obvious enhancement trend in each momentum interval. This result confirms that the D_s^+/D^+ ratios show an increasing trend with the increasing event multiplicity (PV ntracks), especially in the low p_T region of the backward collisions. The current data precision can provide a firm conclusion that D_s^+/D^+ ratio enhancement is observed in high multiplicity p Pb collisions. This enhancement might be due to the charm hadronisation via sequential coalescence in a s quark rich soup, however further comparisons with theoretical calculations are needed to confirm this physics mechanism.

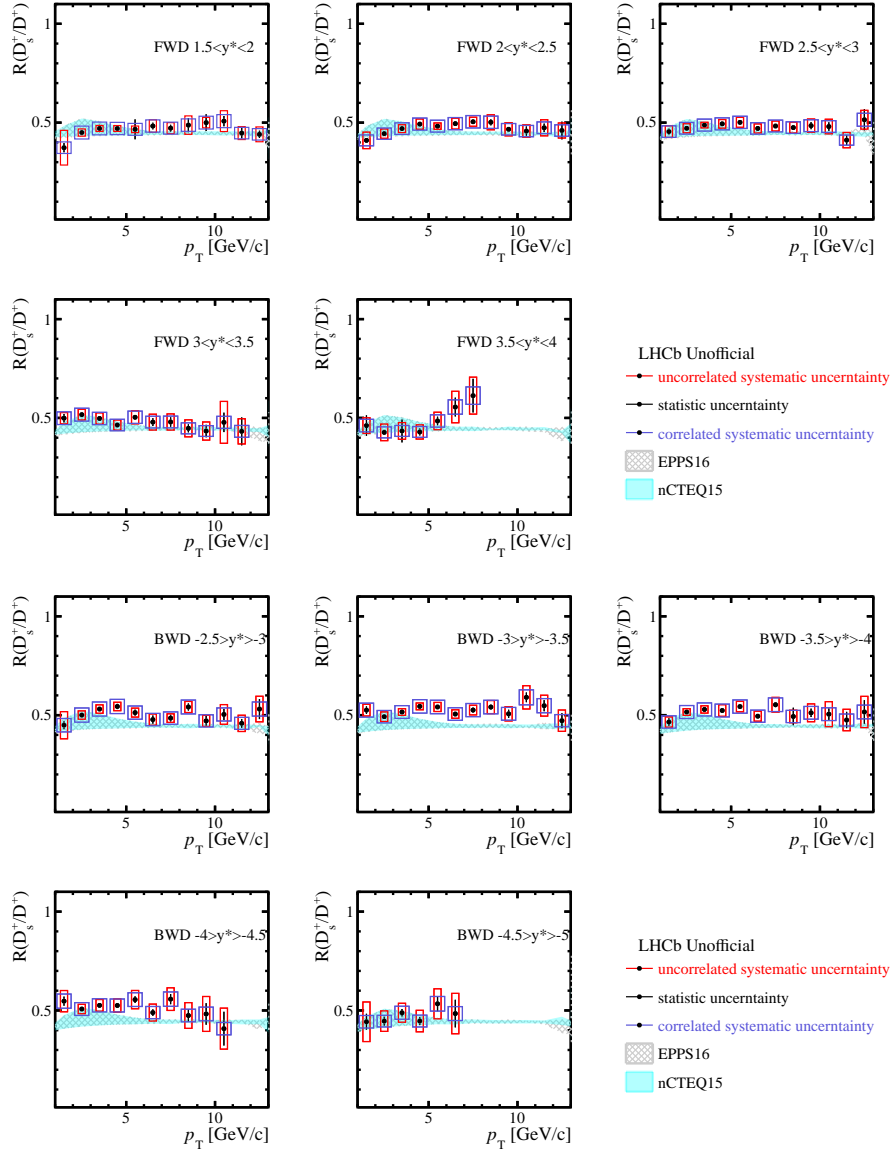


Figure 7.18 The D_s^+/D^+ ratio (including branching fraction) as functions of p_T in different y^* bins in p Pb collisions at $\sqrt{s_{NN}} = 8.16$ TeV. The error bars mark statistical uncertainties and the red boxes mark uncorrelated systematic uncertainties, the blue boxes mark correlated systematic uncertainties. The coloured bands mark the HELAC-Onia theoretical calculations, incorporating the nPDFs of EPPS16 (gray) and nCTEQ15 (cyan).

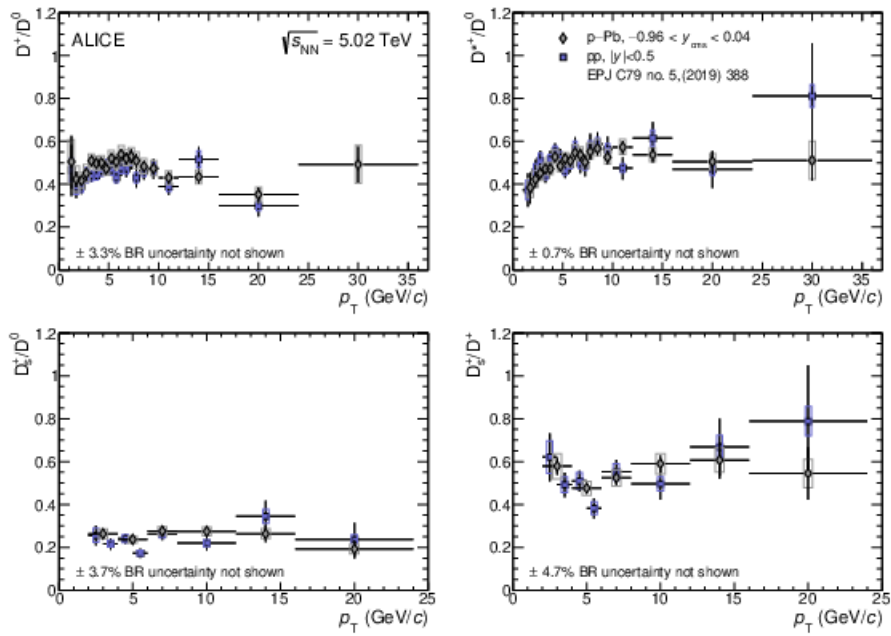


Figure 7.19 ALICE results of the prompt D -meson relative abundances as a function of p_T in pPb collisions at $\sqrt{s_{NN}} = 5.02 \text{ TeV}$ ^[48]. Taken from Ref. [48].

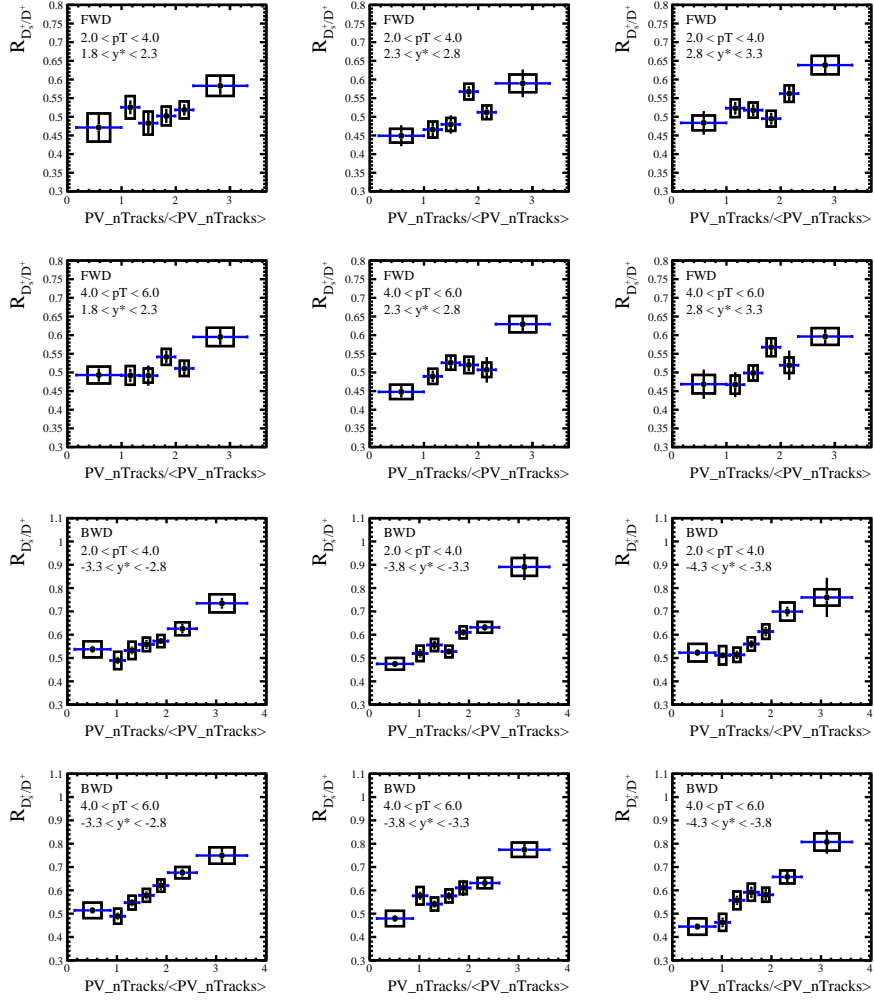


Figure 7.20 The D_s^+/D^+ ratio (including branching fractions) as a function of the event multiplicity (the scaled PV nTracks) in different p_T (within 2-6 GeV/c) and y^* bins in the forward and backward pPb collisions at $\sqrt{s_{NN}} = 8.16$ TeV.

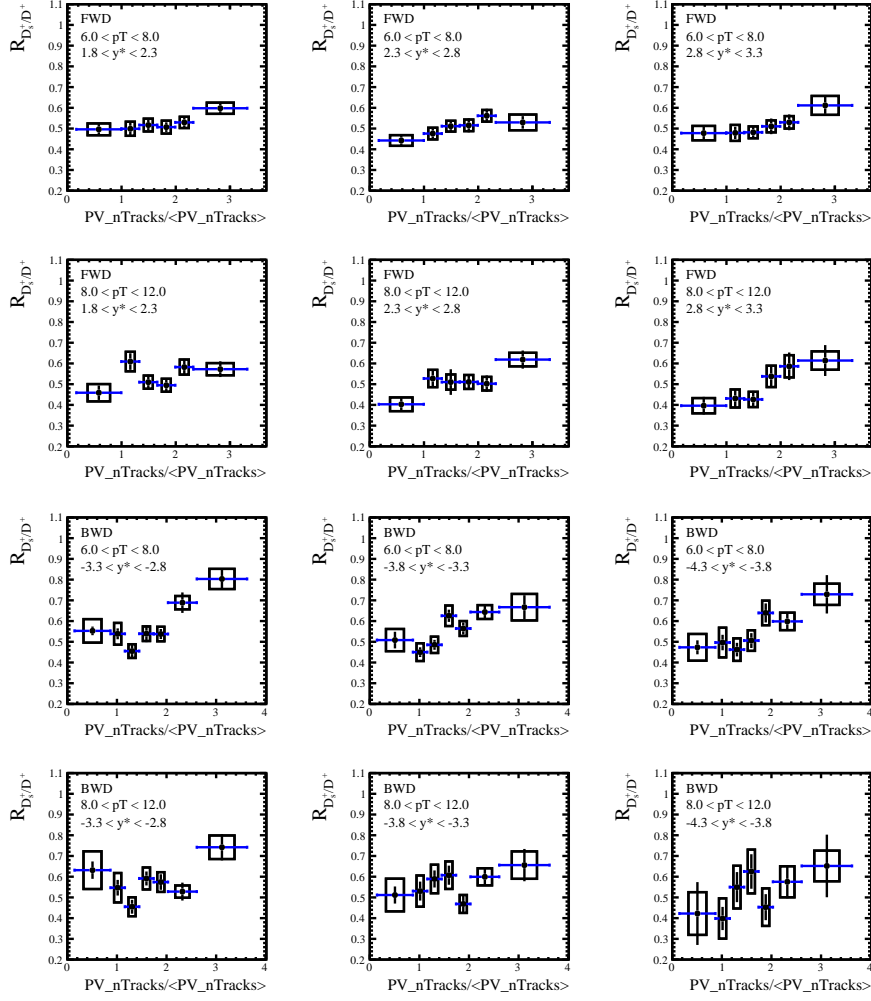


Figure 7.21 The D_s^+/D^+ ratio (including branching fractions) as a function of the event multiplicity (the scaled PV nTracks) in different p_T (within 6-12 GeV/c) and y^* bins in the forward and backward $p\text{Pb}$ collisions at $\sqrt{s_{\text{NN}}} = 8.16$ TeV.

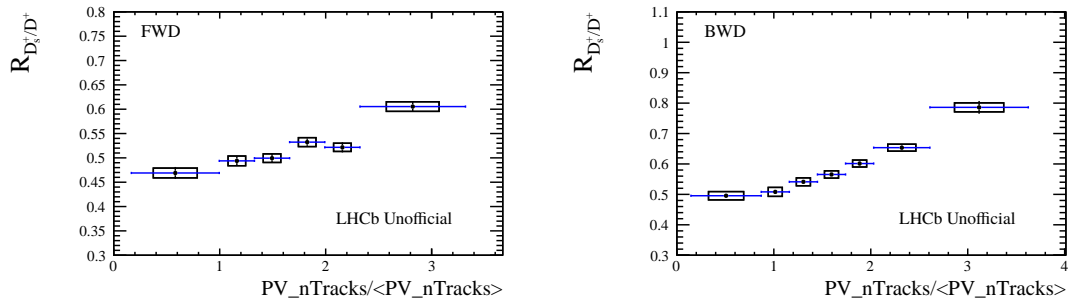


Figure 7.22 The D_s^+/D^+ ratio (including branching fractions) as a function of the event multiplicity (the scaled PV nTracks) in $p\text{Pb}$ collisions at $\sqrt{s_{\text{NN}}} = 8.16$ TeV, integrated over the p_T range of 2-6 GeV/c for the forward and backward collisions.

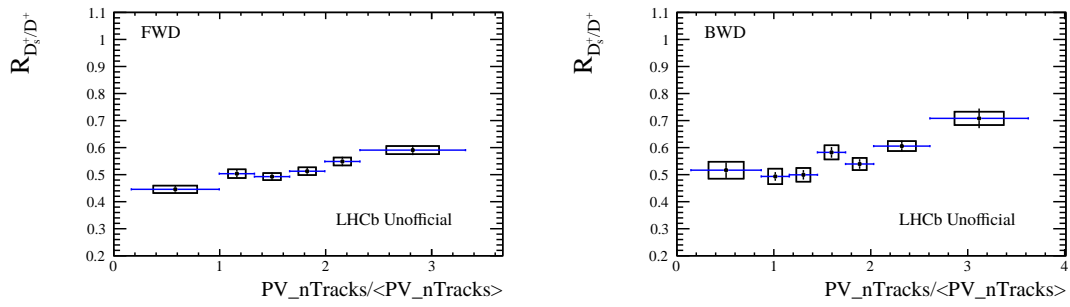


Figure 7.23 The D_s^+/D^+ ratio (including branching fractions) as a function of the event multiplicity (the scaled PV nTracks) in p Pb collisions at $\sqrt{s_{NN}}=8.16$ TeV, integrated over the p_T range of 6-12 GeV/ c for the forward and backward collisions.

Table 7.17 The D_s^+/D^+ ratio (including branching fractions) as a function of p_T in different y^* bins in pPb collisions at $\sqrt{s_{NN}}=8.16$ TeV, for the forward (upper) and backward (lower) rapidity regions. The first error is statistical uncertainty, the second is the component of the systematic uncertainty that is uncorrelated between bins and the third is the correlated component.

p_T [GeV/c]\(y^*	Forward(mb (GeV/c))					
	[1.5, 2]	[2, 2.5]	[2.5, 3]	[3, 3.5]	[3.5, 4]	
[1, 2]	0.373 ± 0.023 ± 0.088 ± 0.029	0.410 ± 0.012 ± 0.042 ± 0.027	0.455 ± 0.015 ± 0.030 ± 0.029	0.499 ± 0.022 ± 0.029 ± 0.032	0.461 ± 0.052 ± 0.039 ± 0.032	
[2, 3]	0.450 ± 0.013 ± 0.018 ± 0.033	0.444 ± 0.004 ± 0.024 ± 0.028	0.472 ± 0.006 ± 0.023 ± 0.030	0.516 ± 0.008 ± 0.027 ± 0.033	0.427 ± 0.013 ± 0.042 ± 0.028	
[3, 4]	0.471 ± 0.019 ± 0.015 ± 0.032	0.470 ± 0.007 ± 0.020 ± 0.029	0.488 ± 0.005 ± 0.014 ± 0.030	0.497 ± 0.007 ± 0.029 ± 0.031	0.434 ± 0.058 ± 0.042 ± 0.028	
[4, 5]	0.470 ± 0.009 ± 0.015 ± 0.031	0.493 ± 0.007 ± 0.026 ± 0.031	0.494 ± 0.006 ± 0.022 ± 0.030	0.464 ± 0.011 ± 0.026 ± 0.029	0.429 ± 0.018 ± 0.036 ± 0.027	
[5, 6]	0.466 ± 0.050 ± 0.017 ± 0.030	0.482 ± 0.009 ± 0.016 ± 0.030	0.501 ± 0.007 ± 0.025 ± 0.031	0.503 ± 0.010 ± 0.033 ± 0.031	0.485 ± 0.022 ± 0.044 ± 0.031	
[6, 7]	0.483 ± 0.017 ± 0.032 ± 0.031	0.495 ± 0.006 ± 0.028 ± 0.031	0.471 ± 0.009 ± 0.023 ± 0.029	0.479 ± 0.020 ± 0.040 ± 0.030	0.555 ± 0.048 ± 0.080 ± 0.036	
[7, 8]	0.472 ± 0.017 ± 0.028 ± 0.030	0.504 ± 0.010 ± 0.023 ± 0.031	0.483 ± 0.012 ± 0.025 ± 0.030	0.480 ± 0.024 ± 0.041 ± 0.030	0.613 ± 0.085 ± 0.094 ± 0.044	
[8, 9]	0.487 ± 0.036 ± 0.047 ± 0.031	0.502 ± 0.016 ± 0.038 ± 0.031	0.475 ± 0.012 ± 0.027 ± 0.029	0.447 ± 0.020 ± 0.043 ± 0.028	–	
[9, 10]	0.500 ± 0.042 ± 0.027 ± 0.032	0.467 ± 0.011 ± 0.033 ± 0.029	0.485 ± 0.018 ± 0.034 ± 0.030	0.434 ± 0.032 ± 0.046 ± 0.027	–	
[10, 11]	0.508 ± 0.026 ± 0.053 ± 0.033	0.457 ± 0.023 ± 0.031 ± 0.028	0.480 ± 0.022 ± 0.037 ± 0.030	0.478 ± 0.049 ± 0.106 ± 0.031	–	
[11, 12]	0.447 ± 0.027 ± 0.033 ± 0.029	0.474 ± 0.021 ± 0.041 ± 0.030	0.412 ± 0.024 ± 0.039 ± 0.026	0.432 ± 0.071 ± 0.064 ± 0.030	–	
[12, 13]	0.441 ± 0.019 ± 0.037 ± 0.029	0.460 ± 0.045 ± 0.038 ± 0.029	0.514 ± 0.053 ± 0.048 ± 0.033	–	–	

p_T [GeV/c]\(y^*	Backward(mb (GeV/c))		
	[-3, -2.5]	[-3.5, -3]	[-4, -3.5]
[1, 2]	0.449 ± 0.020 ± 0.069 ± 0.034	0.525 ± 0.019 ± 0.030 ± 0.035	0.465 ± 0.019 ± 0.026 ± 0.031
[2, 3]	0.500 ± 0.010 ± 0.021 ± 0.036	0.492 ± 0.011 ± 0.024 ± 0.031	0.516 ± 0.005 ± 0.017 ± 0.033
[3, 4]	0.531 ± 0.005 ± 0.021 ± 0.036	0.516 ± 0.012 ± 0.017 ± 0.032	0.529 ± 0.009 ± 0.019 ± 0.033
[4, 5]	0.544 ± 0.013 ± 0.021 ± 0.036	0.544 ± 0.006 ± 0.017 ± 0.034	0.523 ± 0.011 ± 0.029 ± 0.032
[5, 6]	0.513 ± 0.015 ± 0.023 ± 0.033	0.541 ± 0.007 ± 0.023 ± 0.034	0.543 ± 0.008 ± 0.026 ± 0.034
[6, 7]	0.478 ± 0.021 ± 0.029 ± 0.031	0.506 ± 0.007 ± 0.022 ± 0.032	0.495 ± 0.011 ± 0.025 ± 0.031
[7, 8]	0.485 ± 0.017 ± 0.022 ± 0.031	0.526 ± 0.014 ± 0.024 ± 0.033	0.553 ± 0.013 ± 0.037 ± 0.035
[8, 9]	0.541 ± 0.018 ± 0.028 ± 0.035	0.541 ± 0.013 ± 0.033 ± 0.034	0.493 ± 0.044 ± 0.032 ± 0.031
[9, 10]	0.471 ± 0.025 ± 0.028 ± 0.031	0.507 ± 0.021 ± 0.036 ± 0.032	0.512 ± 0.021 ± 0.045 ± 0.032
[10, 11]	0.504 ± 0.028 ± 0.050 ± 0.033	0.590 ± 0.025 ± 0.059 ± 0.038	0.505 ± 0.029 ± 0.063 ± 0.032
[11, 12]	0.458 ± 0.022 ± 0.041 ± 0.030	0.548 ± 0.028 ± 0.053 ± 0.036	0.475 ± 0.041 ± 0.054 ± 0.030
[12, 13]	0.531 ± 0.051 ± 0.065 ± 0.036	0.472 ± 0.038 ± 0.054 ± 0.031	0.516 ± 0.060 ± 0.079 ± 0.035

Table 7.18 The D_s^+/D^+ ratio (including branching fractions) as functions of p_T (within 2-6 GeV/c), y^* and PV nTracks for the forward (upper) and backward (lower) pPb collisions at $\sqrt{s_{NN}}=8.16$ TeV. The first error is statistical uncertainty, the second error is the component of the systematic uncertainty that is uncorrelated between bins and the third is the correlated component.

p_T [GeV/c], y^* * PVnTracks	Forward (mb (GeV/c))									
	[10, 60]	[60, 80]	[80, 100]	[100, 120]	[120, 140]	[140, 200]	[180, 250]	[10, 60]	[60, 80]	[80, 100]
[2, 4], [1.8, 2.3]	0.471 ± 0.040 ± 0.032 ± 0.019	0.525 ± 0.019 ± 0.024 ± 0.019	0.483 ± 0.027 ± 0.028 ± 0.014	0.502 ± 0.019 ± 0.017 ± 0.018	0.519 ± 0.015 ± 0.016 ± 0.016	0.583 ± 0.023 ± 0.013 ± 0.024	0.519 ± 0.015 ± 0.016 ± 0.016	0.573 ± 0.013 ± 0.019 ± 0.017	0.626 ± 0.020 ± 0.018 ± 0.021	0.735 ± 0.023 ± 0.019 ± 0.034
[2, 4], [2.3, 2.8]	0.449 ± 0.028 ± 0.012 ± 0.014	0.466 ± 0.023 ± 0.016 ± 0.014	0.480 ± 0.025 ± 0.013 ± 0.011	0.567 ± 0.014 ± 0.014 ± 0.016	0.512 ± 0.016 ± 0.013 ± 0.012	0.590 ± 0.037 ± 0.014 ± 0.019	0.512 ± 0.016 ± 0.013 ± 0.012	0.610 ± 0.014 ± 0.022 ± 0.014	0.632 ± 0.015 ± 0.017 ± 0.017	0.891 ± 0.056 ± 0.023 ± 0.031
[2, 4], [2.8, 3.3]	0.484 ± 0.032 ± 0.016 ± 0.012	0.523 ± 0.017 ± 0.019 ± 0.015	0.518 ± 0.016 ± 0.017 ± 0.012	0.495 ± 0.016 ± 0.017 ± 0.013	0.562 ± 0.020 ± 0.018 ± 0.013	0.639 ± 0.025 ± 0.015 ± 0.020	0.562 ± 0.020 ± 0.018 ± 0.013	0.614 ± 0.020 ± 0.028 ± 0.015	0.699 ± 0.021 ± 0.032 ± 0.022	0.760 ± 0.084 ± 0.026 ± 0.024
[4, 6], [1.8, 2.3]	0.493 ± 0.018 ± 0.016 ± 0.016	0.492 ± 0.018 ± 0.021 ± 0.014	0.491 ± 0.027 ± 0.016 ± 0.011	0.542 ± 0.017 ± 0.016 ± 0.014	0.511 ± 0.019 ± 0.016 ± 0.012	0.595 ± 0.021 ± 0.016 ± 0.019	0.511 ± 0.019 ± 0.016 ± 0.012	0.620 ± 0.019 ± 0.023 ± 0.013	0.676 ± 0.017 ± 0.018 ± 0.017	0.749 ± 0.035 ± 0.025 ± 0.025
[4, 6], [2.3, 2.8]	0.448 ± 0.015 ± 0.014 ± 0.013	0.489 ± 0.016 ± 0.017 ± 0.011	0.526 ± 0.017 ± 0.016 ± 0.009	0.520 ± 0.017 ± 0.019 ± 0.011	0.507 ± 0.034 ± 0.017 ± 0.010	0.629 ± 0.022 ± 0.016 ± 0.015	0.507 ± 0.034 ± 0.017 ± 0.010	0.610 ± 0.034 ± 0.024 ± 0.011	0.631 ± 0.026 ± 0.018 ± 0.013	0.774 ± 0.036 ± 0.023 ± 0.021
[4, 6], [2.8, 3.3]	0.469 ± 0.039 ± 0.021 ± 0.012	0.467 ± 0.033 ± 0.022 ± 0.011	0.499 ± 0.024 ± 0.018 ± 0.009	0.568 ± 0.025 ± 0.020 ± 0.013	0.519 ± 0.039 ± 0.018 ± 0.010	0.596 ± 0.023 ± 0.017 ± 0.015	0.519 ± 0.039 ± 0.018 ± 0.010	0.581 ± 0.024 ± 0.028 ± 0.011	0.658 ± 0.026 ± 0.023 ± 0.015	0.807 ± 0.050 ± 0.029 ± 0.024

p_T [GeV/c], y^* * PVnTracks	Backward (mb (GeV/c))									
	[10, 60]	[60, 80]	[80, 100]	[100, 120]	[120, 140]	[140, 180]	[180, 250]	[10, 60]	[60, 80]	[80, 100]
[2, 4], [-3.3, -2.8]	0.537 ± 0.015 ± 0.030 ± 0.017	0.489 ± 0.016 ± 0.027 ± 0.025	0.533 ± 0.017 ± 0.032 ± 0.018	0.558 ± 0.020 ± 0.020 ± 0.021	0.573 ± 0.013 ± 0.019 ± 0.017	0.626 ± 0.020 ± 0.018 ± 0.021	0.626 ± 0.020 ± 0.018 ± 0.021	0.573 ± 0.013 ± 0.019 ± 0.017	0.626 ± 0.020 ± 0.018 ± 0.021	0.735 ± 0.023 ± 0.019 ± 0.034
[2, 4], [-3.8, -3.3]	0.475 ± 0.010 ± 0.022 ± 0.012	0.520 ± 0.018 ± 0.027 ± 0.019	0.556 ± 0.019 ± 0.022 ± 0.014	0.528 ± 0.011 ± 0.019 ± 0.015	0.610 ± 0.014 ± 0.022 ± 0.014	0.632 ± 0.015 ± 0.017 ± 0.017	0.632 ± 0.015 ± 0.017 ± 0.017	0.610 ± 0.014 ± 0.022 ± 0.014	0.632 ± 0.015 ± 0.017 ± 0.017	0.891 ± 0.056 ± 0.023 ± 0.031
[2, 4], [-4.3, -3.8]	0.523 ± 0.015 ± 0.033 ± 0.018	0.512 ± 0.012 ± 0.035 ± 0.019	0.514 ± 0.018 ± 0.027 ± 0.014	0.560 ± 0.016 ± 0.025 ± 0.015	0.614 ± 0.020 ± 0.028 ± 0.015	0.699 ± 0.021 ± 0.032 ± 0.022	0.699 ± 0.021 ± 0.032 ± 0.022	0.614 ± 0.020 ± 0.028 ± 0.015	0.699 ± 0.021 ± 0.032 ± 0.022	0.760 ± 0.084 ± 0.026 ± 0.024
[4, 6], [-3.3, -2.8]	0.514 ± 0.014 ± 0.028 ± 0.018	0.489 ± 0.016 ± 0.027 ± 0.018	0.547 ± 0.016 ± 0.026 ± 0.015	0.578 ± 0.017 ± 0.023 ± 0.016	0.620 ± 0.019 ± 0.023 ± 0.013	0.676 ± 0.017 ± 0.018 ± 0.017	0.676 ± 0.017 ± 0.018 ± 0.017	0.620 ± 0.019 ± 0.023 ± 0.013	0.676 ± 0.017 ± 0.018 ± 0.017	0.749 ± 0.035 ± 0.025 ± 0.025
[4, 6], [-3.8, -3.3]	0.479 ± 0.015 ± 0.030 ± 0.013	0.577 ± 0.017 ± 0.035 ± 0.014	0.541 ± 0.015 ± 0.026 ± 0.010	0.576 ± 0.016 ± 0.025 ± 0.013	0.610 ± 0.034 ± 0.024 ± 0.011	0.631 ± 0.026 ± 0.018 ± 0.013	0.631 ± 0.026 ± 0.018 ± 0.013	0.610 ± 0.034 ± 0.024 ± 0.011	0.631 ± 0.026 ± 0.018 ± 0.013	0.774 ± 0.036 ± 0.023 ± 0.021
[4, 6], [-4.3, -3.8]	0.445 ± 0.014 ± 0.032 ± 0.016	0.463 ± 0.021 ± 0.034 ± 0.013	0.557 ± 0.020 ± 0.036 ± 0.012	0.592 ± 0.024 ± 0.034 ± 0.013	0.581 ± 0.024 ± 0.028 ± 0.011	0.658 ± 0.026 ± 0.023 ± 0.015	0.658 ± 0.026 ± 0.023 ± 0.015	0.581 ± 0.024 ± 0.028 ± 0.011	0.658 ± 0.026 ± 0.023 ± 0.015	0.807 ± 0.050 ± 0.029 ± 0.024

Table 7.19 The D_s^+/D^+ ratio (including branching fractions) as functions of p_T (within 6-12 GeV/c), y^* and PV nTracks for the forward (upper) and backward (lower) pPb collisions at $\sqrt{s_{NN}}=8.16$ TeV. The first error is statistical uncertainty, the second error is the component of the systematic uncertainty that is uncorrelated between bins and the third is the correlated component.

p_T [GeV/c], y^* * PVnTracks	Forward (mb (GeV/c))										
	[10, 60]	[60, 80]	[80, 100]	[100, 120]	[120, 140]	[140, 200]	[180, 250]	[140, 180]	[120, 140]	[100, 120]	
[2, 4], [1.8, 2.3]	0.471 ± 0.040 ± 0.032 ± 0.019	0.525 ± 0.019 ± 0.024 ± 0.019	0.483 ± 0.027 ± 0.028 ± 0.014	0.502 ± 0.019 ± 0.017 ± 0.018	0.519 ± 0.015 ± 0.016 ± 0.016	0.583 ± 0.023 ± 0.013 ± 0.024					
[2, 4], [2.3, 2.8]	0.449 ± 0.028 ± 0.012 ± 0.014	0.466 ± 0.023 ± 0.016 ± 0.014	0.480 ± 0.025 ± 0.013 ± 0.011	0.567 ± 0.014 ± 0.014 ± 0.016	0.512 ± 0.016 ± 0.013 ± 0.012	0.590 ± 0.037 ± 0.014 ± 0.019					
[2, 4], [2.8, 3.3]	0.484 ± 0.032 ± 0.016 ± 0.012	0.523 ± 0.017 ± 0.019 ± 0.015	0.518 ± 0.016 ± 0.017 ± 0.012	0.495 ± 0.016 ± 0.017 ± 0.013	0.562 ± 0.020 ± 0.018 ± 0.013	0.639 ± 0.025 ± 0.015 ± 0.020					
[4, 6], [1.8, 2.3]	0.493 ± 0.018 ± 0.016 ± 0.016	0.492 ± 0.018 ± 0.021 ± 0.014	0.491 ± 0.027 ± 0.016 ± 0.011	0.542 ± 0.017 ± 0.016 ± 0.014	0.511 ± 0.019 ± 0.016 ± 0.012	0.595 ± 0.021 ± 0.016 ± 0.019					
[4, 6], [2.3, 2.8]	0.448 ± 0.015 ± 0.014 ± 0.013	0.489 ± 0.016 ± 0.017 ± 0.011	0.526 ± 0.017 ± 0.016 ± 0.009	0.520 ± 0.017 ± 0.019 ± 0.011	0.507 ± 0.034 ± 0.017 ± 0.010	0.629 ± 0.022 ± 0.016 ± 0.015					
[4, 6], [2.8, 3.3]	0.469 ± 0.039 ± 0.021 ± 0.012	0.467 ± 0.033 ± 0.022 ± 0.011	0.499 ± 0.024 ± 0.018 ± 0.009	0.568 ± 0.025 ± 0.020 ± 0.013	0.519 ± 0.039 ± 0.018 ± 0.010	0.596 ± 0.023 ± 0.017 ± 0.015					
p_T [GeV/c], y^* * PVnTracks	Backward (mb (GeV/c))										
	[10, 60]	[60, 80]	[80, 100]	[100, 120]	[120, 140]	[140, 180]	[180, 250]	[140, 180]	[120, 140]	[100, 120]	
[2, 4], [-3.3, -2.8]	0.537 ± 0.015 ± 0.030 ± 0.017	0.489 ± 0.016 ± 0.027 ± 0.025	0.533 ± 0.017 ± 0.032 ± 0.018	0.558 ± 0.020 ± 0.020 ± 0.021	0.573 ± 0.013 ± 0.019 ± 0.017	0.626 ± 0.020 ± 0.018 ± 0.021	0.735 ± 0.023 ± 0.019 ± 0.034				
[2, 4], [-3.8, -3.3]	0.475 ± 0.010 ± 0.022 ± 0.012	0.520 ± 0.018 ± 0.027 ± 0.019	0.556 ± 0.019 ± 0.022 ± 0.014	0.528 ± 0.011 ± 0.019 ± 0.015	0.610 ± 0.014 ± 0.022 ± 0.014	0.632 ± 0.015 ± 0.017 ± 0.017	0.891 ± 0.056 ± 0.023 ± 0.031				
[2, 4], [-4.3, -3.8]	0.523 ± 0.015 ± 0.033 ± 0.018	0.512 ± 0.012 ± 0.035 ± 0.019	0.514 ± 0.018 ± 0.027 ± 0.014	0.560 ± 0.016 ± 0.025 ± 0.015	0.614 ± 0.020 ± 0.028 ± 0.015	0.699 ± 0.021 ± 0.032 ± 0.022	0.760 ± 0.084 ± 0.026 ± 0.024				
[4, 6], [-3.3, -2.8]	0.514 ± 0.014 ± 0.028 ± 0.018	0.489 ± 0.016 ± 0.027 ± 0.018	0.547 ± 0.016 ± 0.026 ± 0.015	0.578 ± 0.017 ± 0.023 ± 0.016	0.620 ± 0.019 ± 0.023 ± 0.013	0.676 ± 0.017 ± 0.018 ± 0.017	0.749 ± 0.035 ± 0.025 ± 0.025				
[4, 6], [-3.8, -3.3]	0.479 ± 0.015 ± 0.030 ± 0.013	0.577 ± 0.017 ± 0.035 ± 0.014	0.541 ± 0.015 ± 0.026 ± 0.010	0.576 ± 0.016 ± 0.025 ± 0.013	0.610 ± 0.034 ± 0.024 ± 0.011	0.631 ± 0.026 ± 0.018 ± 0.013	0.774 ± 0.036 ± 0.023 ± 0.021				
[4, 6], [-4.3, -3.8]	0.445 ± 0.014 ± 0.032 ± 0.016	0.463 ± 0.021 ± 0.034 ± 0.013	0.557 ± 0.020 ± 0.036 ± 0.012	0.592 ± 0.024 ± 0.034 ± 0.013	0.581 ± 0.024 ± 0.028 ± 0.011	0.658 ± 0.026 ± 0.023 ± 0.015	0.807 ± 0.050 ± 0.029 ± 0.024				

CHAPTER 8 SUMMARY AND OUTLOOK

8.1 Summary

In this thesis, the prompt D_s^+ and D^+ production cross-sections are measured in $p\text{Pb}$ collisions at $\sqrt{s_{NN}} = 8.16\text{TeV}$ at LHCb.

The integrated cross-sections of prompt D_s^+ meson production in $p\text{Pb}$ forward data in the full and common fiducial regions are:

$$\sigma_{\text{forward}}(1 < p_T < 13 \text{ GeV}/c, 1.5 < y^* < 4.0) = 42.84 \pm 0.29(\text{stat.}) \pm 3.45(\text{syst.}) \text{ mb},$$

$$\sigma_{\text{forward}}(1 < p_T < 13 \text{ GeV}/c, 2.5 < y^* < 4.0) = 23.65 \pm 0.22(\text{stat.}) \pm 1.79(\text{syst.}) \text{ mb}.$$

The integrated cross-sections of prompt D_s^+ meson production in $\text{Pb}p$ backward data in the full and common fiducial regions are:

$$\sigma_{\text{backward}}(1 < p_T < 13 \text{ GeV}/c, -5.0 < y^* < -2.5) = 42.96 \pm 0.36(\text{stat.}) \pm 4.91(\text{syst.}) \text{ mb},$$

$$\sigma_{\text{backward}}(1 < p_T < 13 \text{ GeV}/c, -4.0 < y^* < -2.5) = 30.96 \pm 0.27(\text{stat.}) \pm 3.62(\text{syst.}) \text{ mb}.$$

The integrated cross-sections of prompt D^+ meson production in $p\text{Pb}$ forward data in the full and common fiducial regions are:

$$\sigma_{\text{forward}}(1 < p_T < 14 \text{ GeV}/c, 1.5 < y^* < 4.0) = 93.98 \pm 0.19(\text{stat.}) \pm 5.04(\text{syst.}) \text{ mb},$$

$$\sigma_{\text{forward}}(1 < p_T < 14 \text{ GeV}/c, 2.5 < y^* < 4.0) = 49.72 \pm 0.09(\text{stat.}) \pm 2.49(\text{syst.}) \text{ mb}.$$

The integrated cross-sections of prompt D^+ meson production in $\text{Pb}p$ backward data in the full and common fiducial regions are:

$$\sigma_{\text{backward}}(1 < p_T < 14 \text{ GeV}/c, -5.0 < y^* < -2.5) = 86.13 \pm 0.17(\text{stat.}) \pm 8.59(\text{syst.}) \text{ mb},$$

$$\sigma_{\text{backward}}(1 < p_T < 14 \text{ GeV}/c, -4.0 < y^* < -2.5) = 62.08 \pm 0.13(\text{stat.}) \pm 6.42(\text{syst.}) \text{ mb}.$$

Combined with the previous D mesons measurement in pp collisions at LHCb, the nuclear modification factor $R_{p\text{Pb}}$ of D_s^+ and D^+ is calculated. A significant suppression of the D_s^+ and D^+ cross-sections at forward rapidities is observed, suggesting the existence of cold nuclear matter effects in $p\text{Pb}$ collisions. In forward rapidity, the CGC and nPDF calculations are in good agreement with the data. In backward rapidity, the nPDF calculations can still describe data well at low p_T , but it is systematically higher than data at high p_T . The forward to backward ratio R_{FB} is also calculated. It reflects the same fact as $R_{p\text{Pb}}$ but with more precision: consistent with the nPDF theoretical predictions at low p_T but

shows more significant tensions at high p_T . This tension indicates that further theoretical and experimental investigations are needed for a full understanding of charm productions at backward rapidity.

The D_s^+/D^+ ratios are also studied in different p_T and rapidity intervals as a function of the event multiplicity (PV nTracks). These ratios show an significant increasing trend with the increasing event multiplicity (PV ntracks), especially at low p_T and in the backward collisions. So the D_s^+/D^+ ratio enhancement in high multiplicity pPb collisions is observed for the first time in this study. This enhancement might be explained by the charm hadronisation via sequential coalescence in a s quark rich soup, and theoretical inputs are urgently needed to further investigate the physics mechanism of this enhancement in high multiplicity small system (pPb) events.

8.2 Outlook

It can be seen from the previous research that there is also strangeness enhancement in small systems. Can't help wondering the limit of strangeness enhancement, smaller collision system? Less energy?

In order to meet the needs of more meta research in the future, LHCb has made many updates before Run 3. First, a new particle filled in the beam: oxygen. Unlike the previous lead, it is lighter and can explore new and smaller collision systems, such as $\sqrt{s_{NN}} = 7\text{TeV}$ OO collisions and $\sqrt{s_{NN}} = 9.9\text{TeV}$ pO collisions. OO collisions fill the multiplicity gap between pPb and $PbPb$ collisions ($pO < pPb < OO < PbPb$). As predicted by ALICE in Figure 8.1, the transition of strangeness enhancement from small system to large system can be studied by measuring the ratio of strange hadrons to non-strange hadrons in different systems. In addition, pO collision can also be used to solve the muon puzzle in cosmic ray. High energy cosmic rays hit the earth and collided with oxygen and nitrogen in the atmosphere and then decay. As an important decay product, muon mainly comes from two sources: prompt production (pO interaction point) and hadronic cascade production. The prediction of the latter process by the existing model has significant deviation from the experimental measurement. This is the Muon Puzzle^[149]. LHCb can accurately measure this process due to its forward acceptance.

Another major update is the upgrade of VELO. The updating of the tracking system greatly improves the reconstruction ability to adapt to the high luminosity. For example, Run 2 can only reconstruct 60% centrality class $PbPb$ collision events, but Run 3 can

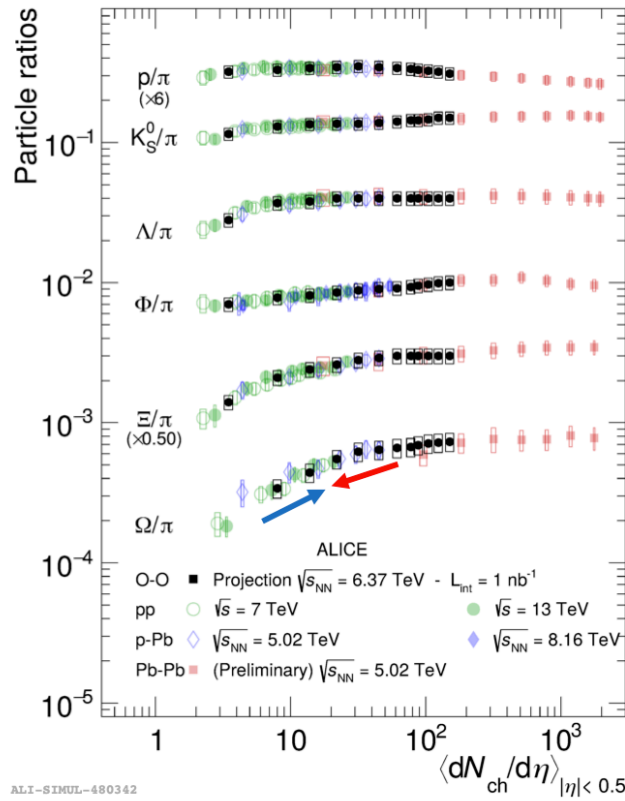


Figure 8.1 The ratio of strange hadrons to non-strange hadrons in different systems, predicted by ALICE^[150].

reconstruct 30% centrality class PbPb collision events. The System for Measuring Overlap with Gas (SMOG) based on VELO has also been upgraded to SMOG2. This is a fixed target experiment in which the proton beam hits the noble gases (helium, neon and argon...) in the storage cell. Compared with SMOG, SMOG2 can provide larger and more stable air pressure. In addition, SMOG2 distinguishes the beam-gas collision zone from the beam-beam collision zone. It is easy to simultaneous data-taking. The above upgrading is to increase our sample statistics and you can find more information here^[151]. Due to the beam energy limitation, it is impossible to run low energy collision experiments on LHC. Therefore, the fixed target experiment has become the only direction to study the low energy strangeness enhancement. Besides, fixed target mode allows to access large x region as shown in Figure 8.2 and imposes more restrictions on the nPDFs.

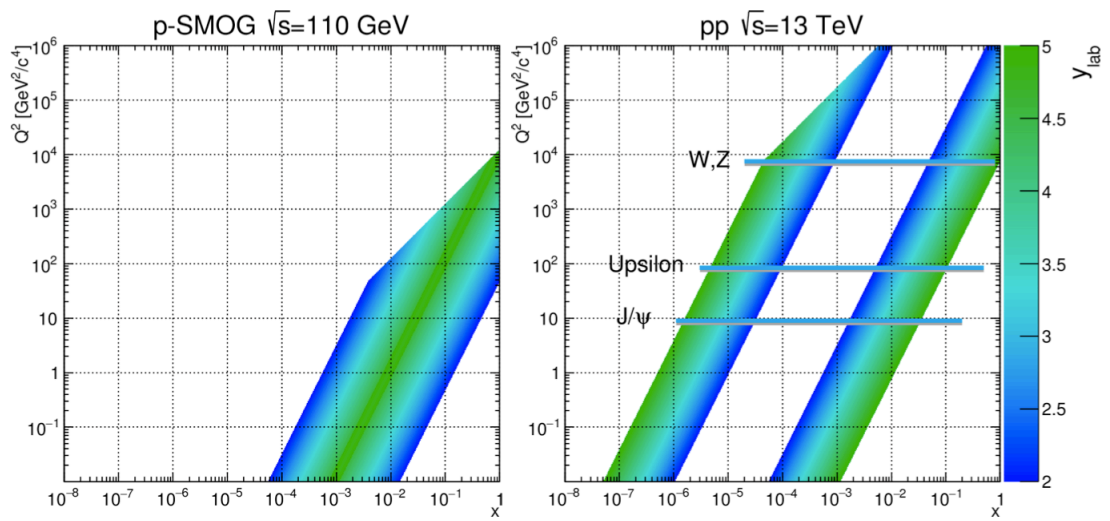


Figure 8.2 Detection area of SMOG^[152].

REFERENCES

- [1] ALTARELLI G. The Standard model of particle physics[J]. 2005.
- [2] Higgs P W. Broken Symmetries and the Masses of Gauge Bosons[J/OL]. Phys. Rev. Lett., 1964, 13: 508-509. DOI: 10.1103/PhysRevLett.13.508.
- [3] Aad G, et al. Observation of a new particle in the search for the Standard Model Higgs boson with the ATLAS detector at the LHC[J/OL]. Phys. Lett. B, 2012, 716: 1-29. DOI: 10.1016/j.physletb.2012.08.020.
- [4] Chatrchyan S, et al. Observation of a New Boson at a Mass of 125 GeV with the CMS Experiment at the LHC[J/OL]. Phys. Lett. B, 2012, 716: 30-61. DOI: 10.1016/j.physletb.2012.08.021.
- [5] Fritzsche H, Gell-Mann M, Leutwyler H. Advantages of the Color Octet Gluon Picture[J/OL]. Phys. Lett. B, 1973, 47: 365-368. DOI: 10.1016/0370-2693(73)90625-4.
- [6] Bethke S. Experimental tests of asymptotic freedom[J/OL]. Progress in Particle and Nuclear Physics, 2007, 58(2): 351-386. <https://doi.org/10.1016%2Fj.pnpnp.2006.06.001>. DOI: 10.1016/j.pnpnp.2006.06.001.
- [7] Workman R L, Others. Review of Particle Physics[J/OL]. PTEP, 2022, 2022: 083C01. DOI: 10.1093/ptep/ptac097.
- [8] Wilson K G. Confinement of Quarks[J/OL]. Phys. Rev. D, 1974, 10: 2445-2459. DOI: 10.1103/PhysRevD.10.2445.
- [9] Huovinen P, Petreczky P. QCD Equation of State and Hadron Resonance Gas[J/OL]. Nucl. Phys. A, 2010, 837: 26-53. DOI: 10.1016/j.nuclphysa.2010.02.015.
- [10] Bazavov A, et al. Equation of state in (2+1)-flavor QCD[J/OL]. Phys. Rev. D, 2014, 90: 094503. DOI: 10.1103/PhysRevD.90.094503.
- [11] Borsanyi S, Fodor Z, Hoelbling C, et al. Full result for the QCD equation of state with 2+1 flavors[J/OL]. Phys. Lett. B, 2014, 730: 99-104. DOI: 10.1016/j.physletb.2014.01.007.
- [12] Fodor Z, Katz S D. Critical point of QCD at finite T and mu, lattice results for physical quark masses[J/OL]. JHEP, 2004, 04: 050. DOI: 10.1088/1126-6708/2004/04/050.
- [13] Caines H. The Search for Critical Behavior and Other Features of the QCD Phase Diagram – Current Status and Future Prospects[J/OL]. Nucl. Phys. A, 2017, 967: 121-128. DOI: 10.1016/j.nuclphysa.2017.05.116.
- [14] Heinz U W, Jacob M. Evidence for a new state of matter: An Assessment of the results from the CERN lead beam program[J]. 2000.
- [15] Abreu M C, et al. Evidence for deconfinement of quarks and gluons from the J / psi suppression pattern measured in Pb + Pb collisions at the CERN SPS[J/OL]. Phys. Lett. B, 2000, 477: 28-36. DOI: 10.1016/S0370-2693(00)00237-9.
- [16] Andersen E, et al. Strangeness enhancement at mid-rapidity in Pb Pb collisions at 158-A-GeV/c [J/OL]. Phys. Lett. B, 1999, 449: 401-406. DOI: 10.1016/S0370-2693(99)00140-9.

REFERENCES

- [17] Aggarwal M M, et al. Freezeout parameters in central 158/A-GeV Pb-208 + Pb-208 collisions [J/OL]. Phys. Rev. Lett., 1999, 83: 926-930. DOI: 10.1103/PhysRevLett.83.926.
- [18] Agakichiev G, et al. Low mass e+ e- pair production in 158/A-GeV Pb - Au collisions at the CERN SPS, its dependence on multiplicity and transverse momentum[J/OL]. Phys. Lett. B, 1998, 422: 405-412. DOI: 10.1016/S0370-2693(98)00083-5.
- [19] Gyulassy M. The QGP discovered at RHIC[C]/NATO Advanced Study Institute: Structure and Dynamics of Elementary Matter. 2004: 159-182.
- [20] Aamodt K, et al. Elliptic flow of charged particles in Pb-Pb collisions at 2.76 TeV[J/OL]. Phys. Rev. Lett., 2010, 105: 252302. DOI: 10.1103/PhysRevLett.105.252302.
- [21] Aad G, et al. Observation of a Centrality-Dependent Dijet Asymmetry in Lead-Lead Collisions at $\sqrt{s_{NN}} = 2.77$ TeV with the ATLAS Detector at the LHC[J/OL]. Phys. Rev. Lett., 2010, 105: 252303. DOI: 10.1103/PhysRevLett.105.252303.
- [22] Aamodt K, et al. Higher harmonic anisotropic flow measurements of charged particles in Pb-Pb collisions at $\sqrt{s_{NN}}=2.76$ TeV[J/OL]. Phys. Rev. Lett., 2011, 107: 032301. DOI: 10.1103/PhysRevLett.107.032301.
- [23] Iancu E. QCD in heavy ion collisions[C/OL]//2011 European School of High-Energy Physics. 2014: 197-266. DOI: 10.5170/CERN-2014-003.197.
- [24] Gelis F. Color Glass Condensate and Glasma[J/OL]. Int. J. Mod. Phys. A, 2013, 28: 1330001. DOI: 10.1142/S0217751X13300019.
- [25] Rafelski J, Muller B. Strangeness Production in the Quark - Gluon Plasma[J/OL]. Phys. Rev. Lett., 1982, 48: 1066. DOI: 10.1103/PhysRevLett.48.1066.
- [26] Koch P, Muller B, Rafelski J. Strangeness in Relativistic Heavy Ion Collisions[J/OL]. Phys. Rept., 1986, 142: 167-262. DOI: 10.1016/0370-1573(86)90096-7.
- [27] Kaczmarek O, Zantow F. Static quark anti-quark interactions in zero and finite temperature QCD. I. Heavy quark free energies, running coupling and quarkonium binding[J/OL]. Phys. Rev. D, 2005, 71: 114510. DOI: 10.1103/PhysRevD.71.114510.
- [28] Baechler J, et al. Strangeness enhancement in central S + S collisions at 200-GeV/nucleon [J/OL]. Nucl. Phys. A, 1991, 525: 221C-226C. DOI: 10.1016/0375-9474(91)90328-4.
- [29] Antinori F, et al. Study of the production of strange and multi-strange particles in lead lead interactions at the CERN SPS: The NA57 experiment[J/OL]. Nucl. Phys. A, 2001, 681: 165-173. DOI: 10.1016/S0375-9474(00)00499-1.
- [30] Agakishiev G, et al. Strangeness Enhancement in Cu+Cu and Au+Au Collisions at $\sqrt{s_{NN}} = 200$ GeV[J/OL]. Phys. Rev. Lett., 2012, 108: 072301. DOI: 10.1103/PhysRevLett.108.072301.
- [31] Abelev B B, et al. Multi-strange baryon production at mid-rapidity in Pb-Pb collisions at $\sqrt{s_{NN}} = 2.76$ TeV[J/OL]. Phys. Lett. B, 2014, 728: 216-227. DOI: 10.1016/j.physletb.2014.05.052.
- [32] Zhao J, Zhou K, Chen S, et al. Heavy flavors under extreme conditions in high energy nuclear collisions[J/OL]. Prog. Part. Nucl. Phys., 2020, 114: 103801. DOI: 10.1016/j.ppnp.2020.103801.
- [33] Mangano M L. Two lectures on heavy quark production in hadronic collisions[J/OL]. Proc. Int. Sch. Phys. Fermi, 1998, 137: 95-137. DOI: 10.3254/978-1-61499-222-6-95.

REFERENCES

- [34] Dulat S, Hou T J, Gao J, et al. New parton distribution functions from a global analysis of quantum chromodynamics[J/OL]. *Phys. Rev. D*, 2016, 93(3): 033006. DOI: 10.1103/PhysRevD.93.033006.
- [35] Ball R D, et al. Parton distributions from high-precision collider data[J/OL]. *Eur. Phys. J. C*, 2017, 77(10): 663. DOI: 10.1140/epjc/s10052-017-5199-5.
- [36] Gribov V N, Lipatov L N. Deep inelastic e p scattering in perturbation theory[J]. *Sov. J. Nucl. Phys.*, 1972, 15: 438-450.
- [37] Kartvelishvili V G, Likhoded A K, Petrov V A. On the Fragmentation Functions of Heavy Quarks Into Hadrons[J/OL]. *Phys. Lett. B*, 1978, 78: 615-617. DOI: 10.1016/0370-2693(78)90653-6.
- [38] Metz A, Vossen A. Parton Fragmentation Functions[J/OL]. *Prog. Part. Nucl. Phys.*, 2016, 91: 136-202. DOI: 10.1016/j.pnpnp.2016.08.003.
- [39] Harland-Lang L A, Martin A D, Motylinski P, et al. Parton distributions in the LHC era: MMHT 2014 PDFs[J/OL]. *Eur. Phys. J. C*, 2015, 75(5): 204. DOI: 10.1140/epjc/s10052-015-3397-6.
- [40] Bjorken J D. Energy loss of energetic partons in quark - gluon plasma: Possible extinction of high p(t) jets in hadron - hadron collisions[C]//1982.
- [41] Adcox K, et al. Suppression of hadrons with large transverse momentum in central Au+Au collisions at $\sqrt{s_{NN}} = 130$ -GeV[J/OL]. *Phys. Rev. Lett.*, 2002, 88: 022301. DOI: 10.1103/PhysRevLett.88.022301.
- [42] Miller M L, Reygers K, Sanders S J, et al. Glauber modeling in high energy nuclear collisions [J/OL]. *Ann. Rev. Nucl. Part. Sci.*, 2007, 57: 205-243. DOI: 10.1146/annurev.nucl.57.090506.123020.
- [43] Acharya S, et al. Prompt D^0 , D^+ , and D^{*+} production in Pb–Pb collisions at $\sqrt{s_{NN}} = 5.02$ TeV [J/OL]. *JHEP*, 2022, 01: 174. DOI: 10.1007/JHEP01(2022)174.
- [44] Xu J, Liao J, Gyulassy M. Consistency of Perfect Fluidity and Jet Quenching in semi-Quark-Gluon Monopole Plasmas[J/OL]. *Chin. Phys. Lett.*, 2015, 32(9): 092501. DOI: 10.1088/0256-307X/32/9/092501.
- [45] Stojku S, Ilic B, Djordjevic M, et al. Extracting the temperature dependence in high- p_{\perp} particle energy loss[J/OL]. *Phys. Rev. C*, 2021, 103(2): 024908. DOI: 10.1103/PhysRevC.103.024908.
- [46] Kang Z B, Ringer F, Vitev I. Effective field theory approach to open heavy flavor production in heavy-ion collisions[J/OL]. *JHEP*, 2017, 03: 146. DOI: 10.1007/JHEP03(2017)146.
- [47] Acharya S, et al. Measurement of D^0 , D^+ , D^{*+} and D_s^+ production in Pb-Pb collisions at $\sqrt{s_{NN}} = 5.02$ TeV[J/OL]. *JHEP*, 2018, 10: 174. DOI: 10.1007/JHEP10(2018)174.
- [48] Acharya S, et al. Measurement of prompt D^0 , D^+ , D^{*+} , and D_s^+ production in p–Pb collisions at $\sqrt{s_{NN}} = 5.02$ TeV[J/OL]. *JHEP*, 2019, 12: 092. DOI: 10.1007/JHEP12(2019)092.
- [49] Paakkinen P. Nuclear parton distribution functions[J]. *Frascati Phys. Ser.*, 2017: 33-40.
- [50] Armesto N. Nuclear shadowing[J/OL]. *Journal of Physics G: Nuclear and Particle Physics*, 2006, 32(11): R367-R393. <https://doi.org/10.1088/0954-3899/32/11/r01>. DOI: 10.1088/0954-3899/32/11/r01.

REFERENCES

- [51] Saito K, Uchiyama T. Effect of the Fermi Motion on Nuclear Structure Functions and the EMC Effect[J/OL]. *Z. Phys. A*, 1985, 322: 299. DOI: 10.1007/BF01411895.
- [52] Geesaman D F, Saito K, Thomas A W. The nuclear EMC effect[J/OL]. *Ann. Rev. Nucl. Part. Sci.*, 1995, 45: 337-390. DOI: 10.1146/annurev.ns.45.120195.002005.
- [53] Brodsky S J, Lu H J. Shadowing and Antishadowing of Nuclear Structure Functions[J/OL]. *Phys. Rev. Lett.*, 1990, 64: 1342. DOI: 10.1103/PhysRevLett.64.1342.
- [54] Nikolaev N N, Zakharov B G. Color transparency and scaling properties of nuclear shadowing in deep inelastic scattering[J/OL]. *Z. Phys. C*, 1991, 49: 607-618. DOI: 10.1007/BF01483577.
- [55] Stodolsky L. Hadron-like behavior of gamma, neutrino nuclear cross-sections[J/OL]. *Phys. Rev. Lett.*, 1967, 18: 135-137. DOI: 10.1103/PhysRevLett.18.135.
- [56] Gribov L V, Levin E M, Ryskin M G. Semihard Processes in QCD[J/OL]. *Phys. Rept.*, 1983, 100: 1-150. DOI: 10.1016/0370-1573(83)90022-4.
- [57] Eskola K J, Paakkinen P, Paukkunen H, et al. EPPS21: a global QCD analysis of nuclear PDFs [J/OL]. *Eur. Phys. J. C*, 2022, 82(5): 413. DOI: 10.1140/epjc/s10052-022-10359-0.
- [58] Eskola K J, Paakkinen P, Paukkunen H, et al. EPPS16: Nuclear parton distributions with LHC data[J/OL]. *Eur. Phys. J. C*, 2017, 77(3): 163. DOI: 10.1140/epjc/s10052-017-4725-9.
- [59] Sirunyan A M, et al. Constraining gluon distributions in nuclei using dijets in proton-proton and proton-lead collisions at $\sqrt{s_{NN}} = 5.02$ TeV[J/OL]. *Phys. Rev. Lett.*, 2018, 121(6): 062002. DOI: 10.1103/PhysRevLett.121.062002.
- [60] Aaij R, et al. Study of prompt D^0 meson production in p Pb collisions at $\sqrt{s_{NN}} = 5$ TeV[J/OL]. *JHEP*, 2017, 10: 090. DOI: 10.1007/JHEP10(2017)090.
- [61] Sirunyan A M, et al. Observation of nuclear modifications in W^\pm boson production in p Pb collisions at $\sqrt{s_{NN}} = 8.16$ TeV[J/OL]. *Phys. Lett. B*, 2020, 800: 135048. DOI: 10.1016/j.physletb.2019.135048.
- [62] Kovarik K, et al. nCTEQ15 - Global analysis of nuclear parton distributions with uncertainties in the CTEQ framework[J/OL]. *Phys. Rev. D*, 2016, 93(8): 085037. DOI: 10.1103/PhysRevD.93.085037.
- [63] Mueller A H, Qiu J w. Gluon Recombination and Shadowing at Small Values of x [J/OL]. *Nucl. Phys. B*, 1986, 268: 427-452. DOI: 10.1016/0550-3213(86)90164-1.
- [64] Altarelli G, Parisi G. Asymptotic Freedom in Parton Language[J/OL]. *Nucl. Phys. B*, 1977, 126: 298-318. DOI: 10.1016/0550-3213(77)90384-4.
- [65] Caporale F, Chachamis G, Murdaca B, et al. Balitsky-Fadin-Kuraev-Lipatov Predictions for Inclusive Three Jet Production at the LHC[J/OL]. *Phys. Rev. Lett.*, 2016, 116(1): 012001. DOI: 10.1103/PhysRevLett.116.012001.
- [66] Kovchegov Y V. Unitarization of the BFKL pomeron on a nucleus[J/OL]. *Phys. Rev. D*, 2000, 61: 074018. DOI: 10.1103/PhysRevD.61.074018.
- [67] Kovner A, Levin E, Li M, et al. The JIMWLK evolution and the s-channel unitarity[J/OL]. *JHEP*, 2020, 09: 199. DOI: 10.1007/JHEP09(2020)199.
- [68] Gelis F, Iancu E, Jalilian-Marian J, et al. The Color Glass Condensate[J/OL]. *Ann. Rev. Nucl. Part. Sci.*, 2010, 60: 463-489. DOI: 10.1146/annurev.nucl.010909.083629.

REFERENCES

- [69] Ducloué B, Lappi T, Mäntysaari H. Forward J/ψ and D meson nuclear suppression at the LHC [J/OL]. Nucl. Part. Phys. Proc., 2017, 289-290: 309-312. DOI: 10.1016/j.nuclphysbps.2017.05.071.
- [70] Gelis F. The initial stages of heavy-ion collisions in the colour glass condensate framework [J/OL]. Pramana, 2015, 84(5): 685-701. DOI: 10.1007/s12043-015-0974-z.
- [71] Antreasyan D, Cronin J W, Frisch H J, et al. Production of Hadrons at Large Transverse Momentum in 200-GeV, 300-GeV and 400-GeV p p and p n Collisions[J/OL]. Phys. Rev. D, 1979, 19: 764-778. DOI: 10.1103/PhysRevD.19.764.
- [72] Accardi A. Cronin effect in proton nucleus collisions: A Survey of theoretical models[J]. 2002.
- [73] Kang Z B, Vitev I, Xing H. Multiple scattering effects on inclusive particle production in the large-x regime[J/OL]. Phys. Rev. D, 2013, 88: 054010. DOI: 10.1103/PhysRevD.88.054010.
- [74] Kang Z B, Vitev I, Wang E, et al. Multiple scattering effects on heavy meson production in p+A collisions at backward rapidity[J/OL]. Phys. Lett. B, 2015, 740: 23-29. DOI: 10.1016/j.physletb.2014.11.024.
- [75] Acharya S, et al. Production of muons from heavy-flavour hadron decays in p-Pb collisions at $\sqrt{s_{NN}} = 5.02$ TeV[J/OL]. Phys. Lett. B, 2017, 770: 459-472. DOI: 10.1016/j.physletb.2017.03.049.
- [76] Adare A, et al. Cold-Nuclear-Matter Effects on Heavy-Quark Production at Forward and Backward Rapidity in d+Au Collisions at $\sqrt{s_{NN}} = 200$ GeV[J/OL]. Phys. Rev. Lett., 2014, 112(25): 252301. DOI: 10.1103/PhysRevLett.112.252301.
- [77] Acharya S, et al. Charm-quark fragmentation fractions and production cross section at midrapidity in pp collisions at the LHC[J/OL]. Phys. Rev. D, 2022, 105(1): L011103. DOI: 10.1103/PhysRevD.105.L011103.
- [78] Greco V, Ko C M, Rapp R. Quark coalescence for charmed mesons in ultrarelativistic heavy ion collisions[J/OL]. Phys. Lett. B, 2004, 595: 202-208. DOI: 10.1016/j.physletb.2004.06.064.
- [79] Kuznetsova I, Rafelski J. Heavy flavor hadrons in statistical hadronization of strangeness-rich QGP[J/OL]. Eur. Phys. J. C, 2007, 51: 113-133. DOI: 10.1140/epjc/s10052-007-0268-9.
- [80] Ravagli L, Rapp R. Quark Coalescence based on a Transport Equation[J/OL]. Phys. Lett. B, 2007, 655: 126-131. DOI: 10.1016/j.physletb.2007.07.043.
- [81] He M, Fries R J, Rapp R. D_s -Meson as Quantitative Probe of Diffusion and Hadronization in Nuclear Collisions[J/OL]. Phys. Rev. Lett., 2013, 110(11): 112301. DOI: 10.1103/PhysRevLett.110.112301.
- [82] Zhao J, Shi S, Xu N, et al. Sequential Coalescence with Charm Conservation in High Energy Nuclear Collisions[J]. 2018.
- [83] Acharya S, et al. Measurement of prompt D_s^+ -meson production and azimuthal anisotropy in Pb-Pb collisions at $\sqrt{s_{NN}}=5.02$ TeV[J/OL]. Phys. Lett. B, 2022, 827: 136986. DOI: 10.1016/j.physletb.2022.136986.
- [84] Adam J, et al. Observation of D_s^{\pm}/D^0 enhancement in Au+Au collisions at $\sqrt{s_{NN}} = 200$ GeV [J/OL]. Phys. Rev. Lett., 2021, 127: 092301. DOI: 10.1103/PhysRevLett.127.092301.

REFERENCES

- [85] Acharya S, et al. Measurement of beauty and charm production in pp collisions at $\sqrt{s} = 5.02$ TeV via non-prompt and prompt D mesons[J/OL]. JHEP, 2021, 05: 220. DOI: 10.1007/JHEP05(2021)220.
- [86] Acharya S, et al. Measurement of D^0 , D^+ , D^{*+} and D_s^+ production in pp collisions at $\sqrt{s} = 5.02$ TeV with ALICE[J/OL]. Eur. Phys. J. C, 2019, 79(5): 388. DOI: 10.1140/epjc/s10052-019-6873-6.
- [87] Adam J, et al. Enhanced production of multi-strange hadrons in high-multiplicity proton-proton collisions[J/OL]. Nature Phys., 2017, 13: 535-539. DOI: 10.1038/nphys4111.
- [88] Abelev B B, et al. Multiplicity Dependence of Pion, Kaon, Proton and Lambda Production in p-Pb Collisions at $\sqrt{s_{NN}} = 5.02$ TeV[J/OL]. Phys. Lett. B, 2014, 728: 25-38. DOI: 10.1016/j.physletb.2013.11.020.
- [89] Adam J, et al. Multi-strange baryon production in p-Pb collisions at $\sqrt{s_{NN}} = 5.02$ TeV[J/OL]. Phys. Lett. B, 2016, 758: 389-401. DOI: 10.1016/j.physletb.2016.05.027.
- [90] Sjostrand T, Mrenna S, Skands P Z. A Brief Introduction to PYTHIA 8.1[J/OL]. Comput. Phys. Commun., 2008, 178: 852-867. DOI: 10.1016/j.cpc.2008.01.036.
- [91] Pierog T, Karpenko I, Katzy J M, et al. EPOS LHC: Test of collective hadronization with data measured at the CERN Large Hadron Collider[J/OL]. Phys. Rev. C, 2015, 92(3): 034906. DOI: 10.1103/PhysRevC.92.034906.
- [92] Bierlich C, Christiansen J R. Effects of color reconnection on hadron flavor observables[J/OL]. Phys. Rev. D, 2015, 92(9): 094010. DOI: 10.1103/PhysRevD.92.094010.
- [93] Kanakubo Y, Okai M, Tachibana Y, et al. Enhancement of strange baryons in high-multiplicity proton-proton and proton-nucleus collisions[J/OL]. PTEP, 2018, 2018(12): 121D01. DOI: 10.1093/ptep/pty129.
- [94] Kanakubo Y, Okai M, Tachibana Y, et al. Strangeness Enhancement in p+p, p+Pb and Pb+Pb Collisions at LHC Energies[J/OL]. JPS Conf. Proc., 2019, 26: 031021. DOI: 10.7566/JPSCP.26.031021.
- [95] Kanakubo Y, Tachibana Y, Hirano T. Unified description of hadron yield ratios from dynamical core-corona initialization[J/OL]. Phys. Rev. C, 2020, 101(2): 024912. DOI: 10.1103/PhysRevC.101.024912.
- [96] Biro T S, Nielsen H B, Knoll J. Color Rope Model for Extreme Relativistic Heavy Ion Collisions [J/OL]. Nucl. Phys. B, 1984, 245: 449-468. DOI: 10.1016/0550-3213(84)90441-3.
- [97] Bierlich C, Gustafson G, Lönnblad L, et al. Effects of Overlapping Strings in pp Collisions [J/OL]. JHEP, 2015, 03: 148. DOI: 10.1007/JHEP03(2015)148.
- [98] Andersson B, Gustafson G, Söderberg B. A general model for jet fragmentation[J/OL]. European Physical Journal C. Particles and Fields, 1983, 20(4): 317-329. DOI: 10.1007/BF01407824.
- [99] Andersson B, Gustafson G. Semiclassical Models for Gluon Jets and Leptoproduction Based on the Massless Relativistic String[J/OL]. Z. Phys. C, 1980, 3: 223. DOI: 10.1007/BF01577421.
- [100] Schwinger J S. On gauge invariance and vacuum polarization[J/OL]. Phys. Rev., 1951, 82: 664-679. DOI: 10.1103/PhysRev.82.664.

REFERENCES

- [101] Sjöstrand T, Mrenna S, Skands P. A brief introduction to PYTHIA 8.1[J/OL]. Computer Physics Communications, 2008, 178(11): 852-867. <https://doi.org/10.1016/j.cpc.2008.01.036>. DOI: 10.1016/j.cpc.2008.01.036.
- [102] Bierlich C, Gustafson G, Lönnblad L, et al. The Angantyr model for Heavy-Ion Collisions in PYTHIA8[J/OL]. JHEP, 2018, 10: 134. DOI: 10.1007/JHEP10(2018)134.
- [103] Nayak R, Pal S, Dash S. Effect of rope hadronization on strangeness enhancement in p–p collisions at LHC energies[J/OL]. Phys. Rev. D, 2019, 100(7): 074023. DOI: 10.1103/PhysRevD.100.074023.
- [104] Evidence for modification of b quark hadronization in high-multiplicity pp collisions at $\sqrt{s} = 13$ TeV[J]. 2022.
- [105] Evans L, Bryant P. LHC machine[J/OL]. Journal of Instrumentation, 2008, 3(08): S08001-S08001. <https://doi.org/10.1088/1748-0221/3/08/s08001>.
- [106] Mobs E. The CERN accelerator complex in 2019. Complexe des accélérateurs du CERN en 2019[J/OL]. 2019. <https://cds.cern.ch/record/2684277>.
- [107] Aaij R, et al. Observation of $J/\psi p$ Resonances Consistent with Pentaquark States in $\Lambda_b^0 \rightarrow J/\psi K^- p$ Decays[J/OL]. Phys. Rev. Lett., 2015, 115: 072001. DOI: 10.1103/PhysRevLett.115.072001.
- [108] Aaij R, et al. Observation of CP Violation in Charm Decays[J/OL]. Phys. Rev. Lett., 2019, 122(21): 211803. DOI: 10.1103/PhysRevLett.122.211803.
- [109] Aaij R, et al. Test of lepton universality in beauty-quark decays[J/OL]. Nature Phys., 2022, 18(3): 277-282. DOI: 10.1038/s41567-021-01478-8.
- [110] Elsässer C. $\bar{b}b$ production angle plots[EB/OL]. https://lhcb.web.cern.ch/lhcb/speakersbureau/html/bb_ProductionAngles.html.
- [111] LHCb detector performance[J/OL]. International Journal of Modern Physics A, 2015, 30(07): 1530022. <https://doi.org/10.1142/2Fs0217751x15300227>. DOI: 10.1142/s0217751x15300227.
- [112] Aaij R, Affolder A, Akiba K, et al. Performance of the LHCb vertex locator[J/OL]. Journal of Instrumentation, 2014, 9(09): P09007-P09007. <https://doi.org/10.1088/1748-0221/9/09/p09007>. DOI: 10.1088/1748-0221/9/09/p09007.
- [113] Alves A A, Jr., et al. The LHCb Detector at the LHC[J/OL]. JINST, 2008, 3: S08005. DOI: 10.1088/1748-0221/3/08/S08005.
- [114] Performance of the LHCb outer tracker[J/OL]. Journal of Instrumentation, 2014, 9(01): P01002-P01002. <https://doi.org/10.1088/1748-0221/9/01/p01002>. DOI: 10.1088/1748-0221/9/01/p01002.
- [115] Abellán Beteta C, et al. Calibration and performance of the LHCb calorimeters in Run 1 and 2 at the LHC[J]. 2020.
- [116] Aaij R, et al. Design and performance of the LHCb trigger and full real-time reconstruction in Run 2 of the LHC[J/OL]. JINST, 2019, 14(04): P04013. DOI: 10.1088/1748-0221/14/04/P04013.

REFERENCES

- [117] Graziani G, Massacrier L M, Robbe P, et al. LHCb Physics Motivations for the 2016 Heavy-ion LHC run[R/OL]. Geneva: CERN, 2016. <https://cds.cern.ch/record/2145943>.
- [118] LHCb. Documentation for the 2016 p-pb/pb-p run[EB/OL]. . <https://twiki.cern.ch/twiki/bin/view/LHCbPhysics/ProtonLead2016>.
- [119] LHCb. End of 2016 data taking period[EB/OL]. . <https://lhcb-outreach.web.cern.ch/2016/12/05/end-of-2016-data-taking-period/>.
- [120] Clemencic M, Corti G, Easo S, et al. The LHCb simulation application, gauss: Design, evolution and experience[J/OL]. *Journal of Physics: Conference Series*, 2011, 331(3): 032023. <https://doi.org/10.1088/1742-6596/331/3/032023>.
- [121] Pierog T, Karpenko I, Katzy J M, et al. EPOS LHC: Test of collective hadronization with data measured at the CERN large hadron collider[J/OL]. *Physical Review C*, 2015, 92(3). <https://doi.org/10.1103/PhysRevC.92.034906>. DOI: 10.1103/physrevc.92.034906.
- [122] Lange D J. The evtgen particle decay simulation package[J/OL]. *Nuclear Instruments and Methods in Physics Research Section A: Accelerators, Spectrometers, Detectors and Associated Equipment*, 2001, 462(1): 152-155. <https://www.sciencedirect.com/science/article/pii/S0168900201000894>. DOI: [https://doi.org/10.1016/S0168-9002\(01\)00089-4](https://doi.org/10.1016/S0168-9002(01)00089-4).
- [123] LHCb. The decfiles package[EB/OL]. . <http://lhcbdoc.web.cern.ch/lhcbdoc/decfiles/>.
- [124] Agostinelli S, et al. GEANT4—a simulation toolkit[J/OL]. *Nucl. Instrum. Meth. A*, 2003, 506: 250-303. DOI: 10.1016/S0168-9002(03)01368-8.
- [125] Li H, Liu G, Ma R, et al. Measurement of Z production cross-sections in proton-lead collisions at $\sqrt{s_{NN}} = 8.16$ TeV[J/OL]. 2019. <https://cds.cern.ch/record/2687462>.
- [126] Aaij R, et al. Precision luminosity measurements at LHCb.[J/OL]. *JINST*, 2014, 9(LHCB-PAPER-2014-047. LHCB-PAPER-2014-047. CERN-PH-EP-2014-221): P12005. 99 p. <https://cds.cern.ch/record/1951625>. DOI: 10.1088/1748-0221/9/12/P12005.
- [127] Alexander J P, Berkelman K, Cassel D G, et al. Absolute measurement of hadronic branching fractions of the D_s^+ meson[J/OL]. *Phys. Rev. Lett.*, 2008, 100: 161804. <https://link.aps.org/doi/10.1103/PhysRevLett.100.161804>.
- [128] Zyla P, et al. Review of Particle Physics[J/OL]. *PTEP*, 2020, 2020(8): 083C01. DOI: 10.1093/ptep/ptaa104.
- [129] Zhang Y. L0 for the 8 tev ppb run[Z]. 2016.
- [130] Zhang Y. Hlt1 for the 8 tev ppb run[Z]. 2016.
- [131] Pivk M, Le Diberder F. : A statistical tool to unfold data distributions[J/OL]. *Nuclear Instruments and Methods in Physics Research Section A: Accelerators, Spectrometers, Detectors and Associated Equipment*, 2005, 555(1-2): 356–369. <http://dx.doi.org/10.1016/j.nima.2005.08.106>.
- [132] Sjöstrand T, Ask S, Christiansen J R, et al. An introduction to PYTHIA 8.2[J/OL]. *Comput. Phys. Commun.*, 2015, 191: 159-177. DOI: 10.1016/j.cpc.2015.01.024.
- [133] collaboration T L. Measurement of the track reconstruction efficiency at LHCb[J/OL]. *Journal of Instrumentation*, 2015, 10(02): P02007-P02007. <https://doi.org/10.1088/1748-0221/10/02/p02007>. DOI: 10.1088/1748-0221/10/02/p02007.

REFERENCES

- [134] Marianna Fontana. The particle identification (pid) in lhcb,[EB/OL]. 2017. https://twiki.cern.ch/twiki/pub/LHCbPhysics/ChargedPID/UK_students_PID_MFontana.pdf, Last accessed on 2022-08-26.
- [135] Lupton O, Anderlini L, Sciascia B, et al. Calibration samples for particle identification at LHCb in Run 2[R/OL]. Geneva: CERN, 2016. <https://cds.cern.ch/record/2134057>.
- [136] LHCb. Pidcalib packages,[EB/OL]. 2021. <https://twiki.cern.ch/twiki/bin/view/LHCb/PIDCalibPackage>, Last accessed on 2022-05-25.
- [137] Aaij R, et al. Study of prompt D^0 meson production in p Pb collisions at $\sqrt{s_{NN}} = 5$ TeV[J/OL]. JHEP, 2017, 10: 090. DOI: 10.1007/JHEP10(2017)090.
- [138] Aaij R, et al. Measurement of the track reconstruction efficiency at LHCb[J/OL]. JINST, 2015, 10: P02007. DOI: 10.1088/1748-0221/10/02/P02007.
- [139] Tolk S, Albrecht J, Dettori F, et al. Data driven trigger efficiency determination at LHCb[J]. 2014.
- [140] Aaij R, et al. Measurements of prompt charm production cross-sections in pp collisions at $\sqrt{s} = 5$ TeV[J/OL]. JHEP, 2017, 06: 147. DOI: 10.1007/JHEP06(2017)147.
- [141] Aaij R, et al. Measurements of prompt charm production cross-sections in pp collisions at $\sqrt{s} = 13$ TeV[J/OL]. JHEP, 2016, 03: 159. DOI: 10.1007/JHEP03(2016)159.
- [142] Measurement of the prompt D^0 nuclear modification factor in p Pb collisions at $\sqrt{s_{NN}} = 8.16$ TeV[J]. 2022.
- [143] Shao H S. HELAC-Onia: An automatic matrix element generator for heavy quarkonium physics [J/OL]. Comput. Phys. Commun., 2013, 184: 2562-2570. DOI: 10.1016/j.cpc.2013.05.023.
- [144] Shao H S. HELAC-Onia 2.0: an upgraded matrix-element and event generator for heavy quarkonium physics[J/OL]. Comput. Phys. Commun., 2016, 198: 238-259. DOI: 10.1016/j.cpc.2015.09.011.
- [145] Kusina A, Lansberg J P, Schienbein I, et al. Gluon shadowing in heavy-flavor production at the lhcb[J/OL]. Phys. Rev. Lett., 2018, 121: 052004. <https://link.aps.org/doi/10.1103/PhysRevLett.121.052004>.
- [146] Ducloué B, Lappi T, Mäntysaari H. Forward J/ψ production in proton-nucleus collisions at high energy[J/OL]. Physical Review D, 2015, 91(11). <https://doi.org/10.1103/PhysRevD.91.114005>. DOI: 10.1103/physrevd.91.114005.
- [147] Ma Y Q, Tribedy P, Venugopalan R, et al. Event engineering studies for heavy flavor production and hadronization in high multiplicity hadron-hadron and hadron-nucleus collisions [J/OL]. Physical Review D, 2018, 98(7). <https://doi.org/10.1103/PhysRevD.98.074025>. DOI: 10.1103/physrevd.98.074025.
- [148] Lansberg J P, Shao H S. Towards an automated tool to evaluate the impact of the nuclear modification of the gluon density on quarkonium, D and B meson production in proton–nucleus collisions[J/OL]. Eur. Phys. J., 2017, C77(1): 1. DOI: 10.1140/epjc/s10052-016-4575-x.
- [149] Albrecht J, et al. The Muon Puzzle in cosmic-ray induced air showers and its connection to the Large Hadron Collider[J/OL]. Astrophys. Space Sci., 2022, 367(3): 27. DOI: 10.1007/s10509-022-04054-5.

REFERENCES

- [150] Brewer J, Mazeliauskas A, van der Schee W. Opportunities of OO and pO collisions at the LHC [C]//Opportunities of OO and pO collisions at the LHC. 2021.
- [151] LHCb Collaboration C M. LHCb SMOG Upgrade[R/OL]. Geneva: CERN, 2019. <https://cds.cern.ch/record/2673690>. DOI: 10.17181/CERN.SAQC.EOWH.
- [152] Bursche A, et al. Physics opportunities with the fixed-target program of the LHCb experiment using an unpolarized gas target[J]. 2018.

APPENDIX A EFFICIENCY TABLES

The efficiencies only show statistical uncertainties.

Table A.1 Geometrical acceptance efficiencies in bins of D_s^+ p_T and y^* for Fwd collision configuration.

p_T [GeV/c]\ y^*	[1.5, 2]	[2, 2.5]	[2.5, 3]	[3, 3.5]	[3.5, 4]
[1, 2]	0.850 ± 0.002	0.950 ± 0.001	0.961 ± 0.001	0.892 ± 0.002	0.729 ± 0.003
[2, 3]	0.897 ± 0.002	0.977 ± 0.001	0.984 ± 0.001	0.954 ± 0.002	0.858 ± 0.003
[3, 4]	0.930 ± 0.002	0.992 ± 0.001	0.995 ± 0.001	0.985 ± 0.001	0.948 ± 0.002
[4, 5]	0.954 ± 0.002	0.998 ± 0.001	0.999 ± 0.000	0.995 ± 0.001	0.978 ± 0.002
[5, 6]	0.967 ± 0.003	0.999 ± 0.001	0.998 ± 0.001	0.997 ± 0.001	0.986 ± 0.003
[6, 7]	0.981 ± 0.003	1.000 ± 0.001	0.997 ± 0.001	0.998 ± 0.001	0.992 ± 0.003
[7, 8]	0.988 ± 0.003	1.000 ± 0.001	1.000 ± 0.001	1.000 ± 0.001	0.987 ± 0.005
[8, 9]	0.990 ± 0.003	1.000 ± 0.001	1.000 ± 0.001	0.998 ± 0.003	0.988 ± 0.007
[9, 10]	0.991 ± 0.004	1.000 ± 0.002	1.000 ± 0.002	0.997 ± 0.004	1.000 ± 0.004
[10, 11]	0.998 ± 0.003	1.000 ± 0.003	1.000 ± 0.003	1.000 ± 0.004	1.000 ± 0.007
[11, 12]	1.000 ± 0.003	1.000 ± 0.004	1.000 ± 0.006	1.000 ± 0.007	1.000 ± 0.012
[12, 13]	1.000 ± 0.005	1.000 ± 0.007	1.000 ± 0.007	1.000 ± 0.011	1.000 ± 0.020

APPENDIX A EFFICIENCY TABLES

Table A.2 Geometrical acceptance efficiencies in bins of D_s^+ p_T and y^* for Bwd collision configuration.

p_T [GeV/c]\y*	[-3, -2.5]	[-3.5, -3]	[-4, -3.5]	[-4.5, -4]	[-5, -4.5]
[1, 2]	0.880 ± 0.002	0.956 ± 0.001	0.957 ± 0.001	0.877 ± 0.002	0.689 ± 0.003
[2, 3]	0.921 ± 0.002	0.982 ± 0.001	0.981 ± 0.001	0.946 ± 0.002	0.835 ± 0.003
[3, 4]	0.948 ± 0.002	0.994 ± 0.001	0.995 ± 0.001	0.982 ± 0.001	0.935 ± 0.003
[4, 5]	0.966 ± 0.002	0.999 ± 0.000	0.998 ± 0.001	0.995 ± 0.001	0.973 ± 0.002
[5, 6]	0.979 ± 0.002	1.000 ± 0.000	0.998 ± 0.001	0.996 ± 0.001	0.982 ± 0.003
[6, 7]	0.986 ± 0.002	1.000 ± 0.001	0.997 ± 0.001	0.997 ± 0.001	0.991 ± 0.003
[7, 8]	0.995 ± 0.002	1.000 ± 0.001	1.000 ± 0.001	0.999 ± 0.002	0.982 ± 0.006
[8, 9]	0.997 ± 0.002	1.000 ± 0.001	1.000 ± 0.001	0.996 ± 0.003	0.987 ± 0.007
[9, 10]	0.994 ± 0.003	1.000 ± 0.002	1.000 ± 0.002	0.997 ± 0.004	1.000 ± 0.005
[10, 11]	0.998 ± 0.003	1.000 ± 0.003	1.000 ± 0.003	1.000 ± 0.005	1.000 ± 0.008
[11, 12]	1.000 ± 0.004	1.000 ± 0.004	1.000 ± 0.006	1.000 ± 0.007	1.000 ± 0.014
[12, 13]	1.000 ± 0.005	1.000 ± 0.007	1.000 ± 0.007	1.000 ± 0.012	1.000 ± 0.021

Table A.3 Geometrical acceptance efficiencies in bins of D_s^+ p_T and y^* and PV nTracks for Fwd collision configuration.

p_T [GeV/c], y^* \PVnTracks	[10, 60]	[60, 80]	[80, 100]	[100, 120]	[120, 140]	[140, 200]
[2, 4], [1.8, 2.3]	0.9667 ± 0.0009	0.9667 ± 0.0009	0.9667 ± 0.0009	0.9667 ± 0.0009	0.9667 ± 0.0009	0.9667 ± 0.0009
[2, 4], [2.3, 2.8]	0.9911 ± 0.0005	0.9911 ± 0.0005	0.9911 ± 0.0005	0.9911 ± 0.0005	0.9911 ± 0.0005	0.9911 ± 0.0005
[2, 4], [2.8, 3.3]	0.9758 ± 0.0009	0.9758 ± 0.0009	0.9758 ± 0.0009	0.9758 ± 0.0009	0.9758 ± 0.0009	0.9758 ± 0.0009
[4, 6], [1.8, 2.3]	0.9912 ± 0.0008	0.9912 ± 0.0008	0.9912 ± 0.0008	0.9912 ± 0.0008	0.9912 ± 0.0008	0.9912 ± 0.0008
[4, 6], [2.3, 2.8]	0.9988 ± 0.0003	0.9988 ± 0.0003	0.9988 ± 0.0003	0.9988 ± 0.0003	0.9988 ± 0.0003	0.9988 ± 0.0003
[4, 6], [2.8, 3.3]	0.9973 ± 0.0005	0.9973 ± 0.0005	0.9973 ± 0.0005	0.9973 ± 0.0005	0.9973 ± 0.0005	0.9973 ± 0.0005

Table A.4 Geometrical acceptance efficiencies in bins of D_s^+ p_T and y^* and PV nTracks for Bwd collision configuration.

p_T [GeV/c], y^* \PVnTracks	[10, 60]	[60, 80]	[80, 100]	[100, 120]	[120, 140]	[140, 180]	[180, 250]
[2, 4], [-3.3, -2.8]	0.9737 ± 0.0008	0.9737 ± 0.0008	0.9737 ± 0.0008	0.9737 ± 0.0008	0.9737 ± 0.0008	0.9737 ± 0.0008	0.9737 ± 0.0008
[2, 4], [-3.8, -3.3]	0.9904 ± 0.0005	0.9904 ± 0.0005	0.9904 ± 0.0005	0.9904 ± 0.0005	0.9904 ± 0.0005	0.9904 ± 0.0005	0.9904 ± 0.0005
[2, 4], [-4.3, -3.8]	0.9724 ± 0.0009	0.9724 ± 0.0009	0.9724 ± 0.0009	0.9724 ± 0.0009	0.9724 ± 0.0009	0.9724 ± 0.0009	0.9724 ± 0.0009
[4, 6], [-3.3, -2.8]	0.9953 ± 0.0006	0.9953 ± 0.0006	0.9953 ± 0.0006	0.9953 ± 0.0006	0.9953 ± 0.0006	0.9953 ± 0.0006	0.9953 ± 0.0006
[4, 6], [-3.8, -3.3]	0.9984 ± 0.0004	0.9984 ± 0.0004	0.9984 ± 0.0004	0.9984 ± 0.0004	0.9984 ± 0.0004	0.9984 ± 0.0004	0.9984 ± 0.0004
[4, 6], [-4.3, -3.8]	0.9965 ± 0.0006	0.9965 ± 0.0006	0.9965 ± 0.0006	0.9965 ± 0.0006	0.9965 ± 0.0006	0.9965 ± 0.0006	0.9965 ± 0.0006

APPENDIX A EFFICIENCY TABLES

Table A.5 Geometrical acceptance efficiencies in bins of D^+ p_T and y^* for Fwd collision configuration.

p_T [GeV/c]\ y^*	[1.5, 2]	[2, 2.5]	[2.5, 3]	[3, 3.5]	[3.5, 4]
[1, 2]	0.698 ± 0.005	0.918 ± 0.003	0.973 ± 0.002	0.909 ± 0.003	0.746 ± 0.005
[2, 3]	0.801 ± 0.005	0.970 ± 0.002	0.982 ± 0.002	0.953 ± 0.003	0.884 ± 0.005
[3, 4]	0.879 ± 0.005	0.986 ± 0.002	0.997 ± 0.001	0.981 ± 0.003	0.908 ± 0.006
[4, 5]	0.927 ± 0.005	0.996 ± 0.001	0.995 ± 0.002	0.987 ± 0.003	0.946 ± 0.007
[5, 6]	0.934 ± 0.007	1.000 ± 0.000	1.000 ± 0.000	0.984 ± 0.004	0.983 ± 0.005
[6, 7]	0.967 ± 0.007	1.000 ± 0.000	1.000 ± 0.000	1.000 ± 0.000	1.000 ± 0.000
[7, 8]	0.977 ± 0.008	1.000 ± 0.000	1.000 ± 0.000	1.000 ± 0.000	1.000 ± 0.000
[8, 9]	0.968 ± 0.010	1.000 ± 0.000	1.000 ± 0.000	1.000 ± 0.000	1.000 ± 0.000
[9, 10]	1.000 ± 0.000	1.000 ± 0.000	1.000 ± 0.000	1.000 ± 0.000	1.000 ± 0.000
[10, 11]	1.000 ± 0.000	1.000 ± 0.000	1.000 ± 0.000	1.000 ± 0.000	1.000 ± 0.000
[11, 12]	1.000 ± 0.000	1.000 ± 0.000	1.000 ± 0.000	1.000 ± 0.000	1.000 ± 0.000
[12, 13]	1.000 ± 0.000	1.000 ± 0.000	1.000 ± 0.000	1.000 ± 0.000	1.000 ± 0.000
[13, 14]	1.000 ± 0.000	1.000 ± 0.000	1.000 ± 0.000	1.000 ± 0.000	1.000 ± 0.000

Table A.6 Geometrical acceptance efficiencies in bins of D^+ p_T and y^* for Bwd collision configuration.

p_T [GeV/c]\ y^*	[-3, -2.5]	[-3.5, -3]	[-4, -3.5]	[-4.5, -4]	[-5, -4.5]
[1, 2]	0.746 ± 0.004	0.936 ± 0.003	0.969 ± 0.002	0.893 ± 0.004	0.706 ± 0.006
[2, 3]	0.839 ± 0.004	0.977 ± 0.002	0.979 ± 0.002	0.946 ± 0.003	0.866 ± 0.005
[3, 4]	0.917 ± 0.004	0.991 ± 0.002	0.997 ± 0.001	0.973 ± 0.003	0.901 ± 0.006
[4, 5]	0.942 ± 0.005	0.999 ± 0.001	0.995 ± 0.002	0.983 ± 0.004	0.929 ± 0.008
[5, 6]	0.969 ± 0.005	1.000 ± 0.000	1.000 ± 0.000	0.983 ± 0.005	0.978 ± 0.006
[6, 7]	0.986 ± 0.004	1.000 ± 0.000	1.000 ± 0.000	1.000 ± 0.000	1.000 ± 0.000
[7, 8]	0.985 ± 0.006	1.000 ± 0.000	1.000 ± 0.000	1.000 ± 0.000	0.992 ± 0.008
[8, 9]	0.969 ± 0.010	1.000 ± 0.000	1.000 ± 0.000	1.000 ± 0.000	1.000 ± 0.000
[9, 10]	1.000 ± 0.000	1.000 ± 0.000	1.000 ± 0.000	1.000 ± 0.000	1.000 ± 0.000
[10, 11]	1.000 ± 0.000	1.000 ± 0.000	1.000 ± 0.000	1.000 ± 0.000	1.000 ± 0.000
[11, 12]	1.000 ± 0.000	1.000 ± 0.000	1.000 ± 0.000	1.000 ± 0.000	1.000 ± 0.000
[12, 13]	1.000 ± 0.000	1.000 ± 0.000	1.000 ± 0.000	1.000 ± 0.000	1.000 ± 0.000
[13, 14]	1.000 ± 0.000	1.000 ± 0.000	1.000 ± 0.000	1.000 ± 0.000	1.000 ± 0.000

APPENDIX A EFFICIENCY TABLES

Table A.7 Geometrical acceptance efficiencies in bins of D^+ p_T and y^* and PV nTracks for Fwd collision configuration.

p_T [GeV/c], y^* \ PVnTracks	[10, 60]	[60, 80]	[80, 100]	[100, 120]	[120, 140]	[140, 200]
[2, 4], [1.8, 2.3]	0.9479 ± 0.0021	0.9479 ± 0.0021	0.9479 ± 0.0021	0.9479 ± 0.0021	0.9479 ± 0.0021	0.9479 ± 0.0021
[2, 4], [2.3, 2.8]	0.9911 ± 0.0010	0.9911 ± 0.0010	0.9911 ± 0.0010	0.9911 ± 0.0010	0.9911 ± 0.0010	0.9911 ± 0.0010
[2, 4], [2.8, 3.3]	0.9776 ± 0.0016	0.9776 ± 0.0016	0.9776 ± 0.0016	0.9776 ± 0.0016	0.9776 ± 0.0016	0.9776 ± 0.0016
[4, 6], [1.8, 2.3]	0.9842 ± 0.0021	0.9842 ± 0.0021	0.9842 ± 0.0021	0.9842 ± 0.0021	0.9842 ± 0.0021	0.9842 ± 0.0021
[4, 6], [2.3, 2.8]	0.9971 ± 0.0010	0.9971 ± 0.0010	0.9971 ± 0.0010	0.9971 ± 0.0010	0.9971 ± 0.0010	0.9971 ± 0.0010
[4, 6], [2.8, 3.3]	0.9958 ± 0.0013	0.9958 ± 0.0013	0.9958 ± 0.0013	0.9958 ± 0.0013	0.9958 ± 0.0013	0.9958 ± 0.0013

Table A.8 Geometrical acceptance efficiencies in bins of D^+ p_T and y^* and PV nTracks for Bwd collision configuration.

p_T [GeV/c], y^* \ PVnTracks	[10, 60]	[60, 80]	[80, 100]	[100, 120]	[120, 140]	[140, 180]	[180, 250]
[2, 4], [-3.3, -2.8]	0.9587 ± 0.0019	0.9587 ± 0.0019	0.9587 ± 0.0019	0.9587 ± 0.0019	0.9587 ± 0.0019	0.9587 ± 0.0019	0.9587 ± 0.0019
[2, 4], [-3.8, -3.3]	0.9896 ± 0.0011	0.9896 ± 0.0011	0.9896 ± 0.0011	0.9896 ± 0.0011	0.9896 ± 0.0011	0.9896 ± 0.0011	0.9896 ± 0.0011
[2, 4], [-4.3, -3.8]	0.9766 ± 0.0017	0.9766 ± 0.0017	0.9766 ± 0.0017	0.9766 ± 0.0017	0.9766 ± 0.0017	0.9766 ± 0.0017	0.9766 ± 0.0017
[4, 6], [-3.3, -2.8]	0.9892 ± 0.0018	0.9892 ± 0.0018	0.9892 ± 0.0018	0.9892 ± 0.0018	0.9892 ± 0.0018	0.9892 ± 0.0018	0.9892 ± 0.0018
[4, 6], [-3.8, -3.3]	0.9977 ± 0.0009	0.9977 ± 0.0009	0.9977 ± 0.0009	0.9977 ± 0.0009	0.9977 ± 0.0009	0.9977 ± 0.0009	0.9977 ± 0.0009
[4, 6], [-4.3, -3.8]	0.9923 ± 0.0018	0.9923 ± 0.0018	0.9923 ± 0.0018	0.9923 ± 0.0018	0.9923 ± 0.0018	0.9923 ± 0.0018	0.9923 ± 0.0018

Table A.9 Ratio of geometrical acceptance efficiencies (D^+/D_s^+) in bins of p_T and y^* for Fwd collision configuration.

p_T [GeV/c] \ y^*	[1.5, 2]	[2, 2.5]	[2.5, 3]	[3, 3.5]	[3.5, 4]
[1, 2]	0.821 ± 0.006	0.966 ± 0.003	1.012 ± 0.002	1.019 ± 0.004	1.023 ± 0.009
[2, 3]	0.894 ± 0.006	0.993 ± 0.002	0.998 ± 0.002	0.999 ± 0.004	1.030 ± 0.007
[3, 4]	0.945 ± 0.006	0.995 ± 0.002	1.002 ± 0.001	0.996 ± 0.003	0.958 ± 0.007
[4, 5]	0.971 ± 0.006	0.998 ± 0.001	0.996 ± 0.002	0.992 ± 0.003	0.967 ± 0.007
[5, 6]	0.966 ± 0.008	1.001 ± 0.001	1.002 ± 0.001	0.987 ± 0.004	0.998 ± 0.006
[6, 7]	0.985 ± 0.007	1.000 ± 0.001	1.003 ± 0.001	1.002 ± 0.001	1.008 ± 0.003
[7, 8]	0.988 ± 0.008	1.000 ± 0.001	1.000 ± 0.001	1.000 ± 0.001	1.013 ± 0.005
[8, 9]	0.978 ± 0.011	1.000 ± 0.001	1.000 ± 0.001	1.002 ± 0.003	1.012 ± 0.007
[9, 10]	1.010 ± 0.004	1.000 ± 0.002	1.000 ± 0.002	1.003 ± 0.004	1.000 ± 0.004
[10, 11]	1.002 ± 0.003	1.000 ± 0.003	1.000 ± 0.003	1.000 ± 0.004	1.000 ± 0.007
[11, 12]	1.000 ± 0.003	1.000 ± 0.004	1.000 ± 0.006	1.000 ± 0.007	1.000 ± 0.012
[12, 13]	1.000 ± 0.005	1.000 ± 0.007	1.000 ± 0.007	1.000 ± 0.011	1.000 ± 0.020

APPENDIX A EFFICIENCY TABLES

Table A.10 Ratio of geometrical acceptance efficiencies (D^+/D_s^+) in bins of p_T and y^* for Bwd collision configuration.

p_T [GeV/c]\y*	[-3, -2.5]	[-3.5, -3]	[-4, -3.5]	[-4.5, -4]	[-5, -4.5]
[1, 2]	0.848 ± 0.005	0.979 ± 0.003	1.013 ± 0.002	1.018 ± 0.005	1.024 ± 0.010
[2, 3]	0.912 ± 0.005	0.996 ± 0.002	0.998 ± 0.002	1.001 ± 0.004	1.037 ± 0.007
[3, 4]	0.967 ± 0.005	0.997 ± 0.002	1.002 ± 0.001	0.991 ± 0.003	0.963 ± 0.007
[4, 5]	0.976 ± 0.005	1.000 ± 0.001	0.996 ± 0.002	0.988 ± 0.004	0.955 ± 0.008
[5, 6]	0.990 ± 0.006	1.000 ± 0.000	1.002 ± 0.001	0.987 ± 0.005	0.995 ± 0.007
[6, 7]	1.000 ± 0.005	1.000 ± 0.001	1.003 ± 0.001	1.003 ± 0.001	1.009 ± 0.003
[7, 8]	0.990 ± 0.006	1.000 ± 0.001	1.000 ± 0.001	1.001 ± 0.002	1.010 ± 0.010
[8, 9]	0.972 ± 0.010	1.000 ± 0.001	1.000 ± 0.001	1.004 ± 0.003	1.013 ± 0.007
[9, 10]	1.006 ± 0.003	1.000 ± 0.002	1.000 ± 0.002	1.003 ± 0.004	1.000 ± 0.005
[10, 11]	1.002 ± 0.003	1.000 ± 0.003	1.000 ± 0.003	1.000 ± 0.005	1.000 ± 0.008
[11, 12]	1.000 ± 0.004	1.000 ± 0.004	1.000 ± 0.006	1.000 ± 0.007	1.000 ± 0.014
[12, 13]	1.000 ± 0.005	1.000 ± 0.007	1.000 ± 0.007	1.000 ± 0.012	1.000 ± 0.021

Table A.11 Ratio of geometrical acceptance efficiencies (D^+/D_s^+) in bins of p_T and y^* and PV nTracks for Fwd collision configuration.

p_T [GeV/c], y^* \PVnTracks	[10, 60]	[60, 80]	[80, 100]	[100, 120]	[120, 140]	[140, 200]
[2, 4], [1.8, 2.3]	0.9805 ± 0.0024	0.9805 ± 0.0024	0.9805 ± 0.0024	0.9805 ± 0.0024	0.9805 ± 0.0024	0.9805 ± 0.0024
[2, 4], [2.3, 2.8]	1.0000 ± 0.0011	1.0000 ± 0.0011	1.0000 ± 0.0011	1.0000 ± 0.0011	1.0000 ± 0.0011	1.0000 ± 0.0011
[2, 4], [2.8, 3.3]	1.0018 ± 0.0019	1.0018 ± 0.0019	1.0018 ± 0.0019	1.0018 ± 0.0019	1.0018 ± 0.0019	1.0018 ± 0.0019
[4, 6], [1.8, 2.3]	0.9930 ± 0.0023	0.9930 ± 0.0023	0.9930 ± 0.0023	0.9930 ± 0.0023	0.9930 ± 0.0023	0.9930 ± 0.0023
[4, 6], [2.3, 2.8]	0.9984 ± 0.0011	0.9984 ± 0.0011	0.9984 ± 0.0011	0.9984 ± 0.0011	0.9984 ± 0.0011	0.9984 ± 0.0011
[4, 6], [2.8, 3.3]	0.9984 ± 0.0014	0.9984 ± 0.0014	0.9984 ± 0.0014	0.9984 ± 0.0014	0.9984 ± 0.0014	0.9984 ± 0.0014

Table A.12 Ratio of geometrical acceptance efficiencies (D^+/D_s^+) in bins of p_T and y^* and PV nTracks for Bwd collision configuration.

p_T [GeV/c], y^* \PVnTracks	[10, 60]	[60, 80]	[80, 100]	[100, 120]	[120, 140]	[140, 180]	[180, 250]
[2, 4], [-3.3, -2.8]	0.9846 ± 0.0022	0.9846 ± 0.0022	0.9846 ± 0.0022	0.9846 ± 0.0022	0.9846 ± 0.0022	0.9846 ± 0.0022	0.9846 ± 0.0022
[2, 4], [-3.8, -3.3]	0.9992 ± 0.0012	0.9992 ± 0.0012	0.9992 ± 0.0012	0.9992 ± 0.0012	0.9992 ± 0.0012	0.9992 ± 0.0012	0.9992 ± 0.0012
[2, 4], [-4.3, -3.8]	1.0043 ± 0.0020	1.0043 ± 0.0020	1.0043 ± 0.0020	1.0043 ± 0.0020	1.0043 ± 0.0020	1.0043 ± 0.0020	1.0043 ± 0.0020
[4, 6], [-3.3, -2.8]	0.9938 ± 0.0019	0.9938 ± 0.0019	0.9938 ± 0.0019	0.9938 ± 0.0019	0.9938 ± 0.0019	0.9938 ± 0.0019	0.9938 ± 0.0019
[4, 6], [-3.8, -3.3]	0.9993 ± 0.0010	0.9993 ± 0.0010	0.9993 ± 0.0010	0.9993 ± 0.0010	0.9993 ± 0.0010	0.9993 ± 0.0010	0.9993 ± 0.0010
[4, 6], [-4.3, -3.8]	0.9958 ± 0.0019	0.9958 ± 0.0019	0.9958 ± 0.0019	0.9958 ± 0.0019	0.9958 ± 0.0019	0.9958 ± 0.0019	0.9958 ± 0.0019

Table A.13 Selection and reconstruction efficiencies in bins of D_s^+ p_T and y^* for Fwd collision configuration.

p_T [GeV/c] \ y^*	[1.5, 2]	[2, 2.5]	[2.5, 3]	[3, 3.5]	[3.5, 4]
[1, 2]	0.00078 \pm 0.00004	0.00280 \pm 0.00008	0.00275 \pm 0.00008	0.00177 \pm 0.00007	0.00082 \pm 0.00005
[2, 3]	0.00938 \pm 0.00017	0.02859 \pm 0.00028	0.02746 \pm 0.00028	0.01991 \pm 0.00026	0.00887 \pm 0.00020
[3, 4]	0.02376 \pm 0.00033	0.06231 \pm 0.00052	0.06124 \pm 0.00054	0.04587 \pm 0.00051	0.02161 \pm 0.00040
[4, 5]	0.04009 \pm 0.00057	0.08994 \pm 0.00083	0.08632 \pm 0.00086	0.07274 \pm 0.00087	0.03573 \pm 0.00072
[5, 6]	0.05482 \pm 0.00088	0.10955 \pm 0.00123	0.10619 \pm 0.00129	0.09273 \pm 0.00134	0.03934 \pm 0.00106
[6, 7]	0.06943 \pm 0.00129	0.12552 \pm 0.00174	0.12414 \pm 0.00187	0.10708 \pm 0.00199	0.03287 \pm 0.00136
[7, 8]	0.08331 \pm 0.00184	0.13647 \pm 0.00239	0.13428 \pm 0.00257	0.11328 \pm 0.00275	0.02131 \pm 0.00149
[8, 9]	0.09044 \pm 0.00246	0.14983 \pm 0.00323	0.14819 \pm 0.00353	0.10916 \pm 0.00361	0.01009 \pm 0.00138
[9, 10]	0.09653 \pm 0.00319	0.15959 \pm 0.00422	0.15594 \pm 0.00470	0.09019 \pm 0.00421	0.00337 \pm 0.00106
[10, 11]	0.10633 \pm 0.00409	0.17306 \pm 0.00540	0.16326 \pm 0.00598	0.07614 \pm 0.00492	–
[11, 12]	0.09784 \pm 0.00483	0.17624 \pm 0.00689	0.16954 \pm 0.00762	0.05144 \pm 0.00525	–
[12, 13]	0.11507 \pm 0.00625	0.17265 \pm 0.00796	0.14250 \pm 0.00862	0.03435 \pm 0.00538	–

Table A.14 Selection and reconstruction efficiencies in bins of D_s^+ p_T and y^* for Bwd collision configuration.

p_T [GeV/c] \ y^*	[-3, -2.5]	[-3.5, -3]	[-4, -3.5]	[-4.5, -4]	[-5, -4.5]
[1, 2]	0.00093 ± 0.00006	0.00237 ± 0.00009	0.00233 ± 0.00010	0.00144 ± 0.00009	0.00069 ± 0.00008
[2, 3]	0.01054 ± 0.00023	0.02582 ± 0.00037	0.02337 ± 0.00038	0.01632 ± 0.00037	0.00662 ± 0.00031
[3, 4]	0.02673 ± 0.00047	0.05643 ± 0.00071	0.05261 ± 0.00076	0.03979 ± 0.00079	0.01729 ± 0.00068
[4, 5]	0.04316 ± 0.00080	0.07865 ± 0.00112	0.07762 ± 0.00128	0.06134 ± 0.00140	0.02803 ± 0.00129
[5, 6]	0.06016 ± 0.00126	0.09968 ± 0.00172	0.09283 ± 0.00195	0.08165 ± 0.00233	0.03039 ± 0.00203
[6, 7]	0.07825 ± 0.00193	0.11972 ± 0.00257	0.11525 ± 0.00303	0.09354 ± 0.00354	0.02300 ± 0.00254
[7, 8]	0.08770 ± 0.00266	0.12875 ± 0.00352	0.12019 ± 0.00418	0.09252 ± 0.00493	0.01205 ± 0.00278
[8, 9]	0.09411 ± 0.00355	0.12997 ± 0.00468	0.13365 ± 0.00584	0.09055 ± 0.00685	0.00845 ± 0.00366
[9, 10]	0.10960 ± 0.00489	0.14424 ± 0.00630	0.14740 ± 0.00807	0.07852 ± 0.00873	–
[10, 11]	0.11760 ± 0.00647	0.14115 ± 0.00793	0.13873 ± 0.01044	0.05656 ± 0.00971	–
[11, 12]	0.12385 ± 0.00815	0.14214 ± 0.01004	0.15278 ± 0.01338	0.03144 ± 0.00797	–
[12, 13]	0.12482 ± 0.00973	0.15397 ± 0.01319	0.12611 ± 0.01518	0.01372 ± 0.00819	–

Table A.15 Selection and reconstruction efficiencies in bins of D_s^+ p_T and y^* and PV nTracks for Fwd collision configuration.

p_T [GeV/c], y^* \ PVnTracks	[10, 60]	[60, 80]	[80, 100]	[100, 120]	[120, 140]	[140, 200]
[2, 4], [1.8, 2.3]	0.0170 ± 0.0004	0.0162 ± 0.0005	0.0176 ± 0.0004	0.0185 ± 0.0004	0.0212 ± 0.0005	0.0209 ± 0.0004
[2, 4], [2.3, 2.8]	0.0203 ± 0.0005	0.0203 ± 0.0005	0.0209 ± 0.0005	0.0212 ± 0.0005	0.0237 ± 0.0005	0.0249 ± 0.0004
[2, 4], [2.8, 3.3]	0.0162 ± 0.0004	0.0149 ± 0.0005	0.0170 ± 0.0005	0.0182 ± 0.0005	0.0188 ± 0.0005	0.0201 ± 0.0004
[4, 6], [1.8, 2.3]	0.0398 ± 0.0011	0.0413 ± 0.0013	0.0449 ± 0.0012	0.0464 ± 0.0012	0.0511 ± 0.0013	0.0538 ± 0.0011
[4, 6], [2.3, 2.8]	0.0451 ± 0.0013	0.0465 ± 0.0014	0.0476 ± 0.0013	0.0528 ± 0.0013	0.0546 ± 0.0014	0.0577 ± 0.0011
[4, 6], [2.8, 3.3]	0.0393 ± 0.0013	0.0404 ± 0.0014	0.0422 ± 0.0013	0.0413 ± 0.0013	0.0493 ± 0.0015	0.0517 ± 0.0012

 Table A.16 Selection and reconstruction efficiencies in bins of D_s^+ p_T and y^* and PV nTracks for Bwd collision configuration.

p_T [GeV/c], y^* \ PVnTracks	[10, 60]	[60, 80]	[80, 100]	[100, 120]	[120, 140]	[140, 180]	[180, 250]
[2, 4], [-3.3, -2.8]	0.0236 ± 0.0010	0.0247 ± 0.0010	0.0240 ± 0.0008	0.0225 ± 0.0007	0.0214 ± 0.0006	0.0189 ± 0.0004	0.0149 ± 0.0003
[2, 4], [-3.8, -3.3]	0.0289 ± 0.0012	0.0261 ± 0.0012	0.0252 ± 0.0009	0.0254 ± 0.0008	0.0227 ± 0.0007	0.0220 ± 0.0004	0.0158 ± 0.0003
[2, 4], [-4.3, -3.8]	0.0210 ± 0.0012	0.0224 ± 0.0012	0.0202 ± 0.0010	0.0205 ± 0.0008	0.0181 ± 0.0007	0.0167 ± 0.0004	0.0138 ± 0.0003
[4, 6], [-3.3, -2.8]	0.0571 ± 0.0028	0.0589 ± 0.0029	0.0566 ± 0.0023	0.0568 ± 0.0020	0.0524 ± 0.0017	0.0490 ± 0.0011	0.0373 ± 0.0008
[4, 6], [-3.8, -3.3]	0.0569 ± 0.0032	0.0578 ± 0.0032	0.0600 ± 0.0027	0.0597 ± 0.0023	0.0557 ± 0.0020	0.0518 ± 0.0012	0.0411 ± 0.0010
[4, 6], [-4.3, -3.8]	0.0599 ± 0.0039	0.0583 ± 0.0039	0.0514 ± 0.0030	0.0465 ± 0.0024	0.0526 ± 0.0023	0.0453 ± 0.0014	0.0372 ± 0.0011

Table A.17 Selection and reconstruction efficiencies in bins of D^+ p_T and y^* for Fwd collision configuration.

p_T [GeV/c] y^*	[1.5, 2]	[2, 2.5]	[2.5, 3]	[3, 3.5]	[3.5, 4]
[1, 2]	0.00081 ± 0.00003	0.00566 ± 0.00007	0.00824 ± 0.00008	0.00726 ± 0.00008	0.00457 ± 0.00008
[2, 3]	0.00983 ± 0.00011	0.04703 ± 0.00023	0.06081 ± 0.00027	0.05285 ± 0.00027	0.02995 ± 0.00024
[3, 4]	0.02829 ± 0.00024	0.10143 ± 0.00043	0.11940 ± 0.00048	0.10355 ± 0.00049	0.06022 ± 0.00044
[4, 5]	0.04989 ± 0.00042	0.14687 ± 0.00068	0.16082 ± 0.00074	0.14476 ± 0.00078	0.07567 ± 0.00068
[5, 6]	0.07223 ± 0.00067	0.18047 ± 0.00100	0.19532 ± 0.00111	0.17544 ± 0.00118	0.06761 ± 0.00091
[6, 7]	0.09311 ± 0.00099	0.20781 ± 0.00143	0.22140 ± 0.00158	0.18495 ± 0.00166	0.04552 ± 0.00106
[7, 8]	0.11235 ± 0.00141	0.22669 ± 0.00195	0.24331 ± 0.00219	0.17957 ± 0.00224	0.02241 ± 0.00104
[8, 9]	0.12289 ± 0.00189	0.24549 ± 0.00261	0.25717 ± 0.00292	0.15110 ± 0.00273	0.00953 ± 0.00091
[9, 10]	0.13946 ± 0.00251	0.25741 ± 0.00341	0.26806 ± 0.00386	0.12057 ± 0.00328	0.00188 ± 0.00056
[10, 11]	0.14670 ± 0.00318	0.27308 ± 0.00437	0.26500 ± 0.00483	0.08761 ± 0.00356	0.00030 ± 0.00030
[11, 12]	0.14739 ± 0.00393	0.28271 ± 0.00545	0.25259 ± 0.00595	0.05230 ± 0.00354	–
[12, 13]	0.16697 ± 0.00501	0.28538 ± 0.00665	0.24081 ± 0.00733	0.02850 ± 0.00330	–
[13, 14]	0.17770 ± 0.00619	0.29727 ± 0.00816	0.19889 ± 0.00810	0.02108 ± 0.00366	–

Table A.18 Selection and reconstruction efficiencies in bins of D^+ p_T and y^* for Bwd collision configuration.

p_T [GeV/c] y^*	[-3, -2.5]	[-3.5, -3]	[-4, -3.5]	[-4.5, -4]	[-5, -4.5]
[1, 2]	0.00111 ± 0.00004	0.00559 ± 0.00009	0.00716 ± 0.00010	0.00620 ± 0.00011	0.00322 ± 0.00011
[2, 3]	0.01232 ± 0.00016	0.04452 ± 0.00029	0.05437 ± 0.00035	0.04623 ± 0.00038	0.02363 ± 0.00035
[3, 4]	0.03394 ± 0.00033	0.09451 ± 0.00055	0.10634 ± 0.00065	0.09312 ± 0.00073	0.04776 ± 0.00070
[4, 5]	0.05988 ± 0.00059	0.13556 ± 0.00089	0.14588 ± 0.00105	0.12880 ± 0.00122	0.05999 ± 0.00116
[5, 6]	0.08393 ± 0.00093	0.16670 ± 0.00135	0.17579 ± 0.00162	0.15710 ± 0.00193	0.05110 ± 0.00163
[6, 7]	0.10557 ± 0.00139	0.19325 ± 0.00195	0.20223 ± 0.00238	0.15841 ± 0.00277	0.03153 ± 0.00193
[7, 8]	0.12484 ± 0.00197	0.21148 ± 0.00274	0.21758 ± 0.00337	0.15613 ± 0.00397	0.01113 ± 0.00163
[8, 9]	0.14630 ± 0.00276	0.22666 ± 0.00372	0.23597 ± 0.00465	0.12252 ± 0.00484	0.00383 ± 0.00139
[9, 10]	0.15336 ± 0.00361	0.23977 ± 0.00494	0.23348 ± 0.00615	0.08960 ± 0.00580	0.00068 ± 0.00050
[10, 11]	0.16574 ± 0.00467	0.24957 ± 0.00651	0.21367 ± 0.00775	0.06461 ± 0.00668	–
[11, 12]	0.17106 ± 0.00584	0.25492 ± 0.00802	0.21393 ± 0.00991	0.02846 ± 0.00551	–
[12, 13]	0.18204 ± 0.00740	0.25928 ± 0.01002	0.20731 ± 0.01217	0.02367 ± 0.00733	–
[13, 14]	0.18660 ± 0.00899	0.24392 ± 0.01195	0.15248 ± 0.01335	0.00959 ± 0.00550	–

Table A.19 Selection and reconstruction efficiencies in bins of D^+ p_T and y^* and PV nTracks for Fwd collision configuration.

p_T [GeV/c], y^* \ PVnTracks	[10, 60]	[60, 80]	[80, 100]	[100, 120]	[120, 140]	[140, 200]
[2, 4], [1.8, 2.3]	0.0245 ± 0.0003	0.0246 ± 0.0004	0.0259 ± 0.0003	0.0275 ± 0.0003	0.0290 ± 0.0004	0.0324 ± 0.0003
[2, 4], [2.3, 2.8]	0.0391 ± 0.0004	0.0381 ± 0.0005	0.0402 ± 0.0004	0.0432 ± 0.0004	0.0463 ± 0.0005	0.0522 ± 0.0004
[2, 4], [2.8, 3.3]	0.0378 ± 0.0004	0.0359 ± 0.0005	0.0383 ± 0.0004	0.0419 ± 0.0005	0.0445 ± 0.0005	0.0510 ± 0.0004
[4, 6], [1.8, 2.3]	0.0644 ± 0.0009	0.0642 ± 0.0010	0.0677 ± 0.0010	0.0737 ± 0.0010	0.0780 ± 0.0011	0.0872 ± 0.0009
[4, 6], [2.3, 2.8]	0.0821 ± 0.0011	0.0795 ± 0.0012	0.0857 ± 0.0011	0.0926 ± 0.0011	0.0988 ± 0.0013	0.1129 ± 0.0011
[4, 6], [2.8, 3.3]	0.0806 ± 0.0012	0.0769 ± 0.0013	0.0818 ± 0.0012	0.0891 ± 0.0012	0.0980 ± 0.0014	0.1099 ± 0.0012

 Table A.20 Selection and reconstruction efficiencies in bins of D^+ p_T and y^* and PV nTracks for Bwd collision configuration.

p_T [GeV/c], y^* \ PVnTracks	[10, 60]	[60, 80]	[80, 100]	[100, 120]	[120, 140]	[140, 180]	[180, 250]
[2, 4], [-3.3, -2.8]	0.0385 ± 0.0008	0.0384 ± 0.0008	0.0352 ± 0.0006	0.0356 ± 0.0005	0.0340 ± 0.0005	0.0322 ± 0.0003	0.0276 ± 0.0003
[2, 4], [-3.8, -3.3]	0.0565 ± 0.0010	0.0555 ± 0.0010	0.0535 ± 0.0008	0.0516 ± 0.0007	0.0491 ± 0.0006	0.0473 ± 0.0004	0.0414 ± 0.0004
[2, 4], [-4.3, -3.8]	0.0546 ± 0.0011	0.0531 ± 0.0011	0.0494 ± 0.0009	0.0492 ± 0.0008	0.0470 ± 0.0007	0.0460 ± 0.0005	0.0399 ± 0.0004
[4, 6], [-3.3, -2.8]	0.0988 ± 0.0022	0.0968 ± 0.0022	0.0935 ± 0.0018	0.0940 ± 0.0015	0.0896 ± 0.0014	0.0863 ± 0.0009	0.0764 ± 0.0008
[4, 6], [-3.8, -3.3]	0.1128 ± 0.0026	0.1169 ± 0.0027	0.1128 ± 0.0022	0.1124 ± 0.0019	0.1098 ± 0.0017	0.1049 ± 0.0011	0.0931 ± 0.0010
[4, 6], [-4.3, -3.8]	0.1197 ± 0.0032	0.1062 ± 0.0031	0.1095 ± 0.0026	0.1014 ± 0.0021	0.1054 ± 0.0020	0.1019 ± 0.0013	0.0901 ± 0.0012

APPENDIX A EFFICIENCY TABLES

Table A.21 Ratio of selection and reconstruction efficiencies (D^+/D_s^+) in bins of p_T and y^* for Fwd collision configuration.

p_T [GeV/c]\y*	[1.5, 2]	[2, 2.5]	[2.5, 3]	[3, 3.5]	[3.5, 4]
[1, 2]	1.043 ± 0.067	2.022 ± 0.060	2.998 ± 0.089	4.107 ± 0.162	5.590 ± 0.386
[2, 3]	1.048 ± 0.022	1.645 ± 0.018	2.214 ± 0.025	2.655 ± 0.037	3.375 ± 0.080
[3, 4]	1.190 ± 0.020	1.628 ± 0.015	1.950 ± 0.019	2.257 ± 0.027	2.787 ± 0.056
[4, 5]	1.244 ± 0.020	1.633 ± 0.017	1.863 ± 0.021	1.990 ± 0.026	2.118 ± 0.047
[5, 6]	1.318 ± 0.024	1.647 ± 0.021	1.839 ± 0.025	1.892 ± 0.030	1.719 ± 0.052
[6, 7]	1.341 ± 0.029	1.656 ± 0.026	1.784 ± 0.030	1.727 ± 0.036	1.385 ± 0.066
[7, 8]	1.349 ± 0.034	1.661 ± 0.032	1.812 ± 0.038	1.585 ± 0.043	1.052 ± 0.088
[8, 9]	1.359 ± 0.042	1.638 ± 0.039	1.735 ± 0.046	1.384 ± 0.052	0.945 ± 0.157
[9, 10]	1.445 ± 0.054	1.613 ± 0.048	1.719 ± 0.057	1.337 ± 0.072	0.557 ± 0.240
[10, 11]	1.380 ± 0.061	1.578 ± 0.055	1.623 ± 0.066	1.151 ± 0.088	–
[11, 12]	1.506 ± 0.085	1.604 ± 0.070	1.490 ± 0.076	1.017 ± 0.125	–
[12, 13]	1.451 ± 0.090	1.653 ± 0.085	1.690 ± 0.114	0.830 ± 0.162	–

Table A.22 Ratio of Selection and reconstruction efficiencies (D^+/D_s^+) in bins of p_T and y^* for Bwd collision configuration.

p_T [GeV/c]\y*	[-3, -2.5]	[-3.5, -3]	[-4, -3.5]	[-4.5, -4]	[-5, -4.5]
[1, 2]	1.196 ± 0.088	2.363 ± 0.100	3.077 ± 0.141	4.313 ± 0.291	4.656 ± 0.570
[2, 3]	1.170 ± 0.030	1.724 ± 0.027	2.327 ± 0.041	2.833 ± 0.068	3.569 ± 0.175
[3, 4]	1.270 ± 0.026	1.675 ± 0.023	2.021 ± 0.032	2.340 ± 0.050	2.761 ± 0.116
[4, 5]	1.387 ± 0.029	1.724 ± 0.027	1.879 ± 0.034	2.100 ± 0.052	2.140 ± 0.107
[5, 6]	1.395 ± 0.033	1.672 ± 0.032	1.894 ± 0.043	1.924 ± 0.060	1.681 ± 0.125
[6, 7]	1.349 ± 0.038	1.614 ± 0.038	1.755 ± 0.051	1.693 ± 0.071	1.371 ± 0.173
[7, 8]	1.424 ± 0.049	1.643 ± 0.050	1.810 ± 0.069	1.688 ± 0.100	0.923 ± 0.253
[8, 9]	1.555 ± 0.066	1.744 ± 0.069	1.766 ± 0.085	1.353 ± 0.115	0.453 ± 0.256
[9, 10]	1.399 ± 0.071	1.662 ± 0.080	1.584 ± 0.096	1.141 ± 0.147	–
[10, 11]	1.409 ± 0.087	1.768 ± 0.110	1.540 ± 0.129	1.142 ± 0.229	–
[11, 12]	1.381 ± 0.102	1.793 ± 0.139	1.400 ± 0.139	0.905 ± 0.289	–
[12, 13]	1.458 ± 0.128	1.684 ± 0.158	1.644 ± 0.220	1.725 ± 1.160	–

APPENDIX A EFFICIENCY TABLES

Table A.23 Ratio of selection and reconstruction efficiencies (D^+/D_s^+) in bins of p_T and y^* and PV nTracks for Fwd collision configuration.

p_T [GeV/c], y^* \ PVnTracks	[10, 60]	[60, 80]	[80, 100]	[100, 120]	[120, 140]	[140, 200]
[2, 4], [1.8, 2.3]	1.4422 ± 0.0413	1.5174 ± 0.0487	1.4741 ± 0.0411	1.4854 ± 0.0396	1.3683 ± 0.0365	1.5475 ± 0.0328
[2, 4], [2.3, 2.8]	1.9251 ± 0.0496	1.8773 ± 0.0533	1.9264 ± 0.0485	2.0365 ± 0.0498	1.9573 ± 0.0480	2.0994 ± 0.0397
[2, 4], [2.8, 3.3]	2.3299 ± 0.0700	2.4018 ± 0.0826	2.2519 ± 0.0661	2.3042 ± 0.0638	2.3660 ± 0.0679	2.5419 ± 0.0555
[4, 6], [1.8, 2.3]	1.6155 ± 0.0519	1.5548 ± 0.0538	1.5061 ± 0.0453	1.5869 ± 0.0458	1.5256 ± 0.0446	1.6205 ± 0.0364
[4, 6], [2.3, 2.8]	1.8219 ± 0.0566	1.7091 ± 0.0574	1.7981 ± 0.0539	1.7549 ± 0.0486	1.8100 ± 0.0523	1.9575 ± 0.0430
[4, 6], [2.8, 3.3]	2.0509 ± 0.0724	1.9033 ± 0.0739	1.9394 ± 0.0661	2.1589 ± 0.0725	1.9881 ± 0.0649	2.1265 ± 0.0532

Table A.24 Ratio of Selection and reconstruction efficiencies (D^+/D_s^+) in bins of p_T and y^* and PV nTracks for Bwd collision configuration.

p_T [GeV/c], y^* \ PVnTracks	[10, 60]	[60, 80]	[80, 100]	[100, 120]	[120, 140]	[140, 180]	[180, 250]
[2, 4], [-3.3, -2.8]	1.6327 ± 0.0769	1.5520 ± 0.0725	1.4703 ± 0.0579	1.5808 ± 0.0545	1.5886 ± 0.0502	1.7048 ± 0.0381	1.8572 ± 0.0415
[2, 4], [-3.8, -3.3]	1.9588 ± 0.0877	2.1297 ± 0.1018	2.1218 ± 0.0844	2.0284 ± 0.0691	2.1616 ± 0.0693	2.1507 ± 0.0468	2.6183 ± 0.0586
[2, 4], [-4.3, -3.8]	2.5971 ± 0.1539	2.3724 ± 0.1384	2.4437 ± 0.1230	2.4010 ± 0.1027	2.5906 ± 0.1044	2.7602 ± 0.0775	2.8861 ± 0.0785
[4, 6], [-3.3, -2.8]	1.7290 ± 0.0940	1.6452 ± 0.0892	1.6541 ± 0.0748	1.6562 ± 0.0638	1.7119 ± 0.0615	1.7632 ± 0.0437	2.0487 ± 0.0511
[4, 6], [-3.8, -3.3]	1.9807 ± 0.1190	2.0216 ± 0.1206	1.8784 ± 0.0911	1.8827 ± 0.0781	1.9704 ± 0.0757	2.0255 ± 0.0535	2.2655 ± 0.0595
[4, 6], [-4.3, -3.8]	1.9983 ± 0.1404	1.8217 ± 0.1315	2.1303 ± 0.1323	2.1782 ± 0.1222	2.0036 ± 0.0946	2.2484 ± 0.0764	2.4221 ± 0.0797

Table A.25 PID efficiencies in bins of D_s^+ p_T and y^* for Fwd collision configuration.

p_T [GeV/c] \ y^*	[1.5, 2]	[2, 2.5]	[2.5, 3]	[3, 3.5]	[3.5, 4]
[1, 2]	0.736 ± 0.009	0.729 ± 0.004	0.791 ± 0.003	0.728 ± 0.006	0.551 ± 0.007
[2, 3]	0.796 ± 0.003	0.794 ± 0.001	0.842 ± 0.001	0.774 ± 0.002	0.562 ± 0.003
[3, 4]	0.839 ± 0.002	0.854 ± 0.001	0.889 ± 0.001	0.804 ± 0.001	0.532 ± 0.003
[4, 5]	0.879 ± 0.001	0.899 ± 0.001	0.926 ± 0.009	0.802 ± 0.002	0.455 ± 0.004
[5, 6]	0.911 ± 0.001	0.925 ± 0.001	0.924 ± 0.001	0.767 ± 0.002	0.377 ± 0.006
[6, 7]	0.935 ± 0.001	0.937 ± 0.001	0.919 ± 0.001	0.702 ± 0.003	0.275 ± 0.007
[7, 8]	0.947 ± 0.001	0.938 ± 0.001	0.902 ± 0.002	0.618 ± 0.005	0.178 ± 0.009
[8, 9]	0.952 ± 0.001	0.929 ± 0.003	0.871 ± 0.002	0.543 ± 0.007	0.126 ± 0.013
[9, 10]	0.953 ± 0.002	0.912 ± 0.002	0.823 ± 0.004	0.452 ± 0.011	0.068 ± 0.014
[10, 11]	0.946 ± 0.002	0.888 ± 0.002	0.783 ± 0.005	0.368 ± 0.014	—
[11, 12]	0.933 ± 0.003	0.868 ± 0.003	0.729 ± 0.007	0.324 ± 0.020	—
[12, 13]	0.921 ± 0.004	0.829 ± 0.005	0.665 ± 0.012	0.268 ± 0.024	—

APPENDIX A EFFICIENCY TABLES

Table A.26 PID efficiencies in bins of D_s^+ p_T and y^* for Bwd collision configuration.

p_T [GeV/c]\ y^*	[-3, -2.5]	[-3.5, -3]	[-4, -3.5]	[-4.5, -4]	[-5, -4.5]
[1, 2]	0.556 ± 0.012	0.615 ± 0.007	0.725 ± 0.006	0.625 ± 0.012	0.455 ± 0.013
[2, 3]	0.678 ± 0.006	0.710 ± 0.002	0.780 ± 0.002	0.685 ± 0.004	0.474 ± 0.007
[3, 4]	0.764 ± 0.003	0.800 ± 0.002	0.834 ± 0.002	0.701 ± 0.003	0.421 ± 0.006
[4, 5]	0.828 ± 0.003	0.854 ± 0.002	0.863 ± 0.002	0.695 ± 0.004	0.354 ± 0.008
[5, 6]	0.882 ± 0.002	0.893 ± 0.002	0.865 ± 0.002	0.645 ± 0.005	0.260 ± 0.011
[6, 7]	0.914 ± 0.003	0.907 ± 0.002	0.857 ± 0.003	0.577 ± 0.008	0.191 ± 0.015
[7, 8]	0.926 ± 0.002	0.906 ± 0.002	0.830 ± 0.004	0.502 ± 0.012	0.115 ± 0.020
[8, 9]	0.933 ± 0.002	0.895 ± 0.003	0.782 ± 0.006	0.411 ± 0.016	0.082 ± 0.033
[9, 10]	0.940 ± 0.002	0.876 ± 0.004	0.760 ± 0.007	0.322 ± 0.022	–
[10, 11]	0.929 ± 0.003	0.839 ± 0.005	0.695 ± 0.012	0.272 ± 0.032	–
[11, 12]	0.925 ± 0.004	0.813 ± 0.006	0.645 ± 0.019	0.151 ± 0.035	–
[12, 13]	0.895 ± 0.007	0.787 ± 0.008	0.590 ± 0.021	0.117 ± 0.026	–

Table A.27 PID efficiencies in bins of D_s^+ p_T and y^* and PV nTracks for Fwd collision configuration.

p_T [GeV/c], y^* \ PVnTracks	[10, 60]	[60, 80]	[80, 100]	[100, 120]	[120, 140]	[140, 200]
[2, 4], [1.8, 2.3]	0.9104 ± 0.0016	0.9174 ± 0.0018	0.8714 ± 0.0026	0.8144 ± 0.0023	0.7808 ± 0.0029	0.7037 ± 0.0027
[2, 4], [2.3, 2.8]	0.9358 ± 0.0011	0.9320 ± 0.0013	0.9010 ± 0.0016	0.8596 ± 0.0016	0.8374 ± 0.0020	0.7650 ± 0.0018
[2, 4], [2.8, 3.3]	0.9208 ± 0.0022	0.9029 ± 0.0025	0.8856 ± 0.0023	0.8520 ± 0.0025	0.8266 ± 0.0028	0.7627 ± 0.0027
[4, 6], [1.8, 2.3]	0.9595 ± 0.0011	0.9606 ± 0.0011	0.9350 ± 0.0016	0.8980 ± 0.0015	0.8804 ± 0.0020	0.8342 ± 0.0018
[4, 6], [2.3, 2.8]	0.9731 ± 0.0009	0.9665 ± 0.0010	0.9509 ± 0.0011	0.9231 ± 0.0011	0.9102 ± 0.0014	0.8724 ± 0.0014
[4, 6], [2.8, 3.3]	0.9320 ± 0.0020	0.9127 ± 0.0022	0.8985 ± 0.0021	0.8706 ± 0.0023	0.8604 ± 0.0025	0.8112 ± 0.0024

Table A.28 PID efficiencies in bins of D_s^+ p_T and y^* and PV nTracks for Bwd collision configuration.

p_T [GeV/c], y^* \ PVnTracks	[10, 60]	[60, 80]	[80, 100]	[100, 120]	[120, 140]	[140, 180]	[180, 250]
[2, 4], [-3.3, -2.8]	0.8749 ± 0.0047	0.8619 ± 0.0051	0.8056 ± 0.0052	0.7586 ± 0.0045	0.7128 ± 0.0046	0.6160 ± 0.0031	0.5389 ± 0.0031
[2, 4], [-3.8, -3.3]	0.9368 ± 0.0028	0.9089 ± 0.0033	0.8756 ± 0.0033	0.8407 ± 0.0031	0.7875 ± 0.0034	0.6921 ± 0.0023	0.5990 ± 0.0044
[2, 4], [-4.3, -3.8]	0.9180 ± 0.0048	0.8845 ± 0.0054	0.8510 ± 0.0052	0.8064 ± 0.0046	0.7553 ± 0.0051	0.6498 ± 0.0038	0.5328 ± 0.0036
[4, 6], [-3.3, -2.8]	0.9488 ± 0.0031	0.9445 ± 0.0034	0.9183 ± 0.0033	0.8880 ± 0.0032	0.8505 ± 0.0035	0.7791 ± 0.0027	0.7154 ± 0.0034
[4, 6], [-3.8, -3.3]	0.9688 ± 0.0020	0.9537 ± 0.0021	0.9358 ± 0.0025	0.9139 ± 0.0022	0.8815 ± 0.0029	0.8092 ± 0.0022	0.7178 ± 0.0029
[4, 6], [-4.3, -3.8]	0.9159 ± 0.0045	0.8916 ± 0.0053	0.8585 ± 0.0055	0.8219 ± 0.0055	0.7668 ± 0.0058	0.6914 ± 0.0044	0.5741 ± 0.0043

APPENDIX A EFFICIENCY TABLES

Table A.29 PID efficiencies in bins of D^+ p_T and y^* for Fwd collision configuration.

p_T [GeV/c]\ y^*	[1.5, 2]	[2, 2.5]	[2.5, 3]	[3, 3.5]	[3.5, 4]
[1, 2]	0.787 ± 0.005	0.783 ± 0.002	0.793 ± 0.001	0.747 ± 0.001	0.613 ± 0.002
[2, 3]	0.828 ± 0.001	0.822 ± 0.001	0.836 ± 0.000	0.779 ± 0.001	0.591 ± 0.001
[3, 4]	0.850 ± 0.001	0.859 ± 0.000	0.872 ± 0.000	0.794 ± 0.001	0.544 ± 0.001
[4, 5]	0.870 ± 0.001	0.887 ± 0.000	0.890 ± 0.000	0.777 ± 0.001	0.488 ± 0.002
[5, 6]	0.891 ± 0.001	0.903 ± 0.000	0.892 ± 0.000	0.734 ± 0.001	0.424 ± 0.003
[6, 7]	0.908 ± 0.001	0.907 ± 0.001	0.877 ± 0.001	0.671 ± 0.002	0.370 ± 0.004
[7, 8]	0.917 ± 0.001	0.902 ± 0.001	0.851 ± 0.001	0.616 ± 0.003	0.309 ± 0.007
[8, 9]	0.921 ± 0.001	0.887 ± 0.001	0.813 ± 0.002	0.562 ± 0.004	0.239 ± 0.013
[9, 10]	0.915 ± 0.001	0.864 ± 0.001	0.773 ± 0.003	0.505 ± 0.006	0.170 ± 0.024
[10, 11]	0.901 ± 0.002	0.838 ± 0.002	0.731 ± 0.004	0.460 ± 0.008	–
[11, 12]	0.882 ± 0.003	0.807 ± 0.003	0.688 ± 0.005	0.415 ± 0.013	–
[12, 13]	0.852 ± 0.004	0.771 ± 0.004	0.652 ± 0.006	0.361 ± 0.020	–
[13, 14]	0.815 ± 0.006	0.743 ± 0.005	0.616 ± 0.008	0.302 ± 0.027	–

Table A.30 PID efficiencies in bins of D^+ p_T and y^* for Bwd collision configuration.

p_T [GeV/c]\ y^*	[-3, -2.5]	[-3.5, -3]	[-4, -3.5]	[-4.5, -4]	[-5, -4.5]
[1, 2]	0.679 ± 0.006	0.685 ± 0.003	0.717 ± 0.002	0.672 ± 0.003	0.548 ± 0.005
[2, 3]	0.743 ± 0.002	0.741 ± 0.001	0.767 ± 0.001	0.700 ± 0.001	0.515 ± 0.002
[3, 4]	0.787 ± 0.001	0.792 ± 0.001	0.809 ± 0.001	0.707 ± 0.001	0.459 ± 0.003
[4, 5]	0.823 ± 0.001	0.830 ± 0.001	0.827 ± 0.001	0.680 ± 0.002	0.402 ± 0.003
[5, 6]	0.853 ± 0.001	0.853 ± 0.001	0.825 ± 0.001	0.629 ± 0.002	0.337 ± 0.005
[6, 7]	0.876 ± 0.001	0.862 ± 0.001	0.810 ± 0.002	0.563 ± 0.004	0.285 ± 0.010
[7, 8]	0.892 ± 0.001	0.857 ± 0.001	0.778 ± 0.003	0.517 ± 0.005	0.232 ± 0.020
[8, 9]	0.898 ± 0.001	0.844 ± 0.002	0.742 ± 0.004	0.456 ± 0.008	0.202 ± 0.039
[9, 10]	0.894 ± 0.002	0.822 ± 0.002	0.700 ± 0.005	0.416 ± 0.013	0.082 ± 0.017
[10, 11]	0.877 ± 0.003	0.790 ± 0.003	0.662 ± 0.007	0.388 ± 0.018	–
[11, 12]	0.867 ± 0.004	0.767 ± 0.005	0.633 ± 0.009	0.276 ± 0.028	–
[12, 13]	0.829 ± 0.006	0.731 ± 0.006	0.598 ± 0.011	0.306 ± 0.048	–
[13, 14]	0.813 ± 0.008	0.706 ± 0.008	0.590 ± 0.016	0.112 ± 0.017	–

APPENDIX A EFFICIENCY TABLES

Table A.31 PID efficiencies in bins of D^+ p_T and y^* and PV nTracks for Fwd collision configuration.

p_T [GeV/c], y^* \ PVnTracks	[10, 60]	[60, 80]	[80, 100]	[100, 120]	[120, 140]	[140, 200]
[2, 4], [1.8, 2.3]	0.9221 ± 0.0007	0.9116 ± 0.0008	0.8802 ± 0.0010	0.8382 ± 0.0009	0.8122 ± 0.0013	0.7292 ± 0.0012
[2, 4], [2.3, 2.8]	0.9394 ± 0.0005	0.9244 ± 0.0005	0.8951 ± 0.0007	0.8568 ± 0.0007	0.8296 ± 0.0009	0.7477 ± 0.0009
[2, 4], [2.8, 3.3]	0.9149 ± 0.0007	0.8921 ± 0.0009	0.8694 ± 0.0009	0.8351 ± 0.0009	0.8100 ± 0.0011	0.7349 ± 0.0010
[4, 6], [1.8, 2.3]	0.9499 ± 0.0005	0.9399 ± 0.0006	0.9180 ± 0.0007	0.8883 ± 0.0007	0.8694 ± 0.0009	0.8124 ± 0.0010
[4, 6], [2.3, 2.8]	0.9603 ± 0.0005	0.9475 ± 0.0005	0.9274 ± 0.0006	0.9018 ± 0.0006	0.8830 ± 0.0008	0.8232 ± 0.0009
[4, 6], [2.8, 3.3]	0.9042 ± 0.0012	0.8891 ± 0.0015	0.8668 ± 0.0014	0.8393 ± 0.0014	0.8209 ± 0.0016	0.7681 ± 0.0014

Table A.32 PID efficiencies in bins of D^+ p_T and y^* and PV nTracks for Bwd collision configuration.

p_T [GeV/c], y^* \ PVnTracks	[10, 60]	[60, 80]	[80, 100]	[100, 120]	[120, 140]	[140, 180]	[180, 250]
[2, 4], [-3.3, -2.8]	0.9072 ± 0.0014	0.8880 ± 0.0018	0.8398 ± 0.0019	0.7997 ± 0.0016	0.7363 ± 0.0020	0.6265 ± 0.0014	0.4867 ± 0.0017
[2, 4], [-3.8, -3.3]	0.9322 ± 0.0010	0.9075 ± 0.0012	0.8706 ± 0.0013	0.8279 ± 0.0012	0.7637 ± 0.0016	0.6449 ± 0.0011	0.4881 ± 0.0013
[2, 4], [-4.3, -3.8]	0.9001 ± 0.0014	0.8743 ± 0.0016	0.8322 ± 0.0017	0.7907 ± 0.0016	0.7305 ± 0.0019	0.6218 ± 0.0014	0.4787 ± 0.0016
[4, 6], [-3.3, -2.8]	0.9416 ± 0.0011	0.9299 ± 0.0013	0.8999 ± 0.0015	0.8722 ± 0.0012	0.8255 ± 0.0016	0.7375 ± 0.0013	0.6125 ± 0.0017
[4, 6], [-3.8, -3.3]	0.9534 ± 0.0010	0.9357 ± 0.0010	0.9108 ± 0.0011	0.8797 ± 0.0012	0.8334 ± 0.0016	0.7392 ± 0.0013	0.6006 ± 0.0018
[4, 6], [-4.3, -3.8]	0.8691 ± 0.0030	0.8508 ± 0.0032	0.8197 ± 0.0029	0.7842 ± 0.0028	0.7371 ± 0.0029	0.6468 ± 0.0022	0.5233 ± 0.0023

Table A.33 Ratio of PID efficiencies (D^+/D_s^+) in bins of p_T and y^* for Fwd collision configuration.

p_T [GeV/c] \ y^*	[1.5, 2]	[2, 2.5]	[2.5, 3]	[3, 3.5]	[3.5, 4]
[1, 2]	1.069 ± 0.015	1.074 ± 0.007	1.003 ± 0.005	1.026 ± 0.009	1.113 ± 0.015
[2, 3]	1.041 ± 0.004	1.035 ± 0.002	0.992 ± 0.001	1.006 ± 0.002	1.051 ± 0.006
[3, 4]	1.012 ± 0.002	1.006 ± 0.001	0.981 ± 0.001	0.988 ± 0.002	1.022 ± 0.006
[4, 5]	0.990 ± 0.002	0.986 ± 0.001	0.961 ± 0.010	0.970 ± 0.002	1.073 ± 0.010
[5, 6]	0.978 ± 0.002	0.977 ± 0.001	0.965 ± 0.001	0.956 ± 0.003	1.126 ± 0.018
[6, 7]	0.971 ± 0.001	0.968 ± 0.001	0.954 ± 0.001	0.956 ± 0.005	1.343 ± 0.039
[7, 8]	0.968 ± 0.001	0.961 ± 0.001	0.944 ± 0.002	0.997 ± 0.009	1.731 ± 0.096
[8, 9]	0.968 ± 0.002	0.954 ± 0.003	0.933 ± 0.003	1.034 ± 0.016	1.895 ± 0.218
[9, 10]	0.960 ± 0.002	0.948 ± 0.002	0.939 ± 0.005	1.116 ± 0.029	2.515 ± 0.622
[10, 11]	0.953 ± 0.003	0.943 ± 0.003	0.934 ± 0.007	1.249 ± 0.051	–
[11, 12]	0.945 ± 0.005	0.929 ± 0.005	0.943 ± 0.011	1.280 ± 0.089	–
[12, 13]	0.924 ± 0.006	0.930 ± 0.007	0.981 ± 0.019	1.348 ± 0.143	–

APPENDIX A EFFICIENCY TABLES

 Table A.34 Ratio of PID efficiencies (D^+/D_s^+) in bins of p_T and y^* for Bwd collision configuration.

p_T [GeV/c]\y*	[-3, -2.5]	[-3.5, -3]	[-4, -3.5]	[-4.5, -4]	[-5, -4.5]
[1, 2]	1.221 ± 0.029	1.113 ± 0.014	0.988 ± 0.009	1.074 ± 0.021	1.205 ± 0.035
[2, 3]	1.096 ± 0.009	1.044 ± 0.004	0.982 ± 0.003	1.023 ± 0.006	1.085 ± 0.017
[3, 4]	1.030 ± 0.005	0.990 ± 0.003	0.970 ± 0.002	1.009 ± 0.005	1.090 ± 0.017
[4, 5]	0.994 ± 0.003	0.973 ± 0.002	0.958 ± 0.002	0.978 ± 0.006	1.135 ± 0.028
[5, 6]	0.967 ± 0.003	0.955 ± 0.002	0.954 ± 0.003	0.976 ± 0.009	1.299 ± 0.061
[6, 7]	0.959 ± 0.003	0.950 ± 0.002	0.945 ± 0.003	0.975 ± 0.015	1.490 ± 0.127
[7, 8]	0.964 ± 0.002	0.946 ± 0.003	0.936 ± 0.005	1.030 ± 0.027	2.019 ± 0.390
[8, 9]	0.963 ± 0.003	0.943 ± 0.003	0.948 ± 0.008	1.109 ± 0.048	2.476 ± 1.106
[9, 10]	0.952 ± 0.003	0.939 ± 0.005	0.921 ± 0.011	1.292 ± 0.098	–
[10, 11]	0.943 ± 0.005	0.943 ± 0.007	0.953 ± 0.019	1.426 ± 0.181	–
[11, 12]	0.937 ± 0.006	0.943 ± 0.009	0.981 ± 0.032	1.831 ± 0.465	–
[12, 13]	0.926 ± 0.009	0.929 ± 0.012	1.014 ± 0.041	2.610 ± 0.705	–

 Table A.35 Ratio of PID efficiencies (D^+/D_s^+) in bins of p_T and y^* and PV nTracks for Fwd collision configuration.

p_T [GeV/c], y^* \ PVnTracks	[10, 60]	[60, 80]	[80, 100]	[100, 120]	[120, 140]	[140, 200]
[2, 4], [1.8, 2.3]	1.0129 ± 0.0019	0.9937 ± 0.0022	1.0101 ± 0.0032	1.0293 ± 0.0031	1.0402 ± 0.0042	1.0362 ± 0.0043
[2, 4], [2.3, 2.8]	1.0039 ± 0.0013	0.9918 ± 0.0016	0.9935 ± 0.0020	0.9968 ± 0.0020	0.9908 ± 0.0026	0.9773 ± 0.0026
[2, 4], [2.8, 3.3]	0.9937 ± 0.0025	0.9880 ± 0.0029	0.9817 ± 0.0027	0.9802 ± 0.0030	0.9798 ± 0.0036	0.9635 ± 0.0036
[4, 6], [1.8, 2.3]	0.9901 ± 0.0012	0.9784 ± 0.0013	0.9819 ± 0.0019	0.9893 ± 0.0019	0.9875 ± 0.0025	0.9739 ± 0.0024
[4, 6], [2.3, 2.8]	0.9869 ± 0.0011	0.9803 ± 0.0011	0.9752 ± 0.0014	0.9769 ± 0.0014	0.9702 ± 0.0018	0.9437 ± 0.0018
[4, 6], [2.8, 3.3]	0.9702 ± 0.0024	0.9742 ± 0.0029	0.9648 ± 0.0028	0.9641 ± 0.0031	0.9541 ± 0.0033	0.9469 ± 0.0033

 Table A.36 Ratio of PID efficiencies (D^+/D_s^+) in bins of p_T and y^* and PV nTracks for Bwd collision configuration.

p_T [GeV/c], y^* \ PVnTracks	[10, 60]	[60, 80]	[80, 100]	[100, 120]	[120, 140]	[140, 180]	[180, 250]
[2, 4], [-3.3, -2.8]	1.0369 ± 0.0058	1.0304 ± 0.0064	1.0425 ± 0.0071	1.0542 ± 0.0066	1.0330 ± 0.0072	1.0170 ± 0.0056	0.9032 ± 0.0061
[2, 4], [-3.8, -3.3]	0.9951 ± 0.0031	0.9985 ± 0.0039	0.9944 ± 0.0041	0.9848 ± 0.0039	0.9698 ± 0.0047	0.9317 ± 0.0035	0.8149 ± 0.0064
[2, 4], [-4.3, -3.8]	0.9805 ± 0.0053	0.9885 ± 0.0063	0.9779 ± 0.0063	0.9806 ± 0.0059	0.9671 ± 0.0070	0.9570 ± 0.0060	0.8984 ± 0.0068
[4, 6], [-3.3, -2.8]	0.9924 ± 0.0034	0.9846 ± 0.0039	0.9799 ± 0.0039	0.9821 ± 0.0038	0.9706 ± 0.0044	0.9465 ± 0.0037	0.8561 ± 0.0046
[4, 6], [-3.8, -3.3]	0.9841 ± 0.0023	0.9811 ± 0.0024	0.9733 ± 0.0028	0.9625 ± 0.0026	0.9454 ± 0.0036	0.9134 ± 0.0030	0.8367 ± 0.0042
[4, 6], [-4.3, -3.8]	0.9489 ± 0.0057	0.9543 ± 0.0067	0.9548 ± 0.0070	0.9541 ± 0.0073	0.9613 ± 0.0081	0.9355 ± 0.0068	0.9116 ± 0.0080

APPENDIX A EFFICIENCY TABLES

Table A.37 Trigger efficiencies in bins of D_s^+ p_T and y^* for Fwd collision configuration.

p_T [GeV/c]\ y^*	[1.5, 2]	[2, 2.5]	[2.5, 3]	[3, 3.5]	[3.5, 4]
[1, 2]	0.781 ± 0.019	0.970 ± 0.004	0.980 ± 0.003	0.988 ± 0.004	0.970 ± 0.012
[2, 3]	0.938 ± 0.004	0.987 ± 0.001	0.994 ± 0.001	0.994 ± 0.001	0.996 ± 0.001
[3, 4]	0.983 ± 0.001	0.997 ± 0.000	0.998 ± 0.000	0.998 ± 0.000	0.999 ± 0.001
[4, 5]	0.995 ± 0.001	0.998 ± 0.000	0.999 ± 0.000	1.000 ± 0.000	0.999 ± 0.001
[5, 6]	0.997 ± 0.001	0.999 ± 0.000	1.000 ± 0.000	0.999 ± 0.000	1.000 ± 0.001
[6, 7]	1.000 ± 0.000	0.999 ± 0.000	1.000 ± 0.000	1.000 ± 0.000	1.000 ± 0.003
[7, 8]	0.997 ± 0.001	0.999 ± 0.001	0.999 ± 0.001	0.999 ± 0.001	1.000 ± 0.011
[8, 9]	0.998 ± 0.001	0.999 ± 0.000	1.000 ± 0.000	1.000 ± 0.001	1.000 ± 0.068
[9, 10]	0.999 ± 0.001	1.000 ± 0.000	0.999 ± 0.001	1.000 ± 0.003	–
[10, 11]	1.000 ± 0.001	1.000 ± 0.001	1.000 ± 0.001	1.000 ± 0.005	–
[11, 12]	1.000 ± 0.002	1.000 ± 0.001	1.000 ± 0.002	1.000 ± 0.016	–
[12, 13]	1.000 ± 0.002	1.000 ± 0.002	1.000 ± 0.003	1.000 ± 0.039	–

Table A.38 Trigger efficiencies in bins of D_s^+ p_T and y^* for Bwd collision configuration.

p_T [GeV/c]\ y^*	[-3, -2.5]	[-3.5, -3]	[-4, -3.5]	[-4.5, -4]	[-5, -4.5]
[1, 2]	0.842 ± 0.013	0.975 ± 0.003	0.969 ± 0.004	0.986 ± 0.004	1.000 ± 0.007
[2, 3]	0.952 ± 0.002	0.985 ± 0.001	0.992 ± 0.001	0.996 ± 0.001	0.996 ± 0.002
[3, 4]	0.991 ± 0.001	0.996 ± 0.000	0.999 ± 0.000	0.998 ± 0.001	0.994 ± 0.002
[4, 5]	0.996 ± 0.001	0.999 ± 0.000	0.998 ± 0.000	0.999 ± 0.000	1.000 ± 0.001
[5, 6]	0.997 ± 0.001	1.000 ± 0.000	0.998 ± 0.000	1.000 ± 0.000	0.988 ± 0.007
[6, 7]	0.998 ± 0.001	1.000 ± 0.000	0.998 ± 0.001	1.000 ± 0.001	1.000 ± 0.020
[7, 8]	0.997 ± 0.001	1.000 ± 0.000	1.000 ± 0.000	1.000 ± 0.001	1.000 ± 0.036
[8, 9]	1.000 ± 0.001	1.000 ± 0.000	1.000 ± 0.001	1.000 ± 0.003	1.000 ± 0.062
[9, 10]	1.000 ± 0.000	1.000 ± 0.001	1.000 ± 0.001	1.000 ± 0.007	–
[10, 11]	1.000 ± 0.001	1.000 ± 0.001	1.000 ± 0.002	0.994 ± 0.018	–
[11, 12]	1.000 ± 0.001	1.000 ± 0.001	1.000 ± 0.002	–	–
[12, 13]	1.000 ± 0.001	1.000 ± 0.002	1.000 ± 0.006	–	–

APPENDIX A EFFICIENCY TABLES

Table A.39 Trigger efficiencies in bins of D_s^+ p_T and y^* and PV nTracks for Fwd collision configuration.

p_T [GeV/c], y^* \ PVnTracks	[10, 60]	[60, 80]	[80, 100]	[100, 120]	[120, 140]	[140, 200]
[2, 4], [1.8, 2.3]	0.9852 ± 0.0026	0.9917 ± 0.0021	0.9889 ± 0.0023	0.9898 ± 0.0023	0.9891 ± 0.0028	0.9868 ± 0.0032
[2, 4], [2.3, 2.8]	0.9963 ± 0.0013	0.9946 ± 0.0016	0.9982 ± 0.0009	0.9945 ± 0.0016	0.9951 ± 0.0019	0.9956 ± 0.0017
[2, 4], [2.8, 3.3]	0.9976 ± 0.0013	0.9990 ± 0.0010	0.9982 ± 0.0011	0.9942 ± 0.0020	0.9963 ± 0.0020	0.9968 ± 0.0018
[4, 6], [1.8, 2.3]	1.0000 ± 0.0006	0.9978 ± 0.0013	0.9993 ± 0.0008	0.9977 ± 0.0013	0.9992 ± 0.0011	0.9981 ± 0.0014
[4, 6], [2.3, 2.8]	1.0000 ± 0.0006	0.9981 ± 0.0012	1.0000 ± 0.0005	0.9984 ± 0.0011	0.9984 ± 0.0014	0.9984 ± 0.0013
[4, 6], [2.8, 3.3]	1.0000 ± 0.0008	0.9986 ± 0.0013	0.9988 ± 0.0012	0.9988 ± 0.0013	0.9979 ± 0.0019	0.9980 ± 0.0018

Table A.40 Trigger efficiencies in bins of D_s^+ p_T and y^* and PV nTracks for Bwd collision configuration.

p_T [GeV/c], y^* \ PVnTracks	[10, 60]	[60, 80]	[80, 100]	[100, 120]	[120, 140]	[140, 180]	[180, 250]
[2, 4], [-3.3, -2.8]	0.9913 ± 0.0036	0.9877 ± 0.0039	0.9875 ± 0.0036	0.9890 ± 0.0033	0.9873 ± 0.0039	0.9896 ± 0.0031	0.9868 ± 0.0079
[2, 4], [-3.8, -3.3]	0.9980 ± 0.0020	0.9962 ± 0.0025	0.9986 ± 0.0016	0.9950 ± 0.0024	0.9958 ± 0.0024	0.9934 ± 0.0024	0.9975 ± 0.0053
[2, 4], [-4.3, -3.8]	1.0000 ± 0.0023	0.9892 ± 0.0049	0.9943 ± 0.0036	0.9958 ± 0.0031	0.9934 ± 0.0043	0.9993 ± 0.0019	0.9969 ± 0.0084
[4, 6], [-3.3, -2.8]	1.0000 ± 0.0018	1.0000 ± 0.0015	1.0000 ± 0.0012	1.0000 ± 0.0011	1.0000 ± 0.0013	0.9987 ± 0.0014	0.9974 ± 0.0054
[4, 6], [-3.8, -3.3]	1.0000 ± 0.0022	1.0000 ± 0.0019	0.9976 ± 0.0023	0.9981 ± 0.0020	1.0000 ± 0.0015	1.0000 ± 0.0011	0.9982 ± 0.0056
[4, 6], [-4.3, -3.8]	1.0000 ± 0.0033	1.0000 ± 0.0030	0.9964 ± 0.0041	1.0000 ± 0.0026	0.9974 ± 0.0039	1.0000 ± 0.0021	0.9966 ± 0.0107

Table A.41 Trigger efficiencies in bins of D^+ p_T and y^* for Fwd collision configuration.

p_T [GeV/c] \ y^*	[1.5, 2]	[2, 2.5]	[2.5, 3]	[3, 3.5]	[3.5, 4]
[1, 2]	0.740 ± 0.006	0.964 ± 0.001	0.979 ± 0.001	0.977 ± 0.001	0.981 ± 0.001
[2, 3]	0.938 ± 0.001	0.986 ± 0.000	0.992 ± 0.000	0.994 ± 0.000	0.993 ± 0.000
[3, 4]	0.985 ± 0.000	0.996 ± 0.000	0.997 ± 0.000	0.998 ± 0.000	0.998 ± 0.000
[4, 5]	0.994 ± 0.000	0.998 ± 0.000	0.998 ± 0.000	0.999 ± 0.000	0.999 ± 0.000
[5, 6]	0.997 ± 0.000	0.999 ± 0.000	0.999 ± 0.000	0.999 ± 0.000	1.000 ± 0.000
[6, 7]	0.998 ± 0.000	0.999 ± 0.000	0.999 ± 0.000	1.000 ± 0.000	1.000 ± 0.000
[7, 8]	0.998 ± 0.000	0.999 ± 0.000	0.999 ± 0.000	1.000 ± 0.000	1.000 ± 0.000
[8, 9]	0.999 ± 0.000	0.999 ± 0.000	1.000 ± 0.000	0.999 ± 0.000	1.000 ± 0.002
[9, 10]	1.000 ± 0.000	0.999 ± 0.000	1.000 ± 0.000	0.999 ± 0.000	1.000 ± 0.012
[10, 11]	1.000 ± 0.000	1.000 ± 0.000	0.999 ± 0.000	1.000 ± 0.000	—
[11, 12]	0.999 ± 0.000	0.999 ± 0.000	0.999 ± 0.000	1.000 ± 0.001	—
[12, 13]	0.998 ± 0.001	0.999 ± 0.000	0.999 ± 0.001	1.000 ± 0.002	—
[13, 14]	1.000 ± 0.000	1.000 ± 0.000	1.000 ± 0.000	1.000 ± 0.004	—

APPENDIX A EFFICIENCY TABLES

Table A.42 Trigger efficiencies in bins of D^+ p_T and y^* for Bwd collision configuration.

p_T [GeV/c]\ y^*	$[-3, -2.5]$	$[-3.5, -3]$	$[-4, -3.5]$	$[-4.5, -4]$	$[-5, -4.5]$
[1, 2]	0.804 ± 0.004	0.965 ± 0.001	0.978 ± 0.001	0.982 ± 0.001	0.972 ± 0.001
[2, 3]	0.955 ± 0.001	0.988 ± 0.000	0.992 ± 0.000	0.994 ± 0.000	0.993 ± 0.000
[3, 4]	0.987 ± 0.000	0.996 ± 0.000	0.997 ± 0.000	0.998 ± 0.000	0.998 ± 0.000
[4, 5]	0.996 ± 0.000	0.998 ± 0.000	0.999 ± 0.000	0.998 ± 0.000	1.000 ± 0.000
[5, 6]	0.996 ± 0.000	0.998 ± 0.000	0.999 ± 0.000	0.999 ± 0.000	0.999 ± 0.000
[6, 7]	0.997 ± 0.000	0.999 ± 0.000	0.999 ± 0.000	0.999 ± 0.000	0.999 ± 0.001
[7, 8]	0.999 ± 0.000	0.999 ± 0.000	0.999 ± 0.000	0.999 ± 0.000	1.000 ± 0.002
[8, 9]	0.999 ± 0.000	0.999 ± 0.000	1.000 ± 0.000	1.000 ± 0.000	1.000 ± 0.012
[9, 10]	0.998 ± 0.000	0.999 ± 0.000	1.000 ± 0.000	1.000 ± 0.000	–
[10, 11]	1.000 ± 0.000	1.000 ± 0.000	0.999 ± 0.000	1.000 ± 0.001	–
[11, 12]	0.999 ± 0.000	1.000 ± 0.000	1.000 ± 0.000	1.000 ± 0.003	–
[12, 13]	0.999 ± 0.000	1.000 ± 0.000	1.000 ± 0.000	1.000 ± 0.007	–
[13, 14]	1.000 ± 0.000	1.000 ± 0.000	1.000 ± 0.001	1.000 ± 0.024	–

APPENDIX A EFFICIENCY TABLES

Table A.43 Trigger efficiencies in bins of D^+ p_T and y^* and PV nTracks for Fwd collision configuration.

p_T [GeV/c], y^* \ PVnTracks	[10, 60]	[60, 80]	[80, 100]	[100, 120]	[120, 140]	[140, 200]
[2, 4], [1.8, 2.3]	0.9870 ± 0.0007	0.9890 ± 0.0007	0.9898 ± 0.0007	0.9899 ± 0.0007	0.9875 ± 0.0010	0.9858 ± 0.0011
[2, 4], [2.3, 2.8]	0.9958 ± 0.0003	0.9943 ± 0.0004	0.9949 ± 0.0004	0.9954 ± 0.0004	0.9952 ± 0.0005	0.9926 ± 0.0006
[2, 4], [2.8, 3.3]	0.9955 ± 0.0004	0.9948 ± 0.0004	0.9958 ± 0.0004	0.9966 ± 0.0004	0.9966 ± 0.0004	0.9959 ± 0.0005
[4, 6], [1.8, 2.3]	0.9976 ± 0.0003	0.9972 ± 0.0004	0.9977 ± 0.0003	0.9987 ± 0.0003	0.9974 ± 0.0005	0.9979 ± 0.0004
[4, 6], [2.3, 2.8]	0.9981 ± 0.0003	0.9987 ± 0.0003	0.9994 ± 0.0002	0.9988 ± 0.0002	0.9989 ± 0.0003	0.9976 ± 0.0004
[4, 6], [2.8, 3.3]	0.9995 ± 0.0002	1.0000 ± 0.0001	0.9990 ± 0.0002	0.9990 ± 0.0003	0.9989 ± 0.0003	0.9989 ± 0.0003

Table A.44 Trigger efficiencies in bins of D^+ p_T and y^* and PV nTracks for Bwd collision configuration.

p_T [GeV/c], y^* \ PVnTracks	[10, 60]	[60, 80]	[80, 100]	[100, 120]	[120, 140]	[140, 180]	[180, 250]
[2, 4], [-3.3, -2.8]	0.9876 ± 0.0005	0.9887 ± 0.0006	0.9910 ± 0.0005	0.9896 ± 0.0005	0.9899 ± 0.0006	0.9892 ± 0.0006	0.9900 ± 0.0013
[2, 4], [-3.8, -3.3]	0.9942 ± 0.0003	0.9939 ± 0.0004	0.9953 ± 0.0003	0.9935 ± 0.0004	0.9942 ± 0.0004	0.9944 ± 0.0004	0.9938 ± 0.0009
[2, 4], [-4.3, -3.8]	0.9978 ± 0.0002	0.9950 ± 0.0004	0.9951 ± 0.0004	0.9978 ± 0.0003	0.9960 ± 0.0004	0.9951 ± 0.0005	0.9946 ± 0.0010
[4, 6], [-3.3, -2.8]	0.9966 ± 0.0003	0.9957 ± 0.0004	0.9981 ± 0.0003	0.9982 ± 0.0003	0.9987 ± 0.0002	0.9975 ± 0.0003	0.9975 ± 0.0007
[4, 6], [-3.8, -3.3]	0.9994 ± 0.0002	0.9973 ± 0.0003	1.0000 ± 0.0000	0.9977 ± 0.0003	0.9988 ± 0.0002	0.9989 ± 0.0002	0.9989 ± 0.0005
[4, 6], [-4.3, -3.8]	0.9991 ± 0.0002	1.0000 ± 0.0001	1.0000 ± 0.0001	0.9982 ± 0.0003	0.9994 ± 0.0002	0.9988 ± 0.0003	0.9986 ± 0.0007

APPENDIX A EFFICIENCY TABLES

Table A.45 Ratio of trigger efficiencies (D^+/D_s^+) in bins of p_T and y^* for Fwd collision configuration.

p_T [GeV/c]\y*	[1.5, 2]	[2, 2.5]	[2.5, 3]	[3, 3.5]	[3.5, 4]
[1, 2]	0.948 ± 0.025	0.994 ± 0.004	0.999 ± 0.003	0.989 ± 0.004	1.012 ± 0.013
[2, 3]	1.000 ± 0.004	0.999 ± 0.001	0.998 ± 0.001	1.001 ± 0.001	0.997 ± 0.001
[3, 4]	1.002 ± 0.002	0.999 ± 0.000	0.999 ± 0.000	1.000 ± 0.000	0.999 ± 0.001
[4, 5]	0.998 ± 0.001	0.999 ± 0.000	1.000 ± 0.000	0.999 ± 0.000	1.000 ± 0.001
[5, 6]	1.000 ± 0.001	1.000 ± 0.000	1.000 ± 0.000	1.000 ± 0.000	1.000 ± 0.001
[6, 7]	0.999 ± 0.000	1.000 ± 0.000	1.000 ± 0.000	1.000 ± 0.000	1.000 ± 0.003
[7, 8]	1.001 ± 0.001	1.000 ± 0.001	1.000 ± 0.001	1.001 ± 0.001	1.000 ± 0.011
[8, 9]	1.001 ± 0.001	1.000 ± 0.001	1.000 ± 0.000	0.999 ± 0.001	1.000 ± 0.068
[9, 10]	1.001 ± 0.001	0.999 ± 0.000	1.000 ± 0.001	0.999 ± 0.003	–
[10, 11]	1.000 ± 0.001	1.000 ± 0.001	0.999 ± 0.001	1.000 ± 0.005	–
[11, 12]	0.999 ± 0.002	0.999 ± 0.001	0.999 ± 0.002	1.000 ± 0.016	–
[12, 13]	0.998 ± 0.002	0.999 ± 0.002	0.999 ± 0.003	1.000 ± 0.039	–

Table A.46 Ratio of trigger efficiencies (D^+/D_s^+) in bins of p_T and y^* for Bwd collision configuration.

p_T [GeV/c]\y*	[-3, -2.5]	[-3.5, -3]	[-4, -3.5]	[-4.5, -4]	[-5, -4.5]
[1, 2]	0.955 ± 0.015	0.989 ± 0.004	1.010 ± 0.004	0.995 ± 0.005	0.972 ± 0.007
[2, 3]	1.004 ± 0.003	1.003 ± 0.001	1.000 ± 0.001	0.998 ± 0.001	0.997 ± 0.002
[3, 4]	0.996 ± 0.001	1.000 ± 0.000	0.998 ± 0.000	1.000 ± 0.001	1.004 ± 0.002
[4, 5]	1.000 ± 0.001	0.999 ± 0.000	1.000 ± 0.000	0.999 ± 0.000	1.000 ± 0.001
[5, 6]	0.999 ± 0.001	0.999 ± 0.000	1.001 ± 0.000	0.999 ± 0.000	1.011 ± 0.007
[6, 7]	0.999 ± 0.001	0.999 ± 0.000	1.001 ± 0.001	0.999 ± 0.001	0.999 ± 0.020
[7, 8]	1.002 ± 0.001	1.000 ± 0.000	0.999 ± 0.000	0.999 ± 0.001	1.000 ± 0.036
[8, 9]	0.999 ± 0.001	0.999 ± 0.000	1.000 ± 0.001	1.000 ± 0.003	1.000 ± 0.063
[9, 10]	0.998 ± 0.001	0.999 ± 0.001	1.000 ± 0.001	1.000 ± 0.007	–
[10, 11]	1.000 ± 0.001	1.000 ± 0.001	0.999 ± 0.002	1.006 ± 0.019	–
[11, 12]	0.999 ± 0.001	1.000 ± 0.001	1.000 ± 0.002	–	–
[12, 13]	0.999 ± 0.002	1.000 ± 0.002	1.000 ± 0.006	–	–

APPENDIX A EFFICIENCY TABLES

Table A.47 Ratio of trigger efficiencies (D^+/D_s^+) in bins of p_T and y^* and PV nTracks for Fwd collision configuration.

p_T [GeV/c], y^* \ PVnTracks	[10, 60]	[60, 80]	[80, 100]	[100, 120]	[120, 140]	[140, 200]
[2, 4], [1.8, 2.3]	1.0018 ± 0.0028	0.9973 ± 0.0023	1.0010 ± 0.0024	1.0001 ± 0.0025	0.9984 ± 0.0030	0.9991 ± 0.0034
[2, 4], [2.3, 2.8]	0.9995 ± 0.0013	0.9997 ± 0.0016	0.9967 ± 0.0010	1.0008 ± 0.0017	1.0001 ± 0.0019	0.9970 ± 0.0018
[2, 4], [2.8, 3.3]	0.9979 ± 0.0013	0.9957 ± 0.0011	0.9976 ± 0.0012	1.0024 ± 0.0020	1.0004 ± 0.0021	0.9991 ± 0.0019
[4, 6], [1.8, 2.3]	0.9976 ± 0.0007	0.9994 ± 0.0014	0.9984 ± 0.0009	1.0010 ± 0.0013	0.9982 ± 0.0012	0.9999 ± 0.0015
[4, 6], [2.3, 2.8]	0.9981 ± 0.0006	1.0007 ± 0.0012	0.9994 ± 0.0006	1.0004 ± 0.0011	1.0005 ± 0.0014	0.9992 ± 0.0014
[4, 6], [2.8, 3.3]	0.9995 ± 0.0008	1.0014 ± 0.0013	1.0001 ± 0.0012	1.0001 ± 0.0014	1.0011 ± 0.0020	1.0009 ± 0.0018

Table A.48 Ratio of trigger efficiencies (D^+/D_s^+) in bins of p_T and y^* and PV nTracks for Bwd collision configuration.

p_T [GeV/c], y^* \ PVnTracks	[10, 60]	[60, 80]	[80, 100]	[100, 120]	[120, 140]	[140, 180]	[180, 250]
[2, 4], [-3.3, -2.8]	0.9962 ± 0.0037	1.0010 ± 0.0040	1.0036 ± 0.0037	1.0006 ± 0.0034	1.0026 ± 0.0040	0.9996 ± 0.0032	1.0033 ± 0.0081
[2, 4], [-3.8, -3.3]	0.9962 ± 0.0021	0.9977 ± 0.0025	0.9966 ± 0.0016	0.9985 ± 0.0024	0.9984 ± 0.0025	1.0010 ± 0.0024	0.9964 ± 0.0054
[2, 4], [-4.3, -3.8]	0.9978 ± 0.0023	1.0059 ± 0.0050	1.0009 ± 0.0036	1.0020 ± 0.0031	1.0025 ± 0.0044	0.9959 ± 0.0019	0.9977 ± 0.0084
[4, 6], [-3.3, -2.8]	0.9966 ± 0.0018	0.9957 ± 0.0016	0.9981 ± 0.0013	0.9982 ± 0.0011	0.9987 ± 0.0013	0.9988 ± 0.0015	1.0001 ± 0.0055
[4, 6], [-3.8, -3.3]	0.9994 ± 0.0022	0.9973 ± 0.0020	1.0024 ± 0.0024	0.9996 ± 0.0021	0.9988 ± 0.0015	0.9989 ± 0.0011	1.0007 ± 0.0056
[4, 6], [-4.3, -3.8]	0.9991 ± 0.0033	1.0000 ± 0.0030	1.0036 ± 0.0041	0.9982 ± 0.0026	1.0020 ± 0.0039	0.9988 ± 0.0022	1.0021 ± 0.0108

Table A.49 Total efficiencies in bins of D_s^+ , p_T and y^* for Fwd collision configuration.

p_T [GeV/c] \ y^*	[1.5, 2]	[2, 2.5]	[2.5, 3]	[3, 3.5]	[3.5, 4]
[1, 2]	0.000395 ± 0.000042	0.001956 ± 0.000114	0.002125 ± 0.000100	0.001178 ± 0.000062	0.000331 ± 0.000029
[2, 3]	0.006525 ± 0.000457	0.022750 ± 0.000881	0.023514 ± 0.000632	0.015173 ± 0.000537	0.004430 ± 0.000197
[3, 4]	0.018950 ± 0.001041	0.054635 ± 0.001677	0.056171 ± 0.001456	0.037627 ± 0.001264	0.011322 ± 0.000494
[4, 5]	0.034780 ± 0.001532	0.083667 ± 0.002120	0.082851 ± 0.002226	0.060240 ± 0.002033	0.016490 ± 0.000759
[5, 6]	0.050024 ± 0.001955	0.104971 ± 0.002444	0.101743 ± 0.002790	0.073590 ± 0.002684	0.015181 ± 0.000838
[6, 7]	0.066118 ± 0.002711	0.122023 ± 0.003235	0.118111 ± 0.003270	0.077846 ± 0.003148	0.009324 ± 0.000687
[7, 8]	0.080807 ± 0.003390	0.132780 ± 0.004162	0.125693 ± 0.003840	0.072641 ± 0.003344	0.003897 ± 0.000427
[8, 9]	0.088387 ± 0.004178	0.144571 ± 0.004981	0.134100 ± 0.004541	0.061476 ± 0.003483	0.001307 ± 0.000263
[9, 10]	0.094509 ± 0.004981	0.151178 ± 0.005735	0.133278 ± 0.005307	0.042256 ± 0.002940	—
[10, 11]	0.104286 ± 0.005594	0.159707 ± 0.007128	0.132774 ± 0.006112	0.029118 ± 0.002664	—
[11, 12]	0.094864 ± 0.006041	0.158963 ± 0.008703	0.128413 ± 0.007017	0.017320 ± 0.002328	—
[12, 13]	0.110146 ± 0.007629	0.148750 ± 0.008797	0.098372 ± 0.007166	0.009551 ± 0.001897	—

Table A.50 Total efficiencies in bins of D_s^+ , p_T and y^* for Bwd collision configuration.

p_T [GeV/c] \ y^*	[-3, -2.5]	[-3.5, -3]	[-4, -3.5]	[-4.5, -4]	[-5, -4.5]
[1, 2]	0.000398 ± 0.000058	0.001404 ± 0.000143	0.001618 ± 0.000172	0.000806 ± 0.000109	0.000225 ± 0.000031
[2, 3]	0.006480 ± 0.000721	0.018340 ± 0.001558	0.018375 ± 0.001463	0.010890 ± 0.000785	0.002705 ± 0.000271
[3, 4]	0.019863 ± 0.001918	0.046250 ± 0.003861	0.045104 ± 0.003643	0.028306 ± 0.002242	0.007014 ± 0.000669
[4, 5]	0.035573 ± 0.003246	0.069363 ± 0.005572	0.069113 ± 0.005295	0.043879 ± 0.002777	0.009994 ± 0.001079
[5, 6]	0.053568 ± 0.004925	0.092039 ± 0.007815	0.082827 ± 0.006029	0.054261 ± 0.005019	0.007930 ± 0.001099
[6, 7]	0.072872 ± 0.006516	0.112379 ± 0.009146	0.101706 ± 0.008856	0.055735 ± 0.005019	0.004507 ± 0.000772
[7, 8]	0.083377 ± 0.006256	0.120720 ± 0.009067	0.103306 ± 0.008762	0.048006 ± 0.005169	0.001409 ± 0.000438
[8, 9]	0.090534 ± 0.006189	0.120405 ± 0.013059	0.108158 ± 0.009227	0.038398 ± 0.004977	0.000705 ± 0.000449
[9, 10]	0.105923 ± 0.011854	0.130730 ± 0.011353	0.115964 ± 0.012174	0.026087 ± 0.004595	–
[10, 11]	0.112865 ± 0.011996	0.122525 ± 0.012099	0.099824 ± 0.011495	0.015840 ± 0.003874	–
[11, 12]	0.118531 ± 0.012471	0.119680 ± 0.012628	0.102065 ± 0.013659	–	–
[12, 13]	0.115675 ± 0.012371	0.125430 ± 0.016095	0.076994 ± 0.011945	–	–

Table A.51 Total efficiencies in bins of D^+ p_T and y^* for Fwd collision configuration.

p_T [GeV/c] \ y^*	[1.5, 2]	[2, 2.5]	[2.5, 3]	[3, 3.5]	[3.5, 4]
[1, 2]	0.361 ± 0.007	4.315 ± 0.024	6.667 ± 0.033	4.776 ± 0.034	1.545 ± 0.017
[2, 3]	4.518 ± 0.023	27.219 ± 0.061	34.712 ± 0.073	23.788 ± 0.070	7.137 ± 0.045
[3, 4]	7.958 ± 0.031	32.848 ± 0.065	36.316 ± 0.073	23.917 ± 0.066	6.726 ± 0.038
[4, 5]	7.786 ± 0.031	24.823 ± 0.057	25.119 ± 0.061	15.839 ± 0.052	3.641 ± 0.034
[5, 6]	6.238 ± 0.028	16.180 ± 0.046	15.421 ± 0.048	8.919 ± 0.038	1.419 ± 0.018
[6, 7]	4.538 ± 0.024	10.209 ± 0.037	9.218 ± 0.037	4.606 ± 0.033	0.426 ± 0.007
[7, 8]	3.121 ± 0.020	6.376 ± 0.029	5.458 ± 0.028	2.232 ± 0.019	0.088 ± 0.005
[8, 9]	2.188 ± 0.017	3.982 ± 0.023	3.265 ± 0.022	1.007 ± 0.014	0.017 ± 0.002
[9, 10]	1.508 ± 0.013	2.504 ± 0.018	1.936 ± 0.017	0.441 ± 0.009	–
[10, 11]	1.041 ± 0.011	1.628 ± 0.015	1.170 ± 0.013	0.169 ± 0.004	–
[11, 12]	0.734 ± 0.010	1.046 ± 0.012	0.693 ± 0.010	0.057 ± 0.002	–
[12, 13]	0.512 ± 0.008	0.674 ± 0.010	0.402 ± 0.007	0.023 ± 0.002	–
[13, 14]	0.345 ± 0.007	0.446 ± 0.008	0.225 ± 0.005	0.006 ± 0.001	–

Table A.52 Total efficiencies in bins of D^+ p_T and y^* for Bwd collision configuration.

p_T [GeV/c] y^*	[-3, -2.5]	[-3.5, -3]	[-4, -3.5]	[-4.5, -4]	[-5, -4.5]
[1, 2]	0.831 ± 0.010	5.909 ± 0.029	7.879 ± 0.038	4.893 ± 0.041	1.297 ± 0.028
[2, 3]	8.600 ± 0.031	35.306 ± 0.067	38.967 ± 0.081	23.005 ± 0.075	5.209 ± 0.043
[3, 4]	13.434 ± 0.041	39.126 ± 0.072	37.497 ± 0.076	20.408 ± 0.062	3.983 ± 0.032
[4, 5]	12.171 ± 0.039	27.106 ± 0.060	23.197 ± 0.058	11.538 ± 0.045	1.691 ± 0.022
[5, 6]	8.891 ± 0.033	16.331 ± 0.046	12.830 ± 0.043	5.529 ± 0.030	0.496 ± 0.010
[6, 7]	6.043 ± 0.027	9.575 ± 0.036	6.887 ± 0.031	2.430 ± 0.021	0.108 ± 0.007
[7, 8]	4.039 ± 0.022	5.546 ± 0.027	3.741 ± 0.023	0.988 ± 0.013	0.019 ± 0.001
[8, 9]	2.667 ± 0.019	3.291 ± 0.021	2.026 ± 0.016	0.395 ± 0.009	–
[9, 10]	1.764 ± 0.015	1.958 ± 0.016	1.101 ± 0.012	0.122 ± 0.004	–
[10, 11]	1.158 ± 0.012	1.194 ± 0.013	0.583 ± 0.009	0.046 ± 0.002	–
[11, 12]	0.773 ± 0.010	0.753 ± 0.010	0.310 ± 0.006	0.016 ± 0.001	–
[12, 13]	0.538 ± 0.010	0.474 ± 0.009	0.178 ± 0.005	0.004 ± 0.001	–
[13, 14]	0.335 ± 0.007	0.300 ± 0.006	0.089 ± 0.004	–	–

APPENDIX B YIELDS AND FRACTIONS

The raw yields candidates from mass fit are given in Tables B.1, B.2, B.3, B.4, B.5, B.6. The fractions of prompt D_s^+ mesons are listed in Table B.7, B.8. The fractions of non-prompt D^+ mesons are listed in Table B.9, B.10. The prompt yield D_s^+ mesons are listed in Table B.11, B.12. The prompt yield D^+ mesons are listed in Table B.13, B.14. Statistical uncertainties only.

Table B.1 Raw yields of D_s^+ candidates in bins of p_T and y^* for Fwd configurations.

p_T [GeV/c] y^*	[1.5, 2]	[2, 2.5]	[2.5, 3]	[3, 3.5]	[3.5, 4]
[1, 2]	428.8 ± 20.4	2479.4 ± 52.7	2898.7 ± 61.8	1842.3 ± 53.9	401.3 ± 24.9
[2, 3]	5505.9 ± 77.4	20688.9 ± 155.8	22413.1 ± 170.0	13394.2 ± 142.8	2857.5 ± 70.3
[3, 4]	9124.0 ± 99.9	26779.8 ± 174.2	26683.2 ± 179.1	15679.7 ± 134.3	3299.5 ± 68.4
[4, 5]	8578.7 ± 96.6	20978.0 ± 153.3	19823.6 ± 150.9	11270.9 ± 111.6	2113.9 ± 51.4
[5, 6]	6790.7 ± 85.5	13667.1 ± 123.0	12239.6 ± 118.5	6853.0 ± 85.9	1000.2 ± 37.1
[6, 7]	4757.2 ± 72.0	8898.5 ± 99.0	7291.2 ± 91.2	3755.4 ± 65.7	315.4 ± 18.5
[7, 8]	3237.1 ± 59.2	5589.5 ± 78.4	4422.4 ± 70.1	1766.0 ± 43.4	71.7 ± 9.4
[8, 9]	2161.1 ± 48.3	3405.1 ± 61.2	2649.4 ± 54.4	834.2 ± 30.7	–
[9, 10]	1552.8 ± 37.8	2149.7 ± 48.2	1579.8 ± 41.8	322.8 ± 19.1	–
[10, 11]	1039.7 ± 33.6	1342.9 ± 38.1	980.8 ± 32.7	155.2 ± 12.7	–
[11, 12]	671.6 ± 26.2	892.8 ± 31.2	569.6 ± 24.0	48.5 ± 6.9	–
[12, 13]	492.6 ± 19.3	576.2 ± 25.0	345.8 ± 19.6	–	–

Table B.2 Raw yields of D_s^+ candidates in bins of p_T and y^* for Bwd configurations.

p_T [GeV/c] \ y^*	[-3, -2.5]	[-3.5, -3]	[-4, -3.5]	[-4.5, -4]	[-5, -4.5]
[1, 2]	802.4 ± 30.3	3269.0 ± 63.4	3447.7 ± 136.8	1770.1 ± 55.2	309.7 ± 25.5
[2, 3]	9528.2 ± 101.3	26715.3 ± 182.3	25327.7 ± 190.8	11983.2 ± 145.0	1754.4 ± 55.4
[3, 4]	14940.7 ± 127.9	32473.9 ± 741.6	28147.0 ± 180.7	13043.7 ± 128.9	1784.7 ± 50.4
[4, 5]	13091.6 ± 119.2	23721.6 ± 164.4	18676.9 ± 146.9	8156.5 ± 94.3	915.7 ± 32.4
[5, 6]	9472.7 ± 101.4	14896.2 ± 128.4	10618.4 ± 109.3	4307.0 ± 70.6	332.6 ± 19.2
[6, 7]	6497.2 ± 83.9	8604.1 ± 96.9	5590.8 ± 78.5	1874.0 ± 44.6	57.7 ± 7.7
[7, 8]	4082.5 ± 66.3	5234.3 ± 75.5	3321.0 ± 60.0	827.2 ± 29.9	–
[8, 9]	2711.9 ± 54.1	2811.3 ± 55.6	1629.5 ± 39.9	311.2 ± 17.3	–
[9, 10]	1723.3 ± 43.2	1679.5 ± 42.6	986.6 ± 32.1	103.1 ± 10.2	–
[10, 11]	1122.4 ± 34.7	1097.5 ± 32.8	498.0 ± 22.1	29.2 ± 5.5	–
[11, 12]	768.4 ± 28.3	625.4 ± 26.3	281.1 ± 17.0	–	–
[12, 13]	536.3 ± 23.7	414.2 ± 20.7	139.7 ± 11.2	–	–

Table B.3 Raw yields of D^+ candidates in bins of p_T and y^* for Fwd configurations.

p_T [GeV/c] y^*	[1.5, 2]	[2, 2.5]	[2.5, 3]	[3, 3.5]	[3.5, 4]
[1, 2]	3609.477 ± 66.472	43152.636 ± 240.519	66670.210 ± 333.759	47759.894 ± 341.931	15450.406 ± 167.696
[2, 3]	45184.999 ± 234.673	272188.717 ± 607.393	347115.374 ± 733.552	237878.696 ± 702.390	71366.316 ± 451.793
[3, 4]	79580.352 ± 311.995	328482.508 ± 652.771	363160.172 ± 733.189	239169.759 ± 656.676	67262.746 ± 375.204
[4, 5]	77860.869 ± 308.733	248235.286 ± 567.980	251194.716 ± 606.568	158388.654 ± 517.479	36409.634 ± 339.653
[5, 6]	62377.212 ± 277.289	161799.662 ± 458.355	154206.627 ± 475.154	89185.248 ± 379.967	14187.636 ± 179.031
[6, 7]	45376.499 ± 235.123	102086.947 ± 367.465	92180.720 ± 367.713	46060.463 ± 334.296	4259.096 ± 71.581
[7, 8]	31212.329 ± 195.393	63757.164 ± 292.557	54576.192 ± 280.798	22315.438 ± 189.263	884.446 ± 46.406
[8, 9]	21882.559 ± 166.625	39819.195 ± 231.412	32645.382 ± 219.904	10068.227 ± 144.774	169.148 ± 18.839
[9, 10]	15083.440 ± 134.032	25043.781 ± 183.961	19358.951 ± 168.433	4408.475 ± 88.262	0.000 ± 0.000
[10, 11]	10406.815 ± 108.626	16275.252 ± 148.500	11701.409 ± 129.224	1691.164 ± 43.309	0.000 ± 0.000
[11, 12]	7340.717 ± 96.678	10459.664 ± 119.733	6931.799 ± 100.387	566.825 ± 21.579	0.000 ± 0.000
[12, 13]	5116.937 ± 84.597	6741.798 ± 96.496	4024.787 ± 74.777	230.002 ± 17.782	0.000 ± 0.000
[13, 14]	3446.070 ± 68.559	4455.314 ± 78.514	2254.066 ± 52.185	63.325 ± 7.749	0.000 ± 0.000

Table B.4 Raw yields of D^+ candidates in bins of p_T and y^* for Bwd configurations.

p_T [GeV/c]	y^*	[-3, -2.5]	[-3.5, -3]	[-4, -3.5]	[-4.5, -4]	[-5, -4.5]
[1, 2]		8307.221 ± 102.913	59087.199 ± 289.997	78792.226 ± 382.574	48926.086 ± 414.201	12964.993 ± 277.112
[2, 3]		85996.218 ± 310.368	353061.189 ± 665.172	389669.682 ± 807.235	230052.446 ± 745.648	52085.121 ± 430.636
[3, 4]		134340.843 ± 407.806	391261.235 ± 723.045	374973.903 ± 756.519	204081.343 ± 623.248	39828.143 ± 315.494
[4, 5]		121705.547 ± 385.171	271055.487 ± 596.426	231969.929 ± 581.004	115384.891 ± 445.557	16907.380 ± 222.123
[5, 6]		88908.528 ± 331.051	163306.810 ± 463.363	128295.376 ± 432.623	55289.493 ± 295.587	4959.169 ± 103.639
[6, 7]		60425.203 ± 273.585	95754.038 ± 356.063	68873.686 ± 314.275	24302.711 ± 210.646	1081.007 ± 94.432
[7, 8]		40385.920 ± 224.356	55456.352 ± 271.873	37407.617 ± 232.195	9883.923 ± 132.934	188.792 ± 14.428
[8, 9]		26667.281 ± 186.493	32913.393 ± 209.257	20263.254 ± 164.103	3950.594 ± 91.518	0.000 ± 0.000
[9, 10]		17638.655 ± 149.136	19578.746 ± 161.426	11007.203 ± 123.184	1222.644 ± 44.396	0.000 ± 0.000
[10, 11]		11579.550 ± 120.341	11942.646 ± 127.772	5833.538 ± 90.373	456.457 ± 23.605	0.000 ± 0.000
[11, 12]		7732.926 ± 100.392	7533.004 ± 99.754	3099.628 ± 62.838	157.331 ± 12.559	0.000 ± 0.000
[12, 13]		5384.678 ± 100.415	4741.470 ± 94.950	1783.432 ± 49.071	37.646 ± 6.838	0.000 ± 0.000
[13, 14]		3347.355 ± 65.586	2998.075 ± 63.339	890.325 ± 38.916	0.000 ± 0.000	0.000 ± 0.000

Table B.5 Raw yields of D_s^+ candidates in bins of p_T and y^* and PV nTracks for Fwd (top) and Bwd (bottom) configurations.

p_T [GeV/c], y^* * PVnTracks	Forward					
	[10, 60]	[60, 80]	[80, 100]	[100, 120]	[120, 140]	[140, 200]
[2, 4], [1.8, 2.3]	3425.5908 ± 61.0306	3327.0264 ± 60.0023	3701.6432 ± 65.0254	3425.2263 ± 61.2756	2608.2033 ± 53.6627	2651.6295 ± 55.1989
[2, 4], [2.3, 2.8]	4580.5742 ± 77.6644	4339.4657 ± 69.7298	4920.3015 ± 81.2559	4485.8267 ± 72.6913	3265.8873 ± 64.2738	3609.3655 ± 70.1273
[2, 4], [2.8, 3.3]	3716.6207 ± 67.9349	3248.3282 ± 61.7847	3771.3436 ± 72.5791	3393.8540 ± 66.6142	2410.7777 ± 54.6587	2580.6942 ± 60.8671
[4, 6], [1.8, 2.3]	2445.1649 ± 52.3711	2494.7402 ± 54.5954	3065.2202 ± 58.5589	2884.6498 ± 56.7143	2157.1709 ± 48.9559	2396.1258 ± 50.8877
[4, 6], [2.3, 2.8]	2686.0766 ± 56.0033	2856.6102 ± 55.8925	3294.6333 ± 62.6645	3061.6654 ± 58.0984	2224.3328 ± 49.6665	2592.4438 ± 57.1125
[4, 6], [2.8, 3.3]	2025.8961 ± 47.5817	2083.8652 ± 48.3158	2299.8458 ± 51.6820	2117.1424 ± 49.2005	1593.9305 ± 42.3514	1723.6933 ± 45.9608

p_T [GeV/c], y^* * PVnTracks	Backward					
	[10, 60]	[60, 80]	[80, 100]	[100, 120]	[120, 140]	[140, 180]
[2, 4], [-3.3, -2.8]	5582.6660 ± 78.4062	5033.3499 ± 73.3750	6148.8070 ± 84.2790	5657.5404 ± 79.1002	4698.5170 ± 72.1996	5336.2943 ± 80.7364
[2, 4], [-3.8, -3.3]	6279.2291 ± 84.9439	5544.4922 ± 81.1763	6693.4551 ± 88.4512	6597.0145 ± 86.6002	5486.5190 ± 82.3053	6350.0921 ± 89.5542
[2, 4], [-4.3, -3.8]	4045.6087 ± 71.9556	3622.1731 ± 64.5084	4186.5769 ± 71.9084	4297.2434 ± 77.2490	3507.0799 ± 67.4655	4018.8343 ± 80.5757
[4, 6], [-3.3, -2.8]	3423.2823 ± 60.4139	3266.4949 ± 59.2968	4088.0843 ± 66.6505	4210.8570 ± 67.5232	3528.6304 ± 62.0881	4363.7315 ± 71.9181
[4, 6], [-3.8, -3.3]	3031.0403 ± 57.3475	3128.5258 ± 58.4203	3775.1487 ± 64.2906	3880.8150 ± 66.4827	3327.8947 ± 61.1195	3879.2997 ± 66.2260
[4, 6], [-4.3, -3.8]	1787.5751 ± 44.6605	1799.4016 ± 44.7277	2149.2241 ± 49.4144	2189.5442 ± 49.7425	1805.9910 ± 44.9533	2149.2519 ± 51.8165

Table B.6 Raw yields of D^+ candidates in bins of p_T and y^* and PV nTracks for Fwd (top) and Bwd (bottom) configurations.

p_T [GeV/c], y^* * APVnTracks	Forward					
	[10, 60]	[60, 80]	[80, 100]	[100, 120]	[120, 140]	[140, 200]
[2, 4], [1.8, 2.3]	40432.8446 ± 208.3840	36703.6000 ± 201.1193	40933.8304 ± 214.2364	37847.5277 ± 207.2668	27058.9793 ± 178.9481	28060.9340 ± 175.0693
[2, 4], [2.3, 2.8]	67895.6749 ± 277.2552	59750.6294 ± 264.2954	67359.1115 ± 276.9992	60287.0302 ± 267.7773	43977.0472 ± 237.1928	45062.3243 ± 243.1883
[2, 4], [2.8, 3.3]	59441.8253 ± 281.1764	50669.4708 ± 259.9453	56045.3212 ± 277.2733	50057.7681 ± 263.9487	35760.4859 ± 220.0719	35658.2603 ± 229.2520
[4, 6], [1.8, 2.3]	28891.6329 ± 177.6597	28316.3323 ± 173.6880	32637.9021 ± 188.9230	30609.2563 ± 181.1867	22567.2703 ± 155.8324	24401.4661 ± 162.7607
[4, 6], [2.3, 2.8]	37264.0287 ± 206.0369	34886.2213 ± 196.8937	40026.2697 ± 216.3673	36933.0288 ± 221.0428	27293.3313 ± 181.9785	28410.6559 ± 189.2309
[4, 6], [2.8, 3.3]	29568.6753 ± 197.9749	27476.8761 ± 193.1876	30671.5315 ± 189.4553	27471.8309 ± 180.4535	20225.8359 ± 160.6303	20402.1568 ± 166.3045

p_T [GeV/c], y^* * APVnTracks	Backward					
	[10, 60]	[60, 80]	[80, 100]	[100, 120]	[120, 140]	[140, 180]
[2, 4], [-3.3, -2.8]	70149.9969 ± 271.4950	60381.9178 ± 256.5050	68695.4849 ± 276.5999	65253.1417 ± 274.1295	51640.4192 ± 236.5861	55852.5244 ± 248.3674
[2, 4], [-3.8, -3.3]	94916.4255 ± 333.1027	81688.9919 ± 303.1764	94668.8776 ± 327.6790	90882.3789 ± 328.0560	71903.0156 ± 308.8666	76736.0444 ± 326.2690
[2, 4], [-4.3, -3.8]	70350.4274 ± 295.9631	60294.0162 ± 278.9614	68860.9228 ± 307.0499	65709.3938 ± 392.5991	52233.7143 ± 259.5909	56108.4973 ± 325.9045
[4, 6], [-3.3, -2.8]	41289.9489 ± 211.2867	38625.0499 ± 206.3471	45002.4640 ± 219.9100	44178.9523 ± 227.8218	36763.1010 ± 202.6569	42343.9113 ± 220.1542
[4, 6], [-3.8, -3.3]	42395.2080 ± 214.9626	39731.1759 ± 215.0411	46010.2518 ± 224.4983	45046.7754 ± 229.3890	37345.9174 ± 212.1874	41978.1927 ± 220.3671
[4, 6], [-4.3, -3.8]	27269.7596 ± 178.7429	24919.8234 ± 175.0409	28738.7165 ± 188.2619	28020.2492 ± 184.0822	22832.4442 ± 175.9992	25698.3271 ± 189.9557

Table B.7 Fractions of prompt D_s^+ in bins of p_T and y^* for Fwd configurations.

p_T [GeV/c] \ y^*	[1.5, 2]	[2, 2.5]	[2.5, 3]	[3, 3.5]	[3.5, 4]
[1, 2]	0.877 ± 0.032	0.821 ± 0.016	0.799 ± 0.021	0.675 ± 0.021	0.582 ± 0.054
[2, 3]	0.910 ± 0.022	0.816 ± 0.004	0.761 ± 0.004	0.750 ± 0.008	0.654 ± 0.011
[3, 4]	0.854 ± 0.032	0.821 ± 0.011	0.770 ± 0.005	0.754 ± 0.008	0.725 ± 0.096
[4, 5]	0.836 ± 0.013	0.820 ± 0.009	0.773 ± 0.006	0.741 ± 0.016	0.730 ± 0.024
[5, 6]	0.791 ± 0.085	0.788 ± 0.013	0.775 ± 0.008	0.793 ± 0.012	0.775 ± 0.017
[6, 7]	0.810 ± 0.019	0.784 ± 0.003	0.765 ± 0.009	0.776 ± 0.029	0.854 ± 0.042
[7, 8]	0.795 ± 0.024	0.790 ± 0.010	0.762 ± 0.014	0.838 ± 0.035	0.929 ± 0.025
[8, 9]	0.843 ± 0.059	0.816 ± 0.020	0.789 ± 0.011	0.809 ± 0.018	–
[9, 10]	0.771 ± 0.062	0.788 ± 0.001	0.791 ± 0.018	0.859 ± 0.034	–
[10, 11]	0.852 ± 0.031	0.813 ± 0.031	0.813 ± 0.022	0.816 ± 0.045	–
[11, 12]	0.782 ± 0.034	0.809 ± 0.020	0.777 ± 0.028	0.863 ± 0.057	–
[12, 13]	0.774 ± 0.000	0.754 ± 0.065	0.780 ± 0.062	–	–

Table B.8 Fractions of prompt D_s^+ in bins of p_T and y^* for Bwd configurations.

p_T [GeV/c] \ y^*	[-3, -2.5]	[-3.5, -3]	[-4, -3.5]	[-4.5, -4]	[-5, -4.5]
[1, 2]	0.952 ± 0.022	0.888 ± 0.027	0.801 ± 0.007	0.760 ± 0.019	0.726 ± 0.028
[2, 3]	0.923 ± 0.015	0.854 ± 0.018	0.805 ± 0.005	0.759 ± 0.008	0.760 ± 0.030
[3, 4]	0.899 ± 0.004	0.875 ± 0.006	0.813 ± 0.013	0.788 ± 0.008	0.836 ± 0.022
[4, 5]	0.876 ± 0.019	0.847 ± 0.007	0.815 ± 0.016	0.816 ± 0.002	0.801 ± 0.021
[5, 6]	0.834 ± 0.023	0.837 ± 0.007	0.815 ± 0.006	0.861 ± 0.022	0.806 ± 0.029
[6, 7]	0.775 ± 0.031	0.821 ± 0.005	0.807 ± 0.014	0.846 ± 0.019	0.947 ± 0.038
[7, 8]	0.794 ± 0.016	0.796 ± 0.017	0.812 ± 0.011	0.853 ± 0.022	–
[8, 9]	0.812 ± 0.020	0.842 ± 0.012	0.813 ± 0.070	0.886 ± 0.028	–
[9, 10]	0.791 ± 0.037	0.838 ± 0.026	0.856 ± 0.018	0.871 ± 0.039	–
[10, 11]	0.857 ± 0.037	0.850 ± 0.018	0.876 ± 0.028	0.871 ± 0.062	–
[11, 12]	0.788 ± 0.021	0.863 ± 0.020	0.859 ± 0.050	–	–
[12, 13]	0.844 ± 0.069	0.766 ± 0.046	0.877 ± 0.072	–	–

Table B.9 Fractions of non-prompt D^+ in bins of p_T and y^* for Fwd configurations.

p_T [GeV/c] \ y^*	[1.5, 2]	[2, 2.5]	[2.5, 3]	[3, 3.5]	[3.5, 4]
[1, 2]	0.013 ± 0.005	0.017 ± 0.002	0.052 ± 0.021	0.088 ± 0.005	0.150 ± 0.003
[2, 3]	0.015 ± 0.002	0.035 ± 0.003	0.041 ± 0.001	0.086 ± 0.002	0.078 ± 0.002
[3, 4]	0.026 ± 0.002	0.030 ± 0.004	0.069 ± 0.001	0.068 ± 0.002	0.071 ± 0.002
[4, 5]	0.034 ± 0.013	0.040 ± 0.005	0.067 ± 0.001	0.086 ± 0.002	0.089 ± 0.005
[5, 6]	0.034 ± 0.004	0.053 ± 0.003	0.076 ± 0.003	0.089 ± 0.003	0.092 ± 0.006
[6, 7]	0.044 ± 0.006	0.059 ± 0.003	0.078 ± 0.004	0.086 ± 0.003	0.093 ± 0.011
[7, 8]	0.051 ± 0.006	0.073 ± 0.004	0.087 ± 0.003	0.084 ± 0.004	0.068 ± 0.021
[8, 9]	0.071 ± 0.004	0.080 ± 0.002	0.084 ± 0.003	0.102 ± 0.005	0.089 ± 0.031
[9, 10]	0.092 ± 0.007	0.075 ± 0.004	0.088 ± 0.005	0.093 ± 0.008	–
[10, 11]	0.067 ± 0.008	0.078 ± 0.003	0.086 ± 0.006	0.064 ± 0.007	–
[11, 12]	0.060 ± 0.009	0.089 ± 0.008	0.089 ± 0.008	0.078 ± 0.018	–
[12, 13]	0.061 ± 0.004	0.084 ± 0.005	0.090 ± 0.010	–	–
[13, 14]	0.067 ± 0.015	0.084 ± 0.008	0.097 ± 0.016	–	–

Table B.10 Fractions of non-prompt D^+ in bins of p_T and y^* for Bwd configurations.

p_T [GeV/c] \ y^*	[-3, -2.5]	[-3.5, -3]	[-4, -3.5]	[-4.5, -4]	[-5, -4.5]
[1, 2]	0.003 ± 0.001	0.022 ± 0.008	0.030 ± 0.002	0.049 ± 0.003	0.083 ± 0.006
[2, 3]	0.015 ± 0.001	0.030 ± 0.004	0.047 ± 0.001	0.063 ± 0.005	0.047 ± 0.002
[3, 4]	0.025 ± 0.010	0.039 ± 0.001	0.054 ± 0.001	0.062 ± 0.003	0.066 ± 0.004
[4, 5]	0.025 ± 0.002	0.037 ± 0.002	0.047 ± 0.002	0.067 ± 0.001	0.043 ± 0.004
[5, 6]	0.031 ± 0.005	0.043 ± 0.001	0.056 ± 0.002	0.066 ± 0.003	0.076 ± 0.011
[6, 7]	0.043 ± 0.005	0.053 ± 0.003	0.068 ± 0.003	0.079 ± 0.003	0.109 ± 0.017
[7, 8]	0.040 ± 0.004	0.061 ± 0.003	0.070 ± 0.003	0.073 ± 0.007	0.136 ± 0.030
[8, 9]	0.049 ± 0.001	0.069 ± 0.020	0.070 ± 0.004	0.066 ± 0.007	0.061 ± 0.024
[9, 10]	0.058 ± 0.003	0.069 ± 0.005	0.080 ± 0.030	0.068 ± 0.014	–
[10, 11]	0.050 ± 0.007	0.066 ± 0.007	0.081 ± 0.010	0.070 ± 0.017	–
[11, 12]	0.063 ± 0.008	0.082 ± 0.010	0.071 ± 0.012	0.070 ± 0.016	–
[12, 13]	0.091 ± 0.018	0.069 ± 0.007	0.074 ± 0.011	–	–
[13, 14]	0.067 ± 0.017	0.081 ± 0.011	0.070 ± 0.012	–	–

Table B.11 Prompt yield D_s^+ in bins of p_T and y^* and PV nTracks for Fwd configurations.

p_T [GeV/c], y^* PVnTracks	[10, 60]	[60, 80]	[80, 100]	[100, 120]	[120, 140]	[140, 200]
[2, 4], [1.8, 2.3]	2992.6348 ± 226.3774	3038.4267 ± 72.3093	3235.8006 ± 171.0044	3014.5938 ± 98.4925	2402.1352 ± 43.9457	2512.5251 ± 83.8723
[2, 4], [2.3, 2.8]	3709.0658 ± 223.2604	3484.7690 ± 164.0586	3992.1162 ± 192.2938	3949.1825 ± 73.3663	2707.5456 ± 59.2876	3057.6845 ± 181.4248
[2, 4], [2.8, 3.3]	2899.1567 ± 181.2913	2593.0134 ± 65.2800	3017.6351 ± 67.4602	2532.2128 ± 61.9947	2010.2173 ± 51.6141	2151.5962 ± 65.1546
[4, 6], [1.8, 2.3]	2124.5843 ± 58.5676	2172.8658 ± 58.6063	2577.7878 ± 132.5039	2510.1928 ± 58.5985	1823.4075 ± 51.4707	2196.0780 ± 52.2057
[4, 6], [2.3, 2.8]	2151.9641 ± 54.8052	2353.0579 ± 55.5037	2768.8942 ± 70.3725	2593.3663 ± 64.5255	1843.5803 ± 116.5385	2264.5996 ± 57.4552
[4, 6], [2.8, 3.3]	1572.9849 ± 125.5934	1596.1070 ± 106.2519	1850.6983 ± 76.1755	1679.7529 ± 50.6556	1262.3878 ± 88.0856	1385.7896 ± 23.3134

Table B.12 Prompt yield D_s^+ in bins of p_T and y^* and PV nTracks for Bwd configurations.

p_T [GeV/c], y^* \ PVnTracks	[10, 60]	[60, 80]	[80, 100]	[100, 120]	[120, 140]	[140, 180]	[180, 250]
[2, 4], [-3.3, -2.8]	5225.3384 ± 95.1545	4486.3634 ± 124.5446	5576.3169 ± 128.3069	5284.2901 ± 166.2275	4368.6675 ± 64.8187	4882.5496 ± 134.8418	1683.3816 ± 47.1734
[2, 4], [-3.8, -3.3]	5453.2181 ± 80.8267	4726.1200 ± 150.2346	5919.7985 ± 185.1685	5683.6757 ± 92.3134	4988.5032 ± 83.0266	5687.9748 ± 102.2959	2085.7973 ± 48.6431
[2, 4], [-4.3, -3.8]	3356.6548 ± 69.5321	3010.4185 ± 36.9563	3428.8350 ± 100.7284	3627.6766 ± 75.9676	2976.7912 ± 73.0664	3497.5398 ± 72.9167	1098.2760 ± 36.7037
[4, 6], [-3.3, -2.8]	2942.1110 ± 58.8739	2783.6242 ± 69.7186	3609.2280 ± 80.5429	3741.9619 ± 91.6090	3261.7794 ± 75.8122	4077.7605 ± 69.1473	1384.9943 ± 48.5843
[4, 6], [-3.8, -3.3]	2433.8674 ± 58.9562	2699.6705 ± 59.8079	3168.6427 ± 65.9466	3360.0427 ± 67.6627	2875.0368 ± 150.7554	3339.9513 ± 120.1995	1240.0126 ± 41.7425
[4, 6], [-4.3, -3.8]	1467.4925 ± 24.1950	1537.6132 ± 55.4160	1803.2388 ± 45.0769	1866.2407 ± 60.1749	1606.8947 ± 49.2620	1870.6798 ± 53.8768	678.4227 ± 30.0671

Table B.13 Prompt yield D^+ in bins of p_T and y^* and PV nTracks for Fwd configurations.

p_T [GeV/c], y^* * APVnTracks	[10, 60]	[60, 80]	[80, 100]	[100, 120]	[120, 140]	[140, 200]
[2, 4], [1.8, 2.3]	37550.2028 ± 1333.6748	35137.6976 ± 630.6662	40348.8261 ± 220.1626	37086.1505 ± 255.9290	26599.8340 ± 184.0978	27895.3273 ± 169.4250
[2, 4], [2.3, 2.8]	65726.8540 ± 312.8800	57393.3973 ± 355.5948	65442.6574 ± 286.8488	58264.6286 ± 290.3526	42256.4566 ± 314.2991	43712.3655 ± 297.8780
[2, 4], [2.8, 3.3]	57167.0110 ± 303.6073	48358.5489 ± 346.9287	53061.5943 ± 301.3512	47819.2210 ± 281.0510	34237.5761 ± 240.0841	34038.0234 ± 226.4339
[4, 6], [1.8, 2.3]	28139.7684 ± 182.6331	27477.9644 ± 190.8975	31691.7801 ± 198.1913	29805.7765 ± 191.2949	21964.4325 ± 160.4027	23826.5180 ± 316.1175
[4, 6], [2.3, 2.8]	35476.2999 ± 211.8215	33162.5992 ± 204.3077	37952.1521 ± 240.7061	35187.3871 ± 293.6017	26286.3127 ± 178.7159	27320.9678 ± 187.7451
[4, 6], [2.8, 3.3]	27475.5010 ± 184.8432	26099.6529 ± 278.8127	28586.1369 ± 246.3174	25347.1716 ± 526.5819	18994.7220 ± 153.4808	19269.9276 ± 376.9451

Table B.14 Prompt yield D^+ in bins of p_T and y^* and PV nTracks for Bwd configurations.

p_T [GeV/c], y^* nPVnTracks	[10, 60]	[60, 80]	[80, 100]	[100, 120]	[120, 140]	[140, 180]	[180, 250]
[2, 4], [-3.3, -2.8]	66709.8254 ± 1041.4084	59686.4926 ± 265.3251	65513.2692 ± 1067.3634	64187.7203 ± 315.7029	51048.6076 ± 244.1071	55014.4748 ± 307.5168	15686.3919 ± 125.5203
[2, 4], [-3.8, -3.3]	92052.8976 ± 373.9688	79641.8810 ± 322.7568	92445.1877 ± 351.4798	88679.1772 ± 366.7096	70617.2023 ± 299.1872	74589.4454 ± 373.8564	20552.2751 ± 165.4293
[2, 4], [-4.3, -3.8]	67688.3893 ± 274.8979	57594.1152 ± 342.2635	66249.2468 ± 320.6230	63417.0572 ± 303.7364	50571.9456 ± 263.7171	54607.4237 ± 254.6609	15514.2690 ± 129.4216
[4, 6], [-3.3, -2.8]	40179.0249 ± 215.4356	37704.8375 ± 209.6358	43818.5741 ± 243.4187	43135.9067 ± 226.4761	35835.8816 ± 350.8463	41297.0963 ± 248.1434	13313.9618 ± 178.2073
[4, 6], [-3.8, -3.3]	40847.6896 ± 217.5235	38237.0675 ± 242.1548	44313.4292 ± 226.0165	43616.0392 ± 219.6210	36181.6208 ± 201.2259	40360.2871 ± 217.6966	12544.6008 ± 115.0140
[4, 6], [-4.3, -3.8]	25729.7761 ± 104.4721	23775.7398 ± 170.1409	27187.4893 ± 262.7758	26914.7331 ± 234.2295	21962.6602 ± 252.5651	24587.3154 ± 174.6281	7648.4853 ± 89.8355

APPENDIX C MASS FIT RESULTS

The $M(D_s^+)$ fit results are included in Figure C.1,C.2,C.3 and C.4.

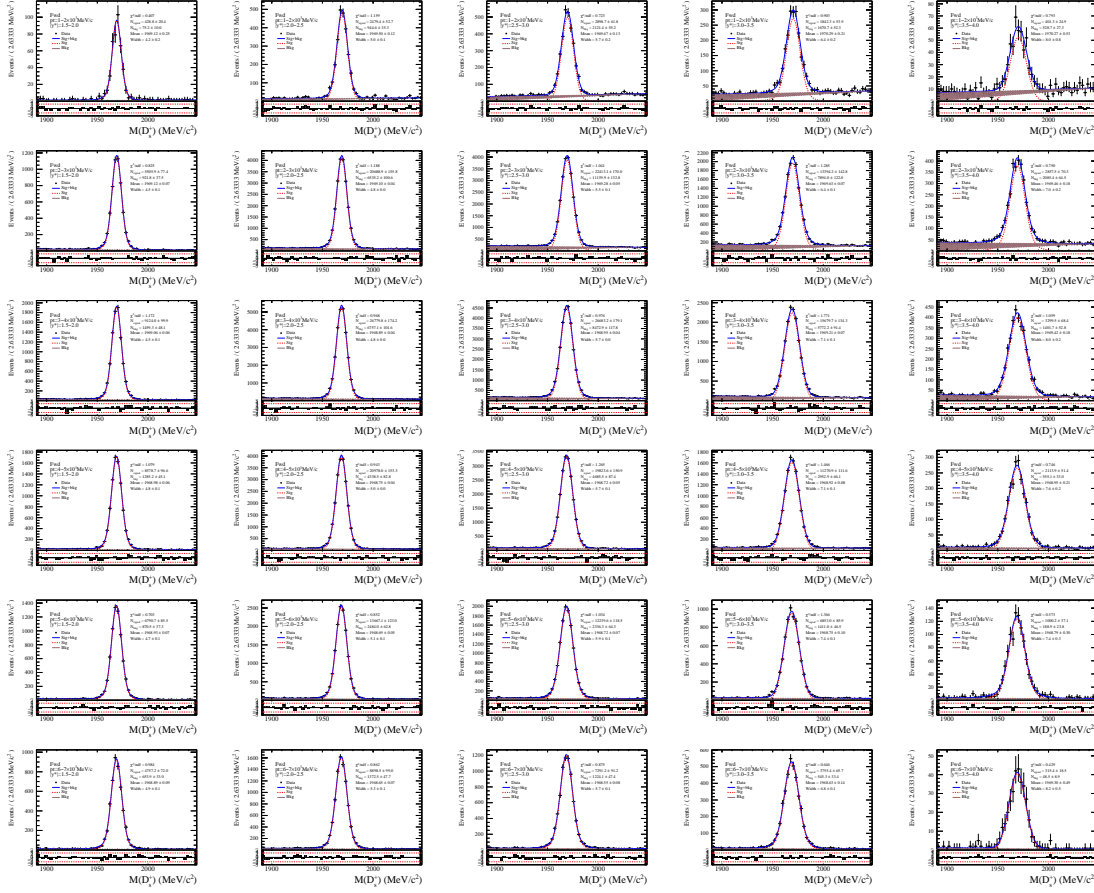


Figure C.1 Invariant mass fit result in each p_T and y^* bin in the Fwd sample in $1 < p_T < 7$ GeV/c. The column runs for p_T bins, the row runs for y^* bins.

APPENDIX C MASS FIT RESULTS

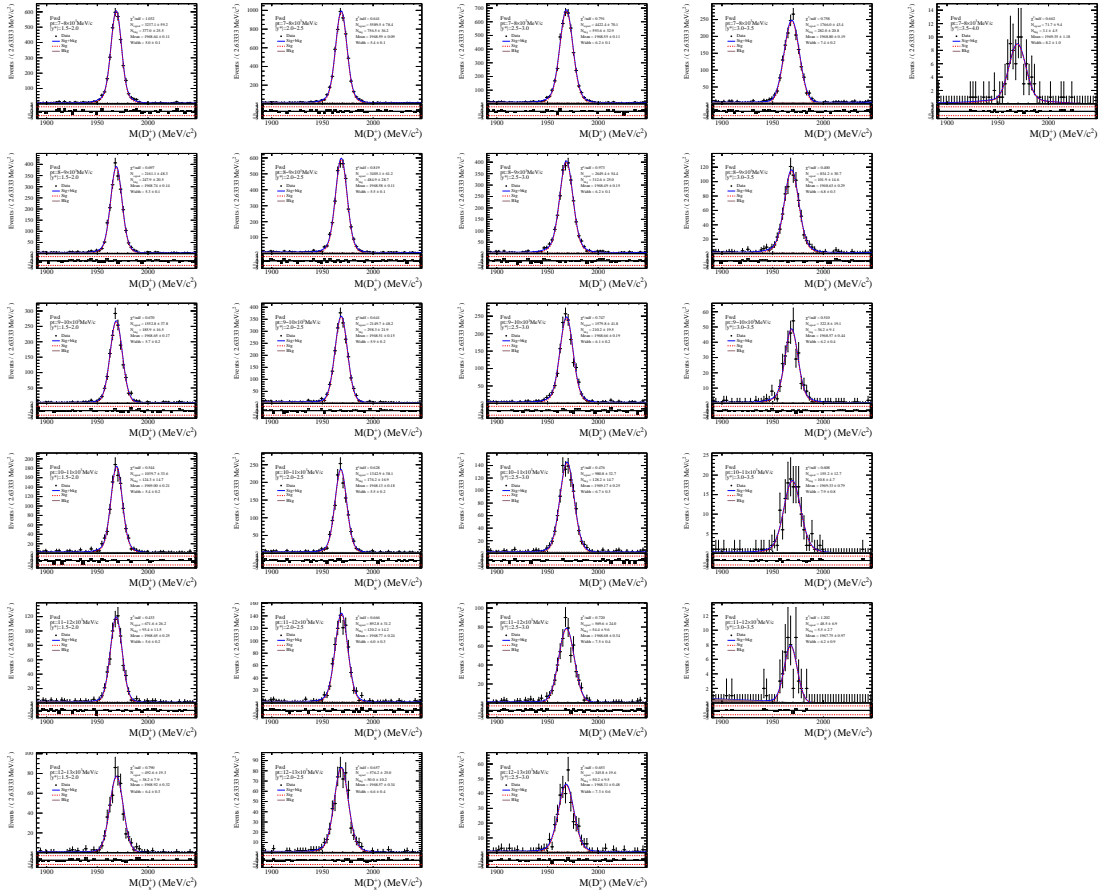


Figure C.2 Invariant mass fit result in each p_T and y^* bin in the Fwd sample in $7 < p_T < 13$ GeV/c. The column runs for p_T bins, the row runs for y^* bins.

APPENDIX C MASS FIT RESULTS

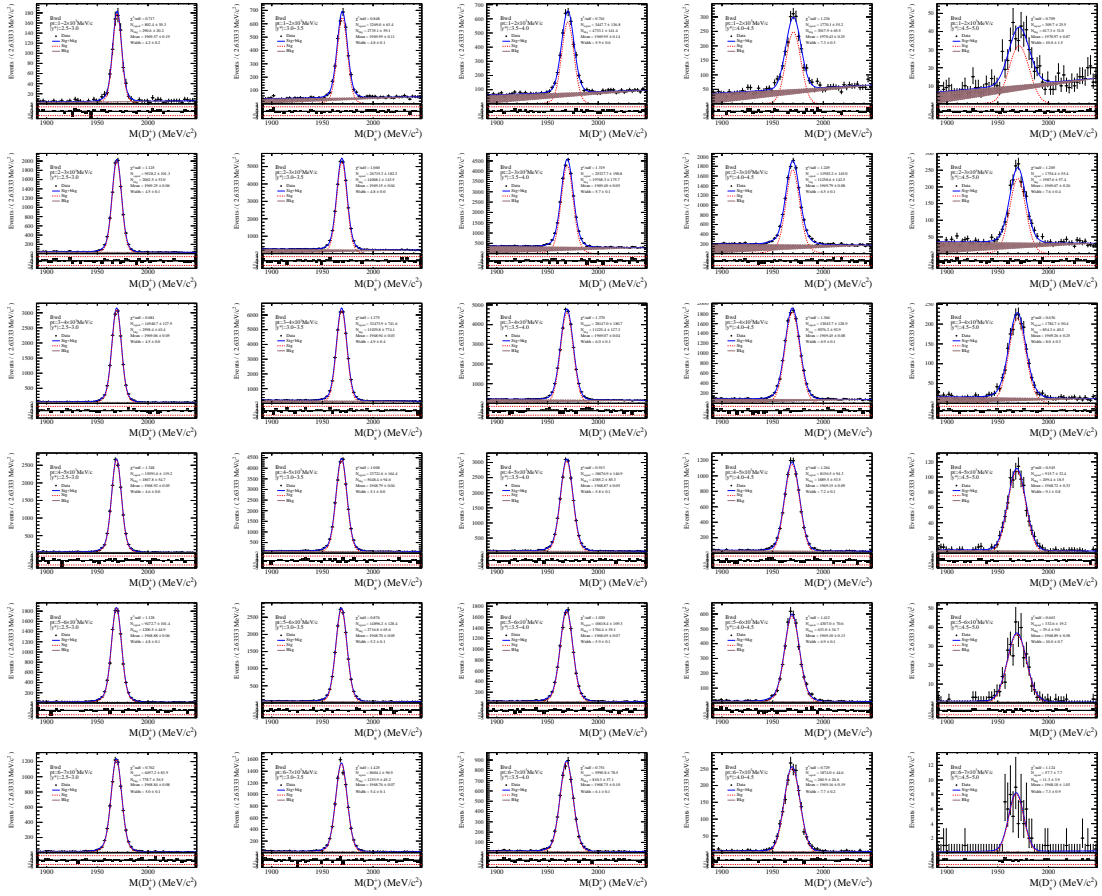


Figure C.3 Invariant mass fit result in each p_T and y^* bin in the Bwd sample in $1 < p_T < 7 \text{ GeV}/c$. The column runs for p_T bins, the row runs for y^* bins.

APPENDIX C MASS FIT RESULTS

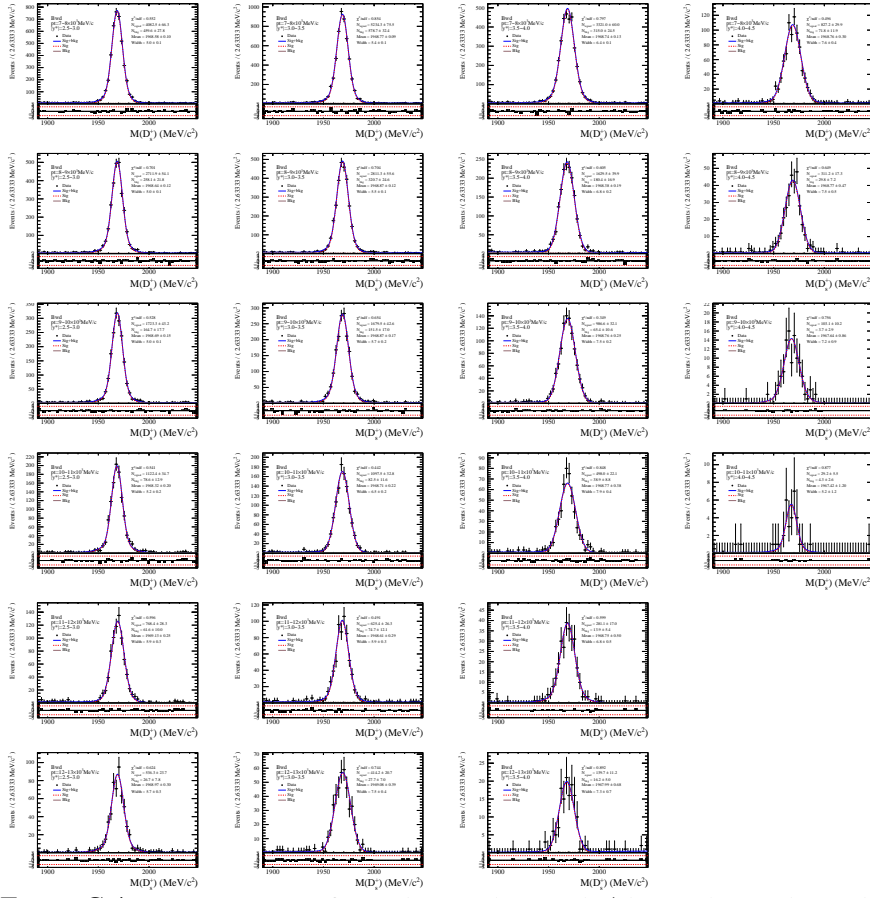


Figure C.4 Invariant mass fit result in each p_T and y^* bin in the Bwd sample in $7 < p_T < 13 \text{ GeV}/c$. The column runs for p_T bins, the row runs for y^* bins.

APPENDIX C MASS FIT RESULTS

The $M(D^+)$ fit results are included in Figure C.5,C.6,C.7 and C.8.

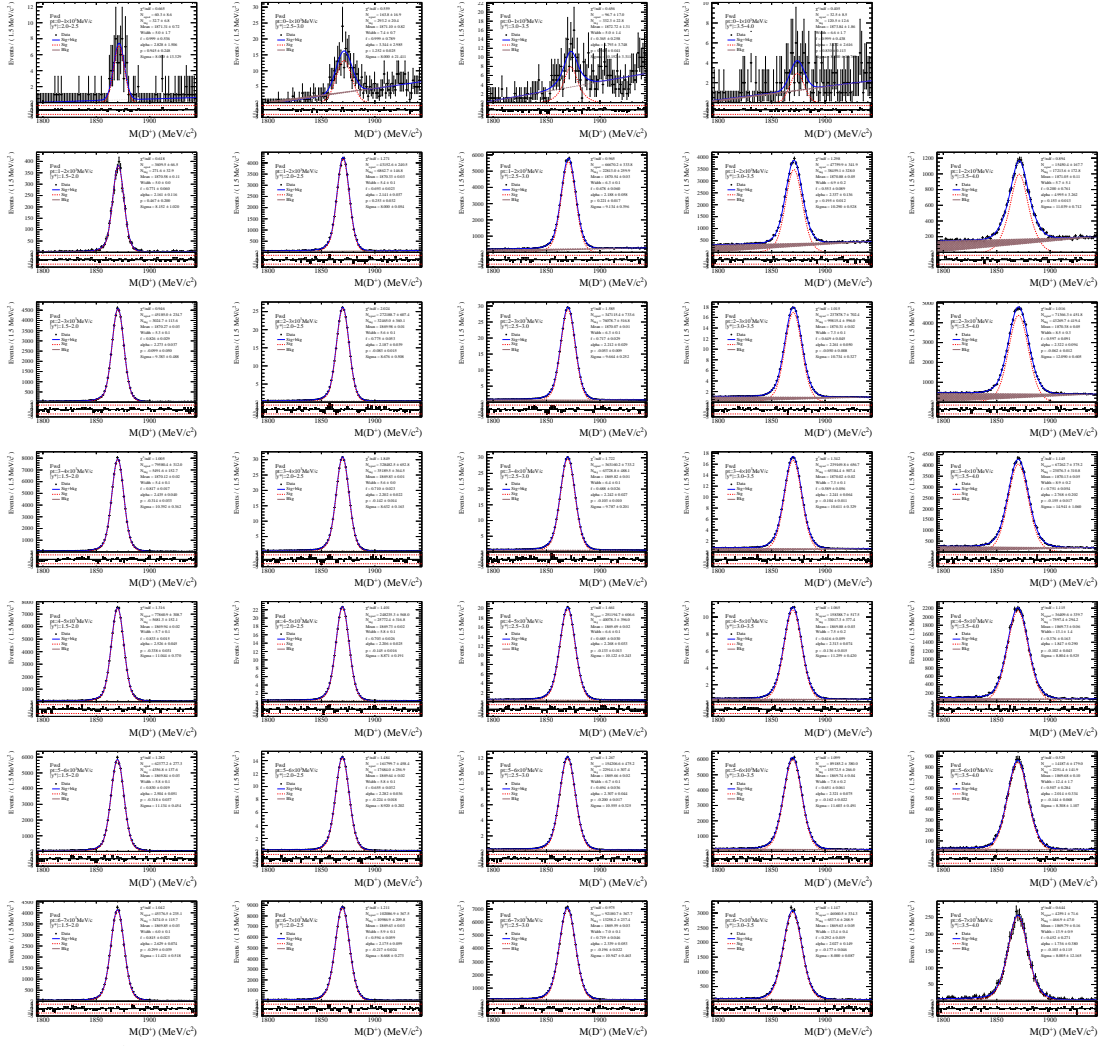


Figure C.5 Invariant mass fit result in each p_T and y^* bin in the Fwd sample in $0 < p_T < 7 \text{ GeV}/c$. The column runs for p_T bins, the row runs for y^* bins.

APPENDIX C MASS FIT RESULTS

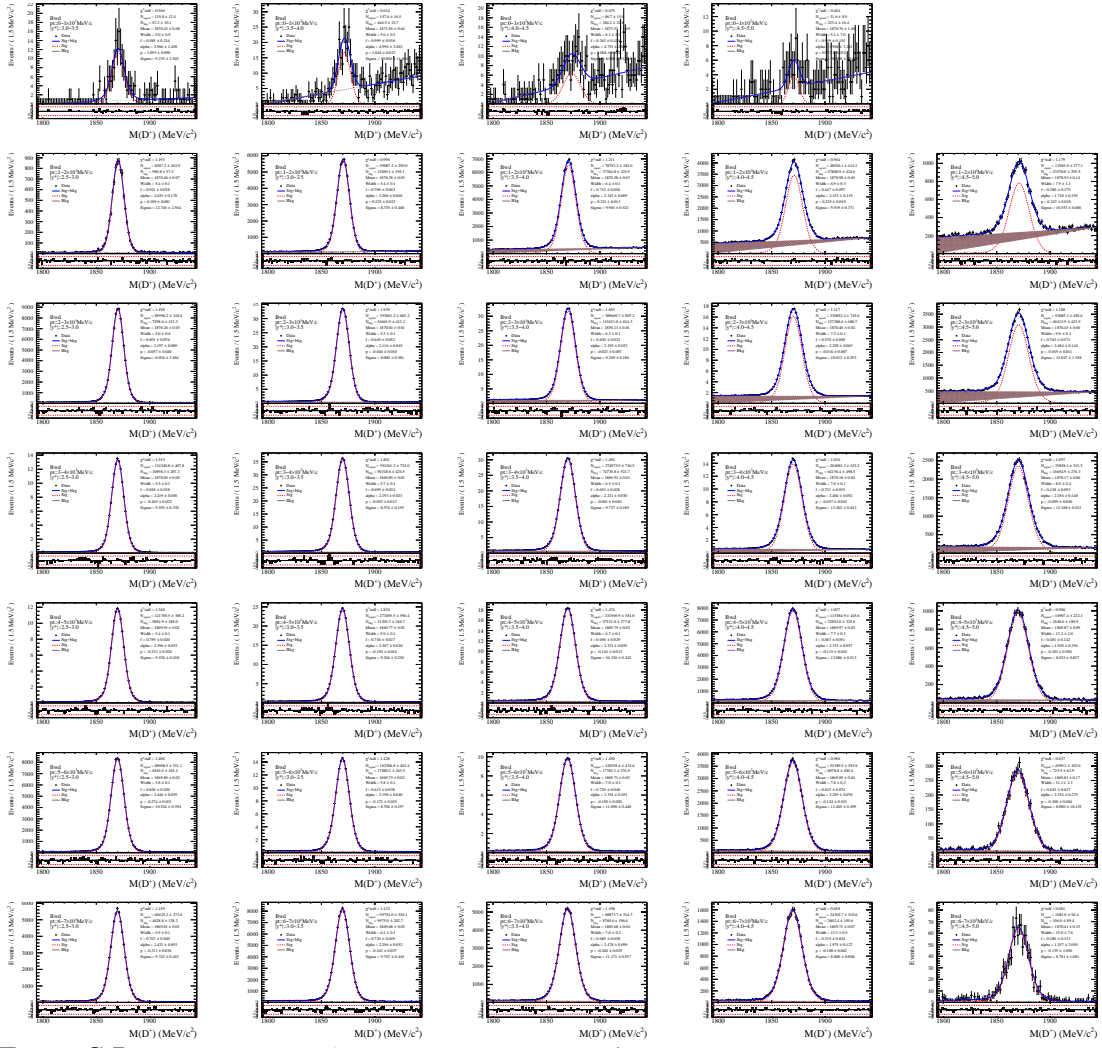


Figure C.7 Invariant mass fit result in each p_T and y^* bin in the Bwd sample in $0 < p_T < 7 \text{ GeV}/c$. The column runs for p_T bins, the row runs for y^* bins.

APPENDIX D $\text{LOG}_{10}\chi_{\text{IP}}^2$ FIT RESULTS

The $\text{log}_{10}\chi_{\text{IP}}^2(D_s^+)$ fit results are included in Figure D.1,D.2,D.3 and D.4.

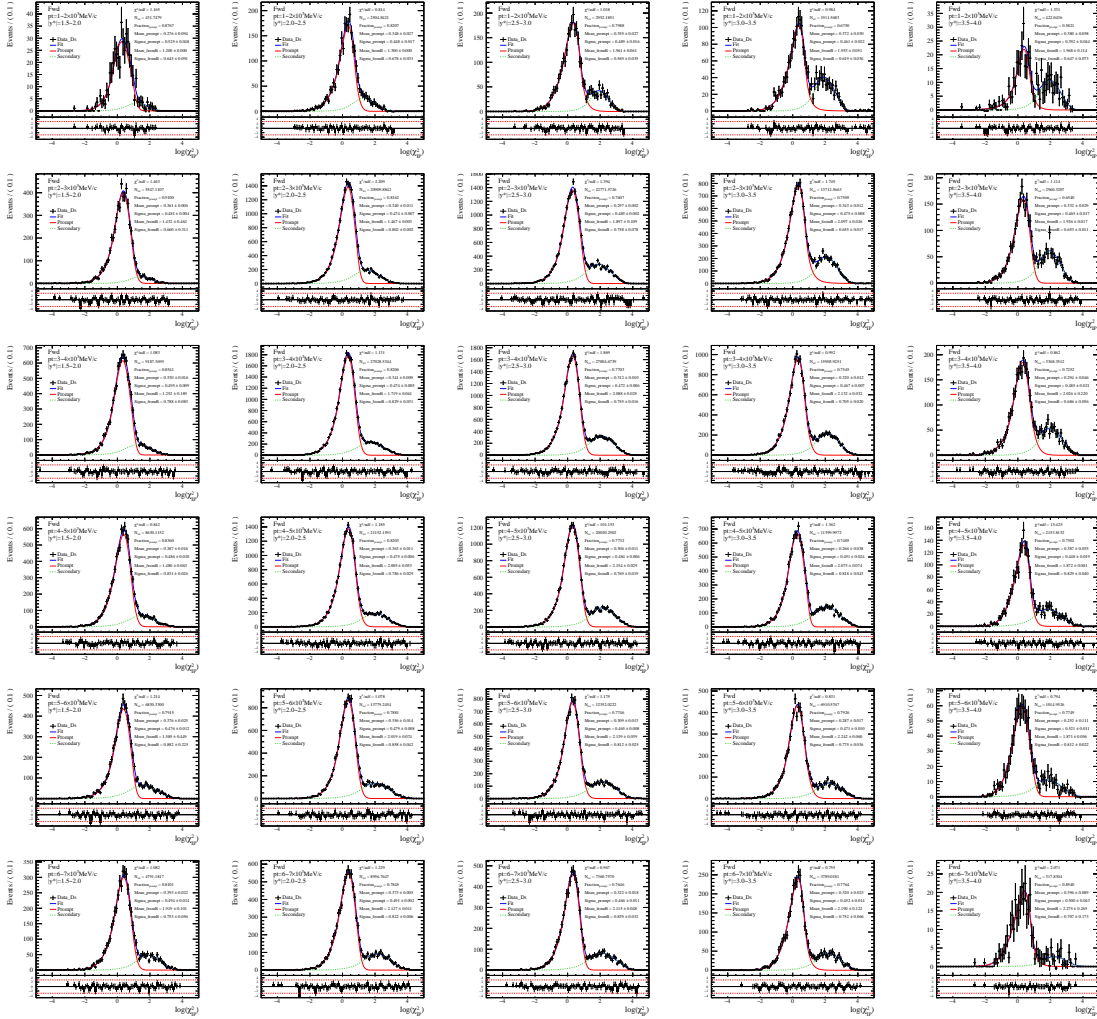


Figure D.1 $\text{log}_{10}\chi_{\text{IP}}^2(D_s^+)$ fit result in each p_T and y^* bin in the Fwd sample in $1 < p_T < 7 \text{ GeV}/c$. The column runs for p_T bins, the row runs for y^* bins.

APPENDIX D $\log_{10}\chi_{IP}^2$ FIT RESULTS

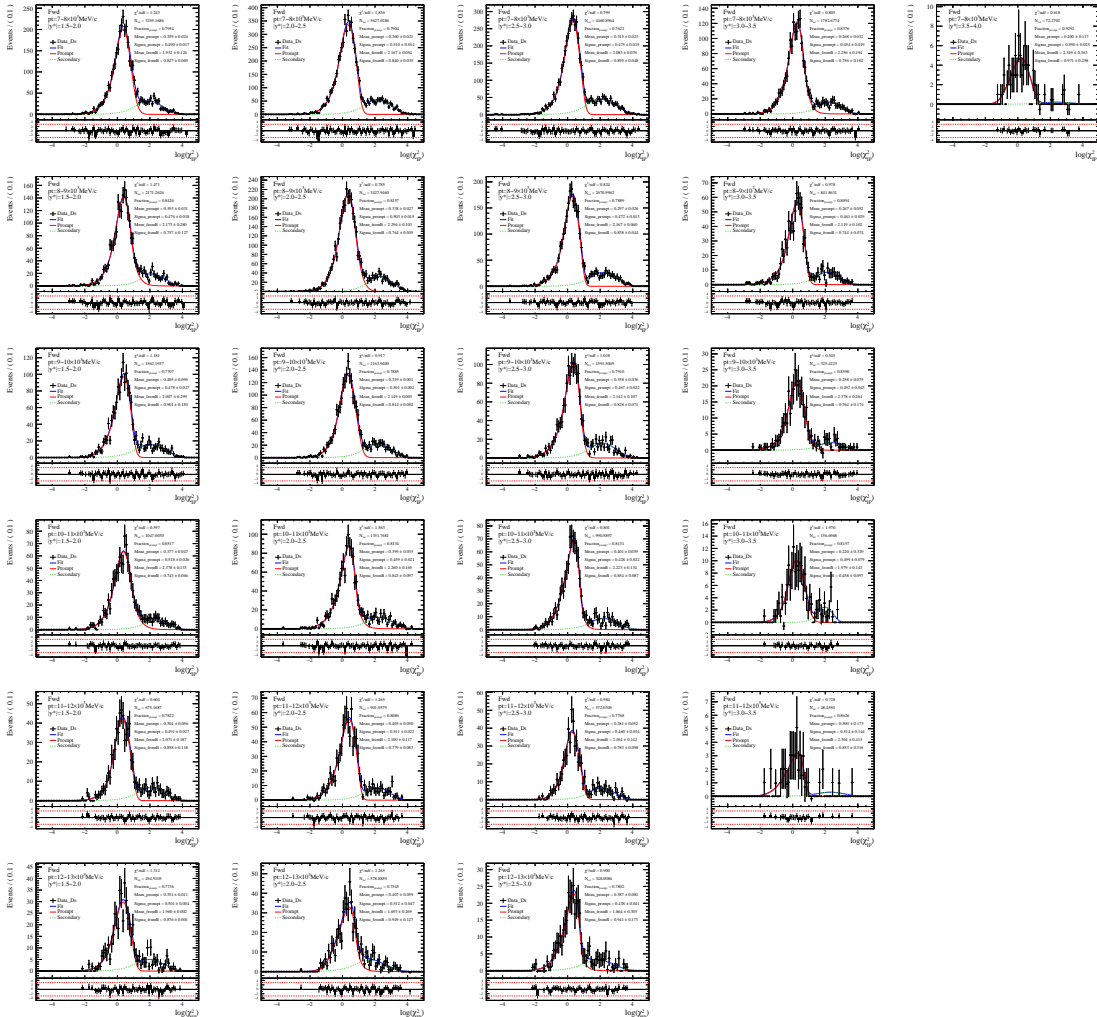


Figure D.2 $\log_{10}\chi_{IP}^2(D_s^+)$ fit result in each p_T and y^* bin in the Fwd sample in $7 < p_T < 13$ GeV/c. The column runs for p_T bins, the row runs for y^* bins.

APPENDIX D $\log_{10}\chi_{IP}^2$ FIT RESULTS

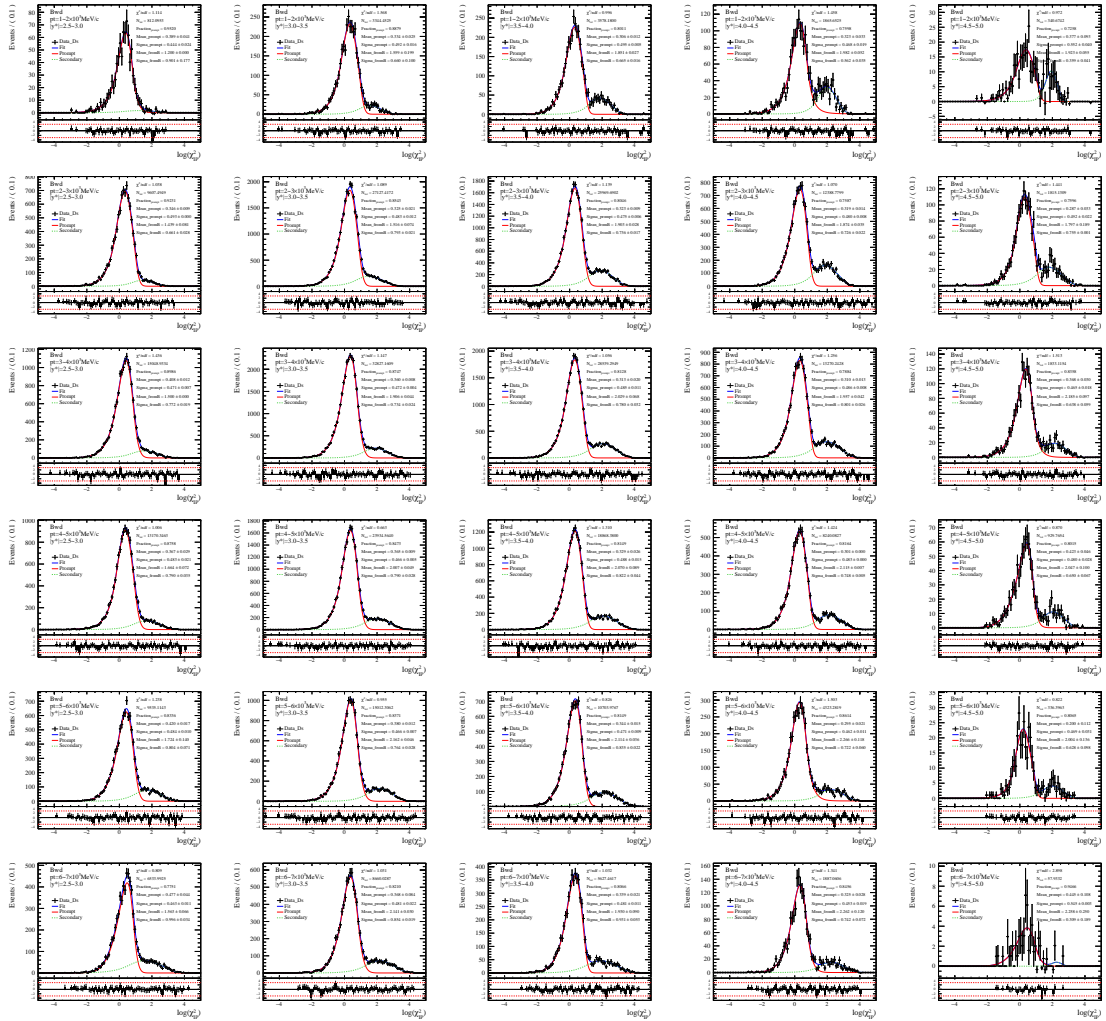


Figure D.3 $\log_{10}\chi_{IP}^2(D_s^+)$ fit result in each p_T and y^* bin in the Bwd sample in $1 < p_T < 7 \text{ GeV}/c$. The column runs for p_T bins, the row runs for y^* bins.

APPENDIX D $\text{LOG}_{10}\chi^2_{\text{IP}}$ FIT RESULTS

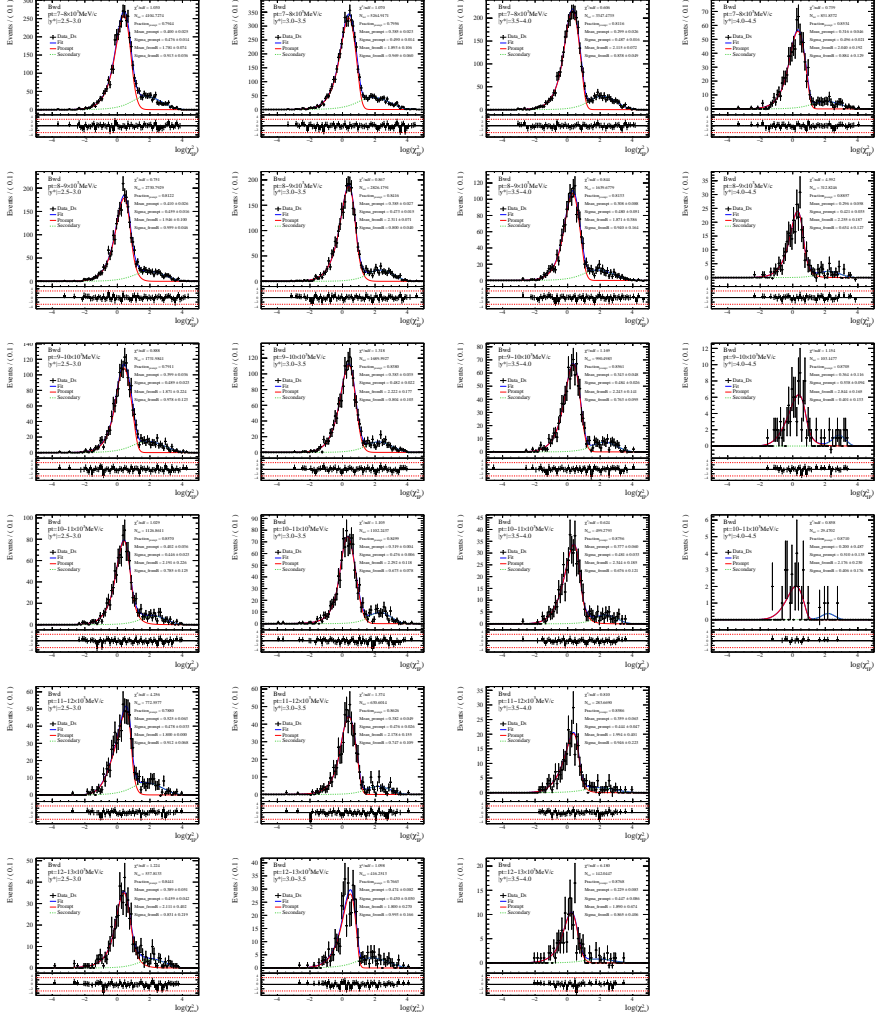


Figure D.4 $\log_{10}\chi^2_{\text{IP}}(D_s^+)$ fit result in each p_T and y^* bin in the Bwd sample in $7 < p_T < 13$ GeV/c. The column runs for p_T bins, the row runs for y^* bins.

APPENDIX D LOG₁₀χ_{IP}² FIT RESULTS

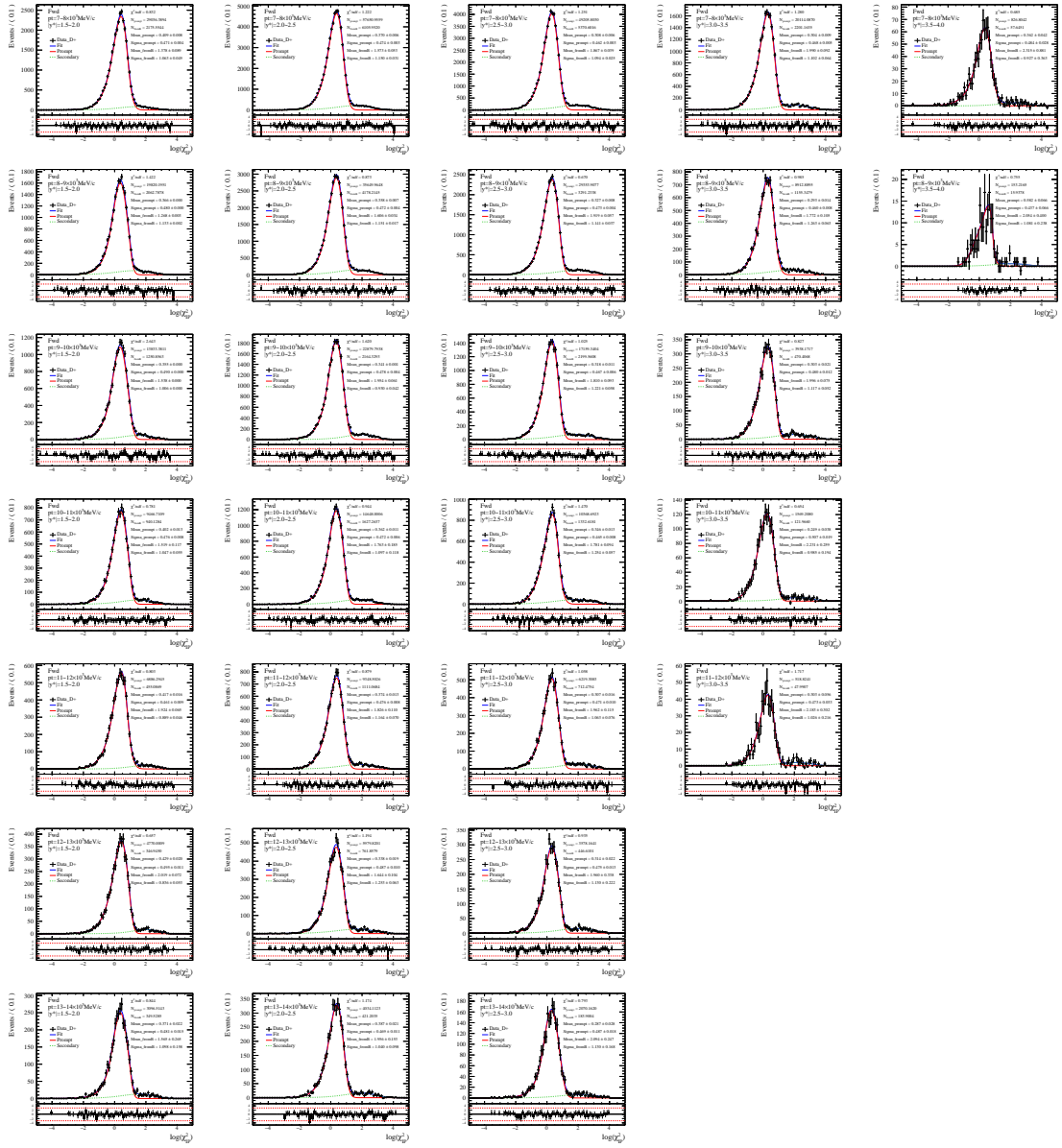


Figure D.6 $\log_{10}\chi_{IP}^2(D^+)$ fit result in each p_T and y^* bin in the Fwd sample in $7 < p_T < 14$ GeV/c. The column runs for p_T bins, the row runs for y^* bins.

APPENDIX D $\text{LOG}_{10}\chi_{\text{IP}}^2$ FIT RESULTS

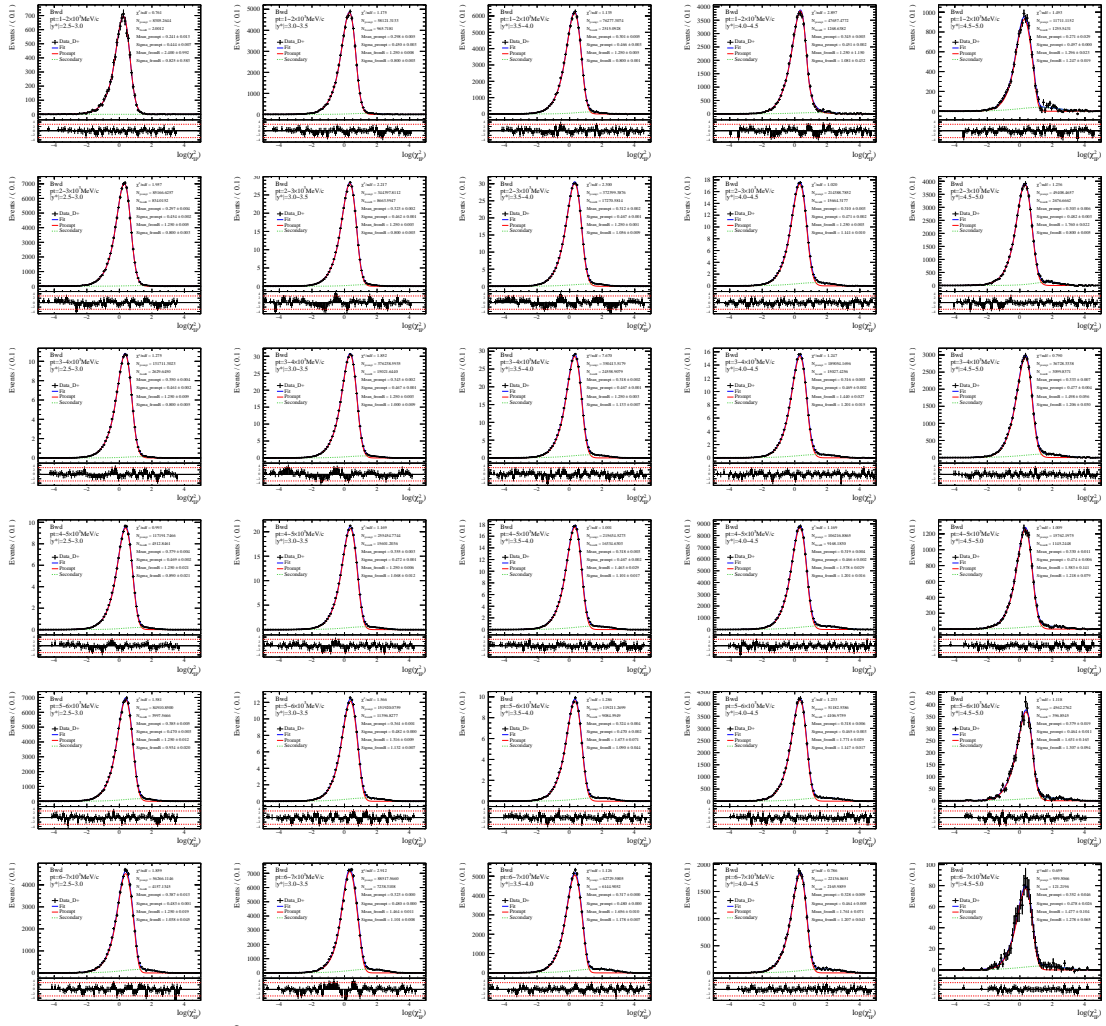


Figure D.7 $\log_{10}\chi_{\text{IP}}^2(D^+)$ fit result in each p_T and y^* bin in the Bwd sample in $1 < p_T < 7 \text{ GeV}/c$. The column runs for p_T bins, the row runs for y^* bins.

APPENDIX D $\text{LOG}_{10}\chi_{IP}^2$ FIT RESULTS

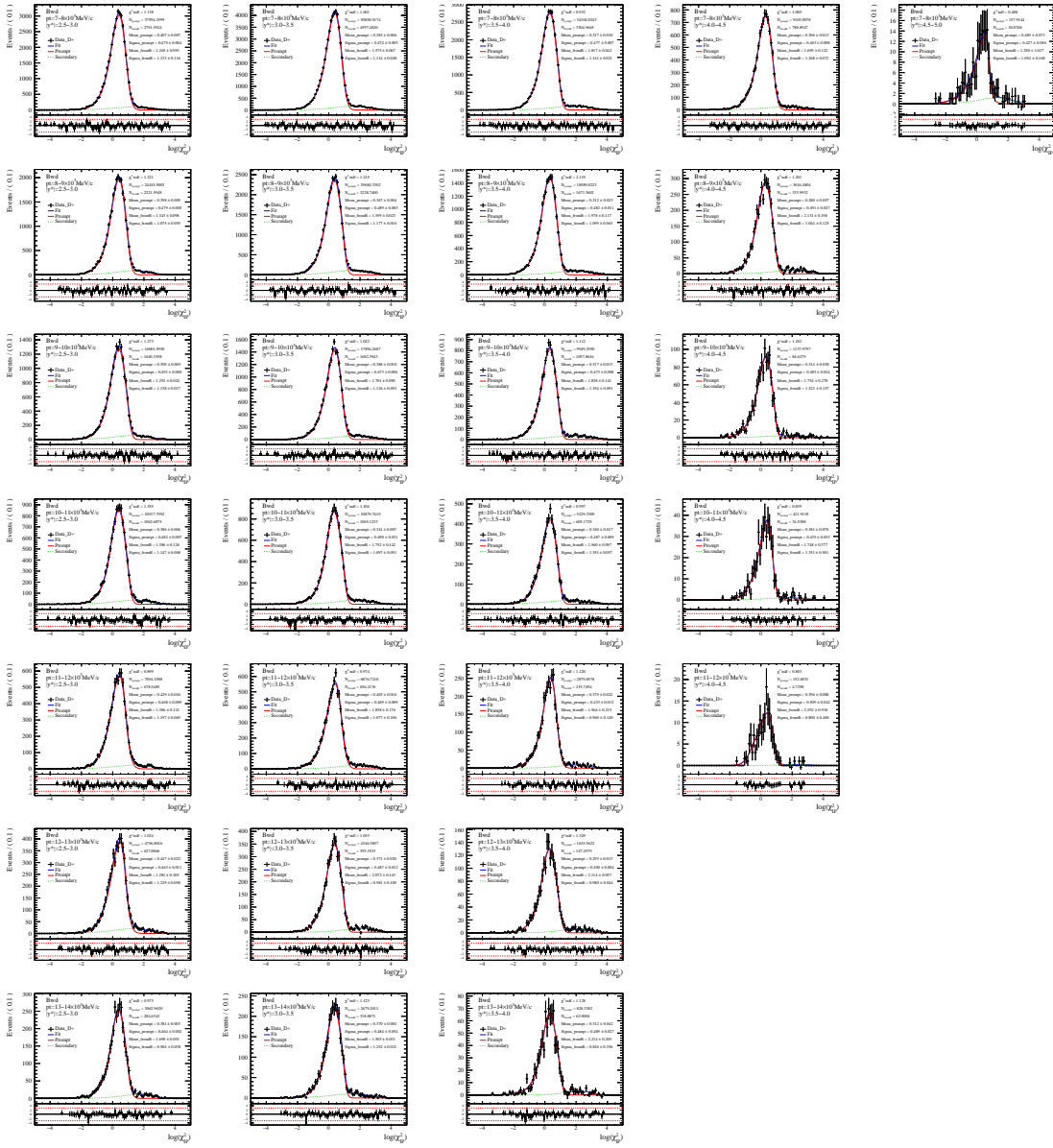


Figure D.8 $\log_{10}\chi_{IP}^2(D^+)$ fit result in each p_T and y^* bin in the Bwd sample in $7 < p_T < 14$ GeV/c. The column runs for p_T bins, the row runs for y^* bins.

APPENDIX E THE INTERPOLATION OF D_S^+ AND D^+ CROSS-SECTIONS IN PP AT 8.16 TEV

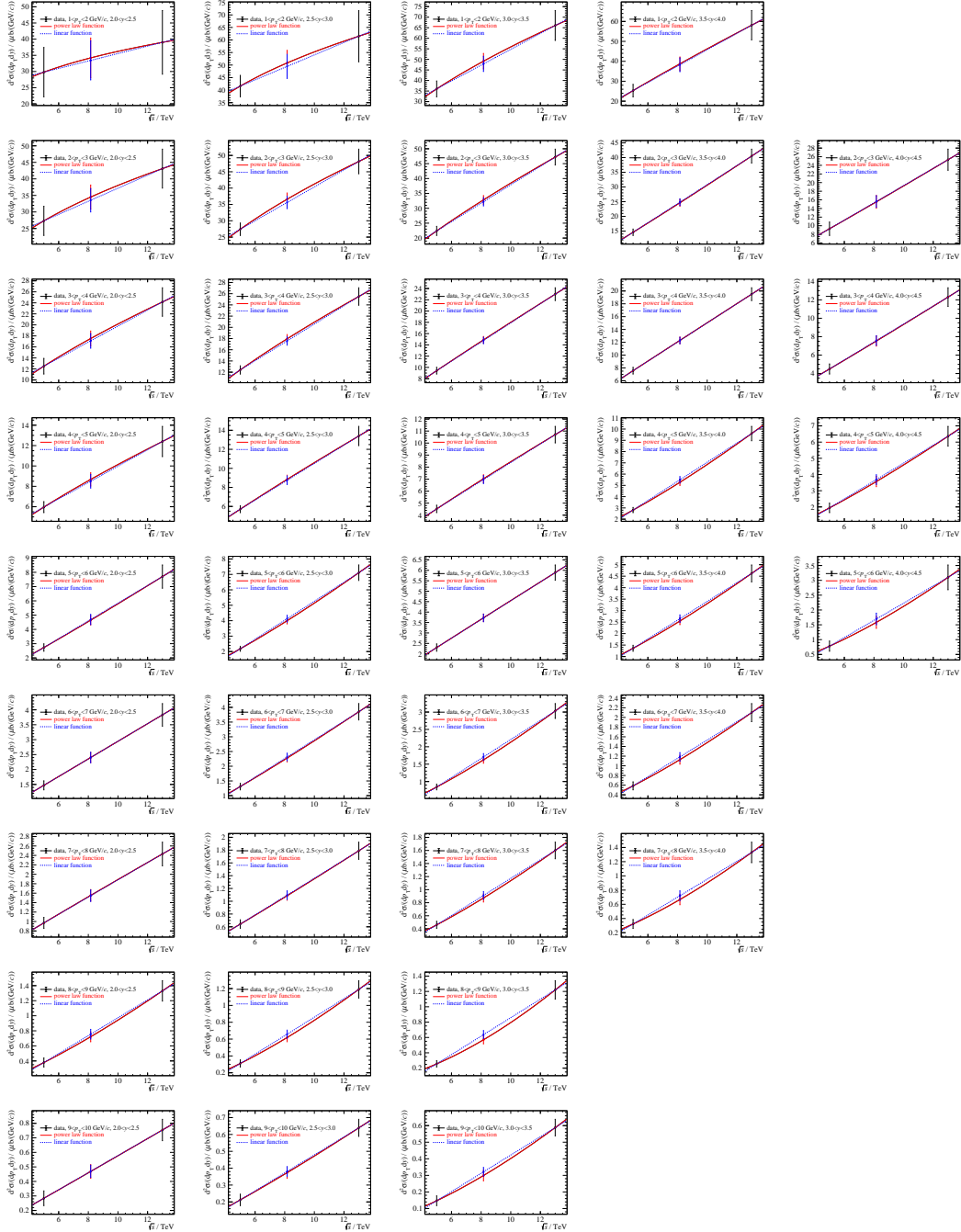


Figure E.1 The interpolation of D_S^+ cross-sections in pp at 8.16 TeV with a power function and a linear function in rapidity range $1 < p_T < 10 \text{ GeV}/c$ and $2.0 < y^* < 4.5$. The data points are LHCb result at 5,13 TeV. The column runs for p_T bins, the row runs for y^* bins.

APPENDIX E THE INTERPOLATION OF D_S^+ AND D^+ CROSS-SECTIONS IN PP AT 8.16 TEV

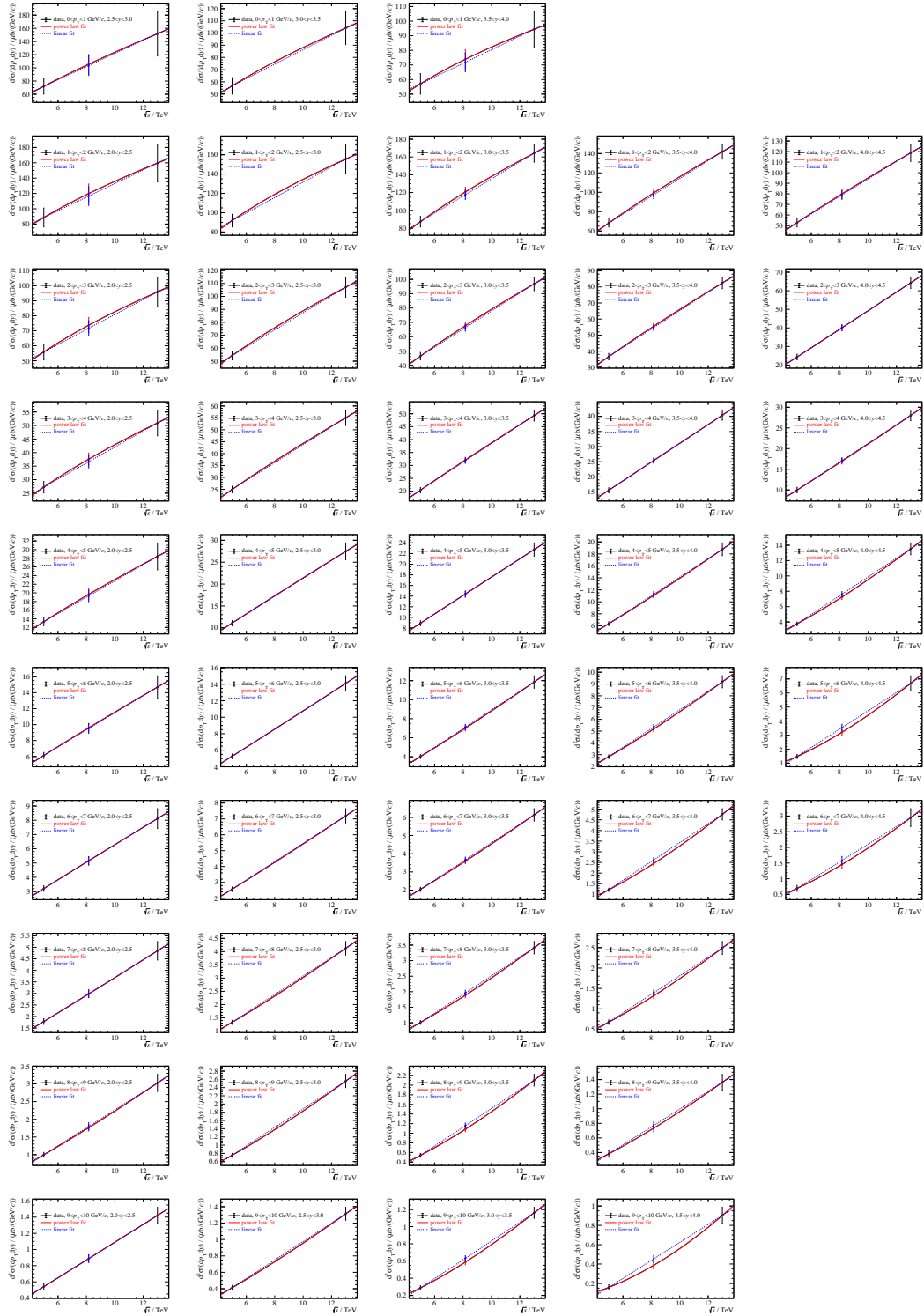


Figure E.2 The interpolation of D^+ cross-sections in pp at 8.16 TeV with a power function and a linear function in rapidity range $0 < p_T < 10 \text{ GeV}/c$ and $2.0 < y^* < 4.5$. The data points are LHCb result at 5,13 TeV. The column runs for p_T bins, the row runs for y^* bins.

ACKNOWLEDGEMENTS

最需要感谢的是我自己，在读博的这五年里没有放弃爱我和关心我的人。

很不幸，我生在了一个迟滞的时代，而我也无力推动它前行。走在命运安排的道路上，一眼就能看到头，所以我是麻木的。我期待路边偶尔出现的花朵，但大多数时候遇到的是坑。有些时候能从坑里爬出来，有些时候爬不出来。但这都不重要，因为爬出来只会给你带来些许快感，还要继续接受折磨；没有爬出来，也没什么关系，至少对我来说是这样。躺着何尝不是一种解脱，投降主义也没什么不妥。不过稍微高级一点的技巧就是通过现有经验，学会避坑。这个技能似乎不光需要经验的积累，还需要精神和物质的自由。但是这个世界是荒诞的，它表面崇尚一套逻辑，背后运行是另一套，仅靠闪避是不够的，你需要带上皮套，但很快你会发现皮套在保护你的同时也会让你恶心反胃，这本质上还是来自这个世界的荒诞。说的太虚无了，收一收，博士五年给我带来的最大的收获就是：人生不易，及时行乐，多做让自己感到快乐的事，来麻痹对世界的厌恶。

在学术上，非常感谢导师朱相雷和北大研究员张艳席，是他们在我对学术迷茫的时候，给我指明了更多可延伸的方向，也给了我很多很好的机会，让我在被生活折磨的同时体会到一些科研的快乐。同时也要感谢孙佳音、王梦臻、陈晨、罗毅恒、王剑桥，他们在我遇到科研上的具体问题的時候总是“耐心的”给予帮助。除了这些大点贡献者还有很多小点贡献者，我没有一一列举并不代表不心怀感激。

在生活上，非常感谢我的父母对我的理解和支持，你们也是我一直不放弃的源泉。不过似乎不需要用文字来证明些什么。

此外还要特别感谢 Aimer、Milet、Utada Hikaru、Miyuki Nakajima、Nakashima Mika、Aimyon、Lisa Ono、Mika Kobayashi、Mizuki、OOR、RADWIMPS、Sawano Hiroyuki、Kajiura Yuki、Seiji Ozawa、Itzhak Perlman、Mozart、Bach、Maria Callas、Vivaldi、Pavarotti、Puccini、Debussy、Chopin、Dvorak、Ludovico、Adele、Lana Del Rey、Taylor Swift、Rihanna、马友友、上海彩虹室内合唱团、告五人、周杰伦、林俊杰、孙燕姿。你们的作品总能满足我的情绪，给我力量让我平静。

jiayou a chun yu, shi yu yuan wei.

要写结尾了，我也不知道写些什么了，但依照八股文的样式多少得写点，你看写着写着都快顶行了，就这样吧。

声 明

声 明

本人郑重声明：所呈交的学位论文，是本人在导师指导下，独立进行研究工作所取得的成果。尽我所知，除文中已经注明引用的内容外，本学位论文的研究成果不包含任何他人享有著作权的内容。对本论文所涉及的研究工作做出贡献的其他个人和集体，均已在文中以明确方式标明。

签 名：李晨曦 日 期：2022.10.28

RESUME

个人简历

1995年7月1日出生于湖南省湘潭市。

2013年9月考入清华大学物理系数理基科专业，2017年7月本科毕业并获得理学学士学位。

2017年9月免试进入清华大学工程物理系攻读物理学博士至今。

在学期间完成的相关学术成果

无

COMMENTS FROM THESIS SUPERVISOR

论文提出了.....

RESOLUTION OF THESIS DEFENSE COMMITTEE

论文提出了.....

论文取得的主要创新性成果包括:

1.
2.
3.

论文工作表明作者在 ××××× 具有 ××××× 知识, 具有 ×××× 能力, 论文 ××××, 答辩 ××××。

答辩委员会表决, (× 票/一致) 同意通过论文答辩, 并建议授予 ××× (姓名) ××× (门类) 学博士/硕士学位。